SCATTERING AMPLITUDES FOR ZZ PRODUCTION AT THE LHC AND TOP-QUARK MASS EFFECTS

By

Bakul Agarwal

A DISSERTATION

Submitted to
Michigan State University
in partial fulfillment of the requirements
for the degree of

Physics—Doctor of Philosophy

2022

ABSTRACT

SCATTERING AMPLITUDES FOR ZZ PRODUCTION AT THE LHC AND TOP-QUARK MASS EFFECTS

By

Bakul Agarwal

With the Large Hadron Collider providing experimental data with unprecedented precision, theoretical predictions must improve similarly to keep up. Among a plethora of processes being studied at the LHC, the production of a pair of vector bosons is of particular importance. Consequently, precise theoretical predictions for these processes are necessary. This thesis discusses primarily the calculation of ZZ production through gluon fusion at 2-loops with full top-quark mass dependence as well as the technological improvements required to successfully perform the calculation. Also discussed briefly is the quark initiated production of $\gamma\gamma + \text{jet}$ at 2-loops where some of these technologies allowed to overcome prior bottlenecks in the calculation of the helicity amplitudes.

The 2-loop corrections for ZZ production through massless quarks had been known; in this work, the 2-loop corrections through the massive top quark are calculated . To achieve this, a new algorithm to systematically construct linear combinations of integrals with a convergent parametric integral representation is developed. This algorithm finds linear combinations of general integrals with numerators, dots, and dimension shifts as well as integrals from subsectors.

To express the amplitudes in terms of these integrals, Integration-By-Parts (IBP) reduction is performed making use of syzygies and finite field based methods. A new algorithm is employed to construct these syzygies using linear algebra. The IBP reductions for $gg \to ZZ$ are successfully performed using these techniques. Further improvements, including predetermining the structure of the coefficients in IBP reductions, are used to successfully perform the reductions for $\gamma\gamma + jet$. Multivariate partial fractioning is used to simplify the final expressions to more manageable forms and render them suitable for fast numerical evaluation.

In the case of $gg \to ZZ$, due to the presence of structures beyond polylogarithms, sector decomposition is employed to numerically evaluate the finite master integrals. Evaluating the amplitudes, agreement is found with previously calculated expansions specifically in the limit of large and small top mass. Improved results are presented for scattering at intermediate energies and/or for non-central scattering angles. With this calculation, the last building block required for the calculation of the full NLO cross-section for $gg \to ZZ$ is known.

Dedicated to my parents.

ACKNOWLEDGEMENTS

The process of obtaining this Ph.D. has been long and gruelling and it would have been impossible without the people who have assisted or influenced me during this journey. It is hard to overstate the importance of a support group and I cannot thank enough everyone who has been a part of mine.

My parents, without whom none of this would be possible, have been incredibly supportive throughout these past years and have always believed in me, even when I have not, and all the sacrifices they have made through their lives have enabled me to make the choices I have. My friends also deserve my gratitude for providing the support I needed during difficult times and giving me the comfort and encouragement when I needed it the most. Special thanks to my little cousin sisters Aanya and Tanya for being a source of cheer and comfort throughout this time.

My journey in Physics wouldn't have even started if not for Pankaj Jain; he has my eternal gratitude. I would like to thank C-.P. Yuan for giving me the opportunity to work with him in the initial years of my Ph.D. I have had a lot of discussions about physics with him over the years and I have thoroughly enjoyed all of them, in addition to learning a lot. He has been very influential during my time at MSU; his idea that Ph.D. students should be able to teach their advisors something at the end of their program has been a guiding principle for me. He puts strong emphasis on having a broad base of knowledge about other areas of research, something I will continue to improve upon.

I would also like to thank the department and the High Energy Physics group. communication between the theorists and the experimentalists in the group has always been great. This has made sure that I am aware of the experimental side of things. My coworkers throughout my Ph.D. have been immensely helpful, both concerning my immediate research as well as topics of broader interest. I would especially like to thank Joshua Isaacson; as a senior graduate student during the time I joined, his guidance and friendship have been

invaluable. He was always keen to discuss physics with me and point me to the right direction whenever I had any doubts, physics or otherwise. I would also like to thank Kirtimaan Mohan, Robert Schabinger, and Jan Winter for always entertaining all the stupid questions I had and providing me with answers, as well as providing valuable moral support, and I cannot thank Rob enough for patiently teaching me things when I needed them. Stephen Jones, my collaborator for a large portion of this work, has been of great help and it'd have been much harder for me to finish this work without his involvement.

I would like to thank Kim Crosslan and Brenda Wenzlick for being amazing, and it is hard to exaggerate how helpful they have been in tackling the MSU bureaucracy. My time at MSU has been made so much easier because of them. Also, my thanks to the members of my thesis committee for being a part of my Ph.D. and for all their helpful comments.

Finally, I would like to thank my advisor Andreas von Manteuffel for providing me with all the knowledge and tools needed to perform my research. I consider myself incredibly lucky to have him as my advisor; he has been an amazing mentor and a constant guide throughout. His depth of knowledge and expertise of the subject always amazes me. I have learned a lot from him during this time, and he has always been very receptive to all the new ideas I've had. His attitude towards solving problems, consistent effort to improving efficiency, and incredible attention to detail are some of the qualities I strive to emulate.

TABLE OF CONTENTS

LIST OF TABLES

LIST OF FIGURES

LIST OF ALGORITHMS

Chapter 1

The Standard Model and perturbative calculations

1.1 Introduction

The Standard Model of particle physics provides a fundamental description of the universe at the smallest scales accessible to us. It provides a "unified" prescription of the electromagnetic, weak nuclear, and strong nuclear forces and, along with General Relativity, describes almost all known physical phenomena. Many excellent predictions have been made to date using the Standard Model with one of the most successful being the anomalous magnetic moment $g-2$ of the electron which is calculated to 10 digits of relative precision [15, 16]. Incredibly, the experimentally measured value [17], which is also one of the most precise measurements to date and of comparable precision, shows excellent agreement with the Standard Model prediction.

The field of subatomic physics started with the discovery of the electron in 1897 using a simple cathode ray tube. Since then, many more new particles have been discovered, most of them composite. The last puzzle of the Standard Model was solved in July 2012 with the discovery of the Higgs Boson [9, 10]. Predicted in 1964 [18–21], the Higgs Boson completed the Standard Model and answered the longstanding question of the origin of gauge boson masses.

The Standard Model roster can be divided into two groups: bosons and fermions. Bosons are integer spin particles and usually appear as force carriers in gauge theories. The photon

Fermions				Bosons
Leptons	ν_e	ν_μ	ν_τ	$W^\pm, Z$
	e^-	μ^-	τ^-	γ
Quarks	u	c	t	g
	d	s	b	h

Table 1.1: Standard Model Particles.

is the force carrier for the electromagnetic force, gluon is the mediator of strong force, and $W^\pm, Z$ are the mediators for the weak force; all known force-carriers are spin-1 particles. Fermions are half-integer spin particles; electrons, protons, and neutrons make up almost all of the visible mass in the universe; protons and neutrons are composite though and themselves composed of quarks and gluons bound together through the strong force. All the fermions also have corresponding anti-particles e.g. positron is the anti-particle of the electron. Anti-particles are characterised by one or more of their quantum numbers having the opposite sign compared to the corresponding particles. The positron e.g. is positively charged, opposite to the electron. Neutrons are neutral, but they posses another quantum number called Baryon number which is $+1$ for the neutron and -1 for the antineutron. Quarks interact through all three forces: strong, weak, and electromagnetic. Electrons, muons, and tau particles do not possess the colour charge and only interact with the weak and electromagnetic forces, while neutrinos are neutral and only interact weakly. The list of Standard Model particles is given in Tab. 1.1.

However, despite its many successes, the Standard Model falls short on many accounts. Perhaps the biggest deficiency is the lack of a viable dark matter [22–25] candidate in the Standard Model. Dark matter accounts for $\sim 80\%$ of the non-relativistic matter content in the universe which is unexplained by the Standard Model. It also does not explain Dark energy [26] which makes up $\sim 70\%$ of the energy density in the universe. The origin of neutrino masses [27] is still a mystery, and while adding a mass term involving right-handed neutrinos is not forbidden in the Standard Model, such a particle would never interact with the rest of the Standard Model particles and is of little consequence. In any case, the extremely

small masses of the neutrinos compared to the rest of the Standard Model roster remain unexplained. Other issues include the Hierarchy problem [28, 29], lack of CP violation in the strong sector [30], and matter anti-matter asymmetry [31] which cannot be explained by the existing CP violation in the weak sector. Consequently, it is of extreme importance to have precise theoretical predictions for physical observables in the Standard Model. Comparing these theoretical predictions to experimental measurements, any deviations would signal existence of some new physics; as such, precision calculations are essential for the particle physics program.

At collider experiments such as the Large Electron-Positron collider (LEP) and the Large Hadron Collider (LHC), the physical observables of interest are scattering cross-sections for various scattering processes such as $e^+e^- \to \mu^+\mu^-$ at the LEP or $pp \to \mu^+\mu^-$ at the LHC. These cross-sections are calculated in quantum field theory using scattering amplitudes. In the case of lepton colliders such as LEP the scattering amplitudes are sufficient (ignoring for the moment parton showers, jet algorithms, etc for hadronic final states). However for the hadron colliders such as the LHC, the situation is not so straightforward.

Hadrons are composite particles composed of quarks and gluons, referred to as "partons" [32]. At very high energies such as at the LHC the constituent particles of the hadrons are undergoing the actual "collisions". This high-energy or short-distance physics is well described using perturbative quantum field theory and is the focus of this work. The long-distance physics inside the hadrons cannot be described using perturbative quantum field theory since at such low energies, Quantum Chromo-Dynamics enters the non-perturbative regime; the expansion parameter, in this case the strong coupling constant α_S, becomes too large. The general expression for a collision between two hadrons h_1, h_2 producing particles c, d in the final state can be written as [1]

$$d\sigma^{h_1 h_2 \to cd} = \int_0^1 \mathrm{d}x_1 \mathrm{d}x_2 \sum_{a,b} f_{a/h_1}(x_1, \mu_F^2) f_{b/h_2}(x_2, \mu_F^2)\, d\hat{\sigma}^{ab\to cd}(Q^2, \mu_F^2) \tag{1.1.1}$$

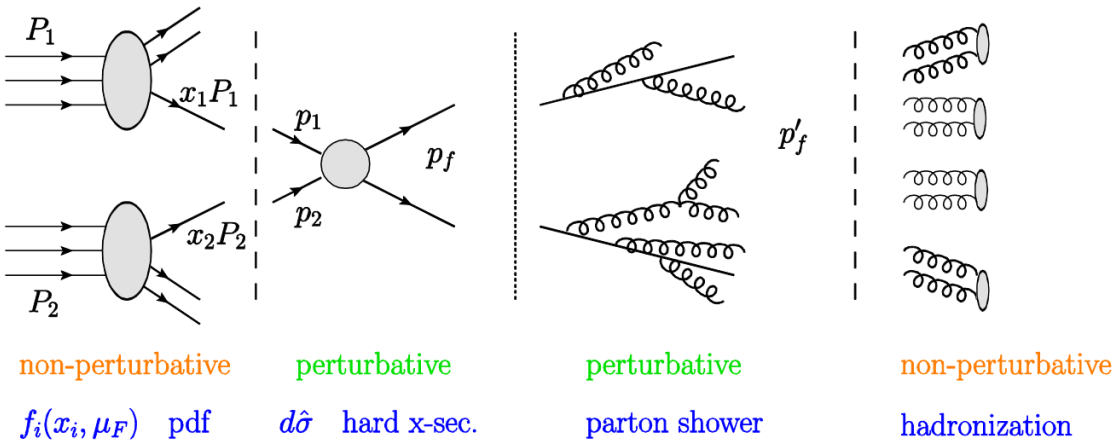

Figure 1.1: Schematic of a scattering process at a hadron collider. For the LHC, the incoming particles are both protons. Reproduced from [7].

where the functions f_{a/h_1}, f_{b/h_2} are the so-called "Parton Distribution Functions" and encode the long-distance physics of the hadrons, and the quantity $d\hat{\sigma}^{ab\to cd}$ denotes the partonic cross-section for the collision process $ab \to cd$ between the partons a, b originating from the hadrons h_1, h_2 respectively and contains the short-distance physics of point-like particle collisions. The above formula splitting the calculation of the short and long distance physics into two separate pieces is based on the factorisation theorem (see Sec. 1.5.7). While it is not known if it is in general possible to treat these two parts of the calculation completely independently, for some processes such as the Drell-Yan process it has been proven that the short-distance physics of the partonic collisions can be "factored" out of the long-distance physics governing hadrons according to the above formula.

Consider the scattering process $pp \to ZZ + X$ at the LHC where X could correspond to any number of jets. The actual scattering process looks similar to the schematic in Fig. 1.1 with P_1 and P_2 corresponding to the momenta of the incoming protons. Since the protons are composite, and composed of quarks and gluons, the hard scattering depicted in Fig. 1.1 can be initiated through qq, qg, and gg initial states. In fact, the quark-quark initialised scattering, as shown in Fig. 1.2, starts at the lowest perturbative order in QCD. The process $gg \to ZZ$ formally only starts at NNLO for the hadronic scattering $pp \to ZZ$.

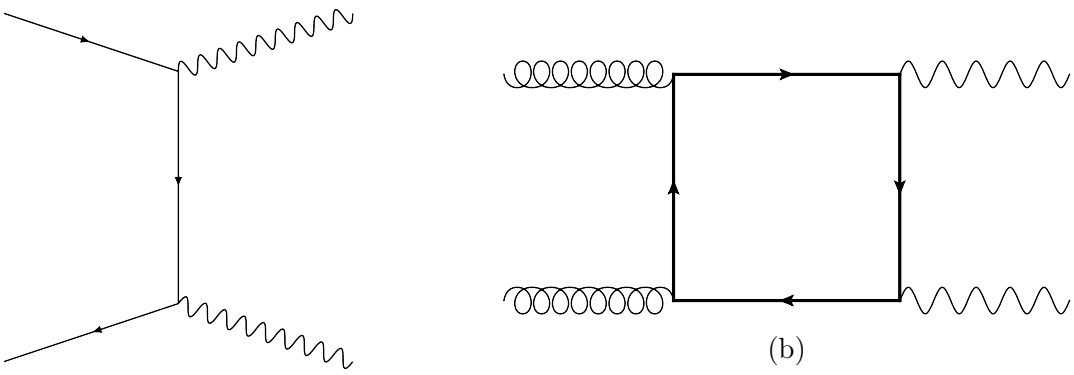

Figure 1.2: Diagrams showing ZZ production from (a) $q\overline{q}$ and (b) gg initial states. The cross section for $gg \to ZZ$ process starts at a relative order $O(\alpha_S^2)$ compared to $q\overline{q} \to ZZ$ for pp scattering.

However, it still contributes significantly to the hadronic cross-section at the LHC; this is due to the fact that the parton distribution functions for gluons, at momenta required to produce a pair of Z-bosons, are larger than those for the quarks. Thus even though the partonic hard-scattering cross-section is expected to be suppressed, the gluonic parton distribution functions compensate for that. Also at higher energies, due to the Goldstone boson equivalence theorem [33, 34], the contribution from top quarks in the loop for $gg \to ZZ$, in particular for longitudinally polarised Z bosons, becomes dominant over all other contributions. This effect is completely absent for the quark initialised process.

In this work we primarily consider the production of a pair of Z-bosons through gluon fusion i.e. $gg \to ZZ$ at 2-loops with exact dependence on the mass of the top quarks propagating through the loops. As mentioned above, the gluonic channel is significant due to large parton distribution functions for gluons at intermediate energies relevant for ZZ production. This is an essential process to be studied at the Large Hadron Collider since it serves as a background process to the Higgs signal process $gg \to h \to ZZ$. It interferes with the Higgs signal process producing a sizeable effect ($\sim 10\%$ [35, 36]). A crucial property of the Higgs boson to be measured at the LHC is its decay width. Direct measurement of the

decay width of the Higgs boson through the resonance peak is limited at the LHC due to the detector resolution ($\sim$ 1 GeV) being much larger compared to the Standard Model value of the width ($\sim$ 4 MeV). An alternate approach to constrain the Higgs width using both on-shell and off-shell Higgs production was proposed in [37]; precisely measuring $gg \to ZZ$ is a crucial component of that. ZZ production also serves as a channel for new physics searches where heavy resonances decay to a pair of Z-bosons. Additionally, the longitudinal modes of the Z-bosons are sensitive to their axial-vector couplings to the fermions; this can be used to constrain anomalous $t\bar{t}Z$ couplings [38, 39]. It is clear that pair production of Z bosons provides multiple avenues to better and more precisely understand the Standard Model.

This work presents the first calculation of helicity amplitudes for $gg \to ZZ$ at 2-loops with full dependence on the top-quark mass. Prior to this, the amplitudes were known exactly only for massless internal quarks and the contributions for top quarks were calculated only using certain approximations. The text describes the steps and techniques used to calculate the scattering amplitudes for this process including some new techniques which facilitated the calculation. The tensor decomposition of the amplitude is described followed by syzygy-based Integration-By-Parts reduction techniques used to reduce the amplitudes. For efficient numerical evaluation of the master integrals, a basis of finite integrals is chosen based on a new technique of combining divergent integrals into finite linear combinations. A method for multivariate partial fractioning to simplify the analytic expressions is described as well.

Note that in this work, only on-shell Z-bosons in the final state are considered; in the future, off-shell Z-bosons as well as the W-bosons may be included in the final state to increase the scope of the calculation. Also, the focus of this work is the calculation of scattering amplitudes for $gg \to ZZ$ To provide meaningful physical predictions, cross sections and distributions need to be calculated; this is left for future work.

1.2 Discovery of the Higgs Boson

1.2.1 Higgs mechanism

Late 1940s and 1950s saw tremendous progress in the field of particle physics. The Dirac equation predicted the magnetic moment of the electron but the experimental measurements indicated a slight deviation. Gauge theories [40] were eventually developed and were incredibly successful in making precise theoretical predictions, especially with the development of the theory of renormalisation. Quantum Electrodynamics successfully predicted the anomalous magnetic moment of the electron as well as the Lamb Shift paving the way for future work in precision calculations and marking another achievement for Quantum theory. Pions, proposed as the force carriers in the Yukawa potential governing the strong nuclear force, were discovered with the masses predicted by theory. A still unsolved puzzle, however, was the origin of masses for force carriers of the weak nuclear force, which were known from experiments to be massive. No consistent way to generate masses for the gauge bosons while preserving the gauge symmetry was known at the time. Another issue was that the scattering of W and Z bosons violated unitarity. Scattering amplitude for the longitudinal modes of W and Z bosons grows with energy indefinitely. Consider $W_L^+W_L^-$ scattering as depicted in Fig. 1.3

$$\mathcal{M}(W_L^+W_L^- \to W_L^+W_L^-) = \mathcal{M}_t + \mathcal{M}_{4pt} + \mathcal{M}_s \,. \tag{1.2.1}$$

Calculating the individual contributions, the 4-point vertex amplitude (Fig. 1.3c) is

$$\begin{aligned}\mathcal{M}_{4pt} =& ig_w^2(2g_{\mu\rho}g_{\nu\sigma} - g_{\mu\nu}g_{\rho\sigma} - g_{\mu\sigma}g_{\nu\rho})\epsilon_L^\mu(p_1)\epsilon_L^\nu(p_2)\epsilon_L^\rho(p_3)\epsilon_L^\sigma(p_4) \\ =& \frac{g^2\left(-5 - 12\cos\theta + \cos 2\theta\right)}{32}\left(\frac{s}{m_W^2}\right)^2 + \frac{g^2\left(1 + 3\cos\theta\right)}{2}\left(\frac{s}{m_W^2}\right) \\ &+ O\left(\frac{s}{m_W^2}\right)^0 ,\end{aligned} \tag{1.2.2}$$

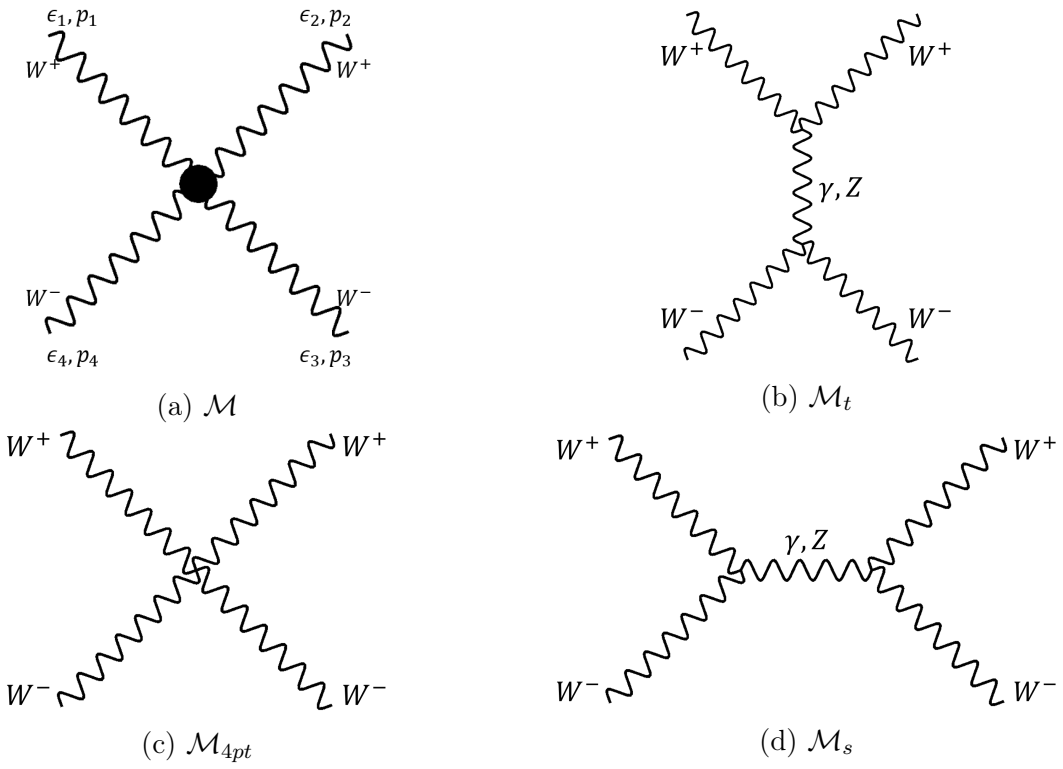

(a) $\mathcal{M}$ (b) $\mathcal{M}_t$

(c) $\mathcal{M}_{4pt}$ (d) $\mathcal{M}_s$

Figure 1.3: WW scattering with the 3 different subprocesses depicted.

where $s = 4E_{cm}^2$ is the Mandelstam variable, the amplitude for s-channel γ, Z exchange (Fig. 1.3d) is

$$\mathcal{M}_s = -\frac{g^2 \cos\theta}{4}\left(\frac{s}{m_W^2}\right)^2 + \frac{7g^2\cos\theta}{4}\left(\frac{s}{m_W^2}\right) + O\left(\frac{s}{m_W^2}\right)^0, \tag{1.2.3}$$

and for the t-channel γ, Z exchange (Fig. 1.3b) is

$$\mathcal{M}_t = \frac{g^2\left(-3+\cos\theta\right)\left(1+\cos\theta\right)}{16}\left(\frac{s}{m_W^2}\right)^2 + \frac{g^2\left(3-\cos\theta\right)}{8}\left(\frac{s}{m_W^2}\right) + O\left(\frac{s}{m_W^2}\right)^0, \tag{1.2.4}$$

where $\cos\theta$ is the scattering angle. Adding the three contributions together,

$$\mathcal{M}(W_L^+W_L^- \to W_L^+W_L^-)_{gauge} = \frac{g^2(1-\cos\theta)}{8}\left(\frac{s}{m_W^2}\right) + O\left(\frac{s}{m_W^2}\right)^0. \tag{1.2.5}$$

The E^4/m_w^4 terms drop out after adding all the different contributions. However, the remainder still grows with energy as $\sim E^2/m_W^2$. Non-unitary behaviour of this kind suggested a missing piece. The answer was found through the field of condensed matter physics in spontaneous symmetry breaking [41].

As a consequence of spontaneous symmetry breaking, Nambu-Goldstone bosons [41, 42] are produced as excitations of the quantum field. While these bosons are themselves massless, they are "absorbed" by the gauge fields providing them with an additional longitudinal degree of freedom and a mass term. In certain cases the symmetries are explicitly broken in addition to being spontaneously broken. The resulting Goldstone bosons are no longer massless, but acquire a mass depending on how softly the symmetry is broken. These are referred to as "Pseudo Nambu-Goldstone bosons". An example is pions, which are produced through explicit breaking of the chiral symmetry in QCD due to the quark masses; this results in pions acquiring a small mass. Since the light quark masses are small ($\sim 5 - 10$ MeV), the pions as a result have a mass that is small compared to the other hadrons.

The Higgs mechanism is best demonstrated through an example. Consider the Lagrangian for a simple theory with a fermion and a spin-1 boson

$$\mathcal{L} = \overline{\psi}(i\gamma^\mu D_\mu - m)\psi - \frac{1}{4}F^{\mu\nu}F_{\mu\nu}\,. \tag{1.2.6}$$

with the covariant derivative $D_\mu = \partial_\mu + igA_\mu$. This Lagrangian is invariant under the gauge transformation given by:

$$\begin{aligned} \psi &\to e^{i\alpha(x)}\psi\,, \\ A_\mu &\to A_\mu - \frac{1}{g}\partial_\mu\alpha(x)\,. \end{aligned} \tag{1.2.7}$$

It is easy to see, however, that adding a mass term $\frac{1}{2}m^2A^2$ will break the gauge symmetry.

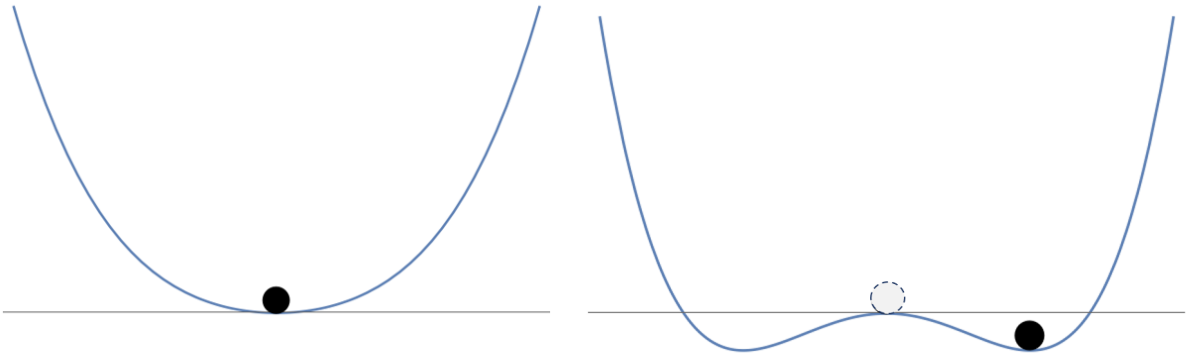

(a) $\mu^2 > 0$ (b) $\mu^2 < 0$

Figure 1.4: Scalar field Φ with two different vacuum configurations. For $\mu^2 < 0$ the vacuum state is no longer symmetric and the field acquires a non-zero expectation value.

To ameliorate this, a complex scalar field with the Lagrangian

$$\mathcal{L}_\Phi = (D^\mu \Phi)^* (D_\mu \Phi) - V(\Phi) \tag{1.2.8}$$

can be added with the potential $V(\Phi)$ given by

$$V(\Phi) = \mu^2 \Phi^* \Phi + \lambda (\Phi^* \Phi)^2 , \qquad \lambda > 0 , \tag{1.2.9}$$

with the covariant derivative D_μ ensuring that the new scalar terms of the Lagrangian are gauge invariant with the field transformation $\Phi \to e^{i\alpha(x)}\Phi$. This potential presents two interesting possibilities: For the case of $\mu^2 > 0$, the minimum of the potential is still at zero. Expanding the field Φ around the minimum point $\Phi = 0$ produces essentially the same Lagrangian in Eq. 1.2.8 and the $U(1)$ symmetry remains unbroken (Fig. 1.4a). For $\mu^2 < 0$, however, the minimum of the potential shifts away from zero (Fig. 1.4b) and the field acquires a non-zero vacuum expectation value given by

$$\langle \Phi \rangle_0 = \sqrt{-\frac{\mu^2}{2\lambda}} e^{i\alpha} \tag{1.2.10}$$

where α is some arbitrary phase. We can define the absolute value of this minimum

$$\frac{v}{\sqrt{2}} = \sqrt{-\frac{\mu^2}{2\lambda}} \tag{1.2.11}$$

as the vacuum expectation value. Expanding the field around the new minimum

$$\Phi = \left(\frac{v+\phi}{\sqrt{2}}\right) e^{i\eta(x)}\,, \tag{1.2.12}$$

where ϕ corresponds to the physical mode and η corresponds to the Goldstone mode, the scalar part of the Lagrangian becomes

$$\begin{aligned}\mathcal{L}_\Phi =& \frac{1}{2}\left(D^\mu(v+\phi)e^{i\eta(x)}\right)^*\left(D_\mu(v+\phi)e^{i\eta(x)}\right) - V(\frac{v+\phi}{\sqrt{2}}e^{i\eta(x)}) \\ =& \frac{1}{2}(\partial_\mu\phi)^2 + \frac{1}{2}\phi^2(\partial_\mu\eta)^2 + g\phi^2 A^\mu\partial_\mu\eta + gv^2A^\mu\partial_\mu\eta + 2gv\phi A^\mu\partial_\mu\eta + g^2v\phi A^2 + \frac{1}{2}g^2\phi^2A^2 \\ &+ \frac{1}{2}g^2v^2A^2 + \mu^2\phi^2 - \frac{\mu^2}{v}\phi^3 + \frac{\mu^2}{4v^2}\phi^4 + v\phi(\partial_\mu\eta)^2 + \frac{1}{2}v^2(\partial_\mu\eta)^2 + (\textit{constant terms})\,.\end{aligned} \tag{1.2.13}$$

This Lagrangian can be simplified greatly using the transformation

$$A_\mu \to A_\mu - \frac{1}{g}\partial_\mu\eta(x)\,. \tag{1.2.14}$$

This amounts to fixing the gauge for the vector boson so that $\alpha(x)$ is fixed to $\alpha(x) = \eta(x)$. With this choice of gauge, the Lagrangian becomes

$$\begin{aligned}\mathcal{L}_\Phi =& \frac{1}{2}(\partial_\mu\phi)^2 - \underbrace{\frac{1}{2}\left(-2\mu^2\right)\phi^2}_{\text{Scalar mass term}} + \underbrace{\frac{-\mu^2}{v}\phi^3 + \frac{\mu^2}{4v^2}\phi^4}_{\text{Scalar self-interaction terms}} \\ &+ \underbrace{\frac{1}{2}g^2v^2A^2}_{\text{Gauge boson mass term}} + \underbrace{g^2v\phi A^2 + \frac{1}{2}g^2\phi^2A^2}_{\text{Gauge-Scalar interaction terms}} + (\textit{constant terms})\,.\end{aligned} \tag{1.2.15}$$

Note that the field $\eta(x)$ completely disappears. The remaining scalar field is actually physical

with mass $m_\phi = \sqrt{-2\mu^2}$. The gauge boson also acquires a mass $m_A = gv$. This is colloquially referred to as the gauge boson "absorbing" the Goldstone mode; the additional degree of freedom required for the longitudinal mode of the now massive gauge boson appears through the Goldstone boson. This is referred to as the "Unitary gauge"; only the physical fields propagate in this gauge.

The Higgs mechanism, described above to generate masses for bosons in a gauge theory, was proposed in three seminal papers in 1964 by Brout and Englert [20], Higgs [18, 19, 43], and Guralnik, Hagen, and Kibble [21]. In the Abelian example above, only one Goldstone boson was generated. For non-Abelian gauge theories the number of Goldstone bosons is equal to the number of broken generators; for a spontaneously broken $SU(N)$, for example, there will be N Goldstone modes. The spontaneously broken $SU(2)_L \times U(1)_Y$ in the Standard Model generates 3 Goldstone bosons that give mass to the three vector bosons $W^\pm$ and Z. The Higgs mechanism can also explain the origin of fermion masses [44]; this can be achieved by adding a Yukawa-type interaction to the Lagrangian in Eq. 1.2.6

$$\mathcal{L} = i\overline{\psi}\not{D}\psi - y_\psi \Phi \overline{\psi}\psi - \frac{1}{4}F^{\mu\nu}F_{\mu\nu}\,. \tag{1.2.16}$$

Expanding Φ around the minimum after symmetry breaking, the Lagrangian becomes

$$\begin{aligned}\mathcal{L} =& i\overline{\psi}\not{D}\psi - \frac{y_\psi}{\sqrt{2}}(v+\phi)\overline{\psi}\psi - \frac{1}{4}F^{\mu\nu}F_{\mu\nu} \\ =& \overline{\psi}\left(i\not{D} - \frac{y_\psi v}{\sqrt{2}}\right)\psi - \frac{y_\psi}{\sqrt{2}}\phi\overline{\psi}\psi - \frac{1}{4}F^{\mu\nu}F_{\mu\nu}\,.\end{aligned} \tag{1.2.17}$$

Identifying $y_\psi v/\sqrt{2} = m_\psi$ as the fermion mass,

$$\mathcal{L} = \overline{\psi}\left(i\not{D} - m_\psi\right)\psi - \frac{m_\psi}{v}\phi\overline{\psi}\psi - \frac{1}{4}F^{\mu\nu}F_{\mu\nu}\,. \tag{1.2.18}$$

It's evident from the above equation that the interaction strength between the fermion and the scalar is proportional to the fermion mass.

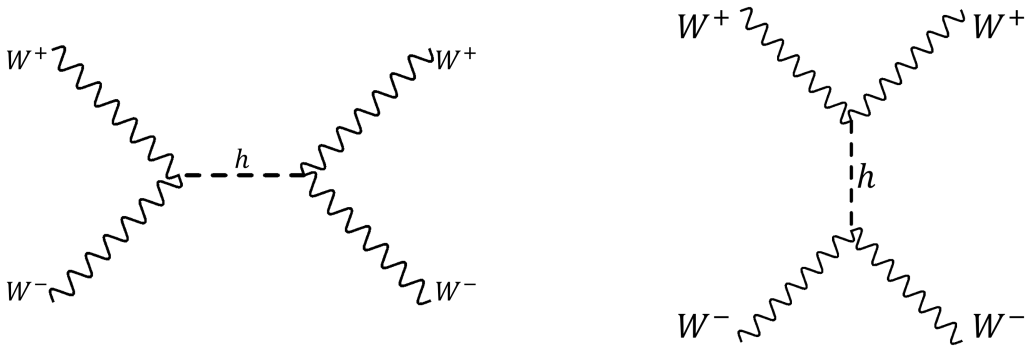

Figure 1.5: WW scattering including the interactions with the Higgs boson.

As was seen in Eq. 1.2.5, the amplitude for $W_L^+W_L^-$ scattering increases indefinitely with energy. This non-unitary behaviour is fixed after including the Higgs boson interactions

$$\mathcal{M}_h = \frac{-g^2(1-\cos\theta)}{8}\left(\frac{s}{m_W^2}\right) + O\left(\frac{s}{m_W^2}\right)^0 \tag{1.2.19}$$

which when added to the pure gauge part of the amplitude in Eq. 1.2.5 gives

$$\begin{aligned}\mathcal{M}(W_L^+W_L^- \to W_L^+W_L^-) &= \mathcal{M}_t + \mathcal{M}_{4pt} + \mathcal{M}_s + \mathcal{M}_h \\ &= O\left(\frac{s}{m_W^2}\right)^0\end{aligned} \tag{1.2.20}$$

implying that the Higgs boson unitarises gauge boson scattering.

It was mentioned previously that the longitudinal modes of the gauge bosons are essentially the Goldstone bosons appearing as a consequence of the spontaneously broken symmetry when considering the unitary gauge. This implies that any amplitude involving the longitudinal modes of the gauge bosons can be calculated by replacing the gauge boson with the corresponding Goldstone boson, known as the Goldstone boson equivalence theorem [33, 34].

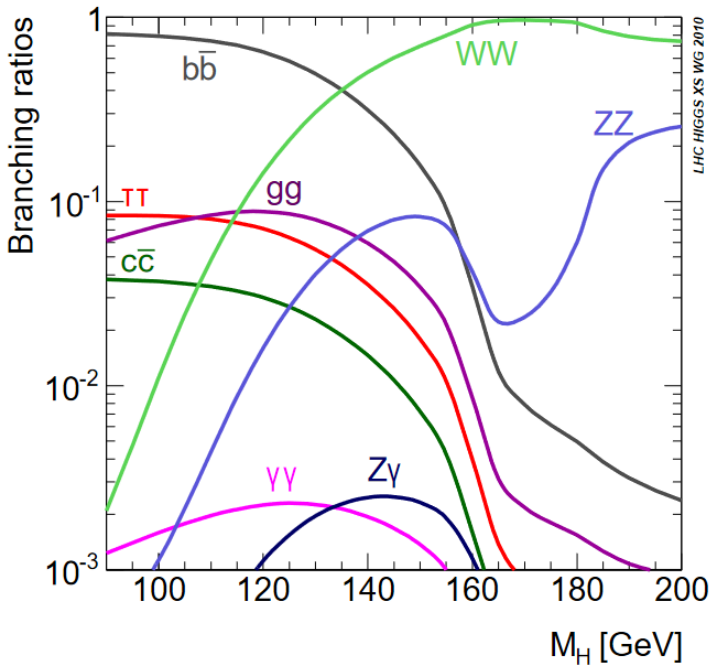

Figure 1.6: Plot of the Standard Model Higgs branching ratios against the Higgs mass. Measured value of Higgs mass is $m_h = 125.25 \pm 0.17$ GeV. Reproduced from [8].

1.2.2 Standard model Higgs

In the Standard Model, the Higgs boson appears as a part of the Higgs doublet which transforms under the $SU(2)_L \times U(1)_Y$ symmetry of the electroweak sector of the Standard model, details of which are provided in Sec. 1.6. Some of the the prominent decay modes for the Standard Model Higgs are shown in Fig. 1.6. It is clear that for the measured mass value $m_h = 125.25$ GeV [1], $h \to b\bar{b}$ is the dominant decay mode with a branching ratio of $\sim 57\%$ (Tab. 1.2). However, $b\bar{b}$ channel has a huge QCD background from production of two jets and identifying those jets as originating from b-quarks (b-tagging) is rather challenging; as such this wasn't the ideal discovery channel. Indeed the discovery of Higgs was reported in the subdominant $h \to ZZ^* \to 4l$ and $h \to \gamma\gamma$ channels [9, 10] with the resonances appearing in the invariant mass spectra (Fig. 1.7 and 1.8). The diphoton channel, $h \to \gamma\gamma$, and the $4l$ channel, $h \to ZZ^* \to 4l$, are particularly suited for discovery owing to their cleaner signature and more manageable backgrounds. Decay in the $b\bar{b}$ channel was discovered only a few years

Decay Channel	BR	Uncertainty (%)	
$h \to bb$	0.574	$+3.2$	-3.3
$h \to WW$	0.218	$+4.2$	-4.2
$h \to gg$	0.0855	$+10.2$	-10.0
$h \to \tau\tau$	0.0629	$+5.7$	-5.6
$h \to cc$	0.0289	$+12.2$	-12.2
$h \to ZZ$	0.0269	$+4.2$	-4.2
$h \to \gamma\gamma$	0.00228	$+4.9$	-4.9
$h \to Z\gamma$	0.00156	$+9.0$	-8.8

Table 1.2: Branching ratios for the Standard Model Higgs boson with $m_h = 125.25$ GeV [1]. Numbers reproduced from [2].

back [45, 46]. More recently, the rare decay $h \to \mu^+\mu^-$ has been observed [47, 48].

The primary production mode for Higgs boson at the LHC is through gluon fusion via a top quark loop (ggF) which accounts for $\sim 88\%$ of the total Higgs cross-section at the LHC with $\sigma_{ggF} = 48.6^{+4.6\%}_{-6.7\%}$ pb [2, 8, 49, 50]. This is largely due to high gluon luminosity at the LHC for low invariant mass (i.e. gluons carry most of the energy of a proton at lower energies probed by the LHC) as well as the large Yukawa coupling of the top quark with the Higgs. Other important production modes are Vector-boson-fusion (VBF) with cross-section $\sigma_{VBF} = 3.78^{+2.2\%}_{-2.2\%}$, "Higgstrahlung" where the Higgs is produced in association with a vector boson with $\sigma_{VH} = 2.25^{+4.8\%}_{-4.4\%}$, and production in association with a top-quark pair ($t\bar{t}h$) with $\sigma_{t\bar{t}h} = 0.50^{+6.8\%}_{-9.9\%}$.

So far the measured properties of the observed particle are consistent with those for the Standard Model Higgs Boson. It is a electrically neutral, spin-0 particle which transforms as a scalar under parity conjugation. It's mass has been measured to be $m_h = 125.25 \pm 0.17$ [1] GeV. The coupling of the Standard Model Higgs to other particles is proportional to the particle mass. This is indeed what has been observed at the LHC as seen in Fig. 1.9; the straight line through the experimentally measured values indicates that the couplings are consistent with the SM prediction. However, to ascertain the true nature of the Higgs boson, two key properties need to be determined precisely: Higgs potential and decay width.

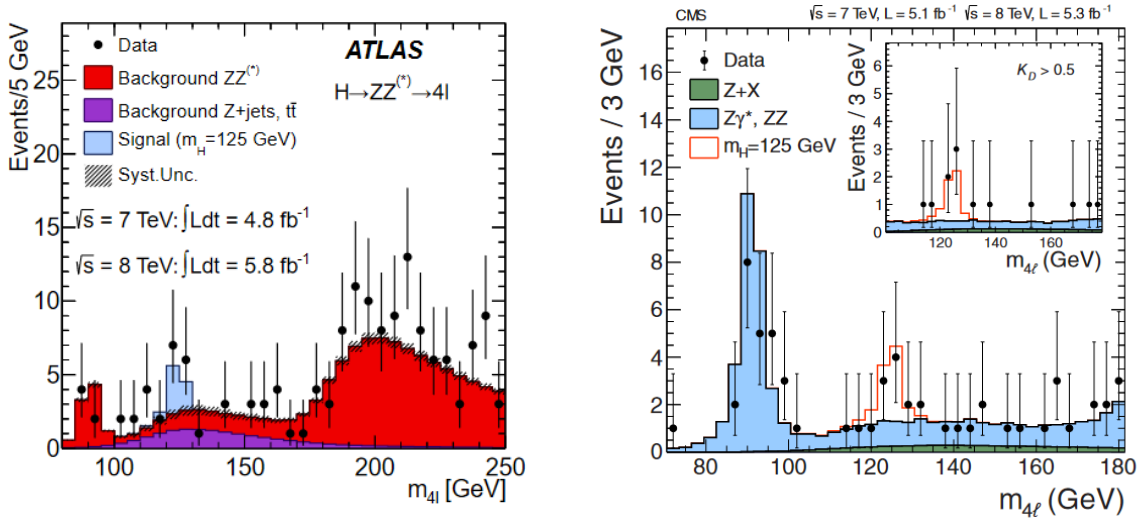

(a) (b)

Figure 1.7: Distribution of four lepton invariant mass for the $h \to ZZ^* \to l^+l^-l^+l^-$ decay channel for (a) ATLAS (Reproduced from [9]) and (b) CMS (Reproduced from [10]) experiments.

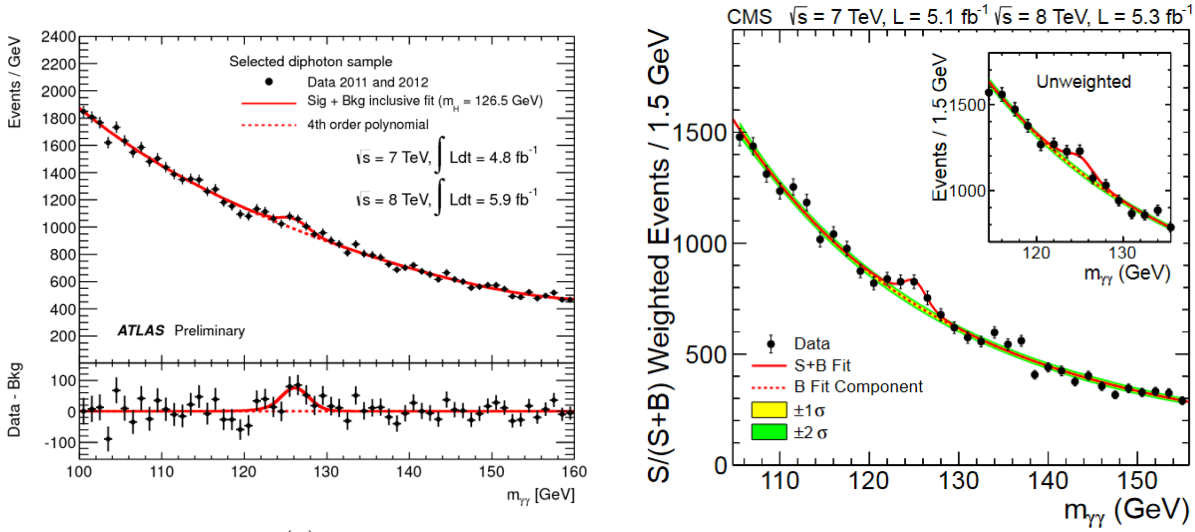

(a) (b)

Figure 1.8: Distribution of the invariant mass of the photon pair for the $h \to \gamma\gamma$ decay channel for (a) ATLAS (Reproduced from [9]) and (b) CMS (Reproduced from [10]) experiments.

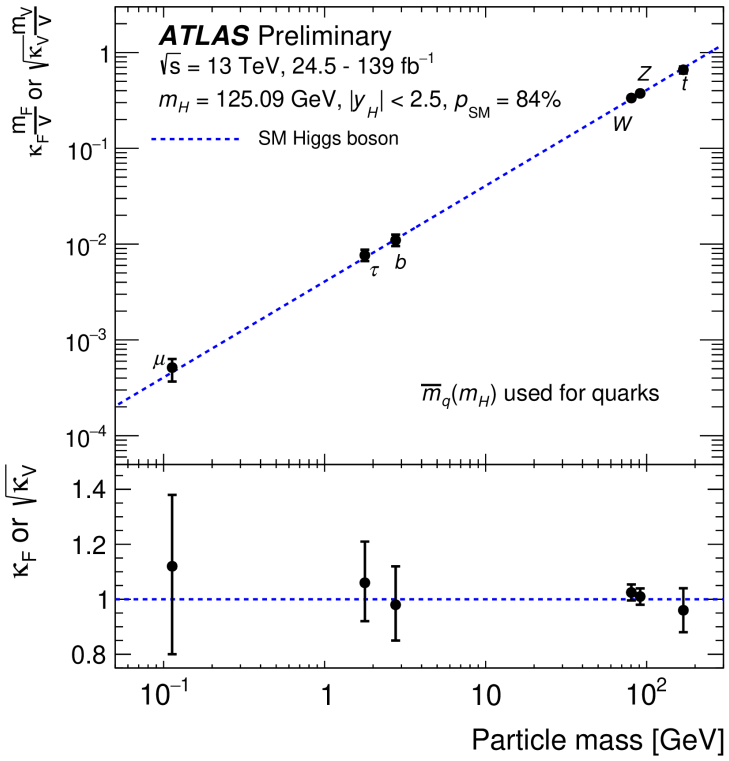

Figure 1.9: Plot of the measured Higgs boson couplings to other Standard Model particles against particle mass. Reproduced from [11].

1.3 Higgs potential and width

1.3.1 Higgs potential

Higgs potential in the gauge-invariant form can be written as

$$V(\Phi) = \mu^2 \Phi^\dagger \Phi + \lambda \left(\Phi^\dagger \Phi\right)^2 , \qquad \lambda > 0 , \tag{1.3.1}$$

where Φ is a complex $SU(2)$ doublet with the general form

$$\Phi = \begin{pmatrix} \phi_2 + i\phi_3 \\ \phi_0 + i\phi_1 \end{pmatrix}. \tag{1.3.2}$$

Choosing a global gauge and expanding the Higgs field around the vacuum

$$\Phi = \frac{1}{\sqrt{2}} \begin{pmatrix} 0 \\ v + h \end{pmatrix}. \tag{1.3.3}$$

the potential becomes

$$V(h) = v\left(\lambda v^2 + \mu^2\right) h + \frac{1}{2}\left(3v^2\lambda + \mu^2\right) h^2 + v\lambda\, h^3 + \frac{\lambda}{4} h^4 \,. \tag{1.3.4}$$

Using Eq. 1.2.11 to substitute μ for v, the potential becomes

$$V(h) = \frac{1}{2}(2\lambda v^2) h^2 + v\lambda\, h^3 + \frac{\lambda}{4} h^4 \,. \tag{1.3.5}$$

where v is the vacuum expectation value (vev). From the above equation, the mass of the Higgs is $m_h^2 = 2\lambda v^2$ which is measured at the LHC. Finally, the potential can be written in terms of Higgs mass and the vacuum expectation value as

$$V(h) = \frac{1}{2} m_h^2 h^2 + \frac{m_h^2}{2v} h^3 + \frac{m_h^2}{8v^2} h^4 \,. \tag{1.3.6}$$

which means that the Higgs trilinear and quartic couplings are

$$\begin{aligned} \lambda_{hhh} &= \frac{3m_h^2}{v} \\ \lambda_{hhhh} &= \frac{3m_h^2}{v^2} \,. \end{aligned} \tag{1.3.7}$$

The vacuum expectation value appears also in the electroweak sector and can be measured

(a) Continuum production of hh (b) hh production through single Higgs

Figure 1.10: Higgs pair production through gluon fusion at LO.

precisely through e.g. muon lifetime measurements. With both the mass and the vacuum expectation value precisely measured, μ and λ and consequently the Higgs potential are completely fixed. This is not the end of the story however since new physics can potentially alter each of these values as well as introduce higher dimensions terms in the Lagrangian; as such it is of extreme importance to measure the Higgs trilinear and quartic couplings and compare them against their theoretically predicted values.

Measuring the Higgs trilinear and quartic couplings is challenging, though, at the LHC. The trilinear coupling can be measured by studying double Higgs production. There are two modes of production for a pair of Higgs bosons through gluon fusion shown in Fig. 1.10; these two modes interfere destructively, with the magnitude of cancellation depending on λ_{hhh}. However, the cross-section at the LHC for $gg \to hh$ in SM is only 31.18 fb [51] (NNLL + NNLO in large top mass approximation). The trilinear coupling can be constrained to $0.5 < \lambda_{hhh} < 4.5$ [52] at the High Luminosity LHC while the quartic coupling $\lambda hhhh$ is essentially out of reach at the LHC. The prospects look a lot better at the proposed 100 TeV Future Circular Collider and the lepton colliders: ILC, CLIC, $\mu^+\mu^-$ collider. Best constraint for the trilinear coupling comes from FCC [53] with an estimated precision of $3.4 - 7.8\%$ at 68% CL. For the quartic coupling, achievable precision is 50% at a 14 TeV muon collider [54].

1.3.2 Measuring Higgs width

Another crucial property to be measured to ascertain the true nature of the observed Higgs boson is its decay width. This is predicted in SM to be $\Gamma_h = 4.07$ MeV [1] and any deviation

from this value would imply presence of new physics. However, being such a small value, it cannot be measured directly at the LHC since the detector resolution is too low to measure it precisely. The best constraint obtained from a direct measurement ($\Gamma_h < 1$ GeV [55–57]) is orders of magnitude larger than the value predicted in Standard Model of $\Gamma_h = 4.07$ MeV. Instead, an alternate method was proposed in [35, 37, 58] to use the offshell Higgs signal to constrain the width. The basic idea is as follows: the production cross-section for $gg \to h \to ZZ^* \to 4l$ can be written as [37]

$$\frac{\mathrm{d}\sigma}{\mathrm{d}M_{4l}^2} \sim \frac{g_{hgg}^2 g_{hZZ}^2}{(M_{4l}^2 - m_h^2)^2 + m_h^2 \Gamma_h^2} \,. \tag{1.3.8}$$

where g_{hgg} and g_{hZZ} are effective couplings of the Higgs to gluons and Z-bosons. In the above equation, all the quantities independent of M_{4l} and Γ_h have been suppressed for simplicity. Integrating the above near the resonance peak gives

$$\sigma_{\text{on-shell}} \sim \frac{g_{hgg}^2 g_{hZZ}^2}{\Gamma_h} \,. \tag{1.3.9}$$

Using the formula for the on-shell cross section in the above equation, the ratio $g_{hgg}^2 g_{hZZ}^2/\Gamma_h$ can be constrained from experimental measurement of the cross section. Away from the resonance peak, however, the denominator in Eq. 1.3.8 is dominated by M_{4l} so the cross-section (after integrating over M_{4l}) depends only on the couplings as

$$\sigma_{\text{off-shell}} \sim \frac{g_{hgg}^2 g_{hZZ}^2}{M_{4l}^4} \,. \tag{1.3.10}$$

Assuming now that the couplings g_{hgg} and g_{hZZ} vary only a little over the whole phase-space and that there are no significant new physics contributions (e.g. a new resonance that alters the couplings drastically), the off-shell cross section can be used to constrain the product $g_{hgg}^2 g_{hZZ}^2$. Using these two measurements, the width Γ_h can be constrained.

1.3.3 Experimental constraints

As mentioned previously, Γ_h cannot be measured directly at the resonance peak at the LHC since it is limited by detector resolution. The off-shell method described above, however, can provide stringent constraint on the width. An upper bound of $\gamma_h < 88$ MeV was calculated in [37] with the possibility of the constraint being improved to $\Gamma_h < 10\,\Gamma_h^{SM}$ with more data. In fact, recent analysis [59] with Run II data has constrained the width much further to $3.2^{+2.8}_{-2.2}$ MeV with the 95% CL constraint $0.08 < \Gamma_h < 9.16$ MeV both of which are consistent with the SM value.

1.4 Theoretical status

1.4.1 ZZ production at LHC

Higher-order perturbative calculations are an essential part of the modern particle physics program. One of the most important processes in that regard is the production of a pair of vector bosons where the vector boson pair could correspond to any combination $VV = ZZ, WW, \gamma\gamma, WZ, Z\gamma, W\gamma$. The specifics below refer only to $gg \to ZZ$ production since that is the primary focus of this work.

ZZ production is key to many new physics searches as well as precision physics [60–64]. In addition, it is a significant background to the crucial Higgs signal process $gg \to h \to VV \to leptons$ [59, 65–67]. It was also observed that it interfere quite significantly ($\sim 10\%$) with offshell Higgs production [35, 36] which is important for indirect width measurement as discussed in Sec. 1.3.2. As such, precise theoretical predictions for this process are indispensable. Since gluons don't couple directly to vector bosons, gluon initiated channels always appear at a higher order in the perturbation series. E.g. $q\overline{q} \to ZZ$ already starts at tree level while $gg \to ZZ$ starts at 1-loop order which is formally NNLO for the hadronic process $pp \to ZZ$. Nevertheless, due to high gluon luminosity at LHC it accounts for most of the

NNLO correction ($\sim 60\%$) [68] to $pp \to ZZ$. The NLO corrections to $gg \to ZZ$ were also found to be significant[69] increasing the total $pp \to ZZ$ cross-section by ($\sim 5\%$) [70]. Consequently, pair production of vector bosons has been one of the focal points of perturbative QCD efforts.

The $qq' \to VV$ processes are all known at NLO in QCD [71–76] as well as NLO EW for most processes [77–84]. This was possible in large part to the so-called "NLO revolution" based on unitarity methods that automated 1-loop calculations [85–91]. Gluon initiated processes are all also known at 1-loop [92–101]. The 2-loop amplitudes are not universally known, however. Complexity at 2-loops increases enormously compared to 1-loop and as such 2-loop processes are calculated on a case-by-case basis. So far no convenient and computationally feasible way to automate the 2-loop processes has been developed. Nevertheless, there has been significant progress in the past decade. In particular for $gg \to ZZ$, the 2-loop contributions including only massless quarks in the loops are known [102, 103]. This does not provide the complete picture, however, and corrections due to massive quark loops are deemed important as a consequence of the Goldstone boson equivalence theorem [33, 34].

This is especially true for loops involving the top quark whose large coupling to Higgs and the longitudinal modes of the gauge bosons (as a consequence of the equivalence theorem) could result in significant corrections in high invariant mass region. The longitudinal modes for the Z-bosons are, moreover, particularly interesting since they provide a window into potential new physics manifesting through loop effects as well as they provide a way to measure the anomalous $t\bar{t}Z$ coupling [38, 39].

Calculating the 2-loop contributions to $gg \to ZZ$ with massive internal quarks provide significant challenges. Naively, due to addition of one more variable to the problem compared to the massless case, an increase in complexity is expected. However, the traditional methods to calculate multiloop amplitudes are insufficient. The 2-loop contributions from top quark loops were calculated in an approximation where the top quark was considered much heavier than every other scale, colloquially referred to as the heavy top-mass Limit, in [104, 105].

Since the expansion has a finite radius of convergence, it cannot be used in all the regions of phase space, particularly for higher invariant mass. This can be improved with the use of Padeé approximants as in [106] to extend the expansion over a larger phase space region. Another approximation using an expansion around the top quark pair production threshold together with the heavy top limit, improved with Padé approximants, was used in [107] for contributions relevant to Higgs production. In [13], the heavy top limit was used together with small top-mass limit to access the regions of higher invariant mass and improved using Padé approximants to access the intermediate region. The amplitudes involving Higgs as a mediator have been computed with exact top mass dependence [108–111]. More recently, contributions to WW production from third generation quark loops (b, t) were computed with exact mass dependence in [112]. It must be pointed out that the 2-loop amplitudes for $gg \to ZZ$ with exact top quark dependence were also calculated independently in [113] which appeared a couple months after this work was completed.

1.4.2 Diphoton production at LHC

Another important class of processes at LHC is the production of a pair of photons. It provides a crucial channel for new physics searches [114, 115] as well as Higgs production. Similar to ZZ, continuum production of $\gamma\gamma$ is also an important background to Higgs signal process. In addition, the transverse momentum of the diphoton pair is sensitive to potential new physics whether through Higgs production or through new heavy resonances. It is, thus, a crucial part of the particle physics program [116] and better theoretical predictions are always desirable.

The NNLO QCD corrections to $pp \to \gamma\gamma$ are known already [117–120]. The ingredients for 3-loop amplitudes for four particle scattering became accessible only in the recent years [121, 122] with the full amplitudes for $qq \to \gamma\gamma$ appearing very recently [123]. Including 1-jet in addition, $pp \to \gamma\gamma + jet$ is known only at NLO [124, 125]. For both $pp \to \gamma\gamma$ at N3LO and $pp \to \gamma\gamma + jet$ at NNLO, the missing component was the 2-loop amplitudes for diphoton plus

jet production where they are required to subtract the IR poles for the former. However, $2 \to 3$ particle scattering amplitudes at 2-loop provided a great challenge and required the development of powerful new techniques. These advances, discussed in detail in this work, led finally to the calculation of first full $2 \to 3$ amplitudes, first in leading colour approximations [126–136], for simpler helicity configuration [137], and then very recently in full colour for all helicities [138, 139].

Calculation of both $gg \to ZZ$ and $qq(g) \to \gamma\gamma + jet$ 2-loop amplitudes required advances in the technology and are the focus of this work along with the results.

1.5 Quantum Chromodynamics

1.5.1 History of QCD

The discovery of the atomic nucleus, and consequently the proton, in the early 20th century led to an obvious problem: the nucleus was too heavy to be accounted for just by the protons. Among the prevalent suggestions was the electrically neutral bound states of electrons and protons, referred to as neutrons, residing inside the nucleus. It was shown, however, that an electron cannot be confined inside the nucleus. This issue was resolved with the discovery of the neutron in 1932. The neutron was found to have certain remarkable properties. Other than the electric charge, it was very similar to the proton; its mass was extremely close to that of the proton and it had the same spin of 1/2. Furthermore, it was found that the strong nuclear force had the same interaction strength for protons and neutrons, i.e. the interaction strength between a pair of protons was the same as between a pair of neutrons or a proton-neutron pair. This led to the development of isospin symmetry, as an analogue of spin for electrons. Protons and neutrons are treated as two "isospin" states of the same particle, the "nucleon", with pions, carriers of the strong nuclear force, acting much like the

classic spin operators in a harmonic oscillator.

$$\begin{aligned} \pi^+|n\rangle &= |p\rangle \\ \pi^-|p\rangle &= |n\rangle \\ \pi^0|p,n\rangle &= |p,n\rangle\,. \end{aligned} \tag{1.5.1}$$

Here $\pi^\pm$ act like the well-known raising and lowering operators $J^\pm$ while π^0 acts like the total spin operator J.

The "isospin" model was very successful in explaining the strong nuclear force in early days especially after the discovery of pions. As more new particles were discovered, they were formed into isospin multiplets e.g. nucleon doublet (p, n) with $I = 1/2$, Sigma triplet $(\Sigma^+, \Sigma^0, \Sigma^-)$ with $I = 1$, etc. A major success of the isospin model was the prediction of rho mesons as the vector bosons which were eventually discovered experimentally. With the observation of the "strange" decays of Kaons, however, a new quantum number "Strangeness" was introduced for the particles [140, 141] and the "Eightfold way" was proposed by Gell-Mann [142] and Ne'eman [143] to classify the known particles. The isospin symmetry was extended to an $SU(3)$ flavour symmetry with particles being grouped into octets and decuplets.

Eventually, the quark model was proposed by Gell-Mann [144] and Zweig [145] to explain the observed spectrum of particles with hadrons being composed of smaller particles called quarks. Three quarks were postulated to transform under the $SU(3)_F$ flavour symmetry. However, while the quark model was successful in explaining the spectrum of hadrons, it gave rise to a new question. Specifically, some of the hadrons seemed to be violating Fermi-Dirac statistics e.g. the Δ^{++} baryon was proposed to be made up of three up quarks,

$$|\Delta^{++}\rangle = |u^\uparrow u^\uparrow u^\uparrow\rangle\,, \tag{1.5.2}$$

with all three up quarks having $J_z = +1/2$. Since the three up quarks are identical fermions,

they cannot occupy the same quantum state [146, 147]. The solution to this problem was introduced as the "colour charge" [148] being an additional degree of freedom possessed by quarks. The Δ^{++} baryon can then be expressed as an anti-symmetric combination of three up quarks with different "colours",

$$|\Delta^{++}\rangle = \frac{1}{\sqrt{6}}\left(|u_r^{\uparrow}u_g^{\uparrow}u_b^{\uparrow}\rangle - |u_r^{\uparrow}u_b^{\uparrow}u_g^{\uparrow}\rangle + |u_b^{\uparrow}u_r^{\uparrow}u_g^{\uparrow}\rangle - |u_b^{\uparrow}u_g^{\uparrow}u_r^{\uparrow}\rangle + |u_g^{\uparrow}u_b^{\uparrow}u_r^{\uparrow}\rangle - |u_g^{\uparrow}u_r^{\uparrow}u_b^{\uparrow}\rangle\right) , \quad (1.5.3)$$

making the resulting combination "colourless". Analogous to quarks, anti-quarks possess the anti-colour charges $\overline{r}, \overline{g}, \overline{b}$. This results in mesons, which are combinations of quarks and anti-quarks, being colourless, e.g.

$$|\pi^{+}\rangle = \frac{1}{\sqrt{3}}\left(|u_r d_{\overline{r}}\rangle + |u_g d_{\overline{g}}\rangle + |u_b d_{\overline{b}}\rangle\right) . \quad (1.5.4)$$

The quarks now form a colour triplet,

$$|u\rangle = \begin{pmatrix} |u_r\rangle \\ |u_g\rangle \\ |u_b\rangle \end{pmatrix} , \quad (1.5.5)$$

that transforms under the new $SU(3)_C$ group. Unlike the $SU(3)_F$ flavour symmetry, however, $SU(3)_C$ colour is an exact symmetry.

In [148], the $SU(3)_C$ colour symmetry of the quarks was first considered as a Yang-Mills gauge theory [40]. Gauge bosons for this theory were called "Gluons", acting as glue holding the quarks together in hadrons. An interesting feature of this theory was that gluons carried the colour charge as well, unlike photons in Quantum Electrodynamics. This leads to the phenomena of asymptotic freedom and confinement, discussed later in this section.

1.5.2 $SU(N)$ gauge theory

A general $SU(N)$ group has $N^2 - 1$ generators; for $SU(3)$ the number of generators is 8 corresponding to the 8 different gluons. The generators of a general $SU(N)$ group can be represented using T^a where the index $a \in \{1, ..., N^2 - 1\}$ refers to the $SU(N)$ charge in the adjoint representation. These T^a are traceless and hermitian.

$$Tr(T^a) = 0\,, \tag{1.5.6}$$

$$(T^a)^\dagger = T^a\,, \tag{1.5.7}$$

and satisfy the following commutation relation:

$$\left[T^a, T^b\right] = i f^{abc} T^c\,. \tag{1.5.8}$$

f^{abc} are the totally anti-symmetric structure constants

$$f^{abc} = -2\,i\,Tr\left(\left[T^a, T^b\right] T^c\right)\,. \tag{1.5.9}$$

Further details of the $SU(N)$ algebra are provided in Appendix A.3.

The Lagrangian for the gluon field can be written as

$$\mathcal{L}_g = -\frac{1}{4} G^{a,\mu\nu} G^a_{\mu\nu}\,, \tag{1.5.10}$$

where the field strength tensor is

$$G^a_{\mu\nu} = \partial_\mu G^a_\nu - \partial_\nu G^a_\mu + g_s f^{abc} G^b_\mu G^c_\nu\,. \tag{1.5.11}$$

It is straightforward to see that the Lagrangian in Eq. 1.5.10 is invariant under the gauge

transformation

$$G^a_\mu \to G^a_\mu - \partial_\mu \theta^a(x) - g_s f^{abc} \theta^b(x) G^c_\mu \,. \tag{1.5.12}$$

Expanding the Lagrangian in Eq. 1.5.10, we get the kinetic term

$$-\frac{1}{4}(\partial^\mu G^{a,\nu} - \partial^\nu G^{a,\mu})(\partial_\mu G^a_\nu - \partial_\nu G^a_\mu)\,, \tag{1.5.13}$$

the 3-point self-interaction term

$$-\frac{g_s}{2} f^{abc}(\partial^\mu G^{a,\nu} - \partial^\nu G^{a,\mu}) G^b_\mu G^c_\nu \,, \tag{1.5.14}$$

and the 4-point self-interaction term

$$+\frac{g_s^2}{4} f^{abe} f^{cde} G^{a,\mu} G^{b,\nu} G^c_\mu G^d_\nu \,. \tag{1.5.15}$$

Unlike with photons in Quantum Electrodynamics, gluons interact with themselves which leads to the phenomena of asymptotic freedom and confinement, discussed later in Sec. 1.5.6. Details on the QCD Lagrangian and the Feynman rules are given in Appendix A.

The above Lagrangian for the gluon field poses a problem though. Specifically, the propagator of the gluon cannot be derived from this Lagrangian using a naive approach. This is evident from considering the kinetic term in the Lagrangian

$$\begin{aligned} \mathcal{L}_{kin} &= -\frac{1}{4}(\partial^\mu G^{a,\nu} - \partial^\nu G^{a,\mu})(\partial_\mu G^a_\nu - \partial_\nu G^a_\mu) \\ &= \frac{1}{2} G^{a,\nu}(g_{\mu\nu}\partial^2 - \partial_\mu \partial_\nu)\delta^{ab} G^{b,\mu} + \dots \,. \end{aligned} \tag{1.5.16}$$

The propagator $D^{ab,\mu\nu}(x-y)$ is defined using

$$\delta^{ac}(g_{\mu\rho}\partial^2 - \partial_\mu\partial_\rho)D^{bc,\nu\rho}(x-y) = i\delta^{ab}\,\delta^\nu_\mu\,\delta^{(4)}(x-y)\,, \tag{1.5.17}$$

which in momentum space becomes

$$\delta^{ac}(-g_{\mu\rho}p^2 + p_\mu p_\rho)\widetilde{D}^{bc,\nu\rho}(p) = i\delta^{ab}\,\delta^\nu_\mu\,. \tag{1.5.18}$$

Here, $(-g_{\mu\rho}p^2 + p_\mu p_\rho)$ is singular due to gauge invariance and hence cannot be inverted to obtain the propagator. This can be resolved by adding a gauge fixing term to the Lagrangian

$$\mathcal{L}_{gauge-fixing} = -\frac{1}{2\xi}(\partial_\mu G^{a,\mu})^2\,. \tag{1.5.19}$$

which, of course, renders the Lagrangian in Eq. 1.5.10 no longer gauge invariant. Eq. 1.5.18 now becomes

$$\delta^{ac}\left(-g_{\mu\rho}p^2 + \left(1-\frac{1}{\xi}\right)p_\mu p_\rho\right)\widetilde{D}^{bc,\nu\rho}(p) = i\delta^{ab}\,\delta^\nu_\mu \tag{1.5.20}$$

which, when inverted, gives

$$\widetilde{D}^{ab,\mu\nu}(p) = \frac{i\delta^{ab}}{p^2}\left(-g^{\mu\nu} + (1-\xi)\frac{p^\mu p^\nu}{p^2}\right)\,. \tag{1.5.21}$$

In the above equation ξ is a free parameter used to fix the gauge. This family of gauges is known as the R_ξ gauges. Some common choices are "Feynman-'t Hooft gauge" $\xi = 1$ which is the most popular choice in particular for higher-order corrections owing to the simplicity of the resulting expressions, and "Landau gauge" ($\xi = 0$). The physical observables, however, are gauge-invariant and as such ξ dependence must drop out at the end.

This procedure of gauge-fixing is made more transparent using the Path-integral formalism. Note that gauge-fixing is a requirement for quantisation in this case. A consequence

of this specific gauge-fixing procedure is the appearance of Faddeev-Popov ghost fields [149] which are required for preserving manifest Lorentz invariance as well as unitarity. The Faddeev-Popov Lagrangian is given by

$$\mathcal{L}_{ghost} = (\partial^\mu c^{*a})(\partial_\mu c^a) - g_s f^{abc}(\partial^\mu c^{*a}) c^b G^c_\mu \,. \tag{1.5.22}$$

The ghosts live in the adjoint representation, like the gluons, and interact only with gluons through a 3-point vertex, appearing as internal lines in Feynman diagrams. Such diagrams are essential to obtain physical results e.g. the gluon self-energy correction at 1-loop (see Appendix D). Feynman rules are given in Appendix A.2.

The name "ghost" arises from the fact that these fields are not physical and are simply a tool to make sense of the path integral and preserve unitarity for the specific gauge choice; they act to cancel the unphysical degrees of freedom appearing from ambiguity in gauge choice. This is also evident from the fact that the ghosts violate the Spin-Statistics theorem; they appear as spin-0 particles (scalar), however they are anti-commuting (fermions). Indeed other choices such as the Axial gauge [150] do not require the presence of such fields. It must be pointed out that the gauge-fixing procedure above, and consequently the appearance of Faddeev-Popov ghosts, is not simply an artefact of a *non-abelian* gauge theory; while the ghosts do appear for Quantum Electrodynamics as well, they do not couple to the photon due to the abelian nature of the theory and hence are irrelevant for any meaningful calculations.

1.5.3 Perturbative QCD

Calculating scattering amplitudes and cross-sections in quantum field theory can be very challenging. Very few theories are exactly solvable; for almost all phenomenological purposes, perturbation theory is used. The observable or quantity of interest is expanded in a small parameter, usually the coupling strength of the interaction. This is justified in most cases, e.g. the coupling constant of QED, the fine structure constant, $\alpha \simeq 1/137$ and the coupling

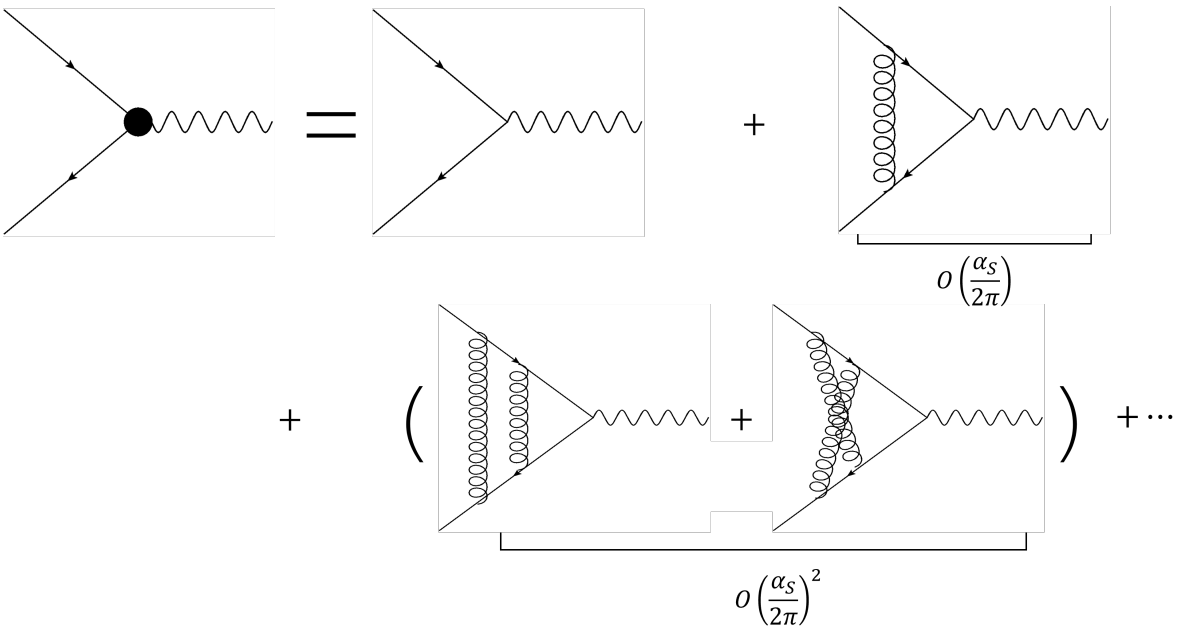

Figure 1.11: Perturbative corrections to $q\overline{q} \to \gamma$ in QCD represented using Feynman diagrams.

constant of QCD $\alpha_S \simeq 0.118$. For QCD, the cross-section can be expanded in the strong coupling constant α_S as:

$$\sigma = \sigma_0 + \left(\frac{\alpha_S}{2\pi}\right)\sigma_1 + \left(\frac{\alpha_S}{2\pi}\right)^2\sigma_2 + \left(\frac{\alpha_S}{2\pi}\right)^3\sigma_3 + ... \tag{1.5.23}$$

where $\sigma_0, \sigma_1, \sigma_2, ...$ are the contributions from each order in perturbative expansion (e.g. Fig. 1.11). Standard technique to calculate these is by the use of Feynman diagrams which provide a highly intuitive pictorial representation of the scattering process in consideration in addition to providing a convenient tool to calculate scattering amplitudes.

While at first glance it might seem that the higher-order corrections are increasingly less important given each successive term is multiplied by higher powers of the coupling constant, they can be large in many cases, perhaps best demonstrated via Higgs boson production through gluon fusion. Fig. 1.12 shows the QCD corrections to this process. It is clear that the perturbative corrections here are extremely important; the Next-to-Leading Order (NLO) correction is about as large as the Leading Order (LO) term and even the Next-to-Next-to-

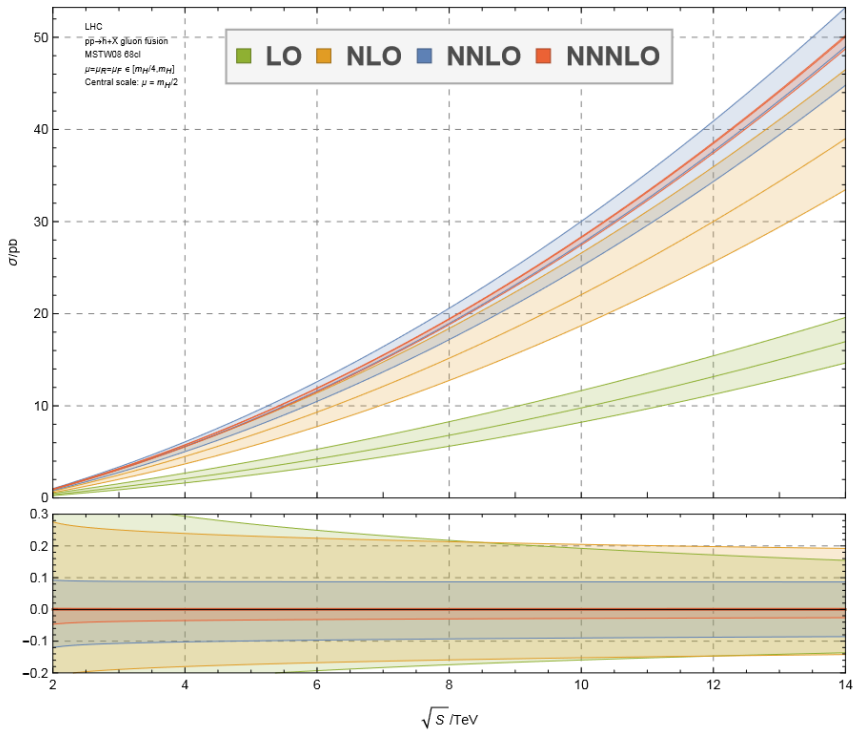

Figure 1.12: QCD corrections to $gg \to h$. The uncertainty bands represent scale uncertainty for the range $\mu \in \{\frac{m_h}{4}, m_h\}$ with the central value at $\mu = m_h/2$. Reproduced from [12].

Leading Order term is significant, only at N3LO does the calculation become stable. The uncertainty bands in the figure are estimated by varying the scale μ; this dependence on scale enters through renormalisation 1.5.5 and factorisation 1.5.7, and physical observables should not depend on it. In a sense, then, the dependence on the scale μ encodes some information about the missing higher order terms and can be used to estimate the uncertainty. However, the uncertainty bands at LO utterly fail to capture the NLO correction; only at N3LO the uncertainty bands become small enough and it lies entirely within the NNLO correction which is suggestive of the series converging (note that the perturbative series is expected to be asymptotic and not convergent).

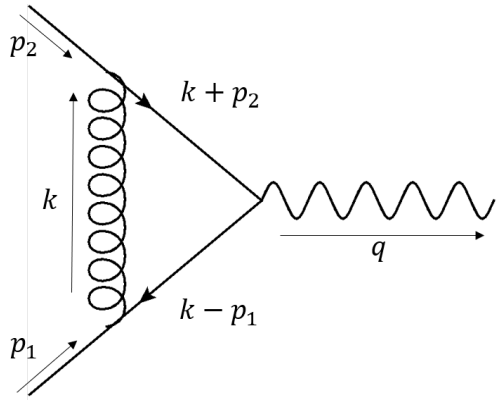

Figure 1.13: 1-loop correction to $q\overline{q} \to \gamma$.

1.5.4 Regularisation

The type of corrections shown in Fig. 1.11 are commonly referred to as the "virtual corrections" owing to the presence of additional virtual particles. Considering the diagram corresponding to the second term in the perturbative expansion in Fig. 1.11 and inserting Feynman rules, it is found that the external momenta are insufficient to constrain the momenta of the internal edges or the "loop". This loop momentum k in Fig. 1.13 is a free quantity that parameterises intermediate states. Quantum Mechanics dictates that all the intermediate states should be summed over; in this case the loop momentum k needs to be integrated over all possible values leading to the expression

$$\mathcal{M} \sim \int \frac{\mathrm{d}^4 k}{(2\pi)^4} \frac{(\not{k} - \not{p}_1)\gamma^\mu(\not{k} + \not{p}_2)}{(k^2)(k - p_1)^2(k + p_2)^2} \,. \tag{1.5.24}$$

A closer look at the above integral shows that it diverges for high values of loop momenta:

$$\int \frac{\mathrm{d}^4 k}{(2\pi)^4} \frac{(\not{k} - \not{p}_1)\gamma^\mu(\not{k} + \not{p}_2)}{(k^2)(k - p_1)^2(k + p_2)^2} \xrightarrow[k\to\infty]{\text{Wick rot.}} \int \mathrm{d}^4 k_E \frac{k_E^2}{k_E^6} \sim \int^\Lambda \frac{\mathrm{d}k_E}{k_E} \,, \tag{1.5.25}$$

where Wick rotation (see Appendix B) has been performed to transform to Euclidean space and the integration domain has been cutoff with a parameter Λ to regulate the divergence. This kind of divergence that manifests for high values of loop momenta is commonly referred

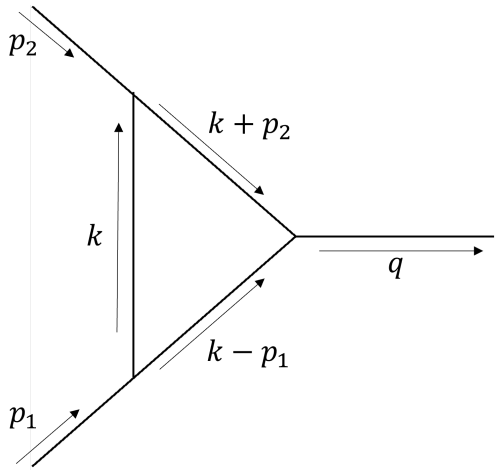

Figure 1.14: A 3-point massless integral. The incoming momenta p_1, p_2 are massless.

to as Ultraviolet (UV) divergence. In this example a cutoff regulator was used; other choices exist e.g. Pauli-Villars regularisation.

In fact this diagram has two different kinds of divergences originating from different regions of loop momentum. The second kind of divergence becomes apparent in the region of small loop-momentum. Considering only the scalar integral from Fig. 1.14 with $p_1^2 = p_2^2 = 0$,

$$I = \int \frac{\mathrm{d}^4 k}{i\pi^2} \frac{1}{(k^2)(k-p_1)^2(k+p_2)^2} \,. \tag{1.5.26}$$

For loop momentum in the soft limit $k \to 0$,

$$I \sim \int \frac{\mathrm{d}^4 k}{i\pi^2} \frac{1}{(k^2)(2k\cdot p_1)(2k\cdot p_2)} \sim \int_{k\to 0} \frac{\mathrm{d}k}{k} \,. \tag{1.5.27}$$

This integral also has a logarithmic divergence similar to Eq. 1.5.25, albeit of a very different nature. This kind of divergence for small loop momentum is called a "Soft divergence". There is another possibility for this integral when the loop momentum goes collinear to either p_1 or p_2.

$$I \sim \int_{k\to p_1} \mathrm{d}^4 k \frac{1}{(k^2)(k-p_1)^2} \,. \tag{1.5.28}$$

These are called "Collinear divergences". The soft and collinear divergences are collectively referred to as Infrared divergences.

As shown in Eq. 1.5.25, one way to regulate the UV divergence is by cutting the integral off at some large scale Λ; this is "Cutoff regularisation" scheme. The divergences then appear in the scale Λ. This scheme can also be used to regulate soft divergences by cutting off the loop momentum at some low energy scale. The most commonly used scheme, however, is dimensional regularisation [151–155]. In this scheme, ordinarily 4-dimensional objects are assumed to be d-dimensional where $d = 4 - 2\epsilon$ is a complex valued quantity in general. At the end, the limit $\epsilon \to 0$ is taken with poles appearing as $1/\epsilon^n \, (n > 0)$. Consider the UV divergent integral

$$I = \int \frac{\mathrm{d}^d k}{i\pi^{d/2}} \frac{1}{(k^2 - m^2)(k+p)^2} \sim \int_{k\to\infty} \frac{\mathrm{d}^d k}{k^4} \,. \tag{1.5.29}$$

This integral is finite for $d < 4$. We can then analytically continue the integral to $d = 4 - 2\epsilon$ with the divergences now appearing as poles in $1/\epsilon$. IR divergences can be similarly regulated:

$$I \sim \int \frac{\mathrm{d}^d k}{i\pi^{d/2}} \frac{1}{(k^2)(2k\cdot p_1)(2k\cdot p_2)} \sim \int_{k\to 0} \frac{\mathrm{d}^d k}{k^4} \,. \tag{1.5.30}$$

This integral converges for $d > 4$. Again, we can analytically continue the integral to $d = 4 - 2\epsilon$.

This provides a unified prescription to deal with both UV and IR divergences and has allowed for much of the progress in perturbative calculations. A huge advantage of using dimensional regularisation is that it preserves gauge symmetries unlike cutoff regularisation.

In Conventional Dimensional Regularisation, all the momenta, external vector polarisations, and Dirac matrices are treated in d-dimensions. This has certain disadvantages e.g. it leads to spurious structures that vanish in $d = 4$; this is discussed in more detail in sec. 2. An alternative approach is the 't Hooft-Veltmann scheme [153] where the loop momenta are treated in d-dimensions while the external vector polarisations are treated in $d = 4$ dimen-

sions. This leads to significant simplifications in many situations and prevents appearance of such spurious structures [156, 157].

Another consequence of dimensional regularisation is that the integral measure in a loop integral gains an additional mass dimension of $(d-4)L$ where L is the number of loops, along with the couplings gaining a mass dimension as well. It is conventional to redefine the coupling to render it dimensionless by introducing a dimensionful parameter μ such that, for example, $g_s' = g_s \mu^{\frac{4-d}{2}}$ with μ known as the "'t Hooft scale". This is done to ensure that all the terms in the Lagrangian have proper dimensions d.

1.5.5 UV renormalisation and IR subtraction

Since the physical observables are finite, these UV and IR divergences need to cancel in some way. The process of removing the UV singularities is called "Renormalisation". The Lagrangian is modified such that the "bare" parameters are replaced by "renormalised" parameters. E.g.

$$m_0 \overline{\psi}_0 \psi_0 \to (Z_m Z_\psi) m_R \overline{\psi}_R \psi_R \tag{1.5.31}$$

with the renormalisation constants Z_m and Z_ψ defined according to

$$\begin{aligned} m_R &= \frac{1}{Z_m} m_0 \\ \psi_R &= \frac{1}{\sqrt{Z_\psi}} \psi_0 \,. \end{aligned} \tag{1.5.32}$$

The UV divergences are absorbed into the renormalisation constants during this redefinition. The renormalised parameters are finite implying that the bare parameters are also divergent. The renormalisation constants are written such that they have a trivial part and a counterterm e.g. $Z_m = 1 + \delta_m$ where 1 refers to the tree level term and δ_m is the counterterm and cancels against the poles order by order in perturbation theory. In principle there are an in-

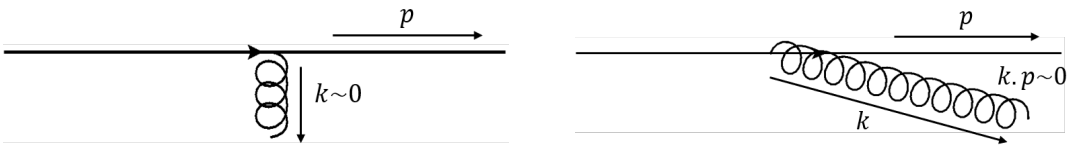

(a) Soft singularity. (b) Collinear singularity.

Figure 1.15: Infrared divergences corresponding to the emission of a real particle from a massless particle. Fig. 1.15a shows emission of a gluon with very small momentum i.e. a soft divergence while Fig. 1.15b shows the emission of a gluon collinear with the external particle.

finite number of renormalisation schemes; the divergences are fixed, however any finite term can be added to the renormalisation constant. Some of the commonly used schemes are the "On-shell" scheme where the renormalised parameters are chosen using on-shell properties of the particles and the modified "Minimal Subtraction" ($\overline{MS}$) scheme [158, 159]; these are the two schemes used in this work. Details of the renormalisation procedure for this calculation are discussed in Sec. 5.2 and Appendix D.

In general, new divergences appear at every order in perturbation theory. These divergences must all be absorbed during the renormalisation procedure to render the result finite. For many theories new "renormalisation constants" are required at every order implying that an infinite number is required to renormalise the theory at all orders, which results in a loss of predictive power. Such theories are called non-renormalisable. To show that a theory is renormalisable and requires only a finite number of counterterms is highly non-trivial; requirements for a renormalisable theory were given in [160–162] with the renormalisability of non-abelian gauge theories with spontaneous symmetry breaking (e.g. Standard Model) proven in [163].

The IR poles cancel against poles appearing in real emission diagrams, which have soft and collinear poles similar to the loop amplitudes through the emission of a soft and collinear particle respectively (see Fig. 1.15). For the case in Fig. 1.15, the propagator for the initial

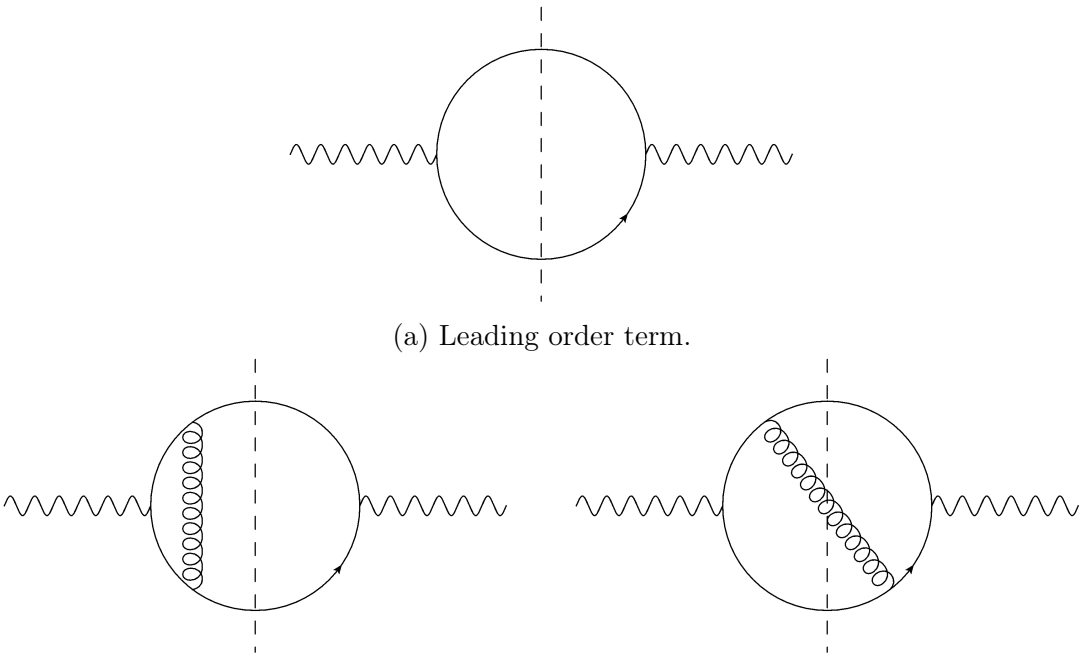

(a) Leading order term.

(b) Virtual correction.

(c) Real correction.

Figure 1.16: QCD corrections to $q\bar{q} \to \gamma$. Fig. 1.16b shows the α_S correction through the exchange of a virtual gluon while Fig. 1.16c show the α_S correction through the emission of a real gluon.

particle is

$$\frac{1}{(p+k)^2} = \frac{1}{2p \cdot k} = \frac{1}{2|\vec{p}||\vec{k}|(1-\cos\theta)} \tag{1.5.33}$$

for a massless particle. For both $k \to 0$ (soft) and $k \to xp$ (collinear) the propagator has a singularity. This is a real physical particle, hence the name real corrections. These divergences appear during phase-space integration over the external momenta and can be regulated using dimensional regularisation just like UV poles. It must be noted that these divergences don't appear for massive particles. Considering the cut diagram in Fig. 1.16c, a gluon is emitted from a quark line. Since both virtual and real corrections occur at the order α_S, it is necessary to add both to get the correct result. This is most readily seen through Fig. 1.16; the amplitude-squared can be thought of as $\gamma \to \gamma$ with the real and virtual corrections simply being different cut configurations. Bloch-Nordsieck theorem [164, 165]

showed that the IR divergences for QED must cancel once all configurations are included i.e. real correction diagrams in addition to the virtual corrections. This was extended to non-abelian gauge theories in [166–168]. Observables for which this is possible are called IR safe observables. However, computing amplitude-squared as in Fig. 1.16 is highly impractical for all but the simplest processes. The standard technique is to subtract the poles from the virtual corrections and add them to the real corrections. Sum of both is finite and produces the full cross-section:

$$\begin{aligned}\sigma_{NLO} &= \sigma_{LO} + \int_N d\sigma_V + \int_{N+1} d\sigma_R \\ &= \sigma_{LO} + \int_N \left(d\sigma_V - \int_1 d\sigma_S \right) + \int_{N+1} \left(d\sigma_R + d\sigma_S \right) . \end{aligned} \tag{1.5.34}$$

Here $d\sigma_S$ is the subtraction term; it must fulfill two conditions: it must have the same singular behaviour as $d\sigma_R$ (the real emission term) such that the sum $d\sigma_R + d\sigma_S$ is finite for $d \to 4$, and it must be integrable in d-dimensions over the 1-particle phase-space and produce the infrared divergences to cancel against the virtual corrections. The pole structure for real and virtual corrections is fixed; there is freedom to choose the finite part of $d\sigma_S$, however. Many subtraction schemes exist with the most widely used ones at NLO being the Catani-Seymour dipole subtraction [14, 169], the Frixione-Kunzst-Signer (FKS) subtraction [170, 171], and the Nagy-Soper subtraction [172], and have been automated successfully [173, 174]. However, the situation at NNLO is far from settled; the reader is referred to [175] for a detailed review of the schemes utilised for NNLO calculations.

1.5.6 Asymptotic freedom

Unlike Quantum Electrodynamics, Quantum Chromodynamics is a non-abelian gauge theory i.e. the force carriers (gluons) also carry the charge and, as a consequence, can interact with each other. This leads to the phenomenon of "asymptotic freedom" [176, 177] at high energies i.e. the coupling strength of strong interaction becomes smaller with increasing energy. On

the flip-side, the coupling increases with decreasing energy leading to the phenomenon of "confinement". This energy dependence of the renormalised coupling strength arises as a consequence of the regularisation and renormalisation procedure. However, the bare coupling should remain constant irrespective of any renormalisation procedure which leads to the equation

$$\frac{d\alpha_{S,0}}{d\mu} = 0\,. \tag{1.5.35}$$

Writing the bare coupling $\alpha_{S,0}$ in terms of the renormalised coupling α_S results in

$$\frac{d\alpha_S(\mu)}{d\log(\mu^2)} = \beta(\alpha_S)\,. \tag{1.5.36}$$

The Beta-function can be expanded order-by-order in α_S as

$$\beta(\alpha_S) = -\alpha_S\left(\left(\frac{\alpha_S}{2\pi}\right)\beta_0 + \left(\frac{\alpha_S}{2\pi}\right)^2\beta_1 + O(\alpha_S^3)\right)\,. \tag{1.5.37}$$

The first few coefficients are given by

$$\begin{aligned}\beta_0 =& \frac{11C_A - 4T_F n_f}{6}\\ \beta_1 =& \frac{17C_A^2 - 10C_A T_F n_f - 6C_F T_F n_f}{6}\end{aligned} \tag{1.5.38}$$

where n_f is the number of active flavours. For QCD, $C_A = 3$ and $T_F = 1/2$ which implies $\beta_0 > 0$ for $n_f < 17$ i.e. the coupling decreases with energy for low number of active flavours; this is the origin of asymptotic freedom. This behaviour is experimentally confirmed as shown in Fig. 1.17.

For QED, on the other hand, $\beta_0 = -2/3$ which means that the coupling grows with

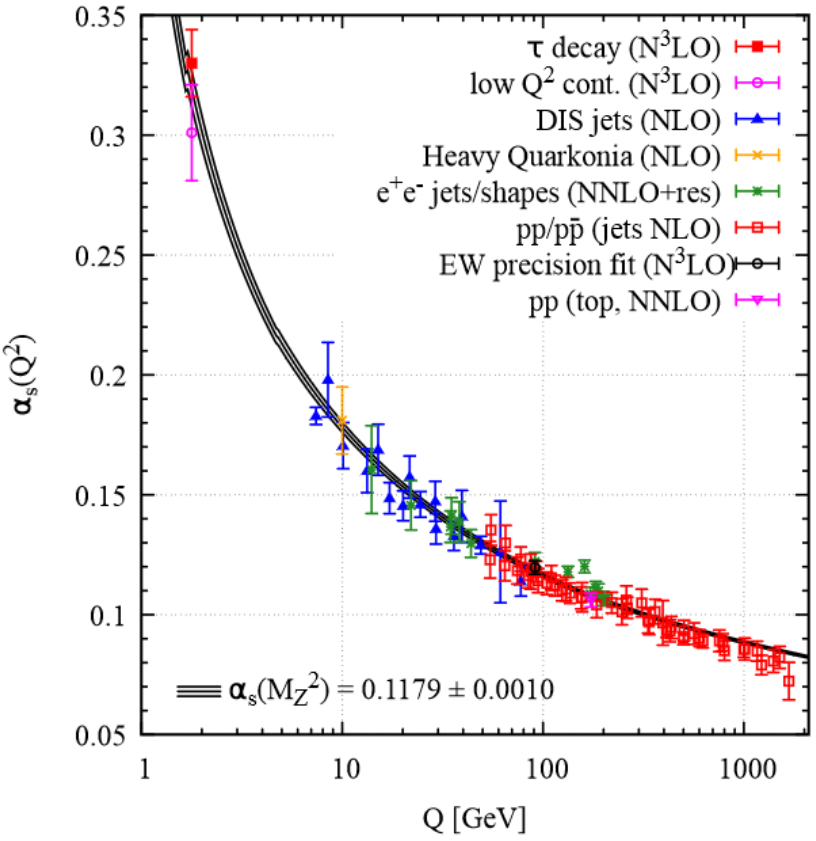

Figure 1.17: Plot showing theoretical prediction for the strong coupling α_S against experimental measurements. Reproduced from [1].

energy. Solving Eq. 1.5.36 to get the analytical expression for the running coupling,

$$\alpha(\mu) = \frac{\alpha(\mu_0)}{1 + \frac{\alpha(\mu_0)}{2\pi}\beta_0 \log \frac{\mu^2}{\mu_0^2}} \tag{1.5.39}$$

It is clear that the above equation has a pole at very high energy, referred to as Landau pole [178], where the running coupling diverges. For QED, the coupling increases with energy and the divergence appears at a very high energy ($\sim 10^{286}$ eV); for QCD this happens as the energy decreases. It makes sense, however, to interpret this as the transition from perturbative to non-perturbative regime when the coupling $\alpha > 4\pi$. Past this point, perturbation theory and, as a consequence, Eq.1.5.39 are no longer valid. The scale at which perturbation theory breaks down for QCD is $\lambda_{QCD} \simeq 200$ MeV; for energies lower than this,

non-perturbative techniques such as Chiral Perturbation Theory and Lattice Gauge Theory need to be used for calculations.

1.5.7 Factorisation

In collider experiments, often composite particles like protons are collided at high energies and the outgoing particles are studied to measure the observables e.g. proton-proton collisions at the LHC. At such high energies, however, the constituent partons [32] are the ones actually undergoing scattering governed by the short-distance physics which is modelled using perturbation theory. But the behaviour of these partons inside the proton, specifically their momentum distribution (Parton Distribution Functions), cannot be described using perturbative QCD. To perform a complete calculation of the cross-section, both short and long distance physics is required. That the full calculation can be factorised into the perturbative and non-perturbative parts which can then be evaluated independently is crucial to this. The scale separating the two is called the factorisation scale (μ_F). A scattering cross-section for the collision of two hadrons $h_1 h_2 \to cd$ (e.g. pp at the LHC) can be written in a factorised form as [1]

$$d\sigma^{h_1 h_2 \to cd} = \int_0^1 \mathrm{d}x_1 \mathrm{d}x_2 \sum_{a,b} f_{a/h_1}(x_1, \mu_F^2) f_{b/h_2}(x_1, \mu_F^2) d\hat{\sigma}^{ab \to cd}(Q^2, \mu_F^2) \tag{1.5.40}$$

where a, b are the colliding partons and Q is the scattering energy. The $f_{a/h_1}, f_{b/h_2}$ in the above equations are the Parton Distribution Functions (PDFs) and specify the probability of finding the parton a, b in the hadron h_1, h_2 with momentum fraction x_1, x_2 respectively. All the unresolved particles that lead to IR poles below the factorisation scale μ_F are absorbed in the PDF definitions. PDFs are process-independent but cannot be calculated using the regular perturbation theory methods. Traditionally they are determined using data [179–181] based on the DGLAP evolution equations [182–184]. There has been significant progress, however, in calculating PDFs through first principles using Lattice methods.

Factorisation has been proven for many processes in gauge theory [185–188]. Like the renormalisation scale, the actual calculation must be independent of the factorisation scale. However, a scale dependence still remains owing to truncation of the series, and should disappear if all the orders are calculated. This scale dependence manifests itself in the Parton Distribution Functions as well as the hard-scattering cross-section (Eq. 1.5.40).

The detectors have finite resolution which means that they cannot measure particles with arbitrarily low energies, neither can they distinguish between two particles extremely close together. Physical observables then need to be devised such that they respect such physical restrictions and are infrared safe i.e. additional soft or collinear radiations do not affect them. One such observable is a jet which is just a collection of final-state partons combined together according to a specific algorithm. They are designed to be simple to use in both experiments and theory as well as insensitive to non-perturbative effects. A way to imagine a jet is to consider a final state parton which radiates additional partons with radiation within a certain cone around the radiating particle being part of the jet. Two major kinds of algorithms are cone algorithms and sequential recombination algorithms. An in-depth discussion of jets is out of scope for this work and the reader is instead referred to [189–191] for details.

1.6 Electroweak sector

1.6.1 Electroweak symmetry breaking

The electroweak sector of the Standard Model describes the electromagnetic and weak interactions through the $SU(2)_L \times U(1)_Y$ gauge symmetry [192–195]. The L in $SU(2)_L$ referes to "left", i.e. the gauge bosons associated with this symmetry interact only with left-handed particles and Y refers to "hypercharge", the additional quantum number possessed by SM fermions. Using the general $SU(N)$ formula for the number of generators, there are 3 $SU(2)_L$ gauge bosons W_1, W_2, W_3 along with B for $U(1)_Y$.

The kinetic term for the gauge bosons can be written as

$$\mathcal{L}_{kin} = -\frac{1}{4}B^{\mu\nu}B_{\mu\nu} - \frac{1}{4}W^{i,\mu\nu}W^{i}_{\mu\nu} \tag{1.6.1}$$

with the field strength tensors given by

$$\begin{aligned} B^{\mu\nu} &= \partial^{\mu}B^{\nu} - \partial^{\nu}B^{\mu} \\ W_{i}^{\mu\nu} &= \partial^{\mu}W_{i}^{\nu} - \partial^{\nu}W_{i}^{\mu} + g_2\,\epsilon_{ijk}\,W_{j}^{\mu}W_{k}^{\nu} \end{aligned} \tag{1.6.2}$$

where g_2 is the coupling strength of $SU(2)_L$. To generate masses for these bosons, the $SU(2)_L \times U(1)_Y$ symmetry must be spontaneously broken through Higgs mechanism. The Higgs part of the Lagrangian can be written as

$$\mathcal{L}_{higgs} = (D^{\mu}\Phi)^{\dagger}(D_{\mu}\Phi) - \mu^2(\Phi^{\dagger}\Phi) - \lambda(\Phi^{\dagger}\Phi)^2\,, \tag{1.6.3}$$

where the covariant derivative D_μ is such that the above Lagrangian is invariant under the $SU(2)_L \times U(1)_Y$ gauge symmetry

$$D_{\mu} = \partial_{\mu} + ig_1\,Y\,B_{\mu} - i\frac{g_2}{2}\,\sigma_i W_{i,\mu}\,. \tag{1.6.4}$$

which can be written as

$$D_{\mu} = \begin{pmatrix} \partial_{\mu} & 0 \\ 0 & \partial_{\mu} \end{pmatrix} - \frac{i}{2}\begin{pmatrix} -g_1B_{\mu} + g_2W_{3,\mu} & g_2(W_{1,\mu} - i\,W_{2,\mu}) \\ g_2(W_{1,\mu} + i\,W_{2,\mu}) & -g_1B_{\mu} - g_2W_{3,\mu} \end{pmatrix} \tag{1.6.5}$$

with the Hypercharge Y set to $1/2$. The gauge fields themselves transform under infinitesimal

transformations as

$$\begin{aligned} B_\mu &\to B_\mu - \partial_\mu \theta(x) \\ W_{i,\mu} &\to W_{i,\mu} - \partial_\mu \theta_i(x) - g_2\, \epsilon^{ijk}\, \theta_j(x)\, W_{k,\mu}\,, \end{aligned} \tag{1.6.6}$$

similar to Eq. 1.5.12. Inserting Eq. 1.6.5 into Eq. 1.6.3 and expanding the Higgs field around the vacuum (keeping only the physical Higgs field) $\Phi = \frac{1}{\sqrt{2}} \begin{pmatrix} 0 \\ v+h \end{pmatrix}$, the gauge bosons gain masses:

$$\mathcal{L}_{gauge-mass} = \frac{v^2}{8} \left(g_2^2 (W_1^2 + W_2^2) + (g_1 B_\mu + g_2 W_{3,\mu})^2 \right) \tag{1.6.7}$$

It is clear that two of the $SU(2)_L$ bosons W_1, W_2 acquire a mass. The third boson W_3 does not acquire a mass itself, but rather the combination $g_1 B_\mu + g_2 W_{3,\mu}$ does. At this point it makes sense to define certain quantities. The electric charge of a particle can be defined as

$$Q = Y + I_3\,, \tag{1.6.8}$$

and the electromagnetic coupling e can be defined as

$$e = \frac{g_1 g_2}{\sqrt{g_1^2 + g_2^2}}\,. \tag{1.6.9}$$

Parameterising the couplings with an angle θ_W,

$$g_1 = g_2 \tan\theta_W\,, \tag{1.6.10}$$

the fields B_μ and $W_{3,\mu}$ can be rotated as

$$\begin{aligned} A_\mu &= \frac{g_2 B_\mu - g_1 W_{3,\mu}}{\sqrt{g_1^2 + g_2^2}} = \cos\theta_W B_\mu - \sin\theta_W W_{3,\mu} \\ Z_\mu &= \frac{g_1 B_\mu + g_2 W_{3,\mu}}{\sqrt{g_1^2 + g_2^2}} = \sin\theta_W B_\mu + \cos\theta_W W_{3,\mu}\,. \end{aligned} \tag{1.6.11}$$

It is also useful to define the linear combinations $W_\pm = W_1 \pm iW_2$. The mass terms then become

$$\mathcal{L}_{gauge-mass} = \frac{g_2^2 v^2}{8}\left(W_+ W_- + \frac{1}{\cos^2\theta_W} Z^2\right) \tag{1.6.12}$$

A couple things are clear from the above equation. Z boson is predicted to be more massive than the $W^\pm$ bosons since $\cos^2\theta_W < 1$. Also, only 3 bosons gain mass with A_μ remaining massless. This can be seen in another way; the Q operator acting on the vacuum state gives

$$\begin{aligned} Q|0\rangle =& (Y + I_3)|0\rangle \\ =& \begin{pmatrix} Y + \frac{1}{2} & 0 \\ 0 & Y - \frac{1}{2} \end{pmatrix} \begin{pmatrix} 0 \\ \frac{v}{\sqrt{2}} \end{pmatrix} = \begin{pmatrix} 0 \\ 0 \end{pmatrix} \end{aligned} \tag{1.6.13}$$

since $Y = 1/2$ for the Higgs field, meaning that Q is conserved compared to, for instance, Y:

$$Y|0\rangle = \begin{pmatrix} Y & 0 \\ 0 & Y \end{pmatrix} \begin{pmatrix} 0 \\ \frac{v}{\sqrt{2}} \end{pmatrix} = \begin{pmatrix} 0 \\ \frac{v}{\sqrt{2}} \end{pmatrix}\,. \tag{1.6.14}$$

This implies that the $SU(2)_L \times U(1)_Y$ gauge symmetry spontaneously breaks down to $U(1)_{EM}$ with the gauge boson of the $U(1)_{EM}$ symmetry, photon, remaining massless. Using Eqs. 1.6.9 and 1.6.10, the masses of the gauge bosons can be written in terms of electric charge e:

$$\mathcal{L}_{gauge-mass} = \frac{e^2 v^2}{8\sin^2\theta_W}\left(W_+ W_- + \frac{1}{\cos^2\theta_W} Z^2\right)\,. \tag{1.6.15}$$

The gauge boson masses are then

$$\begin{aligned} m_W^2 =& \frac{e^2 v^2}{4 \sin^2 \theta_W} \\ m_Z^2 =& \frac{e^2 v^2}{4 \sin^2 \theta_W \cos^2 \theta_W} \,. \end{aligned} \tag{1.6.16}$$

Since e and v are known, measuring one of the gauge boson masses fixes the other.

1.6.2 Custodial symmetry

It is useful to define the ρ-parameter

$$\rho = \frac{m_W^2}{m_Z^2 \cos^2 \theta_W} \,. \tag{1.6.17}$$

At tree level, in SM, $\rho = 1$; this is guaranteed by the so-called "Custodial symmetry" [196, 197]. Before spontaneous symmetry breaking, the Higgs field has a global $SO(4)$ symmetry

$$\Phi^\dagger \Phi = \begin{pmatrix} \phi_2 - i\phi_3 & \phi_0 - i\phi_1 \end{pmatrix} \begin{pmatrix} \phi_2 + i\phi_3 \\ \phi_0 + i\phi_1 \end{pmatrix} = \sum_{i=1}^{4} \phi_i^2 \,. \tag{1.6.18}$$

Alternatively, it can be referred to as a global $SU(2)_L \times SU(2)_R$ symmetry since the two are isomorphic. After spontaneous symmetry breaking, $\phi_0 = h + v$ and the $SO(4)$ is broken to $SO(3)$

$$\Phi^\dagger \Phi \to (h + v)^2 + \sum_{i=1}^{3} \phi_i^2 \tag{1.6.19}$$

with the Goldstone bosons corresponding to $W^\pm, Z$ transforming as a triplet under the residual $SO(3)$, which is the custodial symmetry. This $SO(3)$ isn't exact however and is broken by the mixing between the W_3 and B fields implying that the corrections to the ρ parameter must be proportional to the mixing angle $\sin^2 \theta_W$, which is indeed found through

explicit calculations. On the other hand, non-degenerate fermion doublets coupling to the Higgs also break the custodial symmetry where the symmetry breaking is proportional to the difference in the Yukawa couplings e.g. for the $t-b$ doublet, the correction to the ρ-parameter vanishes in the limit $y_t = y_b$. Thus the custodial symmetry prevents the gauge bosons from acquiring arbitrarily large radiative corrections for their masses.

1.6.3 Electroweak interactions

Consider again the gauge-boson kinetic terms in Eq. 1.6.1. Expanding the field strength tensors gives the gauge boson interaction terms e.g. the 3-point vertices

$$\begin{aligned} &- ig_2 \cos\theta_W \left(\partial^\mu Z^\nu (W^+_\mu W^-_\nu - W^+_\nu W^-_\mu) + Z^\nu (W^{+,\mu}\partial_\mu W^-_\nu + ...)\right) \\ &- ie \left(\partial^\mu A^\nu (W^+_\mu W^-_\nu - W^+_\nu W^-_\mu) + A^\nu (W^{+,\mu}\partial_\mu W^-_\nu + ...)\right) , \end{aligned} \tag{1.6.20}$$

and the 4-point vertices

$$\begin{aligned} &+ \frac{g_2^2}{2} W^{+,\mu} W^{-,\nu} W^+_\mu W^-_\nu + g_2^2 \cos^2\theta_W \, Z^\mu Z_\mu W^{+,\nu} W^-_\nu \\ &- e^2 \, A^\mu A_\mu W^{+,\nu} W^-_\nu - e g_2 \cos\theta_W \, Z^\mu A_\mu W^{+,\nu} W^-_\nu . \end{aligned} \tag{1.6.21}$$

It is interesting to note that the all-W interactions involve purely the $SU(2)_L$ coupling g_2 implying that this is a pure "weak" interaction while those involving the photon field A_μ have the coupling e implying the electromagnetic nature of the interaction, the fact that the photon is coupling to the electrically charged $W^\pm$-bosons. The Z-boson interactions also depend purely on the weak coupling g_2 but only the purely weak part of $Z_\mu = -\sin\theta_W B_\mu + \cos\theta_W W_{3,\mu}$ contributes. Also, Z being electrically neutral, does not couple to the photon.

Considering now the fermions, the Lagrangian can be written as

$$\mathcal{L}_{fermion} = \overline{\Psi}(i\gamma^\mu D^f_\mu)\Psi \tag{1.6.22}$$

where Ψ is the doublet $\Psi = \begin{pmatrix} \psi_2 \\ \psi_1 \end{pmatrix}$ and the covariant derivative for fermions D^f_μ is

$$D^f_\mu = \partial_\mu - ig_1\, Y B_\mu - i\frac{g_2}{2}\, P_L \sigma_i W_{i,\mu}\,, \tag{1.6.23}$$

where $P_L = (1-\gamma^5)/2$. Taking the example of the (left-handed) $e-\nu_e$ doublet $L_e = \begin{pmatrix} \nu_{e,L} \\ e_L \end{pmatrix}$, the interaction term can be written as

$$\mathcal{L}_e = i\overline{L}_e(\partial\!\!\!/ - ig_1\, Y_e B\!\!\!/ - i\frac{g_2}{2}\,\sigma_i W\!\!\!/_i)L_e + i\overline{e}_R(\partial\!\!\!/ - ig_1\, Y_{e_R} B\!\!\!/)e_R + i\overline{\nu}_R(\partial\!\!\!/ - ig_1\, Y_{\nu_R} B\!\!\!/)\nu_R\,. \tag{1.6.24}$$

Since the right-handed fields e_R, ν_R do not form part of an $SU(2)_L$ doublet, $I_3 = 0$ for both. For the neutrino this implies that $Y_{\nu_R} = 0$ from the relation $Q = Y + I_3$, meaning that the right-handed neutrino does not interact with through weak interactions at all. And since it is not charged under $SU(3)_C$ either, it is completely invisible in the Standard Model. In principle nothing forbids its presence, however it is impossible to detect in SM and does not interact with any other SM particles making it irrelevant to any meaningful physical observable. This does not mean, though, that the right-handed neutrinos are pointless; in fact many new physics models predict their interactions. Since neutrinos have been shown to have masses through oscillation experiments [1, 198, 199], assuming that they gain their masses through the Higgs field necessitates the presence of right-handed fields. The other hypercharges can also be inferred similarly; since $Q_e = -1$, $Y_e = -1/2$ which can also be inferred using $Q_\nu = 0$ and $I_3(\nu_{e,L}) = 1/2$. For the right-handed electron, $Y_{e_R} = Q_e = -1$.

Expanding the above Lagrangian in terms of the rotated $A-Z$ basis and using $Q = Y + I_3$

gives

$$\begin{aligned}
\mathcal{L}_e =& i\overline{L}_e \not{\partial} L_e + i\overline{e}_R \not{\partial} e_R + \frac{e}{2\sin\theta_W}\,\overline{L}_e \begin{pmatrix} 0 & W^- \\ W^+ & 0 \end{pmatrix} L_e \\
&+ e\overline{L}_e \begin{pmatrix} Q_e \not{A} + \frac{1}{2\sin\theta_W\cos\theta_W}(1-2Q_e\sin^2\theta_W)\not{Z} & 0 \\ 0 & \frac{-1}{2\sin\theta_W\cos\theta_W}\not{Z} \end{pmatrix} L_e \\
&+ e\,Q_e\,\overline{e}_R \not{A} e_R - e\,Q_e\tan\theta_W\,\overline{e}_R \not{Z} e_R \\
=& i\overline{L}_e \not{\partial} L_e + i\overline{e}_R \not{\partial} e_R + \frac{e}{2\sin\theta_W} \underbrace{\left(\overline{\nu}_{e,L} \not{W}^+ e_L + \overline{e}_L \not{W}^- \nu_{e,L}\right)}_{\text{Charged current weak interaction}} - e \underbrace{(\overline{e}_R \not{A} e_R + \overline{e}_L \not{A} e_L)}_{\text{Electromagnetic interaction}} \\
&+ \frac{e}{\sin 2\theta_W} \underbrace{\left((1-2Q_e\sin^2\theta_W)\overline{e}_L \not{Z} e_L - 2Q_e\sin^2\theta_W \overline{e}_R \not{Z} e_R + \overline{\nu}_{e,L} \not{Z} \nu_{e,L}\right)}_{\text{Neutral current weak interaction}} . \qquad (1.6.25)
\end{aligned}$$

where, with abuse of notation, e is the positron charge. A few things to note from the above equations: The $W^\pm$-bosons act as raising and lowering operators on an $SU(2)$ doublet; Z-boson acts like the I_3 operator, however due to mixing between the $B - W_3$ fields there is also a photon like interaction that, unsurprisingly, depends on the strength of this mixing; $\nu_{e,L}$ has no electromagnetic interactions, as expected, since it is electrically neutral.

The interactions above can be written in a more condensed form (omitting the pure EM term) for a general fermion doublet $\Psi = \begin{pmatrix} \psi_2 \\ \psi_1 \end{pmatrix}$ as

$$\mathcal{L}_{weak} = \frac{e}{2\sin\theta_W}\left(\overline{\psi}_2 \not{W}^+ \psi_1 + \overline{\psi}_1 \not{W}^- \psi_2\right) + \frac{e}{2\sin\theta_W\cos\theta_W}\overline{\psi}_f \not{Z}(v_f + a_f\gamma^5)\psi_f \,. \qquad (1.6.26)$$

with the purely EM interaction term being ignored for brevity. Here v_f, a_f refer to the vector and axial coupling of the Z-boson to the fermion f and are given by

$$\begin{aligned}
v_f =& I_3 - 2Q_f\sin^2\theta_W \\
a_f =& -I_3\,, \qquad (1.6.27)
\end{aligned}$$

where Q_f is the electric charge of the fermion in the units of the positron charge.

Chapter 2

Setup of the calculation

2.1 Form factor decomposition

Let us consider pair production of Z-bosons through gluon fusion,

$$g(p_1) + g(p_2) \rightarrow Z(p_3) + Z(p_4)\,. \tag{2.1.1}$$

The gluons (p_1, p_2) are considered to be incoming and the Z-bosons (p_3, p_4) considered to be outgoing so that momentum conservation implies

$$p_1 + p_2 = p_3 + p_4\,. \tag{2.1.2}$$

The external particles are also considered to be on-shell with the momenta then satisfying the on-shell conditions

$$p_1^2 = p_2^2 = 0, \quad p_3^2 = p_4^2 = m_Z^2\,. \tag{2.1.3}$$

Formally, the scattering amplitude for this process can be written as

$$\mathcal{M} = \mathcal{M}^{ab}_{\mu\nu\rho\sigma}(p_1, p_2, p_3, p_4)\,\epsilon^{a,\mu}_{\lambda_1}(p_1)\,\epsilon^{b,\nu}_{\lambda_2}(p_2)\,\epsilon^{*\rho}_{\lambda_3}(p_3)\,\epsilon^{*\sigma}_{\lambda_4}(p_4) \tag{2.1.4}$$

stripping away the polarisation vectors $\epsilon_{\lambda_i}(p_i)$ for the gluons and the Z-bosons with λ_i denoting the particle helicity. For brevity, the colour and Lorentz indices on the polarisation vectors are henceforth suppressed and the abbreviation $\epsilon_i \equiv \epsilon_{\lambda_i}(p_i)$ is instead used. Note that the amplitude $\mathcal{M}$, or equivalently $\mathcal{M}^{ab}_{\mu\nu\rho\sigma}(p_1, p_2, p_3, p_4)$, is the full scattering amplitude;

no perturbative expansion has been performed yet. In general, it is desirable to maintain the full Lorentz structure of the amplitude since complete polarisation information can be useful to include e.g. decays of the outgoing particles. However, for the perturbative expansion coefficients of the full amplitude, the calculation can be immensely simplified in many cases by the use of explicit representations for the polarisation vectors $\epsilon_{\lambda_i}(p_i)$, for example using the spinor-helicity formalism [90, 200–204]; the most well-known example is perhaps the Parke-Taylor formula [205, 206] where the leading-order amplitude for n-gluon scattering collapses to a remarkably simple 1-line expression.

In general, evaluating $\mathcal{M}^{ab}_{\mu\nu\rho\sigma}(p_1, p_2, p_3, p_4)$ directly can be an extremely difficult task. The expressions involve a large number of tensor loop integrals, and while techniques exist to handle them in a systematic way, most of the powerful modern methods involve scalar loop integrals where the open Lorentz indices are contracted with loop or external momenta. As such, it is highly beneficial to separate the Lorentz structure from the amplitude. Lorentz invariance dictates that the amplitude $\mathcal{M}^{ab}_{\mu\nu\rho\sigma}(p_1, p_2, p_3, p_4)$ can be decomposed in terms of all possible, in this case rank-4, Lorentz tensors. These Lorentz tensors can be composed of the independent external momenta as well as general process-independent tensors such as the metric tensor $g_{\mu\nu}$ and the totally anti-symmetric Levi-Civita tensor $\epsilon_{\mu\nu\rho\delta}$. For the process at hand, a total of 138 tensor structures appear in the decomposition [102]:

$$\begin{aligned}\mathcal{M}^{\mu\nu\rho\sigma}(p_1, p_2, p_3, p_4) \;=\; & a_1\, g^{\mu\nu}\, g^{\rho\sigma} \;+\; a_2\, g^{\mu\rho}\, g^{\nu\sigma} \;+\; a_3\, g^{\mu\sigma}\, g^{\nu\rho} \\ & + \sum_{i,j=1}^{3} \big(a_{1,ij}\, g^{\mu\nu}\, p_i^\rho\, p_j^\sigma \;+\; a_{2,ij}\, g^{\mu\rho}\, p_i^\nu\, p_j^\sigma \;+\; a_{3,ij}\, g^{\mu\sigma}\, p_i^\nu\, p_j^\rho \\ & \qquad + \; a_{4,ij}\, g^{\nu\rho}\, p_i^\mu\, p_j^\sigma \;+\; a_{5,ij}\, g^{\nu\sigma}\, p_i^\mu\, p_j^\rho \;+\; a_{6,ij}\, g^{\rho\sigma}\, p_i^\mu\, p_j^\nu \big) \\ & + \sum_{i,j,k,l=1}^{3} a_{ijkl}\, p_i^\mu\, p_j^\nu\, p_k^\rho\, p_l^\sigma \;. \end{aligned} \tag{2.1.5}$$

In the above, parity-odd tensors involving the Levi-Civita tensor have been dropped. This is because of Bose symmetry and charge-parity conservation for this process [96]. Note that

the colour indices have been dropped in the above equation for brevity.

Fundamentally, the decomposition in Eq. 2.1.5 is completely independent of the underlying process and should hold for any $2 \to 2$ scattering process involving four vector bosons as well as satisfying Bose symmetry and conserving charge-parity. All the physics is now contained in the coefficients $a_{ij..}$ which are referred to as "form factors". It would be quite difficult to calculate all 138 form factors; thankfully, that is not needed and certain identities can be exploited to reduce this number. Transversality of the gluon polarisation vectors (from Ward identities) implies

$$\epsilon_1 \cdot p_1 = 0\,, \qquad \epsilon_2 \cdot p_2 = 0\,. \tag{2.1.6}$$

Further reduction can be achieved by explicitly choosing a gauge for the external particles such as

$$\epsilon_1 \cdot p_2 = 0\,, \qquad \epsilon_2 \cdot p_1 = 0\,, \qquad \epsilon_3 \cdot p_3 = 0\,, \qquad \epsilon_4 \cdot p_4 = 0\,, \tag{2.1.7}$$

which reduces the total number of independent form factors to 20. The above gauge choice for the polarisation vectors corresponds to the following polarisation sums:

$$\begin{aligned}
\sum_{\text{pol}} \epsilon_1^{a,\mu}\, \epsilon_1^{*b,\nu} = \sum_{\text{pol}} \epsilon_2^{a,\mu}\, \epsilon_2^{*b,\nu} &= \left(-g^{\mu\nu} + \frac{p_1^\mu p_2^\nu \,+\, p_2^\mu p_1^\nu}{p_1.p_2} \right) \delta^{ab}\,, \\
\sum_{\text{pol}} \epsilon_3^{\mu}\, \epsilon_3^{*\nu} &= -g^{\mu\nu} + \frac{p_3^\mu p_3^\nu}{p_3.p_3}\,, \\
\sum_{\text{pol}} \epsilon_4^{\mu}\, \epsilon_4^{*\nu} &= -g^{\mu\nu} + \frac{p_4^\mu p_4^\nu}{p_4.p_4}\,.
\end{aligned} \tag{2.1.8}$$

It is useful to define the Mandelstam variables

$$s = (p_1 + p_2)^2\,, \quad t = (p_1 - p_3)^2\,, \quad u = (p_2 - p_3)^2\,. \tag{2.1.9}$$

Since they are Lorentz-invariant, it is convenient to express the amplitude in terms of these quantities. Momentum conservation (Eq. 2.1.2) allows us to write down a relation between the Mandelstam variables:

$$s + t + u = 2\, m_Z^2 \tag{2.1.10}$$

The amplitude can then be written in terms of the remaining 20 form factors as

$$\mathcal{M}^{\mu\nu\rho\sigma}(p_1, p_2, p_3, p_4) \;=\; \sum_{i=1}^{20} A_i(s, t, m_Z^2, m_1^2, m_2^2, ...)\, T_i^{\mu\nu\rho\sigma}\,, \tag{2.1.11}$$

where the A_i are the form factors depending only on the Mandelstam variables (s, t), mass of the Z-boson (m_Z), and masses of the internal particles denoted by $m_1, m_2, ...$ The remaining 20 tensors T_i are as follows:

$$\begin{aligned}
&T_1^{\mu\nu\rho\sigma} = g^{\mu\nu} g^{\rho\sigma}\,, && T_2^{\mu\nu\rho\sigma} = g^{\mu\rho} g^{\nu\sigma}\,, && T_3^{\mu\nu\rho\sigma} = g^{\mu\sigma} g^{\nu\rho}\,, && T_4^{\mu\nu\rho\sigma} = p_1^\rho\, p_1^\sigma\, g^{\mu\nu}\,,\\
&T_5^{\mu\nu\rho\sigma} = p_1^\rho\, p_2^\sigma\, g^{\mu\nu}\,, && T_6^{\mu\nu\rho\sigma} = p_1^\sigma\, p_2^\rho\, g^{\mu\nu}\,, && T_7^{\mu\nu\rho\sigma} = p_2^\rho\, p_2^\sigma\, g^{\mu\nu}\,, && T_8^{\mu\nu\rho\sigma} = p_1^\sigma\, p_3^\nu\, g^{\mu\rho}\,,\\
&T_9^{\mu\nu\rho\sigma} = p_2^\sigma\, p_3^\nu\, g^{\mu\rho}\,, && T_{10}^{\mu\nu\rho\sigma} = p_1^\rho\, p_3^\nu\, g^{\mu\sigma}\,, && T_{11}^{\mu\nu\rho\sigma} = p_2^\rho\, p_3^\nu\, g^{\mu\sigma}\,, && T_{12}^{\mu\nu\rho\sigma} = p_1^\sigma\, p_3^\mu\, g^{\nu\rho}\,,\\
&T_{13}^{\mu\nu\rho\sigma} = p_2^\sigma\, p_3^\mu\, g^{\nu\rho}\,, && T_{14}^{\mu\nu\rho\sigma} = p_1^\rho\, p_3^\mu\, g^{\nu\sigma}\,, && T_{15}^{\mu\nu\rho\sigma} = p_2^\rho\, p_3^\mu\, g^{\nu\sigma}\,, && T_{16}^{\mu\nu\rho\sigma} = p_3^\mu\, p_3^\nu\, g^{\rho\sigma}\,,\\
&T_{17}^{\mu\nu\rho\sigma} = p_1^\rho\, p_1^\sigma\, p_3^\mu\, p_3^\nu\,, && T_{18}^{\mu\nu\rho\sigma} = p_1^\rho\, p_2^\sigma\, p_3^\mu\, p_3^\nu\,, && T_{19}^{\mu\nu\rho\sigma} = p_2^\rho\, p_1^\sigma\, p_3^\mu\, p_3^\nu\,, && T_{20}^{\mu\nu\rho\sigma} = p_2^\rho\, p_2^\sigma\, p_3^\mu\, p_3^\nu\,.
\end{aligned} \tag{2.1.12}$$

To extract the form factors from the amplitude, projection operators $P_i^{\mu\nu\rho\sigma}$ can be constructed such that they fulfill

$$\sum_{\text{pol}} P_i^{\mu\nu\rho\sigma} \epsilon_{1\mu}^* \epsilon_{2\nu}^* \epsilon_{3\rho} \epsilon_{4\sigma} \epsilon_{1\mu'} \epsilon_{2\nu'} \epsilon_{3\rho'}^* \epsilon_{4\sigma'}^* \mathcal{M}^{\mu'\nu'\rho'\sigma'} = A_i\,. \tag{2.1.13}$$

To find these projection operators, they can be decomposed in terms of the $T_i^{\mu\nu\rho\sigma}$:

$$P_i^{\mu\nu\rho\sigma} \;=\; \sum_{j=1}^{20} B_{ij}(s, t, m_Z^2)\, (T_j^{\mu\nu\rho\sigma})^\dagger\,, \qquad i = 1, ..., 20\,. \tag{2.1.14}$$

Note that the coefficients B_{ij} are functions of only the external kinematic configuration, independent of the internal particles. The actual expressions for B_{ij} are too complicated to be provided here and the reader is instead referred to the VVamp project website. To calculate them is relatively straightforward, however. Inserting Eqs. 2.1.11 and 2.1.14 into Eq. 2.1.13,

$$\sum_{j=1}^{20} B_{ij}(s,t,m_Z^2)\,(T_j^{\mu\nu\rho\sigma})^\dagger\, T_k^{\mu'\nu'\rho'\sigma'} \sum_{\text{pol}} \left(\epsilon_{1\mu}^*\epsilon_{2\nu}^*\epsilon_{3\rho}\epsilon_{4\sigma}\epsilon_{1\mu'}\epsilon_{2\nu'}\epsilon_{3\rho'}^*\epsilon_{4\sigma'}^*\right) = \delta_{ik}\,. \tag{2.1.15}$$

Polarisation sums from Eq. 2.1.8 can then be inserted into the above equation and the resulting linear system solved to obtain the coefficients B_{ij}. Not all 20 form factors are independent though. With identical bosons in both the initial and final states, the process exhibits Bose symmetry which implies that the amplitude must be invariant under the exchange of the incoming gluons or the outgoing Z-bosons [102]:

$$\begin{aligned} 1 \leftrightarrow 2 \quad &: \quad p_1 \leftrightarrow p_2, \quad \epsilon_{\lambda_1}(p_1) \leftrightarrow \epsilon_{\lambda_2}(p_2)\,, \\ 3 \leftrightarrow 4 \quad &: \quad p_3 \leftrightarrow p_4, \quad \epsilon_{\lambda_3}(p_3) \leftrightarrow \epsilon_{\lambda_4}(p_4)\,. \end{aligned}$$

This symmetry results in certain relations between the form factors. First. there are the identities:

$$A_7 = A_4\,, \quad A_{12} = -A_{11}\,, \quad A_{13} = -A_{10}\,, \quad A_{14} = -A_9\,, \quad A_{15} = -A_8\,, \quad A_{20} = A_{17}\,. \tag{2.1.16}$$

Second, the following relations under the swapping of the Mandelstam invariants $t \leftrightarrow u$:

$$
\begin{aligned}
&A_1(s,t) = A_1(s,u)\,, && A_4(s,t) = A_4(s,u)\,, && A_7(s,t) = A_7(s,u)\,,\\
&A_{16}(s,t) = A_{16}(s,u)\,, && A_{17}(s,t) = A_{17}(s,u)\,, && A_{20}(s,t) = A_{20}(s,u)\,,\\
&A_2(s,t) = A_3(s,u)\,, && A_5(s,t) = A_6(s,u)\,, && A_8(s,t) = A_{13}(s,u)\,,\\
&A_9(s,t) = A_{12}(s,u)\,, && A_{10}(s,t) = A_{15}(s,u)\,, && A_{11}(s,t) = A_{14}(s,u)\,,\\
&A_{18}(s,t) = A_{19}(s,u)\,. && && \qquad (2.1.17)
\end{aligned}
$$

It must be noted that everything to this point has been treated in general d-dimensions i.e. the external momenta and consequently the form factors and the projection operators are all in d-dimensions. This has the advantage of being compatible with dimensional regularisation and all the techniques used for solving loop integrals.

At this point, it makes sense to switch to physically relevant 4-dimensional observables. A convenient choice is the so-called "helicity amplitudes", derived by explicitly fixing the helicities for the external particles. Note that such helicity amplitudes are inherently 4-dimensional quantities. It is rather straightforward to derive the expressions for the helicity amplitudes in terms of the form factors A_i. It must be pointed out that since the Z-bosons are massive, their helicities are frame dependent; in this case, the momenta are considered to be in the center-of-momentum frame for both the incoming and outgoing states. This allows the momenta to be parameterised according to

$$
\begin{aligned}
p_1^\mu &= \frac{\sqrt{s}}{2}\,(1,0,0,1)\,, && p_3^\mu = \frac{\sqrt{s}}{2}\,(1,\beta\sin\theta,0,\beta\cos\theta)\,,\\
p_2^\mu &= \frac{\sqrt{s}}{2}\,(1,0,0,-1)\,, && p_4^\mu = \frac{\sqrt{s}}{2}\,(1,-\beta\sin\theta,0,-\beta\cos\theta)\,, \qquad (2.1.18)
\end{aligned}
$$

where $\beta = \sqrt{1-4m_Z^2/s}$ and θ is the angle between the direction of the incoming gluon (p_1) and the outgoing Z-boson with momentum p_3. The polarisation vectors can then be written

as following [6]:

$$
\begin{aligned}
\epsilon^{\mu}_{\pm}(p_1) &= \frac{1}{\sqrt{2}}\,(0, \mp 1, -i, 0)\,, \\
\epsilon^{\mu}_{\pm}(p_2) &= \frac{1}{\sqrt{2}}\,(0, \pm 1, -i, 0)\,, \\
\epsilon^{\mu}_{\pm}(p_3) &= \frac{1}{\sqrt{2}}\,(0, \mp\cos\theta, -i, \pm\sin\theta)\,, \qquad \epsilon^{\mu}_{0}(p_3) = \frac{\sqrt{s}}{2m_Z}\,(\beta, \sin\theta, 0, \cos\theta)\,, \\
\epsilon^{\mu}_{\pm}(p_4) &= \frac{1}{\sqrt{2}}\,(0, \pm\cos\theta, -i, \mp\sin\theta)\,, \qquad \epsilon^{\mu}_{0}(p_4) = \frac{\sqrt{s}}{2m_Z}\,(\beta, -\sin\theta, 0, -\cos\theta)\ . \qquad (2.1.19)
\end{aligned}
$$

It can be easily shown that the above choice of polarisation vectors satisfies the polarisation sums in Eqs. 2.1.6, 2.1.7, and 2.1.8.

A straightforward calculation would show that there are a total of $2^2 \times 3^2 = 36$ helicity amplitudes for this process. However, parity invariance reduces the number of independent helicity amplitudes by a factor of two [157]:

$$
\mathcal{M}_{\lambda_1\lambda_2\lambda_3\lambda_4} = (-1)^{\delta_{\lambda_3 0}+\delta_{\lambda_4 0}}\,\mathcal{M}_{-\lambda_1-\lambda_2-\lambda_3-\lambda_4}\,. \qquad (2.1.20)
$$

Above identity under parity transformation holds for general external kinematics. For the special case at hand where the gluons and Z-bosons are on-shell, following symmetry relations also hold [13, 96]:

$$
\begin{aligned}
\mathcal{M}_{+++-} &= \mathcal{M}_{++-+} \\
\mathcal{M}_{+---} &= \mathcal{M}_{+-++} \\
\mathcal{M}_{++\pm 0} &= \mathcal{M}_{++0\pm} \\
\mathcal{M}_{+-\pm 0} &= -\mathcal{M}_{+-0\mp}\,, \qquad (2.1.21)
\end{aligned}
$$

where the identities in Eq. 2.1.16 have been used to derive the above relations. Another set of relations can be derived if the variables s, θ are eliminated in favour of β, t using

$\theta = \arccos((t-u)/(\beta s)) \in [0, \pi]$, $u = 2m_Z^2 - s - t$, and $s = 4m_Z^2/(1-\beta^2)$:

$$\begin{aligned}
\mathcal{M}_{++++}(\beta, t) &= \mathcal{M}_{++--}(-\beta, t), \\
\mathcal{M}_{+-+-}(\beta, t) &= \mathcal{M}_{+--+}(-\beta, t), \\
\mathcal{M}_{+\pm+0}(\beta, t) &= \mathcal{M}_{+\pm-0}(-\beta, t)\,.
\end{aligned} \tag{2.1.22}$$

Eqs. 2.1.20, 2.1.21, and 2.1.22 together reduce the total number of independent helicity amplitudes to 8. The explicit expressions for the helicity amplitudes in terms of the form factors A_i, as defined through Eq. 2.1.19, are provided in an ancillary file with [6].

Before taking all the symmetries into account, there are 20 form factors A_i, while there are only 18 helicity amplitudes. In fact, looking at the analytic forms of the projection operators, they have spurious poles in the space-time dimension d of the form $\frac{1}{d-4}$. This is clearly not physical and suggests some redundancy between the form factors. It is not unimaginable that for $d = 4$ certain linear relations appear between the form factors. This phenomenon was already observed in [102] where allowing the Z-bosons to decay to fermions and considering specific fermion helicities, only 18 independent "helicity amplitudes" were found. These helicity amplitudes, corresponding to the helicities of the final-state fermions, were found to be gauge-invariant physically relevant quantities, unlike the form factors A_i; explicit calculation done as part of final checks in this work (see Sec. 5.2.2) showed that while the form factors A_i are dependent on the specific regularisation scheme for γ^5, the helicity amplitudes written in [102] are not. Choosing specific helicities for the external particles also forces them to be four-dimensional. This prescription where external particles are treated in $d = 4$ while all the internal quantities are treated in general d is colloquially referred to as the 't Hooft-Veltmann scheme.

Another disadvantage of using the form factors defined as in Eq. 2.1.13 is that they are not orthogonal. An alternate approach was used in [13] to remedy this using the Gram-Schmidt orthogonalisation procedure. Starting from the 20 tensors as in Eq. 2.1.12, the Gram-Schmidt

procedure results in 20 new tensors that are orthogonal linear combinations of the original tensors. Crucially, 2 of the linear combinations vanish in $d \to 4$ limit with only 18 remaining, further indicating the redundancy in the original decomposition. A general prescription to construct physically relevant form factors in d-dimensions was provided in [156, 157]. The authors used the 't Hooft-Veltmann prescription, considering all objects in d-dimensions except the external momenta which are treated in 4-dimensions. Lastly, it must be pointed out that in this work only the contribution from top quarks in the loop are considered.

2.2 1-loop amplitude

2.2.1 Generation of the unreduced amplitude

The form factor decomposition in the previous subsection was general and valid to all orders in perturbation theory. Here, the amplitude in Eq. 2.1.4 is perturbatively expanded in the strong coupling constant α_S as

$$\mathcal{M} = \mathcal{M}_0 + \left(\frac{\alpha_S}{2\pi}\right) \mathcal{M}_1 + O(\alpha_S^2)\,. \tag{2.2.1}$$

Here $\mathcal{M}_0$ corresponds to the leading-order amplitude. Z-bosons don't have "colour" charge and hence don't directly couple to gluons. This process, thus, starts at 1-loop through closed quark loops. `Qgraf` [207] is used to generate the Feynman diagrams. All the quarks other than the top quark are treated as massless and only the Higgs is allowed to couple to the top quark. A total of 10 diagrams are found out of which 2 are zero due to colour conservation since a single gluon couples to a closed quark loop. Of the remaining 8, 2 are mediated via offshell production of the Higgs boson (Figs. 2.1a and 2.1b); remaining 6 are the "box" type contributions. Note that only 2 of these "box" diagrams are truly independent, the rest can be obtained through simple crossings of the external legs. In particular, Figs. 2.1d and 2.1e can be obtained by by crossing the incoming gluons and the outgoing Z-bosons, respectively,

in Fig. 2.1c. We can further exchange the Z-bosons in Fig. 2.1d to obtain Fig. 2.1f. However, since the Z-bosons are onshell (Eq. 2.1.3), and have the same invariant mass, crossing both the gluons and the Z-bosons leaves the diagram unchanged which implies the diagrams in Figs. 2.1c and 2.1d are equal to Figs. 2.1f and 2.1e respectively.

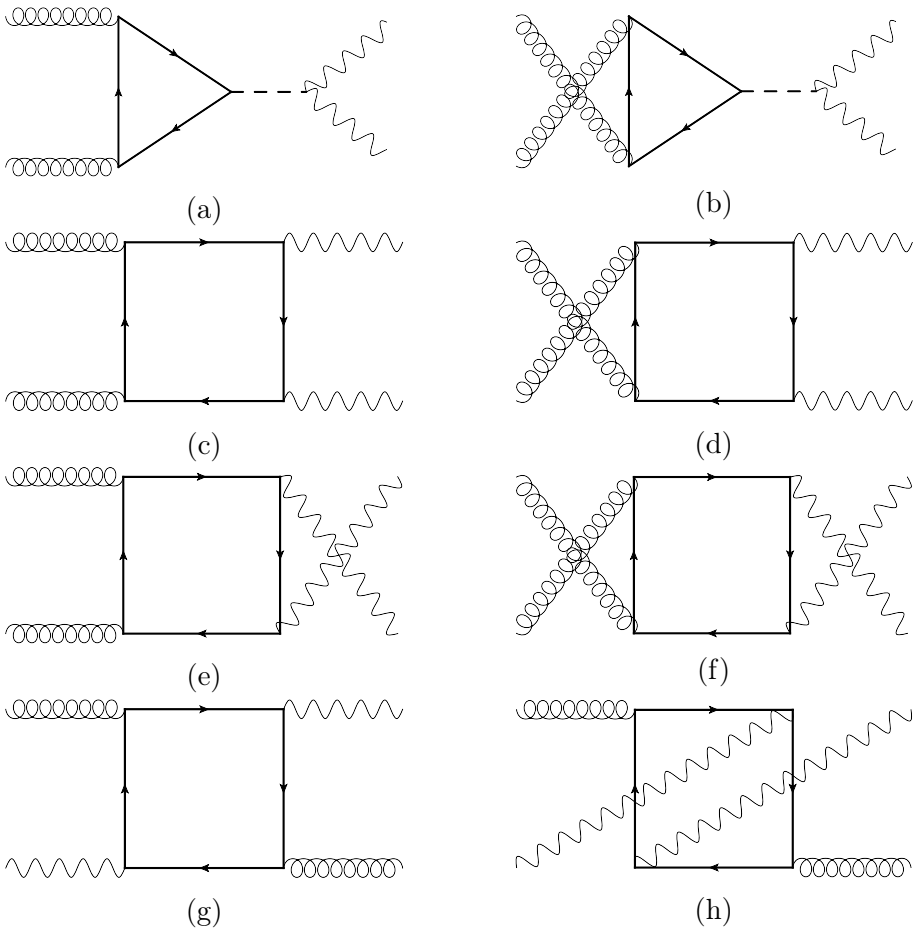

Figure 2.1: Feynman diagrams for the process $gg \to ZZ$ at 1-loop (LO). Figs. 2.1a and 2.1b are the Higgs exchange diagrams, and Figs. 2.1c- 2.1h are the diagrams for continuum production of Z-bosons. Note that out of the 6 continuum diagrams, only 2 are independent and the rest can be obtained through various crossings of external legs.

The next step is to insert Feynman rules in the diagrams to obtain the amplitudes. The Feynman rules employed here are given in the appendix A. Custom `FORM` [208–210] scripts are used to insert the Feynman rules into the diagrams to generate algebraic expressions. The colour structure of the remaining non-zero diagrams is quite simple; it is essentially a

gluon propagator like structure, so the colour factor is simply given by

$$\mathcal{C} = \mathcal{C}_0 \, \delta_{ab} \, . \tag{2.2.2}$$

For the tree-level propagator, $\mathcal{C}_0$ is just 1 (see Appendix A.2). At 1-loop, $\mathcal{C}_0 = T_F = \frac{1}{2}$ for the diagram involving only a closed quark loop (see Appendix A.4). At higher loops, more complicated structures appear in $\mathcal{C}_0$ i.e. the quadratic Casimirs C_F, C_A; see Appendix A.3 for a definition of the quadratic Casimir operators.

The Z-boson couples to the fermion through both a vector and an axial-vector coupling with the vertex written as

$$\begin{aligned} \mathcal{V}_\mu^{Vf\bar{f}} &= ie \left[L^Z_{f\bar{f}} \gamma_\mu \left(\frac{1-\gamma_5}{2} \right) + R^Z_{f\bar{f}} \gamma_\mu \left(\frac{1+\gamma_5}{2} \right) \right] \\ &= i \frac{e}{2 \sin\theta_W \cos\theta_W} \gamma_\mu \left(v_t + a_t \gamma_5 \right) \end{aligned} \tag{2.2.3}$$

from the EW couplings in Eq. 1.6.26, where the coupling to the left-handed fermion is $L^Z_{f\bar{f}} = (I_3^f - q_f \sin^2\theta_W)/(\sin\theta_W \cos\theta_W)$ and to the right-handed fermion is $R^Z_{f\bar{f}} = -q_f \sin\theta_W / \cos\theta_W$. Here e is the positron charge and q_f is the electric charge of the fermion in terms of e. For the top quark, the vector and axial couplings (v_t, a_t) are given by θ_W by $v_t = \frac{1}{2} - \frac{4}{3}\sin^2\theta_W$ and $a_t = -\frac{1}{2}$, respectively, in terms of the weak mixing angle θ_W, as defined in Eq. 1.6.10.

At this point it is necessary to discuss the γ-matrices, in particular the γ^5 matrix. γ-matrices are an essential part of most scattering amplitude calculations in the Standard Model. A brief description of their properties is provided in Appendix C. While the γ-matrices that satisfy the anti-commutation relation $\{\gamma^\mu, \gamma^\nu\} = 2g_{\mu\nu}$ can be consistently treated in d-dimensions, the γ^5 matrix, as defined, is inherently a 4-dimensional object. As such, it is not clear how to incorporate it in Conventional Dimensional Regularisation (CDR) [151–154] where objects are treated in d-dimensions, along with the usual γ-matrices. There are several schemes used to work around this issue; see Appendix C for details. This

calculation employs Kreimer's [211–213] anti-commuting γ^5 scheme to properly treat γ^5 in d-dimensions. In this scheme, the anti-commuting property of γ^5 is kept while traces are no longer assumed to be cyclic. In other schemes such as the 't Hooft, Veltman, Breiten-Lohner, and Maison scheme [153, 214–216], the anti-commutation relation is given up and cyclicity of the trace is kept. This scheme necessarily treats 4 and $d-4$ dimensional objects separately. A fundamental disadvantage of this is that the Ward identities are not preserved requiring the addition of extra counterterms to the Lagrangian. The reader is referred to Appendix C for a more detailed discussion of γ-matrices and different γ^5 schemes.

The two Z-bosons coupled to a fermion line can in general generate 3 different contributions: vector-vector (v_t^2), axial-vector ($a_t v_t$), and axial-axial (a_t^2), and it is useful to split the amplitude into these 3 parts. The vector-vector and axial-axial contributions are identical for massless quarks [96]. This can be understood by looking at the traces involved; for traces involving an even number of γ^5's, the γ^5's disappear as a result of the anti-commutation relations and the fact that $(\gamma^5)^2 = 1$; the resulting trace is identical to that of the vector-vector case. For the case of a massive quark the difference must be proportional to the quark mass. E.g.

$$Tr\left[(\not{p}_1 + m)\gamma^\mu(\not{p}_2 + m)\gamma^\nu\right] - Tr\left[(\not{p}_1 + m)\gamma^\mu\gamma^5(\not{p}_2 + m)\gamma^\nu\gamma^5\right] = 8m^2 g^{\mu\nu} \tag{2.2.4}$$

The axial-vector ($a_t v_t$) contribution to this amplitude vanishes identically as a consequence of Bose symmetry and charge-parity conservation for this process [96]. The absence of any terms containing the ϵ-tensor in Eq. 2.1.5 can also be explained through this since the Levi-Civita tensor violates parity and hence any such terms are forbidden through charge-parity conservation.

The projection operators from Eq. 2.1.13 are then applied to obtain analytical expressions for individual form factors.

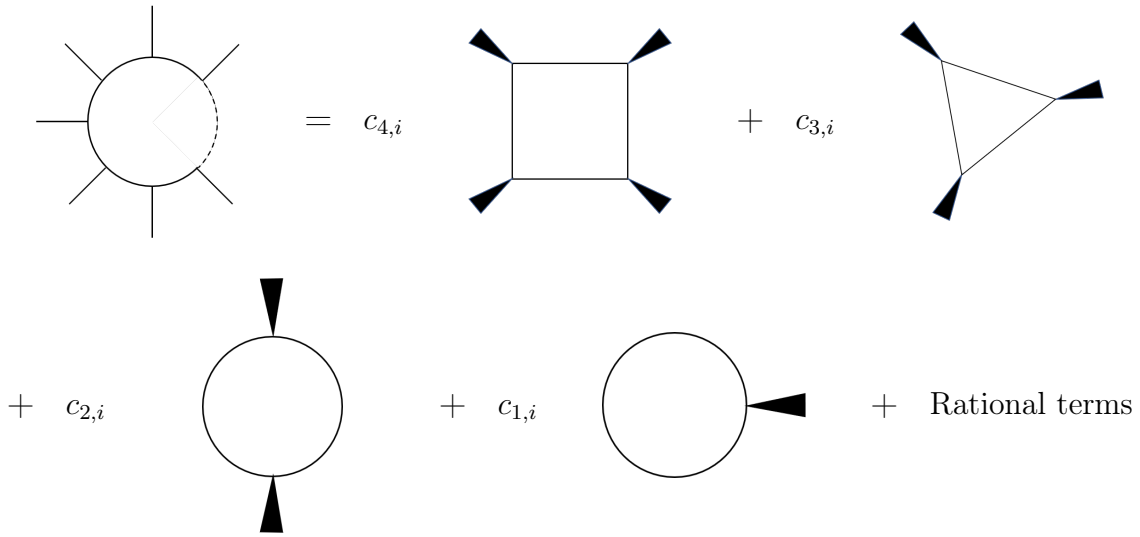

Figure 2.2: Decomposition of a general 1-loop Feynman integral in $d = 4$.

2.2.2 Reduction to master integrals

The form factors contain only scalar loop integrals (see Sec. 1.5.4 for a brief discussion on loop integrals) without any open Lorentz indices. The list of scalar loop integrals isn't the minimal list of integrals that needs to be evaluated, however. Indeed it can be shown that at 1-loop, all the integrals can be related to a minimal set of integrals often referred to as the basis integrals or "master integrals". In fact, any 1-loop integral can be written as a linear combination of basis integrals [217–219]. In $d = 4$, this linear combination is simply

$$I = c_{1,i}\, A_i + c_{2,i}\, B_i + c_{3,i}\, C_i + c_{4,i}\, D_i + O(d-4) \tag{2.2.5}$$

as depicted in Fig. 2.2, where A_i, B_i, C_i, D_i are all possible 1-, 2-, 3-, and 4-propagator scalar Feynman integrals

$$A_0(m_1^2) = \int \frac{\mathrm{d}^d k}{i\pi^{d/2}} \frac{1}{D_1}\,, \tag{2.2.6}$$

$$B_0(p^2, m_1^2, m_2^2) = \int \frac{\mathrm{d}^d k}{i\pi^{d/2}} \frac{1}{D_1 D_2}\,, \tag{2.2.7}$$

$$C_0(p_1^2, p_2^2, s_{12}, m_1^2, m_2^2, m_3^2) = \int \frac{\mathrm{d}^d k}{i\pi^{d/2}} \frac{1}{D_1 D_2 D_3}\,, \tag{2.2.8}$$

$$D_0(p_1^2, p_2^2, p_3^2, p_4^2, s_{12}, s_{23}, m_1^2, m_2^2, m_3^2, m_4^2) = \int \frac{\mathrm{d}^d k}{i\pi^{d/2}} \frac{1}{D_1 D_2 D_3 D_4}\,, \tag{2.2.9}$$

with

$$\begin{aligned} D_1 &= k^2 - m_1^2\,, \\ D_2 &= (k+p_1)^2 - m_2^2\,, \\ D_3 &= (k+p_1+p_2)^2 - m_3^2\,, \\ D_4 &= (k+p_1+p_2+p_3)^2 - m_4^2\,. \end{aligned} \tag{2.2.10}$$

The assertion in Eq. 2.2.5 is in fact more general. Any N-point function can be written as a linear combination of $4-$ and lower point functions in $d = 4$ dimensions.

The first approach to perform the tensor decomposition to obtain scalar integrals was proposed by Passarino-Veltmann in [220]. Consider the following 1-loop 2-propagator tensor integral as an example:

$$I^\mu(p, m) = \int \frac{\mathrm{d}^d k}{(2\pi)^d} \frac{k^\mu}{(k^2 - m^2)(k+p)^2}\,. \tag{2.2.11}$$

Here Conventional Dimensional Regularisation (CDR) is being employed to regulate the divergences. The only rank-1 Lorentz tensor possible for this integral is p^μ. Using this, the integral can be written as

$$I^\mu(p, m) = \int \frac{\mathrm{d}^d k}{(2\pi)^d} \frac{k^\mu}{(k^2 - m^2)(k+p)^2} = p^\mu B_1(p^2, m)\,, \tag{2.2.12}$$

where the scalar part has been defined as $B_1(p^2, m)$, which can be related to the original

integral by contracting with p_μ as

$$\begin{aligned} p^2 B_1(p^2,m) = p_\mu I^\mu(p,m) &= \int \frac{\mathrm{d}^d k}{(2\pi)^d} \frac{k\cdot p}{(k^2-m^2)(k+p)^2} \\ &= \frac{1}{2}\int \frac{\mathrm{d}^d k}{(2\pi)^d} \frac{(k+p)^2-(k^2-m^2)-(m^2+p^2)}{(k^2-m^2)(k+p)^2} \\ &= \frac{1}{2}\int \frac{\mathrm{d}^d k}{(2\pi)^d} \frac{1}{(k^2-m^2)} - \frac{1}{2}\int \frac{\mathrm{d}^d k}{(2\pi)^d} \frac{1}{(k+p)^2} \\ &\quad - \frac{1}{2}(p^2+m^2)\int \frac{\mathrm{d}^d k}{(2\pi)^d} \frac{1}{(k^2-m^2)(k+p)^2} \\ &= \frac{1}{2}\left(A_0(m) - A_0(0) - (p^2+m^2)B_0(p^2,m,m)\right) . \end{aligned} \tag{2.2.13}$$

$A_0(0)$ can be shown to vanish identically in dimensional regularisation (see Sec. 3.1); $A_0(m)$ and $B_0(p^2,m)$ are the standard 1-loop scalar integrals from Eqs. 2.2.6 and 2.2.7, also known as Passarino-Veltmann functions. Higher rank tensor integrals can be similarly decomposed:

$$I^{\mu\nu}(p,m) = \int \frac{\mathrm{d}^d k}{(2\pi)^d} \frac{k^\mu k^\nu}{(k^2-m^2)(k+p)^2} = g^{\mu\nu} B_{00}(p^2,m) + p^\mu p^\nu B_{11}(p^2,m) . \tag{2.2.14}$$

Note the appearance of $g^{\mu\nu}$ as a rank-2 tensor. The B_{00}, B_{11} functions in the above equations can be similarly written in terms of $A_0(m)$ and $B_0(p^2,m)$ after contracting with rank-2 tensors $g_{\mu\nu}$ and $p_\mu p_\nu$ and solving the resulting linear system. These, along with the 3 and 4 propagator Passarino-Veltmann functions C_0 and D_0, form a basis of integrals at 1-loop in 4-dimensions. The basis integrals can then be evaluated either analytically using a multitude of methods (see Sec. 4.1), or numerically using several libraries e.g. `LoopTools` [221], `QCDLoop` [222], `OneLOop` [223], `Golem` [224], `Collier` [225], `Package-X` [226]. Passarino-Veltmann reduction has been used to calculate a number of 1-loop processes including the 1-loop amplitude for $gg \to ZZ$ in [93, 96, 97].

The conventional Passarino-Veltmann reduction, however, has certain limitations:

1. In Eq. 2.2.13, for instance, B_1 cannot be solved for the case where $p^2 = 0$. In particular, the reduction procedure for integrals with ≥ 2 propagators involves inverting the so-

called "Gram matrices" and these Gram matrices become singular in certain regions of phase-space. This can lead to severe numerical instabilities and makes it challenging to write efficient numerical algorithms.

2. Applying the reduction procedure to higher tensor rank integrals is a rather cumbersome procedure and leads to an explosion in the number of terms in intermediate stages. This results in severe algebraic complexity in the case of analytic calculation and loss of precision in the case of numerical calculation.

3. For processes with large number of diagrams and/or external legs the integral-by-integral reduction procedure is extremely tedious.

Several new approaches have been developed and refined in the past few decades to resolve the above issues; the reader is referred to [91, 227] for an overview of the modern 1-loop amplitude methods. By far the most popular method for 1-loop computations is the OPP method proposed by Ossola-Papadopoulos-Pittau in [86], closely related to the ideas of generalised unitarity cuts [85, 228]. Further progress regarding efficient numerical implementations and automation [87, 229–232] lead to the so-called "NLO revolution" as a result of complete automation of 1-loop amplitudes. There are a number of public libraries for integral reduction based on OPP method: `CutTools` [233], `Samurai` [234], `Ninja` [235]. The computation of the amplitudes and NLO corrections has been automated in many publicly available codes such as `BlackHat` [236], `HELAC-NLO` [237], `MadGraph` [238], `GoSam2.0` [239], and `OpenLoops2` [240].

Traditional Passarino-Veltmann reduction relies on step-by-step procedure to reduce high rank tensor integrals to find the coefficients of the master integrals. Using the OPP method, the coefficients can be calculated directly as follows. Consider the integrand of a general 4-point Feynman diagram

$$\mathcal{I}(\overline{k}) = \frac{N(k)}{\overline{D}_1\overline{D}_2\overline{D}_3\overline{D}_4} \tag{2.2.15}$$

where $\overline{D}_i$ are the propagators in d-dimensions $\overline{D}_i = (\overline{k} + q_i)^2 - m_i^2$ with $\overline{k}$ being the d-dimensional loop momentum, k the 4-dimensional loop momentum, and q_i, m_i being the momentum flowing through the edge and the mass of the edge respectively. Note that the numerator $N(k)$ is a strictly 4-dimensional polynomial in the loop momentum k; this creates a mismatch between the numerator and the denominator that leads to the rational terms. For now, it suffices to consider everything in $d = 4$ (except in the definition of the integrals where regularisation is required); the rational terms are computed later. The result of Eq. 2.2.5 can be extended to integrands as shown in [241] with the numerator decomposed as

$$\begin{aligned} N(k) = &\left(d(1234) + \tilde{d}(1234;k)\right) \\ &+ \left(c(123) + \tilde{c}(123;k)\right) D_4 + \left(c(124) + \tilde{c}(124;k)\right) D_3 + ... \\ &+ \left(b(12) + \tilde{b}(12;k)\right) D_3 D_4 + \left(b(13) + \tilde{b}(13;k)\right) D_2 D_4 + ... \\ &+ \left(a(1) + a(1;k)\right) D_2 D_3 D_4 + \left(a(2) + a(2;k)\right) D_1 D_3 D_4 + ... \\ &+ \tilde{P}(k) D_1 D_2 D_3 D_4 \,. \end{aligned} \tag{2.2.16}$$

The coefficients $d(1234), c(123)$, etc. are independent of the loop-momentum and drop out of the integration. These are the true coefficients same as $c_{i,j}$ in Eq. 2.2.5. The other loop-momentum dependent coefficients $\tilde{d}(1234;k)$, etc. are "spurious" and vanish after integration; however, these are still required to compute the lower coefficients e.g. to solve for $c(123)$ both $d(1234)$ and $\tilde{d}(1234;k)$ are needed. In principle the problem now reduces to calculating the above equation for sufficient values of k and inverting the system to find the coefficients. This approach is, however, very inefficient since it requires inverting large systems and may lead to numerical instabilities. Instead, the values of loop-momentum can be chosen such that some of the propagators go on-shell e.g.

$$D_1 = D_2 = D_3 = D_4 = 0 \,. \tag{2.2.17}$$

Denoting the solution to the above constraints by $k = k_0^{\pm}$ and substituting into Eq. 2.2.16 results in

$$d(1234) + \tilde{d}(1234; k_0^{\pm}) = N(k_0^{\pm})\,. \tag{2.2.18}$$

It turns out that $\tilde{d}(1234; k_0^+) = -\tilde{d}(1234; k_0^-) = \tilde{d}(1234)\,T(k_0^+)$, where the general tensor $T(k)$ is known. This allows the computation of the coefficients:

$$\begin{aligned} d(1234) =& \frac{1}{2}\left(N(k_0^+) + N(k_0^-)\right) \\ \tilde{d}(1234) =& \frac{1}{2T(k_0^+)}\left(N(k_0^+) - N(k_0^-)\right) \end{aligned} \tag{2.2.19}$$

Once the 4-point coefficients are known, the lower point coefficients can be calculated by setting fewer propagators on shell. Effectively, the on-shell conditions convert the linear system into a block-triangular form that can be solved much more easily. Details of the above procedure as well as derivation can be found in [86].

The OPP and generalised unitarity methods resolve the issues with singular Gram determinants as well as explosion of terms. A huge advantage is that the procedure can be applied to sum of Feynman diagrams instead of each individual Feynman integral. The method is not generally applicable beyond 1-loop, however. The decomposition in Eqs. 2.2.13 or 2.2.16 works because the resultant numerator can be written as a linear combination of the propagator factors in the denominator [241]. This is not possible in general beyond 1-loop; such numerators are called "Irreducible Scalar Products". A much more general approach called "Integration-By-Parts" (IBP) reduction [242] is most commonly used for processes beyond 1-loop. Details of IBP reduction and its application to this work are provided in Sec. 3.

2.2.3 Results

To calculate the 1-loop amplitudes for $gg \to ZZ$, first tensor decomposition of the unreduced amplitudes, as described in Sec. 2.1, is performed to obtain the form factors. The scalar integrals in the form factors are reduced to master integrals using Passarino-Veltmann reduction with the numerator algebra performed using custom `FORM` scripts and `Package-X` [226]. The master integrals are then evaluated using `LoopTools` [221]. Helicity amplitudes are calculated from the form factors and are used to present the results below. After the calculation, our results are compared to published results in [13]; agreement is found for each form factor and helicity amplitude.

In Fig. 2.3a, the 1-loop amplitude-squared $|\mathcal{M}|^2$ summed over all helicity configurations is compared for 3-different contributions: Only the top-quark contribution, top-quark contribution with Higgs exchange diagrams included, and the contribution of a massless up-type quark. It is clear that the top-quark contribution (in black) grows with energy. After including the Higgs mediated diagrams, however, the growth is reduced and the amplitude-squared plateaus; this is the unitarising effect of the Higgs boson. Another important observation is that even after including the Higgs mediated diagrams, the contribution from top-quark dominates over the massless contribution for high energies. This further underlines the importance of a full 2-loop computation for this process. Fig. 2.3b shows the same data but zoomed in to the region of smaller invariant mass. While the massless contribution is fairly uniform and dominates in the low-energy region, the massive (top quark) contribution starts to increase past $\sqrt{s} = 2m_t$ when the top quarks in the loop can be produced on-shell.

This unitarising behaviour and the threshold effect for $\sqrt{s} = 2m_t$ is even more apparent in the individual helicity amplitudes as shown in Fig. 2.4. Fig 2.4a shows the individual helicity amplitudes without the Higgs mediated diagrams included. In this case the "$++00$" mode (shown in red) is dominant and increases with energy, much like Fig. 2.3a. This is easily understood through the Equivalence theorem where the "00" mode corresponds to scattering

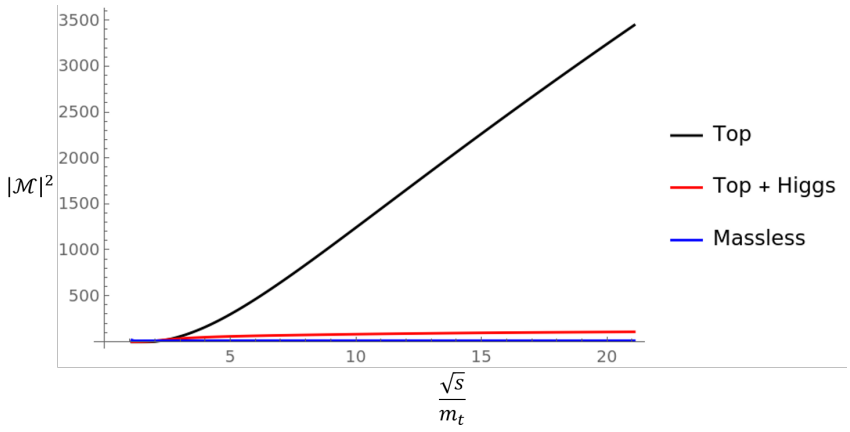

(a)

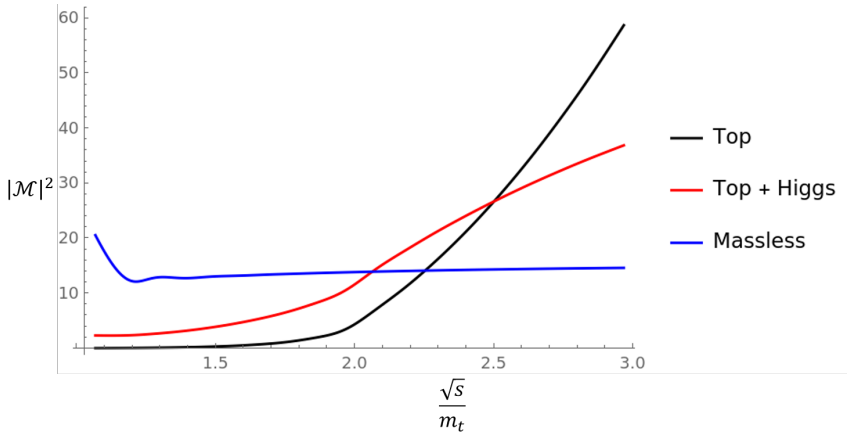

(b)

Figure 2.3: Comparison of $|\mathcal{M}|^2$ for $gg \to ZZ$ for three different type of contributions, summed over all helicities for the external particles. Without including the Higgs mediated contributions, the top quark contribution increases with energy.

of two gluons producing two Goldstone bosons where the coupling of the Goldstone bosons to the top quark is proportional to the top mass. Including the Higgs diagrams (Fig. 2.4b) it is clear that the "$++00$" mode does not increase indefinitely with energy. In fact, at very high energies, the "$+-00$" mode takes over and becomes the dominant mode. Another interesting feature of the above plot is the stark threshold effect observed in the "$++00$" mode. This is absent in the "$+-00$" mode as a consequence of a mismatch in the helicities; the top quark pair produced on-shell can have a total spin of $J = 0$ or $J = 1$ with $J = 0$ preferred for the "00" mode for the Z-bosons while the initial state has a total spin of 2.

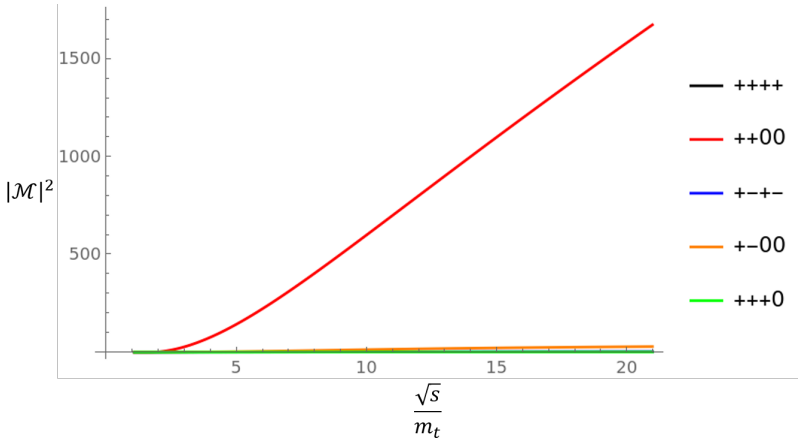

(a)

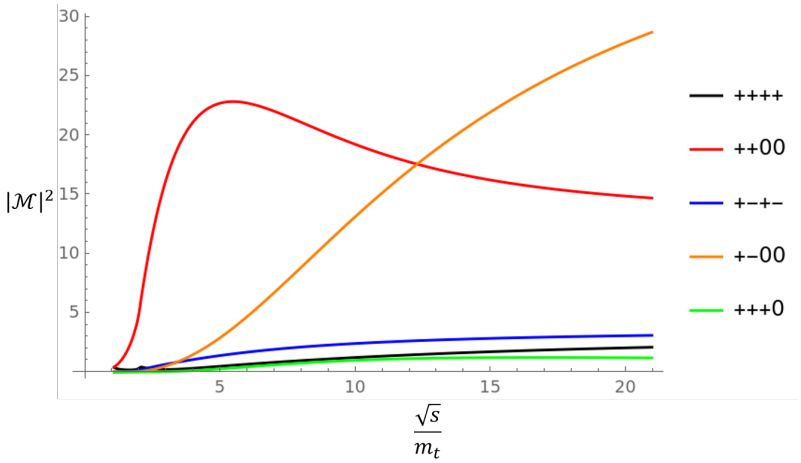

(b)

Figure 2.4: Comparison of $|\mathcal{M}|^2$ for $gg \to ZZ$ for different helicity configurations for the top quark contribution. The bottom panel (Fig. 2.4b) also includes the Higgs mediated diagrams.

Fig. 2.5 shows the ratio of individual helicities to the total $|\mathcal{M}|^2$ for both the top (Fig. 2.5a) and massless (Fig. 2.5b) contributions. For the massive case, the longitudinal mode "00" has the largest contribution, unsurprisingly with the "$+-00$" helicity being the dominant mode for high energies. For the massless case, however, the longitudinal modes are almost negligible and the "$++++$" and "$+-+-$" helicities contribute the most.

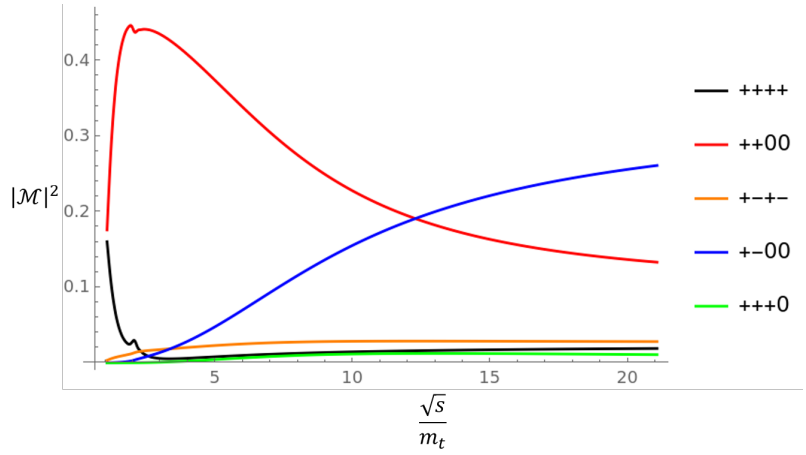

(a)

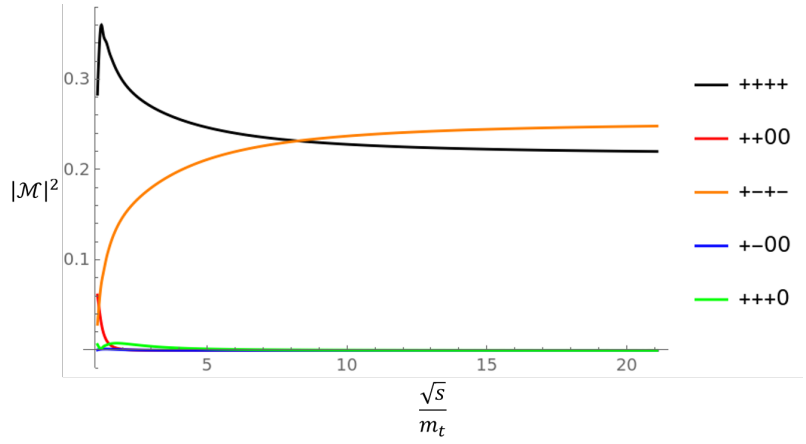

(b)

Figure 2.5: Ratio of contribution of individual helicity configurations to the total $|\mathcal{M}|^2$ for $gg \to ZZ$ for (a) top quark contribution including the Higgs diagrams, and (b) massless quark contribution.

2.3 2-loop amplitude

2.3.1 Generation of diagrams

At 2-loops, the contributions to this process involving s-channel Higgs production are already known [108–111] and those for the massless quarks were computed in [102, 103]. As such, only the top-quark contribution is considered here. The diagrams for the 2-loop amplitude are generated using `Qgraf` [207]. A total of 166 diagrams are generated that contain at

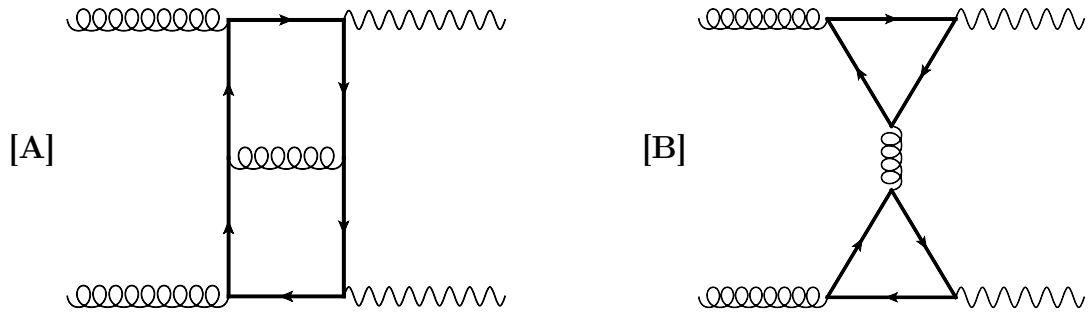

Figure 2.6: Example Feynman diagrams representing the two classes of diagrams at 2-loops.

least 1 top-quark propagator. Additional diagrams containing only massless bottom quarks have been generated as well; see the discussion for diagrams of **Class B** below. A total of 49 out of the 166 diagrams containing at least 1 top-quark propagator vanish from colour conservation since they have a single gluon coupled to a closed quark loop. The remaining diagrams can broadly be split into two different "classes" (see Fig. 2.6):

Class A: In diagrams of class A, both Z-bosons are attached to the same closed fermion loop. As described previously, the anti-commuting, Kreimer's γ^5 scheme is used to handle γ^5 in d-dimensions. In general, a reading point prescription is used to ensure that all traces are read from the same point since cyclicity is not preserved. For a closed fermion loop, however, in case of an even number of γ^5's, it is rather straightforward to eliminate the γ^5 using the anti-commutation identities. This allows for a trivial implementation of the γ^5 scheme for this class of diagrams.

Class B: In this class of diagrams, the Z-bosons couple to different closed fermion loops. The vector-vector (v_t^2) contribution for these diagrams can be shown to vanish due to Furry's theorem. The vector-axial ($a_t v_t$) piece vanishes identically, as discussed previously, as a result of charge-parity conservation for this process. However, the axial-axial (a_t^2) piece vanishes only for a sum over a degenerate $SU(2)_L$ doublet. Since the third generation quarks (t, b) are not degenerate, a finite term remains from the top-bottom mass splitting. Hence, for consistency, additional diagrams of this type containing only massless bottom quarks are also included. For these diagrams, there is a single γ^5 in each fermion loop which is non-trivial

to handle and requires a careful application of the anti-commuting γ^5 scheme. It must be pointed out that these diagrams are effectively 1-loop*1-loop type diagrams and as such are a lot easier to reduce to master integrals than **Class A**.

2.3.2 Class A

After generating the diagrams in class A, the Feynman rules are inserted for which custom `FORM` scripts are employed. The resulting algebraic expressions for the form factors are required to be interpreted as linear combinations of Feynman integrals. For this, `Reduze 2` [243–246] is employed to map them to the 4 different integral families shown in Tab. 2.1.

An "integral family" is essentially a set of Feynman propagators that can be used to classify the integrals appearing in one or more topologies. The concept of an "integral family" is discussed in a bit more detail in Sec. 3. For the purpose of this section it suffices to say that an integral family is a set of Feynman propagators grouped together such that all possible scalar products between the momenta in the integral family (both loop momenta and external momenta) are uniquely determined in terms of the inverse propagators. E.g. considering an integral family with L loop momenta and E independent external momenta, the number of distinct scalar products (dependent on a loop momentum) is $N = L(L+1)/2 + EL$. This is the number of propagators that an integral family must contain. For a 4-point topology at 1-loop, this number is 4; at 2-loops, it is 9. Note that for a 4-point topology at 2-loops, only 7 propagators can be present assuming all the vertices connect 3 edges. The 2 "extra" propagators, even though they do not form a part of the topology are required to specify all the scalar products.

For simplification of the expressions, Feynman gauge is used ($\xi = 1$) for internal gluons. After mapping the diagrams to the above integral families, a total of 29247 integrals are found in the amplitude. In the worst case, the integrals have up to 4 inverse propagators in the numerator. The algebraic expressions at this stage of the calculation are quite large, occupying ~ 50 GB of disk space.

A	B	C	D
$k_1^2 - m_t^2$	k_1^2	$k_1^2 - m_t^2$	k_1^2
$(k_1 + p_1)^2 - m_t^2$	$(k_1 + p_1)^2$	$(k_1 + p_1)^2 - m_t^2$	$(k_1 + p_1)^2$
$(k_1 + p_1 + p_2)^2 - m_t^2$	$(k_1 + p_1 + p_2)^2$	$(k_1 + p_1 - p_3)^2 - m_t^2$	$(k_1 + p_1 + p_2)^2$
$(k_1 + p_4)^2 - m_t^2$	$(k_1 + p_4)^2$	$(k_1 + p_4)^2 - m_t^2$	$k_2^2 - m_t^2$
$k_2^2 - m_t^2$	$k_2^2 - m_t^2$	$k_2^2 - m_t^2$	$(k_2 + p_1 + p_2)^2 - m_t^2$
$(k_2 + p_1)^2 - m_t^2$	$(k_2 + p_1 - p_3)^2 - m_t^2$	$(k_2 + p_1 - p_3)^2 - m_t^2$	$(k_2 + p_4)^2 - m_t^2$
$(k_2 + p_1 + p_2)^2 - m_t^2$	$(k_2 - p_3)^2 - m_t^2$	$(k_2 + p_4)^2 - m_t^2$	$(k_2 - k_1)^2 - m_t^2$
$(k_2 + p_4)^2 - m_t^2$	$(k_2 + p_4)^2 - m_t^2$	$(k_2 - k_1)^2$	$(k_2 - k_1 + p_2)^2 - m_t^2$
$(k_1 - k_2)^2$	$(k_1 + k_2 + p_4)^2 - m_t^2$	$(k_1 - k_2 + p_1)^2$	$(k_2 - k_1 + p_4)^2 - m_t^2$

Table 2.1: List of integral families and their propagators for the 2-loop amplitude.

Usually, topologies that have many common denominators are combined together in one integral family. Even so, there can still be common propagators, often related through a shift of loop momentum, between topologies from different topologies. This, however, leads to redundancy in the definition of integrals and certain symmetry relations can be written down that relate integrals from different integral families. Such relations aren't limited to different families, though, and similar relations between different "sectors" of the same integral family exist as well as within a sector. Using such relations generated using `Reduze 2`, the total number of integrals in the diagrams can be reduced to 4504. Adding diagrams together and considering only form factors, this number drops to 1584 due to further cancellations and the total size of the expressions drastically reduces to < 1 GB. This really underlines the importance of working with objects like form factors instead of individual diagrams as well as the use of symmetry relations; the resulting algebraic expressions are a lot more manageable and the number of Feynman integrals appearing in the expressions reduces drastically.

Unlike the case of 1-loop, at 2-loops the master integrals are not known a priori. Additionally, the methods traditionally applied at 1-loop e.g. Passarino-Veltmann reduction or OPP method are not adequate beyond 1-loop. The conventional approach to reduce integrals beyond 1-loop is Integration-By-Parts reduction [242]. `Reduze 2` is used to perform a numerical reduction (i.e. with exact rational numbers substituted for kinematic variables) to find the list of masters. A total of 264 master integrals are found out of which 172 are not

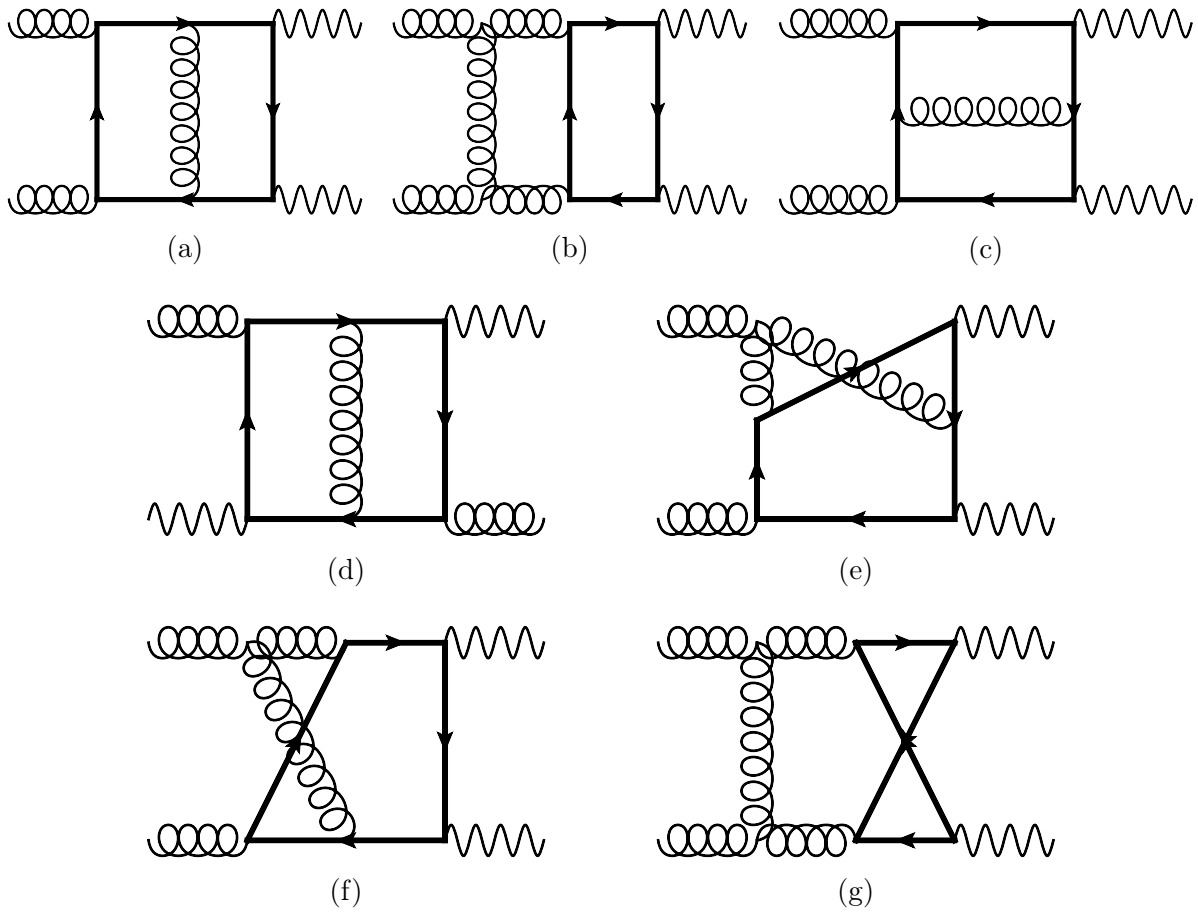

Figure 2.7: Representative Feynman diagrams in class A with irreducible topologies. The number of master integrals in the above top-level topologies are 3, 4, 3, 3, 5, 5, and 4 respectively.

related via any crossing i.e. exchange of external legs. In terms of topologies, there are 85 irreducible ones i.e. the topologies containing master integrals and which cannot be completely expressed in terms of integrals from subtopologies, with a 6 propagator topology having the most number of master integrals (6). Of the 13 top-level topologies i.e. the topologies with 7 propagators, 7 are irreducible (Fig. 2.7) and the other 6 are reducible (Fig. 2.8).

For diagrams of **Class A** two different colour structures appear given by the two quadratic

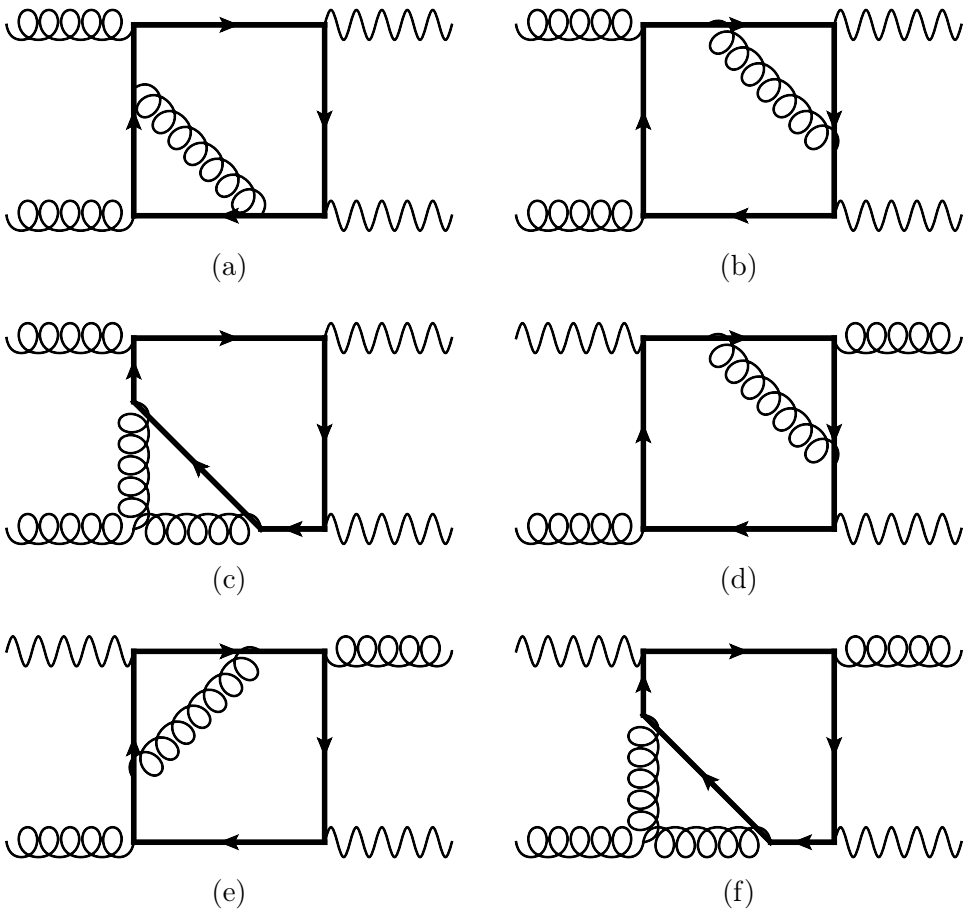

Figure 2.8: Representative Feynman diagrams in class A with reducible topologies.

Casimir invariants C_F and C_A i.e. the colour structure of a diagram can be written as

$$\mathcal{C} = (a_1 C_F + a_2 C_A)\, T_F \delta_{ab}\,. \tag{2.3.1}$$

Interestingly, it is observed that the diagrams contributing to the C_F piece are purely planar while a mix of planar and non-planar diagrams contributes to the C_A piece. Since the planar diagrams are expected to be simpler to reduce than the non-planar diagrams, the C_F piece is expected to be simpler.

Full IBP reduction for diagrams of class **A** is extremely challenging and the conventional approach proved inadequate. For instance, `Reduze 2` was used to perform the reduction for this process for the case of massless internal quarks in [102]. However, we find in our

experiments that it was only able to solve reductions for the massive case only for integrals with 1 inverse propagator while the full problem requires the solution for integrals with up to 4 inverse propagators. The new developments required to solve this problem are discussed in Chapter 3.

2.3.3 Class B

Diagrams in **Class B** have contributions with a single γ^5 in each loop which leads to a non-trivial structure and requires careful application of the reading point prescription in Kreimer's scheme. Details of the γ^5 scheme and the reading point prescription are given in Appendix C.

Since these diagrams are effectively 1-loop*1-loop, they are significantly simpler and hence treated separately from **Class A**. As described previously, the only surviving terms are of the axial-axial type (a_t^2). These should also be proportional to m_t^2 assuming all the other quark flavours are massless. The colour factor for this class of diagrams is particularly simple since this is just a product of two 1-loop diagrams.

$$\mathcal{C} = T_F^2 \, \delta_{ab} \, . \tag{2.3.2}$$

In the context of this process, the application of the anti-commuting scheme is relatively simple since every trace must be read from the same point due to the presence of only 1 γ^5 in each loop. Passarino-Veltmann reduction is used along with the 1-loop tool `Package-X` [226] for manipulation of tensor objects to reduce the amplitudes to master integrals. Exact results for these diagrams were previously presented in [106] with which full agreement is found at the level of helicity amplitudes.

Chapter 3

IBP reduction using syzygies

3.1 Integration-by-parts reduction

A general L-loop scalar Feynman integral with N propagators can be represented by

$$I(\nu_1, ..., \nu_N) = \int \left(\prod_{l=1}^{L} \frac{\mathrm{d}^d k_l}{i\pi^{\frac{d}{2}}} \right) \prod_{i=1}^{N} \frac{1}{(q_i^2 - m_i^2)^{\nu_i}} \tag{3.1.1}$$

where $k_1, ..., k_L$ are the loop momenta, $p_1, ..., p_E$ are the independent external momenta, q_i are the momenta of the propagators (linear combinations of loop and external momenta), m_i are the masses of the propagators, $\nu_i \leq 0$ are (integer) exponents of the propagators, and $d = 4 - 2\epsilon$ is the number of space-time dimensions. Here, positive powers $\nu_i > 0$ of the propagators are also allowed, that is, an *integral family* is considered allowing for general propagators. Note that in an integral family, all possible scalar products between the momenta (both loop and external) are fixed in terms of the kinematic invariants and inverse propagators. This requires the total number of propagators in an integral family to be equal to $L(L+1)/2 + LE$. Feynman integrals often contain fewer propagators than this; the remaining propagators can appear in the numerator as irreducible scalar products. E.g. the 4-point topologies at 2-loops considered in this work (Figs. 2.7 and 2.8) have a maximum of 7 distinct propagators with the remaining 2 being used to express the irreducible scalar products.

The total derivative of an integral in dimensional regularisation vanishes. This allows the

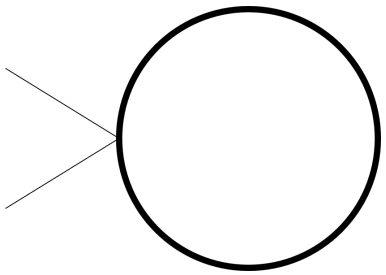

Figure 3.1: A tadpole graph with the thick loop corresponding to the massive propagator with mass m.

following linear relations between different integrals [242]

$$0 = \int \left(\prod_{l=1}^{L} \frac{\mathrm{d}^d k_l}{i\pi^{d/2}} \right) \frac{\partial}{\partial k_j^\mu} \left(v^\mu \prod_{i=1}^{N} \frac{1}{(q_i^2 - m_i^2)^{\nu_i}} \right), \tag{3.1.2}$$

where v_μ could be any linear combination of loop and external momenta. The surface term from the integration of the above integrand can be shown to vanish for small values of d. Extending the formula to general d using analytic continuation leads to the relations known as "Integration-By-Parts" identities.

It is instructive to look at an example. Consider a Feynman integral with just one propagator in d dimensions e.g. in Fig. 3.1

$$I = \int \frac{\mathrm{d}^d k}{i\pi^{d/2}} \frac{1}{(k^2 - m^2)} \tag{3.1.3}$$

often referred to as a "tadpole" integral. Taking the derivative of the integrand with respect to the loop momentum (and dropping the $i\pi^{d/2}$ factor for brevity), as in Eq. 3.1.2, yields

$$\int \mathrm{d}^d k \, \frac{\partial}{\partial k_\mu} \frac{k_\mu}{(k^2 - m^2)} = \int \mathrm{d}^d k \left[\left(\frac{\partial k_\mu}{\partial k_\mu} \right) \frac{1}{(k^2 - m^2)} + k_\mu \frac{\partial}{\partial k_\mu} \frac{1}{(k^2 - m^2)} \right] \tag{3.1.4}$$

$$= (d-2) \int \mathrm{d}^d k \, \frac{1}{(k^2 - m^2)} - 2m^2 \int \mathrm{d}^d k \, \frac{1}{(k^2 - m^2)^2}. \tag{3.1.5}$$

The left hand side of the above equation, which is a total derivative, can be shown to be

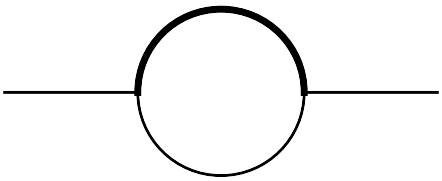

Figure 3.2: A two-point function with one massive propagator. The thick line corresponds to the massive propagator.

vanish for small d. This leads to the following linear relation between integrals

$$(d-2)\int \mathrm{d}^d k \, \frac{1}{(k^2-m^2)} \;=\; 2m^2 \int \mathrm{d}^d k \, \frac{1}{(k^2-m^2)^2}. \tag{3.1.6}$$

This relation can be generalised for an arbitrary exponent of the propagator. Denoting with $I(\nu)$ the integral with a general exponent ν for the propagator,

$$I(\nu) = \int \mathrm{d}^d k \, \frac{1}{(k^2-m^2)^\nu}, \tag{3.1.7}$$

the general relation is

$$(d-2\nu)\, I(\nu) = 2m^2 \nu \, I(\nu+1). \tag{3.1.8}$$

The above relation implies that in this tower of integrals $I(\nu)$, only one is independent and the rest are simply related to it. It must be pointed out that any of these integrals can be chosen to be the independent integral or, as is referred to more commonly, the "master" integral. Some choices might offer certain advantages over others e.g. finiteness in $d = 4$ dimensions. We will explore this in more detail in chapter 4. It is interesting to note that setting $m = 0$ in Eq. 3.1.8 gives zero i.e. $\forall\, \nu \neq d/2,\ I(\nu) = 0$. In other words, massless tadpole integrals vanish in dimensional regularisation. This is a part of the more general statement: scaleless integrals i.e. integrals with no dependence on external kinematic variables vanish in dimensional regularisation.

In the above example, it was possible to derive an analytical solution for the IBP relation; this is not possible in practice for general IBP systems. Consider a slightly more complicated example, the 2-point integral with one massive and one massless propagator (Fig. 3.2). An integral with general exponents for this topology can be written as

$$I(\nu_1, \nu_2) = \int \mathrm{d}^d k \, \frac{1}{\left(k^2 - m^2\right)^{\nu_1} \left((k+p)^2\right)^{\nu_2}} \tag{3.1.9}$$

where p is the external momentum entering the loop. Taking derivative with respect to the loop-momentum vector k^μ and choosing $v^\mu = k^\mu, p^\mu$,

$$\begin{aligned} 0 = \int \mathrm{d}^d k \frac{\partial}{\partial k_\mu} \frac{k_\mu}{\left(k^2 - m^2\right)^{\nu_1} \left((k+p)^2\right)^{\nu_2}} &= (d - 2\nu_1 - \nu_2)\, I(\nu_1, \nu_2) - 2m^2 \nu_1\, I(\nu_1 + 1, \nu_2) \\ &\quad - \nu_2\, I(\nu_1 - 1, \nu_2 + 1) + \nu_2 \left(p^2 - m^2\right) I(\nu_1, \nu_2 + 1), \end{aligned} \tag{3.1.10}$$

$$\begin{aligned} 0 = \int \mathrm{d}^d k \frac{\partial}{\partial k_\mu} \frac{p_\mu}{\left(k^2 - m^2\right)^{\nu_1} \left((k+p)^2\right)^{\nu_2}} &= (\nu_1 - \nu_2)\, I(\nu_1, \nu_2) - \nu_1\, I(\nu_1 + 1, \nu_2 - 1) \\ &\quad + \nu_1 \left(p^2 + m^2\right) I(\nu_1 + 1, \nu_2) + \nu_2\, I(\nu_1 - 1, \nu_2 + 1) \\ &\quad - \nu_2 \left(p^2 - m^2\right) I(\nu_1, \nu_2 + 1)\,. \end{aligned} \tag{3.1.11}$$

It is clear that a trivial analytical solution akin to Eq. 3.1.8 is not possible in this situation. To make the equations a bit simpler, it helps to start with $\nu_2 = 0$ which gives

$$0 = (d - 2\nu_1)\, I(\nu_1, 0) - 2m^2 \nu_1\, I(\nu_1 + 1, 0)\,, \tag{3.1.12}$$

$$0 = \nu_1\, I(\nu_1, 0) - \nu_1\, I(\nu_1 + 1, -1) + \nu_1 \left(p^2 + m^2\right) I(\nu_1 + 1, 0)\,. \tag{3.1.13}$$

In the above equations, Eq. 3.1.12 is just the solution for the tadpole integrals (Eq. 3.1.8), while Eq. 3.1.13 provides solutions for integrals with negative exponents for the second propagator i.e. for the propagator appearing in the numerator. E.g. choosing $I(1, 0)$ as the

master integral and setting $\nu_1 = 1$ results in

$$I(2,0) = \frac{d-2}{2m^2}\, I(1,0)\,, \tag{3.1.14}$$

$$I(2,-1) = \frac{d(p^2+m^2)-2p^2}{2m^2}\, I(1,0)\,. \tag{3.1.15}$$

The above equations provide solutions for $I(2,0)$ and $I(2,-1)$. Repeated application of Eqs. 3.1.12 and 3.1.13 will allow the solution of integrals $I(\nu,-1)\ \forall\ \nu \geq 1$.

Setting, instead, $\nu_1 = 0$,

$$0 = (d-\nu_2)\, I(0,\nu_2) - \nu_2\, I(-1,\nu_2+1) + \nu_2(p^2-m^2)\, I(0,\nu_2+1)\,, \tag{3.1.16}$$

$$0 = -\nu_2\, I(0,\nu_2) + \nu_2\, I(-1,\nu_2+1) - \nu_2\,(p^2-m^2)\, I(0,\nu_2+1)\,. \tag{3.1.17}$$

Since scaleless integrals vanish in dimensional regularisation, $I(0,\nu_2) = 0\ \forall\ \nu_2 \geq 0$. The above equations then imply

$$I(-1,\nu_2) = 0\,. \tag{3.1.18}$$

Now the case where $\nu_1, \nu_2 \neq 0$ can be considered. Setting $\nu_1 = \nu_2 = 1$ results in the following equations:

$$0 = (d-3)\, I(1,1) - 2m^2\, I(2,1) - \ I(0,2) + \ (p^2-m^2)\, I(1,2), \tag{3.1.19}$$

$$0 = -\ I(2,0) + \ (p^2+m^2)\, I(2,1) + \ I(0,2) - \ (p^2-m^2)\, I(1,2)\,. \tag{3.1.20}$$

Here $I(0,2) = 0$ (since it is scaleless) and $I(2,0)$ is given in Eq. 3.1.14. This leaves $I(1,1)$, $I(2,1)$, and $I(1,2)$ undetermined. With 3 remaining integrals and only 2 equations, it appears that the above 3 integrals cannot all be expressed in terms of the tadpole integral. Indeed, another master integral is required with both $\nu_1, \nu_2 \geq 1$. Choosing $I(1,1)$ as the

master integral in addition to $I(1,0)$, the identities can be written as

$$0 = (d-3)\, I(1,1) - 2m^2\, I(2,1) + (p^2 - m^2)\, I(1,2)\,, \tag{3.1.21}$$

$$0 = -\, I(2,0) + (p^2 + m^2)\, I(2,1) - (p^2 - m^2)\, I(1,2)\,. \tag{3.1.22}$$

Solving the above equations gives $I(2,1)$ and $I(1,2)$ in terms of the chosen master integrals $I(1,0)$ and $I(1,1)$.

To summarise, the reduction procedure is started by choosing the lowest value of $\nu = \nu_1 + \nu_2 + ... = 1$. For $\nu_1 = 1, \nu_2 = 0$, the system gets reduced to that of a massive tadpole while for $\nu_1 = 0, \nu_2 = 1$ the equations lead to scaleless integrals that vanish. In the next step, the value of ν is increased to 2. Starting with $\nu_1 = \nu_2 = 1$, the solutions require another master integral. However, it can be shown that for higher values of ν, all the other integrals can be expressed in terms of these 2 master integrals. This systematic way of generating and solving linear relations for integer exponents ν_i starting from lowest values of $\nu = \nu_1 + \nu_2 + ...$ was first presented by Laporta [247]. Many public codes based on this algorithm are available for this purpose [244, 248–251].

`Reduze 2`, based on Laporta's algorithm was used to perform the reductions for $gg \to ZZ$ amplitudes at 2-loops for the case of massless internal quarks in [102]. It was found that it was insufficient for the process at hand, however. In fact, even for the planar topologies which are expected to be significantly simpler than the non-planar topologies, the reductions for integrals with up to one inverse propagator, denoted by $s \leq 1$ (i.e. $\nu < 0$ for some propagator), were incredibly difficult and required several months of CPU time. The integrals with $s = 2$ were totally out of reach with conventional methods.

In particular, conventional IBP solvers have the following major issue.

1. Perhaps the most significant drawback is the presence of integrals with doubled propagators, also referred to as dots, in IBP identities. As is evident from Eqs. 3.1.21 and 3.1.22, IBP identities generated this way necessarily contain these doubled propa-

gators for the conventional choice of vectors $v^\mu = (k_1^\mu, ..., p_1^\mu, ...)$. These integrals don't often appear in the amplitude and as such their reductions aren't required.

2. While it is possible to avoid generating solutions for such integrals with doubled propagators, reduction procedure for just the integrals required for the amplitude still proceeds through row-reduction of linear systems containing these integrals. This means that a much larger linear system than is optimal is being solved, further slowing down the process.

A solution was first provided to the above issues in [252] to avoid generating such integrals with doubled propagators with specific choices of the generating vectors v_μ using a Gröbner basis approach. An alternate approach using linear algebra was instead proposed in [253], which forms the basis of the approach used in this work. Before discussing these solutions in detail, however, it is useful to introduce an alternate representation for the Feynman integrals.

3.2 Baikov representation

Consider the general L-loop integral family with E independent external momenta and N edges (propagators) from Eq. 3.1.1, with only $T \leq N$ propagators appearing in the integral i.e. $\nu_i > 0$ for $i \leq T$. Let Q denote the set of all loop momenta and independent external momenta i.e. $Q = (k_1, ..., k_L, p_1, ..., p_E)$. This integral has a total of Ld integration variables. Since the integral has no open Lorentz indices, however, it is easy to see that it depends only upon the scalar products between the loop momenta and the external momenta appearing in the propagators, $Q_i \cdot Q_j$, as well as internal masses and d. Maximum number of such scalar products is $L(L+1)/2 + LE$ for $i \leq j$ and $i \leq L$, $j \leq L + E$. For an integral with T distinct propagators appearing in the integral, the integral only depends on T scalar products, implying that only $T \leq L(L+1)/2 + LE$ degrees of freedom are required to characterise the integral. The rest of the $Ld - T$ variables can simply be integrated over.

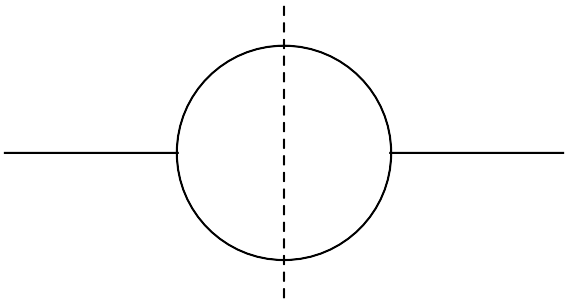

Figure 3.3: A two-point function with massless propagators. The dashed line corresponds to the cut propagators.

This can be looked at in a slightly different way by considering the loop momentum k_1, for example, and dividing it's components into $k_{1,\perp}$ and $k_{1,\parallel}$ where $k_{1,\parallel}$ is the projection of k_1 onto the space spanned by $(k_2, ..., k_L, p_1, ..., p_E)$ and $k_{1,\perp}$ is orthogonal to it. This allows performing the integrations over $k_{1,\perp}$ independent of the actual Feynman propagators; the number of remaining integration variables left is often less than that in the momentum-space representation.

The general L-loop N edge Feynman integral in Eq. 3.1.1 can be written in Baikov's representation as

$$I(\nu_1, ..., \nu_N) = \mathcal{N}_0 \int \mathrm{d}z_1 ... \mathrm{d}z_N \; \frac{1}{\prod_{i=1}^{N} z_i^{\nu_i}} \; P^{\frac{d-L-E-1}{2}} \,, \tag{3.2.1}$$

Here $\mathcal{N}_0$ is a normalisation factor depending on the spacetime dimensions d and kinematics, P is the Jacobian of the transformation known as the Baikov polynomial, and $z_1, ..., z_N$ are the integration variables called the Baikov parameters which are just the inverse propagators $z_i = q_i^2 - m_i^2$. The Baikov polynomial P in general depends on the Baikov parameters and the kinematic invariants. This representation was first proposed in [254] and later clarified in [255]; the reader is referred to the above references for further details.

It was shown in [256, 257] that it is in general highly non-trivial to write down the integration domain explicitly. While it is rather challenging to perform the actual integration in this representation, a huge advantage the Baikov representation allows over the traditional

momentum-space representation is in performing unitarity cuts [258]. Cutting propagators in this representation is reduced to the simple task of taking the residue of the integrand at 0 for the corresponding Baikov parameter [259, 260].

Evaluating Feynman integrals on cuts is useful for many purposes. The discontinuity of a Feynman integral across a branch cut is given by the cut integral

$$\mathrm{Disc}_{s_i}(I) = -\mathrm{Cut}_{s_i} I \tag{3.2.2}$$

where s_i corresponds to some Mandelstam invariant. This relation was derived in [261, 262] and is a consequence of the optical theorem [263]:

$$\mathcal{M}(i \to f) - \mathcal{M}^*(f \to i) = i \sum_x \int \mathrm{d}\Pi_x \mathcal{M}(i \to x)\mathcal{M}^*(f \to x)\,. \tag{3.2.3}$$

In the above equation, i refers to the initial state, f to final state, and x to all possible intermediate states. $d\Pi_x$ is the n-particle phase space weight for the intermediate state x. This simplifies to

$$2\mathrm{Im}\,\mathcal{M}(i \to i) = \sum_x \int \mathrm{d}\Pi_x |\mathcal{M}(i \to x)|^2\,. \tag{3.2.4}$$

The imaginary part of the massless bubble integral in Fig. 3.3, for instance, can be calculated by evaluating the integral on the s-channel cut denoted via the dashed line. The integral in Fig. 3.3 is known to evaluate to (for $d = 4 - 2\epsilon$)

$$I = \frac{1}{\epsilon} + 2 - \log(-p^2 - i0) + O(\epsilon)\,, \qquad p^2 < 0 \tag{3.2.5}$$

where p is the incoming external momentum (see Appendix B.2). This integral is analytic for $p^2 < 0$ and can be analytically continued to the region $p^2 > 0$ using the principal branch

of the logarithm. This results in the integral picking up an imaginary part

$$I = \frac{1}{\epsilon} + 2 - \log(p^2) - i\pi + O(\epsilon)\,, \qquad p^2 > 0\,. \tag{3.2.6}$$

i.e. $\mathrm{Im}\, I = -i\pi$ and the discontinuity is given by $\mathrm{Disc}_s(I) = -2i\pi$.

In Baikov representation, the integral can be written as

$$I = \mathcal{N}_0 \int \mathrm{d}z_1 \mathrm{d}z_2 \, \frac{(sz_1 - \frac{1}{4}(-(p^2+i0) - z_1 + z_2)^2)^{1/2-\epsilon}}{z_1 z_2} \tag{3.2.7}$$

with the normalisation factor

$$\mathcal{N}_0 = \frac{2i\pi^{\frac{3}{2}-\epsilon}}{\Gamma(\frac{3}{2}-\epsilon)(p^2+i0)^{1-\epsilon}} \tag{3.2.8}$$

The s-channel cut here corresponds to setting both the propagators on-shell i.e. computing the residue at $z_1 = z_2 = 0$ [257], which results in

$$\mathrm{Cut}_s I = \frac{4i\pi}{p^2}\,\frac{p^2}{2} + O(\epsilon) = 2i\pi + O(\epsilon)\,. \tag{3.2.9}$$

It is clear that the above results satisfy the cut-discontinuity equation (Eq. 3.2.2).

In addition to specific kinematic cuts as in the above example, the integrals can also be evaluated on maximal cuts i.e. setting all propagators on-shell (this is different from optical theorem). This is of particular importance in the method of evaluating Feynman integrals using differential equations since the integrals evaluated on maximal cuts correspond to the homogeneous solution of the differential equations [255, 264]. Since the homogeneous solution is expressed using the same class of functions as the full solution, it can be used to determine if the differential equations admit a polylogarithmic solution. In addition, the solution on maximal cut can be used to determine the "uniformly transcendental" basis of master integrals [265, 266] which satisfy particularly simple differential equations. The reader

is referred to [256, 257] for a detailed discussion and more complicated examples of integrals evaluated on maximal cuts, including integrals involving elliptic functions. However, the representation in Eq. 3.2.1 is not the most convenient representation for performing the integration explicitly. In fact, the number of integration variables can, in many cases, be reduced by performing the variable transformation loop-by-loop [256, 257].

Similar to the momentum-space representation, the IBP relations can also be written down in the Baikov representation [255]. For the general integral in Eq. 3.2.1, the Integration-By-Parts identities in Baikov representation are given by

$$0 = \int \mathrm{d}z_1 ... \mathrm{d}z_N \sum_{i=1}^{N} \left(\frac{\partial f_i}{\partial z_i} + \frac{d-L-E-1}{2P} f_i \frac{\partial P}{\partial z_i} - \nu_i \frac{f_i}{z_i} \right) \frac{1}{\prod_{i=1}^{N} z_i^{\nu_i}} P^{\frac{d-L-E-1}{2}} . \quad (3.2.10)$$

Here f_i are arbitrary polynomials in the Baikov parameters and the kinematic invariants. The freedom in choosing the polynomials f_i reflects the freedom in choosing the vectors $v\mu$ in the momentum-space representation. Certain choices of f_i can provided advantages over the others; this is discussed in the next section (Sec. 3.3).

Integration-By-Parts relations can also be generated on cuts [267, 268] using the general formula in Eq. 3.2.10 which can be useful to simplify the system of equations by reducing them into smaller and more manageable parts as well as potentially provide significant performance improvement as argued in [268]. The IBPs generated on cuts can also be used to obtain the differential equations on cuts e.g. on maximal cuts which can be used to solve for the homogeneous solution of the differential equations.

3.3 Syzygies for IBP reduction

In the above general equation for IBP relations via Baikov representation (Eq. 3.2.10), the simplistic choice of the polynomials $f_i = 1$ leads to equations that have terms with $1/P$. It is straightforward to see that such terms generate integrals with shifted dimensions in the IBP relations. In general it is highly desirable to avoid such integrals in the IBP systems

since they do not commonly occur in the amplitudes. In addition, presence of such integrals leads to bloated linear systems which are relatively difficult to solve. To avoid such integrals is relatively straightforward, however, by simply imposing the constraint [267–269]

$$\left(\sum_{i=1}^{N} f_i \frac{\partial P}{\partial z_i}\right) + f_{N+1} P = 0 \tag{3.3.1}$$

on the polynomials f_i. This is known, in algebraic geometry, as a syzygy constraint. Note the presence of a new polynomial f_{N+1}; together with the rest of the f_i, it forms a syzygy. The formal mathematical definition and details of syzygies is beyond the scope of this work and the reader is referred to [270] for more details regarding syzygies in the context of Feynman integral reduction. For the purposes here, a syzygy is basically a relation between polynomials in certain variables. E.g. consider a set of polynomials $e_i = \{x, x+y, y^2\}$. The equation

$$f_1 e_1 + f_2 e_2 + f_3 e_3 = 0 \tag{3.3.2}$$

is satisfied by $f_i = \{\{y, -y, 1\}, \{x+y, -x, 0\}\}$. This set of solutions forms a syzygy module. Note that any linear combination of the two syzygies, with the variables (x, y) allowed in the coefficients, also forms a syzygy. This is easy to see by replacing f_i by $a(x,y) f_{1,i} + b(x,y) f_{2,i}$ in Eq. 3.3.2 where $f_{1,i}$ and $f_{2,i}$ are the two different solutions.

For the case at hand, syzygies are formed by polynomials in the Baikov parameters with the kinematic invariants appearing in the coefficients. Explicit solutions to the "no dimension-shift" constraint in Eq. 3.3.1 were pointed out in [271] in Baikov representation.

These f_I^{no-dim} are simply linear polynomials in the Baikov parameters and kinematics. Note that these f_i^{no-dim} generate integration-by-parts relations identical to those in the momentum-space representation [271]. E.g. for the bubble function with one massive

propagator in Fig. 3.2, the no dimension-shift syzygies are

$$f_i^{no-dim} = \{\{-p^2 - z_1 + z_2, p^2 - z_1 + z_2, 0\}, \{2(m^2 + z_1), -p^2 - z_1 + 2(m^2 + z_1) + z_2, -2\}\}\,. \tag{3.3.3}$$

Substituting the above syzygies into Eq. 3.2.10, it can be seen that the IBP relations from Eqs. 3.1.10 and 3.1.11 are recovered.

As seen in Sec. 3.1, IBP relations generated this way contain integrals with doubled propagators (dots) and it is highly desirable to avoid generating such integrals. Looking at the general IBP equation in Baikov representation (Eq. 3.2.10), it is clear that such doubled propagators are generated by the term $\nu_i f_i / z_i$. They can be avoided by imposing the so-called "no dot" constraint

$$f_i^{no-dot} \;=\; b_i\, z_i \quad \forall\, i = 1, \ldots, N' \text{ with } \nu_i \geq 1 \,\text{and}\, N' < N\,, \tag{3.3.4}$$

Here N' is the set of positive indices in the sector while N is the total number of propagators in the integral family. This is a rather trivial constraint. Essentially, the f_i are required to be proportional to z_i so as to cancel the z_i in the denominator of the offending term. For the bubble function with one massive propagator in Fig. 3.2, the no-dot syzygies are simply

$$f_i^{no-dot} = \{\{z_1, 0, 0\}, \{0, z_2, 0\}, \{0, 0, 1\}\}\,. \tag{3.3.5}$$

To impose the two constraints individually is quite straightforward. Finding f_i that satisfy simultaneously both the constraints in Eqs. 3.3.1 and 3.3.4 is, however, a highly non-trivial problem in general. The initial strategy, based on the syzygy approach using Baikov representation, proposed in [268] was to simply replace the f_i in the no dimension-shift constraint in Eq. 3.3.1 with $b_i z_i$ and solve for b_i. This was found to be computationally expensive and impractical for complicated topologies. The approach proposed in [270] to

simultaneously solve the two constraints by computing a module intersection of the two syzygy modules was suggested to be better. Computing module intersections is a well-known problem in Algebraic geometry and several computer algebra packages exist for this task e.g. `Singular` [272].

The usual module intersection approach using `Singular` was found to be inadequate for the purpose of this calculation, however. For the planar topologies, for example, which are expected to be significantly simpler in complexity, even syzygies for sectors with 6-lines (propagators) were found to be out of reach, using `Singular` out of the box. With a few optimisations with the assistance of the author of [270], further improvement was found rendering 6-line planar sectors solvable. However, the top-level (7-line) sectors in the planar as well as non-planar topologies remained intractable. In addition, the approach was found to be computationally expensive requiring several days of run-time with large amounts of RAM.

3.4 Linear algebra based syzygy construction

In light of the inadequacy of the module intersection based method implemented through `Singular`, it was clear that an alternate approach was required to compute the syzygies. Specifically, it was observed that the module intersection method was computationally expensive and not feasible for the problem at hand. Instead, a custom linear algebra based syzygy solver was employed to compute the syzygies required for this work.

The basic idea behind the algorithm is as follows. As mentioned in the previous section, it is straightforward to write down the solutions to the no dimension-shift constraint as well as the no dot constraint. The important point to note here is that if certain syzygies satisfy a constraint, then so does any linear combination of those syzygies where the coefficients are

allowed to depend on the variables i.e.

$$\left(\sum_{j=1}^{N} F_j^{no-dim}\,\frac{\partial P}{\partial z_j}\right) + F_{N+1}^{no-dim}\,P = 0 \tag{3.4.1}$$

where $F_j^{no-dim} = \sum_i a_i(z_1, ..., z_N, s_{12}, ...) f_{j,i}^{no-dim}$ is the linear combination and a_i are the polynomials. The linear combination F_j^{no-dim} must now satisfy the no dot constraint $F_j^{no-dim} = b_j z_j$ which provides constraints on the polynomials a_i.

In principle, the above construction should provide exactly the same syzygies as the module intersection method if solving for general polynomials a_i. However, solving for general a_i would require a Gröbner basis computation which is identical to the module intersection approach. Instead, this method can be used to algorithmically construct the solutions up to a certain polynomial degree by choosing an ansatz for the a_i, starting with degree 0 polynomials for a_i. Substituting an ansatz for a_i in Eq. 3.4.1 turns the problem into row reduction of a matrix. A custom linear solver based on Finite field methods [273, 274] is used to provide fast and efficient row reduction of the resulting linear system.

A brief description of the algorithm first implemented for the multivariate case in, and reproduced from, [6] is provided below.

While the module intersection method provides all possible syzygy solutions, it was observed that for amplitude calculations only syzygies up to a certain degree are needed. Indeed, in contrast with the module intersection approach based on `Singular`, the linear algebra approach presented above was able to generate the required syzygies. For the top-level planar topologies, the method was relatively quick requiring only O(10) CPU hours while the non-planar topologies turned out to be significantly more difficult requiring $O(100)$ CPU hours per topology. This approach was also used to generate the required syzygies for the 5-point 2-loop topologies needed for the calculation of $\gamma\gamma + jet$ amplitude in [134, 138].

While this method was able to solve the syzygies for calculations at the frontier of perturbative QCD, there are certain limitations. In particular:

Algorithm 3.1 Syzygies for linear relations without dimension shifts or dots [6]

Input: Syzygies of degree 1 solving Eq. 3.3.1, maximal required degree $n_{\max}$.

Output: Syzygies $S_1, \ldots, S_{n_{\max}}$ up to degree $n_{\max}$ solving Eqs. 3.3.1 and 3.3.4.

1: Start with syzygies of degree $n = 1$. Let I_1 be a complete set of solutions (f_i) to the no-dimension-shift constraint from Eq. 3.3.1, which are linear in the Baikov parameters z_k. These can directly be written down [271]. Abbreviating the momenta squared with variables $z_{N+1}, \ldots$, the vectors in I_1 are of homogeneous degree 1 in the variables z_k.

2: At degree n, form a matrix M_n, where each element of $(f_i) \in I_n$ corresponds to a row. The columns enumerate both the component i of (f_i) and the power products of z_i in them; the entries of the matrix are the coefficients. A column is called admissible, if it satisfies the no-doubled propagator constraint in Eq. 3.3.4, and non-admissible otherwise. All admissible columns are ordered to the right of the non-admissible columns.

3: Perform a row reduction of M_n. In the row reduced form, select all rows, which have an admissible pivot column and form the corresponding syzygies S_n from them. S_n forms a complete set of linear combinations of the syzygies in I_n, which satisfy Eq. 3.3.4 for all of their terms, and are therefore our solutions at degree n.

4: If n is the user-defined maximal degree, stop and return the solutions $S_1, \ldots, S_n$. Otherwise, proceed.

5: For each vector of polynomials $(f_i) \in I_n$ and each z_k, form the vector of polynomials $(z_k f_i)$. This gives the set I_{n+1}, which are solutions of Eq. 3.3.1 of degree $n+1$ in the z_k but not necessarily solutions of Eq. 3.3.4.

6: Replace $n \to n+1$ and go to step 2.

1. Solutions are only produced up to a certain polynomial degree by construction. In case higher degree solutions are required, the task can be challenging in certain cases. E.g. For some of the non-planar topologies, syzygies for degree up to 5 were constructed, but these were found to be insufficient. It was estimated that computing the degree 6 syzygies would be unfeasible with the available computing resources. Instead, some

identities involving integrals with doubled propagators were indeed required for a complete and successful IBP reduction. It has been suggested that syzygies up to a certain degree, dependent on the specific problem at hand, are sufficient to obtain reductions for integrals with arbitrarily high numerators. This is not proven, however.

2. By the nature of the construction wherein the kinematic variables are treated as indeterminates of the ring similar to the Baikov parameters, often identities are generated with "true" degree less than the expected degree. In other words, the kinematic variables sometimes inflate the polynomial degree of the syzygy so that a degree "n" syzygy is effectively only "n-1" (or lower). This can happen in two ways, either by having a kinematic variable as an overall factor or by having each and every individual term containing a kinematic variable. This can in principle be fixed by considering the kinematic variables in the coefficient field instead of as indeterminates like the Baikov parameters. It was suggested that in this approach the degree of syzygies required can be less than in the original formulation. This is not very well understood, however, and requires further investigation.

3. This construction may also result in syzygies that are polynomials multiplied by a Baikov variable as an overall prefactor. Such syzygies are redundant: the loop edge corresponding to the Baikov variable present as the overall prefactor is either part of the topology under consideration or appears as an inverse propagator (in the numerator). In the first case the syzygies simply generate identities from a lower topology that are presumably contained in the identities generated specifically for that topology; these are indeed dropped [275]. In the second case, the prefactor simply increases the "tensor rank" of every integral in the identity by 1 which can alternatively be achieved by increasing the rank of seed integrals in the syzygies with one degree.

Despite the above limitations, the method has been very successful in solving syzygies for challenging problems.

3.5 IBP reduction using syzygies

The syzygies generated using the approach outlined in the previous section are used to generate IBP templates to generate relations between integrals, similar to templates generated through conventional IBP relations e.g. in Eqs. 3.1.10 and 3.1.11. Seed integrals with specific propagator exponents are then inserted into the templates to generate the required IBP relations, similar to Laporta's algorithm, which are subsequently solved using a row-reduction procedure. An in-house custom linear solver, `Finred` [276], based on Finite field methods [273, 274] is used for this. Instead of solving the symbolic linear system directly, the equations are sampled over a finite field and the symbolic dependence is reconstructed through rational reconstruction. This method allows a very high degree of parallelisation and hence can be much faster than the traditional approach.

In the case of ZZ production, top quark and Z-boson masses are set to numbers: $m_t = 1$ and $m_Z^2 = 5/18 m_t^2$. The chosen ratio for m_Z corresponds to the mass of the Z-boson in terms of top-quark mass. This is to further simplify the linear relations to facilitate solving the system. Note that setting $m_t = 1$ simply amounts to factoring out powers of m_t from the quantities of interest rendering the rest of the kinematic variables, and the form factors, dimensionless. In this way, all the Feynman integrals were successfully reduced to master integrals. Even with the above simplifications, the reductions proved to be rather challenging nevertheless and required a significant amount of computational resources. The reductions took months of run-time on the High Performance Computing Cluster (HPCC) at MSU. The resulting reduction tables occupied over 200 GB of disk space and involved extremely complicated rational functions with up to total degree 190 in the kinematic variables. As somewhat expected, the non-planar topologies proved to be the most challenging accounting for almost all of the CPU time as well as disk space.

Note that choice of basis integrals has not been mentioned yet; for ZZ the reductions were performed in terms of the conventional Laporta basis of integrals where the integrals

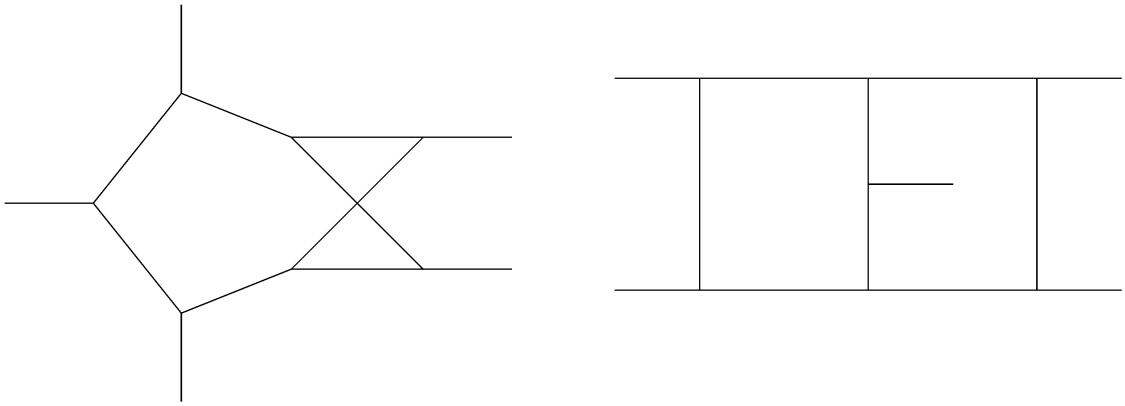

(a) The hexagon-box topology

(b) The double-pentagon topology

Figure 3.4: The non-planar topologies for 5-point 2-loop $\gamma\gamma$ + jet production.

with least numerator rank and no dots along with specific ordering prescription are simply chosen as master integrals. This is optimised for evaluation later; the details are discussed in the next section (Sec. 4). An interesting point to note is that within the planar topologies, Figs. 2.7a, 2.7c, and 2.7b, with adjacent gluons are significantly simpler than the topology in Fig. 2.7d with the gluons at the opposite vertices.

For the case of $\gamma\gamma$ + jet, however, the situation is a lot more complicated due to the presence of an additional external particle. Indeed, while the planar topologies had been reduced, complete IBP reductions for a 5-point amplitude at 2-loops (including the non-planar topologies) had been out of reach until very recently. The solutions for the non-planar topologies were facilitated with the assistance of two key improvements. First, a canonical basis (see Sec. 4.1 for a brief description) was chosen for the reductions instead of the conventional Laporta basis. This already led to a reduction by a factor of 2 in the number of samples required for a full reconstruction, effectively reducing the required CPU time to half as well. Second, a new algorithm was used to guess the complete symbolic form of the denominators of the rational coefficients in the reduction identities [138, 277, 278]. This further led to a reduction in the number of samples by a factor of ~ 10 and effectively made the reductions computationally feasible for the extremely challenging hexagon-box and double-pentagon topologies.

For both the processes, the reduction identities are generated with the rational coefficients in front of the master integrals over a common denominator. This representation is not ideal for a couple of reasons. First, reduction identities occupy a huge amount of disk space in this representation and are rather difficult to deal with for complicated processes. Second, having everything over a common denominator can often lead to numerical instabilities. Instead, multivariate partial fractioning of the rational coefficients results in a substantially simpler form of the reduction identities, in particular for the non-planar topologies. For the case of ZZ, this resulted in a reduction from over ~ 10 GB to < 500 MB of disk space. Similarly, a reduction by a factor of ~ 100 is achieved for the most complicated reduction identities for $\gamma\gamma + \text{jet}$. Multivariate partial fractioning is discussed in more detail in Sec. 5.1.

While such drastic simplifications are certainly impressive, a deeper understanding behind this would be highly desirable. It has been suggested that the difference in complexity is due to combining structures with different singular behaviours and limits. Ideally, it would be extremely useful to generate reduction identities directly in the partial fractioned form. While an efficient algorithm to do this is not yet known, recent progress in understanding this partial fractioning procedure as well as general structure of the singularities holds promise for the future.

Chapter 4

Finite basis integrals

4.1 Evaluation of Feynman integrals

Once the Feynman integrals are reduced to a set of master integrals, the next step is to evaluate them. There are a number of methods used to evaluate master integrals, both analytically and numerically. This section will focus on the methods of differential equations [279–284] and sector decomposition [161, 285–287], used for $\gamma\gamma + jet$ and ZZ production respectively.

4.1.1 Differential equations

Consider the tadpole integral from Eq. 3.1.3. This integral is dependent only on the mass m. Taking the derivative under the integral sign with respect to m^2,

$$\begin{aligned}\frac{\mathrm{d}}{\mathrm{d}m^2} I(m^2) &= \int \frac{\mathrm{d}^d k}{i\pi^{d/2}} \frac{\mathrm{d}}{\mathrm{d}m^2} \frac{1}{k^2 - m^2} \\ &= -\int \frac{\mathrm{d}^d k}{i\pi^{d/2}} \frac{1}{(k^2 - m^2)^2} \,. \end{aligned} \tag{4.1.1}$$

The integral in the second line of the above equation, resulting from the derivative, can be reduced to $I(m^2)$ using IBP relation from Eq. 3.1.6. This results in the following differential equation for $I(m^2)$:

$$\frac{\mathrm{d}}{\mathrm{d}m^2} I(m^2) = -\frac{d-2}{2m^2} I(m^2) \,. \tag{4.1.2}$$

The above differential equation can be solved given appropriate boundary conditions to obtain $I(m^2)$.

Consider now a more general system with m master integrals denoted by $I_1, ..., I_m$. Taking the derivative with respect to the dimensionless kinematic variable y_α and using IBP reduction to reduce the right hand side integrals to master integrals, the derivatives can be written as

$$\frac{\partial}{\partial y_\alpha}\vec{I} = A_\alpha \vec{I}, \tag{4.1.3}$$

where $\vec{I}$ is the vector of master integrals $(I_1, ..., I_m)$ and A_α is an $m \times m$ matrix whose entries are rational functions in the invariants and the dimensional regulator ϵ. Repeating the procedure for all the kinematic variables results in the following form

$$\mathrm{d}\vec{I} = \mathbf{A}\vec{I}, \tag{4.1.4}$$

where $\mathbf{A}$ is an $m \times m$ matrix of one-forms

$$\mathbf{A} = \sum_\alpha A_\alpha(\vec{y}, \epsilon)\, \mathrm{d}y_\alpha \tag{4.1.5}$$

It turns out that in many cases, the above system can be drastically simplified following an *algebraic* basis change $\vec{I} = T(\vec{y}, \epsilon)\, \vec{I}'$ [283, 288] such that the differential equation in Eq. 4.1.4 becomes

$$\mathrm{d}\vec{I}' = \epsilon \mathbf{A}'(\vec{y})\vec{I}'\,. \tag{4.1.6}$$

The above form is colloquially referred to as the *canonical* or ϵ-form. Note that the entries of the transformation matrix T are rational functions in the kinematic variables $\vec{y}$ and ϵ. In the canonical form, the differential equations in most known cases can be easily solved order

by order in ϵ in terms of iterated integrals that evaluate to multiple polylogarithms (MPLs) (see [289–295]). Efficient numerical codes are available for evaluation of such multiple polylogarithms [296–303] allowing a fast and convenient numerical implementation of Feynman amplitudes expressed in terms of such functions.

The method of differential equations is very powerful and has been used to evaluate a large number of Feynman integrals for many different processes. E.g. this method was used to calculate the master integrals for the massless ZZ amplitudes [304–307] as well as the master integrals for massless 5-point scattering [308–311] required for the $\gamma\gamma$+jet calculation.

Despite the large-scale applicability and success of this method, however, there are some limitations. In particular, reducing the system to the canonical form through an algebraic transformation matrix $T(\vec{y}, \epsilon)$ is impossible in many cases; such systems evaluate to a class of functions beyond MPLs. This is expected to be the case for $gg \to ZZ$ with massive internal quarks. There has been considerable progress over the recent years in understanding such functions beyond polylogarithms, mostly concerning their elliptic generalisations [312–317]. However, most of the progress has been achieved for simple topologies with very few mass scales; for processes such as $gg \to ZZ$ with many different mass scales, evaluation in terms of such functions remains extremely challenging. Furthermore, it isn't clear if the so-called *elliptic multiple polylogarithms* (eMPLs) are enough to represent the master integrals for this process and functions beyond even eMPLs could appear. On the other hand, for certain cases, even if the ϵ-form is achievable, the functions cannot be evaluated in terms of multiple polylogarithms [318].

An alternative approach that has been recently used for many phenomenological applications is the solution of differential equations by expansions [112, 113, 319–323]. Instead of solving the differential equations analytically, a series expansion is constructed around a point and the equations are solved numerically term-by-term in the expansion parameters. This method is extremely useful for problems involving elliptic functions or beyond given the lack of understanding concerning these functions. Another advantage is that any given

system of differential equations can be solved, in principle, regardless of whether a canonical form can be achieved or not. This is, again, especially beneficial for elliptic integrals since it can be challenging to obtain the canonical form in many cases with only a few cases where this has been successfully done [324, 325].

4.1.2 Feynman parametric representation

Consider the general L-loop integral in d dimensions with N distinct propagators in the momentum space representation from Eq. 3.1.1

$$I(\nu_1, ..., \nu_N) = \int \left(\prod_{l=1}^{L} \frac{\mathrm{d}^d k_l}{i\pi^{d/2}} \right) \prod_{j=1}^{N} \frac{1}{(q_j^2 - m_j^2 + i\,0)^{\nu_j}} \tag{4.1.7}$$

with integer exponents $\nu_j \in \mathbb{Z}$. Note the $i0$ for the correct Feynman propagator prescription. If all indices ν_j are positive, then the identity (see e.g. [326, 327])

$$\frac{1}{D^{\nu_j}} = \frac{(-1)^{\nu_j}}{\Gamma(\nu_j)} \int_0^\infty \mathrm{d}x_j \, x_j^{\nu_j - 1} \, e^{x_j \, D} \qquad \text{for } \nu_j > 0,\, D < 0 \tag{4.1.8}$$

can be used to write down the integral as

$$I(\nu_1, ..., \nu_N) = (-1)^{\nu} \int \left(\prod_{j=1}^{N} \frac{\mathrm{d}x_j \, x_j^{\nu_j - 1}}{\Gamma(\nu_j)} \right) \int \left(\prod_{l=1}^{L} \frac{\mathrm{d}^d k_l}{\pi^{d/2}} \right) e^{\sum_{j=1}^{N} x_j \, (q_j^2 + m_j^2 - i\,0)} \tag{4.1.9}$$

where $\nu = \sum_j \nu_j$ is the sum of all propagator exponents. The integral over loop momenta is just a Gaussian integral and can be performed easily after combining the propagators and performing Wick rotation; see e.g. [326, 328] for more details. The resulting expression is the Feynman parametric representation of this integral:

$$I(\nu_1, ..., \nu_N) = (-1)^{\nu} \, \Gamma(\nu - L\,d/2) \int \left(\prod_{j=1}^{N} \frac{\mathrm{d}x_j \, x_j^{\nu_j - 1}}{\Gamma(\nu_j)} \right) \delta \left(1 - \sum_{j=1}^{N} x_j \right) \frac{\mathcal{U}^{\nu - (L+1)\,d/2}}{\mathcal{F}^{\nu - L\,d/2}} \quad (\nu_j > 0)\,. \tag{4.1.10}$$

The $\mathcal{U}$ and $\mathcal{F}$ polynomials in the above equation are the Symanzik polynomials of the first and second kind respectively. $\mathcal{U}$ and $\mathcal{F}$ are both homogeneous polynomials in the Feynman parameters $x_1, ..., x_N$ of degrees L and $L+1$ respectively. The $\mathcal{U}$ polynomial is strictly non-negative while the $\mathcal{F}$ polynomial vanished for certain kinematic configurations which, in fact, correspond to the branch cuts of the integral.

The Feynman parametric representation can be used to directly evaluate the Laurent expansion in ϵ of the integrals in many cases. E.g. the calculation of the massless bubble integral in Fig. 3.3 (without the s-channel cut) is shown in Appendix B. In particular, the work on linear reducibiliy [329, 330] has expanded the applicability of the method to much more complicated examples. A maple implementation of the integration algorithm, `HyperInt` [331], is also available that performs direct symbolic integration for Feynman integrals that evaluate to multiple polylogarithms. The integrals in Feynman parametric representation can also be evaluated numerically using e.g. Monte-Carlo methods; this is the method of choice for evaluating the master integrals for ZZ and is discussed later in the chapter. A crucial roadblock, before evaluating integrals in the Feynman parametric representation numerically, is the presence of divergences. It is discussed in the next section on how to deal with the divergences.

4.2 Finite integrals

As discussed in Sec 1.5.4, Feynman integrals often have divergences. Those originating from regions of large values of loop momentum are called Ultraviolet (UV) poles and those originating from soft or collinear configurations causing the propagators in the denominators to vanish are called Infrared (IR) poles. It is instructive to study the structure of integrands as well as origin of divergences in the Feynman parametric representation.

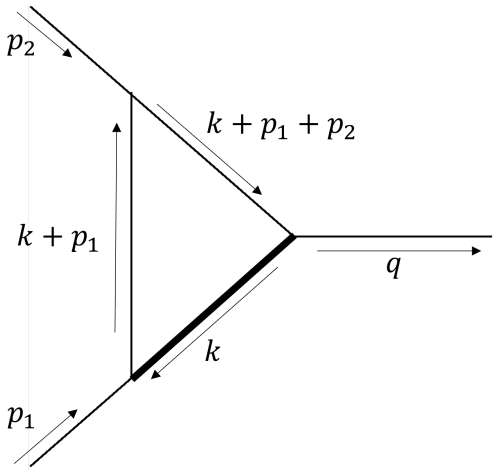

Figure 4.1: 3-point integral with 1 massive propagator.

4.2.1 Divergences in Feynman parametric representation

Consider the 3-propagator massless integral with 1-mass in d-dimensions in Fig. 4.1:

$$I = \int \frac{\mathrm{d}^d k}{i\pi^{d/2}} \frac{1}{(k^2 - m^2)(k + p_1)^2 (k + p_1 + p_2)^2} \,. \tag{4.2.1}$$

This integral can be written in Feynman parametric representation as

$$I = -\Gamma(1+\epsilon) \int_0^\infty \mathrm{d}x_1 \mathrm{d}x_2 \mathrm{d}x_3 \, \delta\left(1 - \sum_{j=1}^{3} x_j\right) \frac{\mathcal{U}^{-1+2\epsilon}}{\mathcal{F}^{1+\epsilon}} \tag{4.2.2}$$

where the Symanzik polynomials are given by

$$\begin{aligned} \mathcal{U} =& x_1 + x_2 + x_3 \,, \\ \mathcal{F} =& (m^2 x_1 + Q^2 x_3)(x_1 + x_2 + x_3) \end{aligned} \tag{4.2.3}$$

where $Q^2 = -q^2 = -(p_1 + p_2)^2$. This integral is known to be IR divergent and hence the integrand cannot simply be expanded in ϵ. Naively expanding the integrand around $\epsilon = 0$ leads to an incorrect result; the divergence isn't explicit in ϵ but rather hidden in the integrand. To see this, consider the region $Q^2 > 0$ where the $\mathcal{U}$ and $\mathcal{F}$ polynomials for the

above integral are both strictly non-negative. The only possible divergences then occur at the endpoints of the integration region.

To simplify the expression, integration in x_2 can be trivially performed using the delta distribution resulting in

$$I = -\Gamma(1+\epsilon) \int_0^\infty \mathrm{d}x_1 \mathrm{d}x_3 \, \frac{1}{(m^2 x_1 + Q^2 x_3)^{1+\epsilon}} \,. \tag{4.2.4}$$

Under the scaling $\{x_1, x_3\} \to \{x_1/\lambda, x_3/\lambda\}$ and the limit $\lambda \to 0$, the integrand behaves as $1/\lambda$ indicating a non-integrable divergence near the boundary. This is the origin of the IR divergence.

For UV divergences, consider a different example, a 2-loop "double" tadpole integral:

$$I = \int \frac{\mathrm{d}^d k_1 \mathrm{d}^d k_2}{(i\pi^{d/2})^2} \, \frac{1}{(k_1^2 - m^2)(k_2^2 - m^2)} \,. \tag{4.2.5}$$

The above integral clearly has a UV divergence in both loops since this is simply a product of two 1-loop tadpole integrals. In Feynman parametric representation, the integral becomes

$$I = -\Gamma(-2+2\epsilon) \int_0^\infty \mathrm{d}x_1 \mathrm{d}x_2 \, \delta\left(1 - x_1 - x_2\right) \, \frac{\mathcal{U}^{-4+3\epsilon}}{\mathcal{F}^{-2+2\epsilon}} \tag{4.2.6}$$

with $\mathcal{U} = x_1 x_2$ and $\mathcal{F} = m^2(x_1 + x_2)\,\mathcal{U}$. This simplifies to

$$I = -\Gamma(-2+2\epsilon) \, (m^2)^{2-2\epsilon} \int_0^\infty \mathrm{d}x_1 \mathrm{d}x_2 \, \delta\left(1 - x_1 - x_2\right) \, \frac{(x_1 + x_2)^{2-2\epsilon}}{(x_1 x_2)^{2-\epsilon}} \,. \tag{4.2.7}$$

In this case, the Gamma function prefactor is divergent in the limit $\epsilon \to 0$:

$$\Gamma(-2+2\epsilon) = \frac{1}{4\epsilon} + O(\epsilon) \,. \tag{4.2.8}$$

Using the Cheng-Wu theorem [332], the variable x_1 can be taken out of the delta distribution. The integrand then diverges in the limit $\lambda \to 0$ for the scaling $x_1 \to x_1/\lambda$; this is the other

UV divergence.

The above approach of determining the scaling behaviour of integrands near boundaries was presented in [333, 334]. These boundary divergences prevent a naive Monte-Carlo implementation since the integrand cannot be expanded around $\epsilon = 0$. A universal approach to resolve these singularities and enable an expansion in ϵ is sector decomposition [161, 285–287, 335]. After performing sector decomposition, the resulting expressions can be integrated numerically. Public codes that implement sector decomposition and perform numerical integration for arbitrary loop integrals in physical kinematical region are available e.g. `Fiesta4` [336] and `pySecDec` [3].

4.2.2 Finite integrals with dimension shifts

The usual approach to Integration-By-Parts reduction using Laporta's algorithm leads to a conventional basis of master integrals which prefers master integrals with the lowest number of propagators and irreducible scalar products in the numerator. This basis is, however, rather difficult to evaluate numerically using sector decomposition due to the presence of boundary singularities which can cause severe numerical instability during Monte-Carlo evaluation. A natural solution would be to use integrals that are finite in $d = 4$ to avoid such issues. Indeed it was observed in [337, 338] that the use of finite integrals in the basis leads to significantly improved numerical stability. In addition, finite integrals often require fewer orders in their ϵ expansion which makes them easier to evaluate numerically requiring less computing resources to achieve similar precision. Another advantage is that the poles in the regulator ϵ drop out of the Feynman integrals and become explicit. The resulting analytic expressions for the amplitude are a lot more convenient and easier to simplify (see Sec. 5.1). These factors together improve the overall numerical performance significantly.

To construct such finite integrals, one approach is to use integrals in dimensions different than $d = 4$. This was explored in [339] by considering finite integrals in $d = 6$. This approach is often used in conjunction with increasing propagator exponents, with finite integrals often

requiring both dimension-shifts and higher powers of propagators. Consider the massless scalar integral with 3-propagators in Eq. 1.5.26 in d-dimensions:

$$I = \int \frac{\mathrm{d}^d k}{i\pi^{d/2}} \frac{1}{(k^2)(k-p_1)^2(k+p_2)^2}\,. \tag{4.2.9}$$

In the limit of small loop-momentum,

$$I \sim \int \frac{\mathrm{d}^d k}{i\pi^{d/2}} \frac{1}{(k^2)(2k.p_1)(2k.p_2)} \sim \int_{k\to 0} \frac{\mathrm{d}^d k}{k^4}\,. \tag{4.2.10}$$

This integral has an IR divergence for $k \to 0$ in $d = 4$. It was shown in Sec. 1.5.4 that this integral will converge for $d > 4$. This is the general idea behind introducing dimensionally-shifted integrals to cure IR divergences; for large enough values of d, the singular behaviour in soft or collinear regions is cured. The opposite approach works for UV divergences. E.g. the bubble integral with 1-mass,

$$I = \int \frac{\mathrm{d}^d k}{i\pi^{d/2}} \frac{1}{(k^2-m^2)(k+p)^2} \sim \int_{k\to\infty} \frac{\mathrm{d}^d k}{k^4}\,, \tag{4.2.11}$$

is finite for $d < 4$. Alternatively, the exponent of one of the propagators can be increased to cure the singular behaviour for large values of loop-momentum. For example,

$$I = \int \frac{\mathrm{d}^d k}{i\pi^{d/2}} \frac{1}{(k^2-m^2)^2(k+p)^2} \sim \int_{k\to\infty} \frac{\mathrm{d}^d k}{k^6} \tag{4.2.12}$$

is now finite for $d < 6$. It is straightforward to see that increasing propagators tames the behaviour for large loop-momentum.

It was shown in [334, 340] that a basis of integrals which are simultaneously finite in both UV and IR regions, constructed using dimension-shifts and higher propagator powers, can always be found. From the above examples it is clear that the dimension shifts act in opposite way to IR and UV poles. Consequently, finite integrals often require a combination

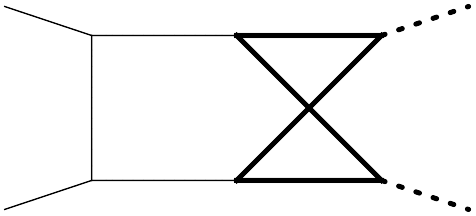

(a) Divergent integral in $d = 4 - 2\epsilon$

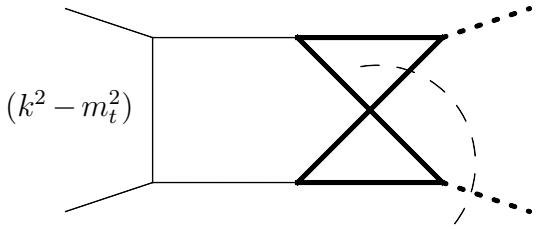

(b) Divergent integral in $d = 4 - 2\epsilon$ with an irreducible numerator

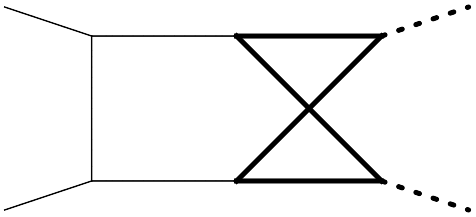

(c) Finite integral in $d = 6 - 2\epsilon$

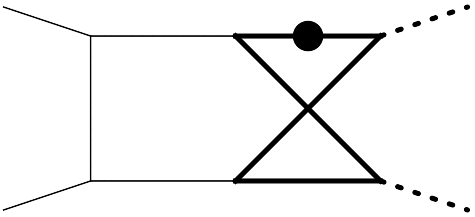

(d) Finite integral with a dot in $d = 6 - 2\epsilon$

Figure 4.2: Examples of divergent and finite integrals in the limit $\epsilon \to 0$ for a non-planar topology. Thick solid lines represent the top-quark while thick dashed lines represent Z-bosons. Topology (b) contains an irreducible numerator, where k is the difference of the momenta of the edges marked by the thin dash lines. Reproduced from [6].

of both dimension shifts and higher propagator powers.

Examples of such finite integrals for a non-planar topology are shown in Fig. 4.2. Fig. 4.2a shows the corner integral for the topology while 4.2b shows an integral with 1 irreducible numerator; both are divergent in $d = 4 - 2\epsilon$. The corner integral, as shown in Fig. 4.2c, is in fact finite in $d = 6 - 2\epsilon$. Another finite integral can be constructed by increasing the exponent of one of the propagators (colloquially referred to as adding a "dot") as shown in Fig. 4.2d.

4.2.3 Finite integrals with numerators

As described in the previous subsection, it is rather straightforward to find finite integrals of such kind involving dimension shifts and dots, especially using e.g. `Reduze 2`. However, inte-

grals with dots typically do not appear in amplitudes which is in fact the primary motivation for syzygy based IBP reduction as discussed in Sec. 3; this is especially true for the top-level topologies. Furthermore, dimension-shifted integrals require reductions for L additional dots for topologies with L-loops which can also be quite challenging. It is therefore desirable to consider alternative approaches to construct finite integrals.

Here, a different approach to construct finite integrals by considering linear combinations of divergent integrals is explored. The Feynman parametric representation of a general linear combination is considered and the boundary regions are analysed to put constraints on the coefficients [341]. This ensures that the non-integrable divergences of the individual integrals cancel for the combined integrand resulting in a single Feynman parametric integral that is finite. Before the algorithm to construct such integrals with numerators, first described in [6], is presented, it is useful to define some relevant quantities and formulas.

Similar to Eq. 4.1.8, propagators with negative exponents i.e. numerators with $\nu_j < 0$ can be included by employing the identity [328, 342]

$$\frac{1}{D^{\nu_j}} = \left[\frac{\partial^{-\nu_j}}{\partial x_j^{-\nu_j}}\, e^{x_j\, D}\right]_{x_j=0} \qquad \text{for } \nu_j \leq 0\,. \tag{4.2.13}$$

Consider an integral $I(\nu_1, ..., \nu_N)$. Let $\mathcal{N}_+$ be the set of all positive ν_j, $\mathcal{N}_-$ the set of all negative ν_j, and $r = \sum_{j\in N_+} \nu_j$. Then an integral with positive *or* negative indices, using Eqs. 4.1.8 and 4.2.13 respectively, can be written as

$$\begin{aligned} I(\nu_1, ..., \nu_N) = (-1)^r\, \Gamma(\nu - L\, d/2) \int \left(\prod_{j\in\mathcal{N}_+} \frac{\mathrm{d}x_j\, x^{\nu_j-1}}{\Gamma(\nu_j)}\right) \delta\left(1 - \sum_{j\in\mathcal{N}_+} x_j\right) \\ \left[\left(\prod_{j\in\mathcal{N}_-} \frac{\partial^{|\nu_j|}}{\partial x_j^{|\nu_j|}}\right) \frac{\mathcal{U}^{\nu-(L+1)d/2}}{\mathcal{F}^{\nu-L\,d/2}}\right]_{x_j=0\,\forall\, j\in\mathcal{N}_-} \qquad (\nu_j \neq 0). \end{aligned} \tag{4.2.14}$$

Using the above formula, an integral with an arbitrary combination of numerators and dots can be expressed in Feynman parametric representation.

The ultimate objective here is to combine different integrals sharing a common parent topology into one merged parametric representation. To that end, it would be desirable to include integrals from subtopologies as well to write down the most general ansatz for a finite linear combination. However, integrals from subtpologies, if their Feynman parametric representations are generated naively using the above formula, have $\mathcal{U}$ and $\mathcal{F}$ polynomials different from the parent topology, and hence the linear combination cannot be combined over a common "denominator" easily. It would be useful, then, to be able to express the subsector integrals in a similar way to the numerator integrals using the same Symanzik polynomials as the parent topology. This can be achieved by taking derivatives with respect to the Feynman parameters corresponding to the pinched lines without setting them to zero,

$$\frac{1}{D^{\nu_j}} = -\int_0^\infty \mathrm{d}x_j \frac{\partial^{-\nu_j+1}}{\partial x_j^{-\nu_j+1}} e^{x_j D} \qquad \text{for } \nu_j \leq 0,\, D < 0. \tag{4.2.15}$$

Here line corresponds to a propagator with a positive index i.e. a propagator present in the topology. Before writing down the general formula, it is necessary to specify some notation.

Let $\mathcal{N} = \{1, \ldots, N\}$ be the set of all indices, $\mathcal{N}_T$ the set of positive indices of the parent topology (parent lines), $\mathcal{N}_t$ the set of positive indices ν_j of the current topology which could either be the parent topology or a subtopology, $\mathcal{N}_{\Delta t} = \mathcal{N}_T \setminus \mathcal{N}_t$ i.e. the set of pinched lines, $\mathcal{N}_{\setminus T} = \mathcal{N} \setminus \mathcal{N}_T$ be the set of negative indices of the parent topology (parent numerators), $r = \sum_{j\in\mathcal{N}_t} \nu_j$ the sum of positive indices of the current integral, and $\Delta t = |\mathcal{N}_{\Delta T}|$ the number of pinched lines. The general integral can then be written in the Feynman parametric representation as

$$\begin{aligned} I(\nu_1, ..., \nu_N) = (-1)^{r+\Delta t}\, \Gamma(\nu - L\, d/2) \int \left(\prod_{j\in\mathcal{N}_T} \mathrm{d}x_j\right) \left(\prod_{j\in\mathcal{N}_t} \frac{x^{\nu_j-1}}{\Gamma(\nu_j)}\right) \delta\left(1 - \sum_{j\in\mathcal{N}_T} x_j\right) \\ \left[\left(\prod_{j\in\mathcal{N}_{\setminus T}} \frac{\partial^{|\nu_j|}}{\partial x_j^{|\nu_j|}}\right) \left(\prod_{j\in\mathcal{N}_{\Delta t}} \frac{\partial^{|\nu_j|+1}}{\partial x_j^{|\nu_j|+1}}\right) \frac{\mathcal{U}^{\nu-(L+1)d/2}}{\mathcal{F}^{\nu - L\, d/2}}\right]_{x_j=0\ \forall\ j\in\mathcal{N}_{\setminus T}} (\nu_j \in \mathbb{Z}). \end{aligned} \tag{4.2.16}$$

Algorithm 4.1 Finite Feynman integrals [6]

Input: Dimensionally regularized multiloop integrals with a common parent sector, possibly involving higher powers of propagators, irreducible numerators, or dimension shifts.

Output: Linear combinations of the input integrals which are finite, i.e. they have a convergent Feynman parametric representation for $\epsilon = 0$.

1: From the n_s input or "seed" integrals, form a general linear combination

$$I \;=\; \sum_{i=1}^{n_s} a_i I_i \,, \tag{4.2.17}$$

where I_i are the seed integrals and a_i are the unknown coefficients. The a_i are assumed to depend on the kinematic invariants and the dimensional regulator ϵ.

2: Using Eq. 4.2.16, write the Feynman parametric representation for each seed integral and bring their linear combination over a common denominator such that

$$I = (-1)^{\nu_0} \int \left(\prod_{j \in \mathcal{N}_T} \mathrm{d}x_j \right) \delta(1 - \sum_{j \in \mathcal{N}_T} x_j) \; \mathcal{P} \; \frac{\mathcal{U}^{\,\nu_0 - (L+1)\,(d_0 - 2\epsilon)/2}}{\mathcal{F}^{\,\nu_0 - L\,(d_0 - 2\epsilon)/2}} \tag{4.2.18}$$

where $\mathcal{N}_T$ is the set of distinct propagators in the parent sector, ν_0 is the effective number of propagators, and $d_0 \in \mathbb{Z}$ the effective number of space-time dimensions to be expanded around. The numerator $\mathcal{P}$ is a homogeneous polynomial in the Feynman parameters,

$$\mathcal{P} \;=\; \sum_j c_j \, M_j(x_1, ..., x_{\mathcal{N}_T}), \tag{4.2.19}$$

where the coefficients c_j are polynomials in a_i, the kinematic variables, and ϵ, and $M_j(x_1, ..., x_{N_p})$ are monomials in Feynman parameters. Note that the numerator polynomial $\mathcal{P}$ in general depends on ϵ and it is crucial to keep this dependence to produce correct results. It is sufficient, however, to set $\epsilon = 0$ in the exponents of the $\mathcal{U}$ and $\mathcal{F}$ polynomials for the convergence analysis in the following two steps.

3: Check the scaling behaviour of the integrand near an integration boundary using the prescription outlined in [333, 334].

4: Make sure a convergent integration of Eq. 4.2.18 is not prevented by a rapid growth of the integrand near the boundary. This can be achieved by requiring the coefficients of the offending monomials in the numerator to vanish, which provides constraints on the a_i.

5: Repeat 3-4 until all boundaries are checked.

At the end of this exercise, we are left with $I = \sum_{i=1}^{n_{\text{fin}}} a_i \left(\sum_{j=1}^{n_s} b_{ij}\, I_j\right)$, where $n_{\text{fin}} \geq 0$ is the number of finite integrals found, and $\sum b_{ij}\, I_j$ are the finite combinations.

This expression for a completely general integral was first presented in [6]. Note that the pinched lines are allowed to appear as numerators i.e. $\nu_j \leq 0$ for $j \in \mathcal{N}_{\Delta t}$. Also, the Symanzik polynomials $\mathcal{U}$ and $\mathcal{F}$ are calculated by taking all indices $\mathcal{N}$ into account.

With the definitions above and the formula for a general Feynman integral, the algorithm 4.1 to construct general linear combinations that are finite in $d = 4$ can be presented. This algorithm was first described in [6].

Applying this algorithm to a set of seed integrals from topology in Fig. 4.2a with the constraint of integrals with only up to 1 numerator rank, the following linear combination is obtained:

$$I_{fin,1} \;=\; s\,(m_z^2 - s - t)\; I_{1,1} + s\; I_{2,1} + s\; I_{3,1} - s\; I_{4,1} - s\; I_{5,1} - (m_z^2 - s - t)\; I_{6,1} - (m_z^2 - t)\; I_{7,1}\,. \tag{4.2.20}$$

The integrals $I_{1,1}$ etc. are as defined in Fig. 4.3. Allowing for integrals with up to numerator rank 2 in the list of seed integrals generates several new linear combinations. Amongst them, the linear combination

$$I_{fin,2} \;=\; s\,(m_z^2 - s - t)\; I_{1,2} + s\; I_{2,2} + s\; I_{3,2} - s\; I_{4,2} - s\; I_{5,2} - (m_z^2 - s - t)\; I_{6,2} - (m_z^2 - t)\; I_{7,2}\,, \tag{4.2.21}$$

with the constituent integrals given in Fig. 4.4, is quite similar to the linear combination in

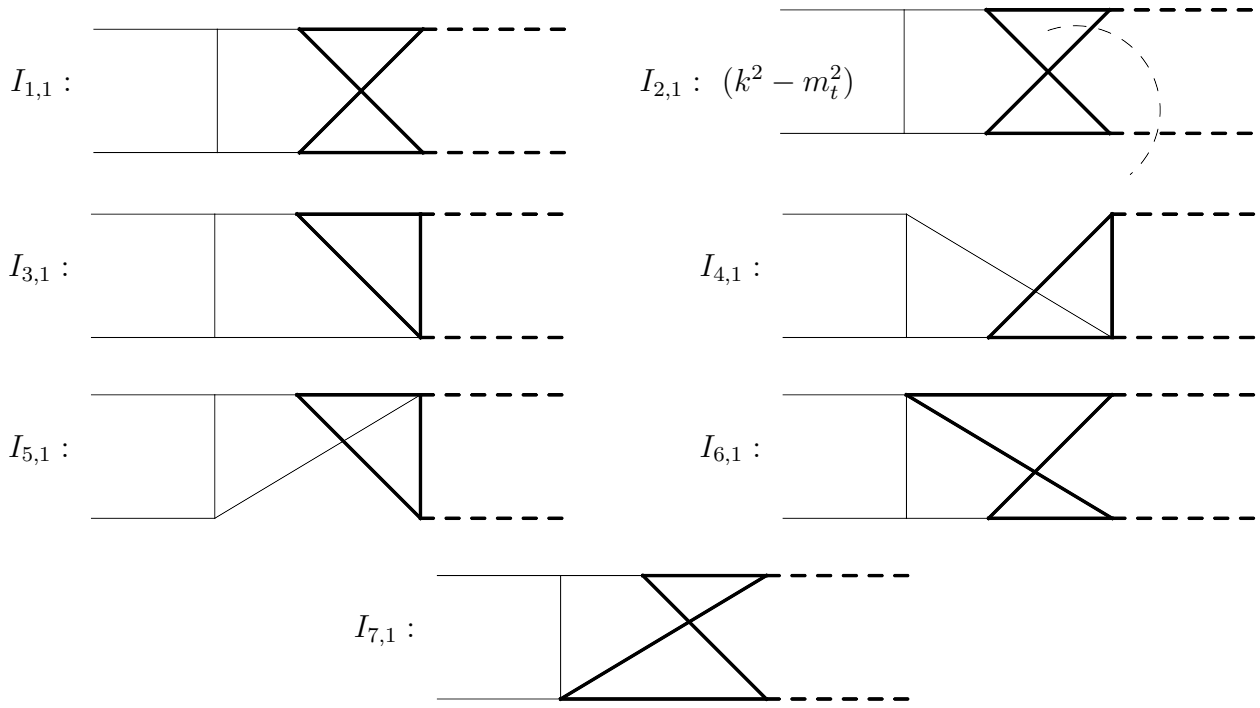

Figure 4.3: Integrals appearing in the linear combination in Eq. 4.2.20. $I_{1,1}$ is the corner integral of the topology under consideration. $I_{2,1}$ is a second integral in the topology, but with a numerator $(k^2 - m_t^2)$, where k is equal to the difference of the momenta of the edges marked by the thin dashed lines. Integrals $I_{3,1}, I_{4,1}, I_{5,1}, I_{6,1}, I_{7,1}$ belong to subtopologies. All integrals are defined in $d = 4 - 2\epsilon$ dimensions. Reproduced from [6].

Eq. 4.2.20. In fact, this linear combination can be generated simply by appending an additional inverse propagator $k^2 - m_t^2$ to all the constituent integrals. Indeed it is straightforward to see that additional numerators can be added to any finite linear combination keeping them finite in the IR limit. However, adding numerators can lead to UV divergences; it is clear in the current example that this is not the case though through power counting, but adding additional numerators might lead to UV poles. One way to ensure UV convergence is to consider integrals with dots. In fact another linear combination can be generated by just adding a dot (on a specific propagator) in all integrals of the combination in Eq. 4.2.20. It must be pointed out, though, that such linear combinations obtained by adding numerators

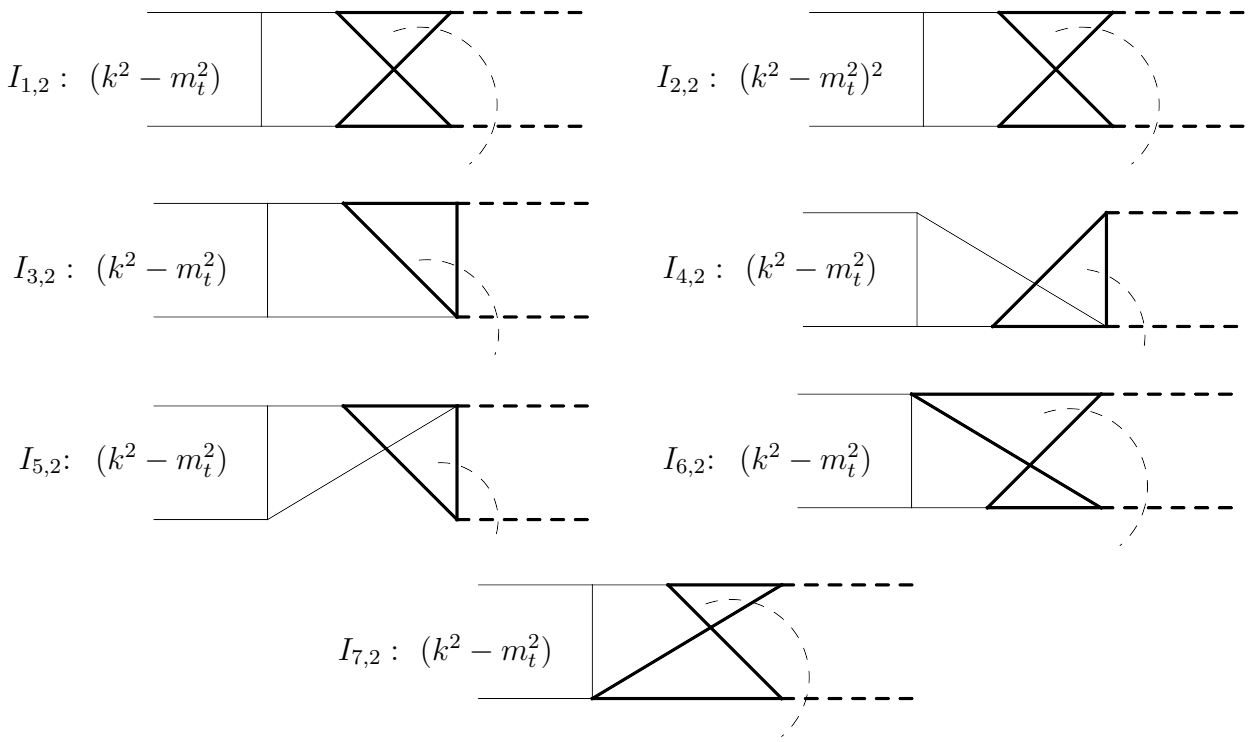

Figure 4.4: Integrals appearing in the linear combination in Eq. 4.2.21. $I_{1,2}$ is the corner integral of the topology under consideration but with a numerator $(k^2 - m_t^2)$, identical to $I_{2,1}$ from Eq. 4.2.20. $I_{2,2}$ is $I_{1,2}$ but with an extra numerator $(k^2 - m_t^2)$ where k is equal to the difference of the momenta of the edges marked by the thin dashed lines. Integrals $I_{3,2}, I_{4,2}, I_{5,2}, I_{6,2}, I_{7,2}$ are the same as $I_{3,1}, I_{4,1}, I_{5,1}, I_{6,1}, I_{7,1}$ but with an extra numerator $(k^2 - m_t^2)$. All integrals are defined in $d = 4 - 2\epsilon$ dimensions. Reproduced from [6].

or dots to other finite linear combinations aren't the only possibilities. It was observed that the number of finite linear combinations increases, in general, with the numerator rank.

4.2.4 Choice of finite integrals for $gg \to ZZ$

The algorithm presented above expands significantly the choice of integrals available for a basis of finite integrals. In principle, the amplitude can be expressed only in terms of such finite linear combinations defined in $d = 4 - 2\epsilon$ containing integrals with only additional numerators. In fact, such a basis can be constructed for $gg \to ZZ$ where only finite linear

combinations are used to replace IR divergent integrals. There are, however, certain limitations to this approach and in practice it was found to be useful to consider also integrals with dimension-shifts and dots. This is largely due to the following reasons:

1. In certain cases, the corner integral of a topology already has a UV divergence. This cannot be cured using a subtopology/numerator subtraction. In particular, UV divergences arising from the Γ prefactor in Eq. 4.2.16 cannot be cured through a subtraction since they only affect the endpoint divergences. Additionally, integrals from subtopologies or with numerators will in general have worse UV behaviour, unless an integral with many dots is considered. It is possible to consider an integral from a supertopology instead but this often leads to increase in complexity both analytically and numerically, and as such is not desirable.

2. While finite linear combinations exist for higher numerator ranks and, in fact, the number of available finite integrals grows with numerator rank, choosing such integrals leads to extreme proliferation in the number of terms in the numerator polynomial from Eq. 4.2.19. E.g. starting at numerator rank 1, the number of terms is $O(10)$ e.g. for the linear combination in Eq. 4.2.20. For the linear combinations with numerator rank 2 this increases to $O(1000)$ e.g. for the integral in Eq. 4.2.21 while for rank 3 this becomes $O(100000)$. Note that these numbers depend on the topology under consideration and in general the numerator polynomials would be simpler for lower topologies. A significant disadvantage of this is that the `pySecDec` libraries required to compute such integrals can reach sizes of ~ 1 GB on the disk and are, hence, difficult to compile on GPUs. Trying to condense the numerator polynomials results in the appearance of spurious poles which worsen the numerical stability further.

3. As mentioned previously, finite linear combinations containing both numerators and dots can also be constructed. This approach was explored to avoid the linear combinations with high numerator rank. While these integrals, as long as numerator ranks

Integral	Max. order in ϵ	Rel. error	Time(s)
Divergent corner integral (Fig. 4.2a)	0	$\sim 2 \cdot 10^{-3}$	45
Divergent numerator integral (Fig. 4.2b)	0	$\sim 4 \cdot 10^{-2}$	63
Finite integral in $d = 6 - 2\epsilon$, (Fig. 4.2c)	1	$\sim 8 \cdot 10^{-6}$	60
Finite integral in $d = 6 - 2\epsilon$ with dot (Fig. 4.2d)	1	$\sim 8 \cdot 10^{-4}$	55
Finite linear combination in Eq. 4.2.20	1	$\sim 1 \cdot 10^{-4}$	18
Finite linear combination in Eq. 4.2.21	0	$\sim 5 \cdot 10^{-4}$	150

Table 4.1: Numerical performance of different non-planar integrals for a physical phase-space point. Timings generated with `pySecDec` [3] using the `QMC` algorithm [4, 5] on a single Nvidia Tesla V100S GPU, with number of evaluations $neval = 10^7$. Note that the divergent integrals are only evaluated to $O(\epsilon^0)$ since they start at ϵ^{-1}. Reproduced from [6].

are small, have more manageable numerator polynomials, their numerical performance in the physical region of kinematics, i.e. the region where contour deformation is required, suffers drastically. This is largely due to the higher power of the $\mathcal{F}$ polynomial in the denominator. In general, integrals with lower exponent of the $\mathcal{F}$ polynomial are preferred.

Table 4.1 shows a comparison for the numerical performance for different divergent and finite integrals from the non-planar topology in Fig. 4.2a. The first two orders in the ϵ expansion are evaluated for most integrals except the finite linear combination in Eq. 4.2.21. From the table it is clear that finite integrals show significantly improved numerical performance compared to divergent integrals. The dimensionally-shifted finite integral in Fig. 4.2c has the lowest exponent for the $\mathcal{F}$ polynomial, specifically the integrand $\sim 1/\mathcal{F}$; unsurprisingly, it shows the best numerical performance. What is indeed surprising is that the finite linear combination in Eq. 4.2.20, which has the integrand $\sim 1/\mathcal{F}^3$ has a numerical performance on par with the dimension-shifted integral without dots and better than the dimension-shifted integral with a dot (which has the integrand $\sim 1/\mathcal{F}^2$. The linear combination with an additional numerator (Eq. 4.2.21) also has the integrand $\sim 1/\mathcal{F}^2$. However, the numerical performance is worse than the "simpler" finite linear combination due largely to significantly more complicated numerator polynomial and consequently much larger `pySecDec` libraries

which are harder to evaluate on GPUs.

At the end, the best numerical performance for $gg \to ZZ$ is achieved using a combination of both finite linear combinations and dimensionally-shifted integrals. Finite linear combinations with low numerator ranks are supplemented with dimensionally-shifted integrals with low number of dots. To cure the UV poles, however, especially the ones appearing in lower topologies such as the double tadpole, integrals with dots are used. This does not affect the numerical performance though since the integrals are rather trivial to evaluate numerically as well as calculating IBP reductions for them is rather easy. The full list of finite master integrals is given in the ancillary files provided with [6].

It has been mentioned previously that choosing a canonical basis of master integrals leads to a simpler form of the IBP relations, in general, over the generic choice of basis. For $gg \to ZZ$, the canonical basis is not known and is expected to be rather challenging to find. In the absence of a canonical basis, a d-factoring basis of master integrals is used to simplify the IBP reductions. That is, in addition to choosing the basis integrals to be finite, they are chosen in such a way that the d-dependence of the denominators appearing in the reduction identities factors out. Simply speaking, there are no irreducible denominator factors appearing in the IBP identities that are simultaneously polynomials in both the kinematic variables and d for the basis of integrals used for final numerical evaluation. This was done using the code provided in [343] (see also [344]). It is also worth mentioning that provided that a canonical basis is found, the structure of IBP reductions as well as the amplitude can be simplified further by the use of a canonical basis that is also finite, referred to as a uniform weight finite basis [345].

Chapter 5

Compiling the 2-loop amplitude

5.1 Inserting reductions into the amplitude

Even with the d-factoring basis of finite master integrals, the IBP identitites are extremely complicated. For $gg \to ZZ$, the IBP identities occupy over 200 GB of disk space before any processing. This would be a nightmare to deal with, and hence several techniques are used to simplify them.

5.1.1 Multivariate partial fractioning

The reduction identities are first processed through `Fermat` [246] which performs a GCD (Greatest Common Divisor) calculation to simplify the coefficients. This already results in a reduction in size by about a factor of 10-20 depending on the topology. The form obtained from `Fermat` where all the terms are put over a common denominator, however, is not ideal for numerical evaluation. In addition, further simplifications can be obtained by employing multivariate partial fractioning on the reduction coefficients. Partial fraction decomposition is simply the expansion of a rational function to a sum of simpler rational functions, or rather rational decomposition of poles. E.g.

$$\frac{x}{x^2-1} = \frac{1}{2(x-1)} + \frac{1}{2(x+1)}\,. \tag{5.1.1}$$

The simple example above demonstrates how partial fraction decomposition can be used to simplify expressions. However, naive approach to partial fractioning, for instance using

`Mathematica`, can lead to appearance of new denominators in the multivariate case. E.g.

$$\frac{x^2 y}{(x^2+y-1)(y+1)} = \frac{-x^2}{(x^2-2)(y+1)} + \frac{x^2(x^2-1)}{(x^2-2)(x^2+y-1)}\,. \tag{5.1.2}$$

In the above example, a new denominator factor x^2-2 appears. For scattering amplitudes, such spurious denominators that weren't present before can cause problems. They can cause severe numerical instabilities especially if they have poles in the physical kinematical region. They can also make the final expressions more complicated. Instead, a mutivariate partial fractioning procedure based on polynomial reductions with respect to a Gröbner basis [277, 278, 346, 347] is used. In this approach more complicated polynomials can be related to simpler polynomials where "simpler" is defined according to a polynomial ordering. E.g. for the above example, assuming an ordering where variable y is preferred over x, and the denominator $1/(1+y)$ is preferred over $1/(-1+y+x^2)$, a polynomial reduction with respect to the Gröbner basis using `Singular` [272] yields

$$\begin{aligned}\frac{x^2 y}{(x^2+y-1)(y+1)} =& -2\left(\frac{1}{-1+y+x^2}\right)\left(\frac{1}{1+y}\right) \\ & -\left(\frac{1}{-1+y+x^2}\right) y + 2\left(\frac{1}{-1+y+x^2}\right) - \left(\frac{1}{1+y}\right) + 1\,.\end{aligned} \tag{5.1.3}$$

which has a maximum degree of 1 in the numerator compared to 3 for the left-hand-side expression. The result is also much simpler than the naive partial fraction result in Eq. 5.1.2 where even degree 4 terms are present in the numerator. Note that this decrease in degree is not guaranteed for any arbitrary ordering.

This approach to multivariate partial fractioning is used to simplify the reduction identities for both $gg \to ZZ$ and $\gamma\gamma + jet$ production. In both cases, a reduction in disk size by a factor of 100 is observed.

5.1.2 Backsubstitution of IBPs

For $gg \to ZZ$, the partial fractioning is implemented using `Singular` with a polynomial ordering that prefers polynomials with lower degrees in kinematic variables and smaller coefficients [278]. As mentioned in Sec. 3.5, the reduction identities are first calculated in the traditional Laporta basis with a generic ordering preferring master integrals with lower numerator ranks. Partial fractioning these IBP identities reduces their size drastically and makes the backsubstitution procedure a lot more manageable. Custom `FORM` scripts are then used to backsubstitute the reduction identities into the form factors. Partial fractioning is again performed on the resulting expressions which simplify drastically at this step; the total size of amplitudes reduces from ∼300 GB to ∼600 MB. Note that for this step, first partial fractioning in only the denominators dependent on d (including the denominators that depend on both d and kinematics) is performed. In a second step, partial fractioning is performed in denominators that depend only on the kinematic variables. This is simply to facilitate the calculation of the Gröbner basis since the traditional Laporta basis is not d-factoring i.e. there are irreducible denominator factors that are polynomials in d as well as kinematic variables, e.g.

$$-75 + 25\,d + 540\,t - 180\,t\,d - 972\,t^2 + 324\,t^2\,d + 450\,s - 90\,s\,d - 972\,s\,t + 324\,s\,t\,d\,,$$

where s, t are the Mandelstam variables defined in Eq. 2.1.9. Such denominators make the Gröbner basis computation extremely challenging.

In the next step, a basis change is performed to express the form factors in terms of the basis of finite integrals as chosen in Sec. 4.2.4; this basis *is* d-factoring. The basis change identities are themselves partial fractioned and then backsubstituted into the reduced amplitude in terms of the traditional Laporta basis. The form factors, which are now in the d-factoring finite basis, are then partial fractioned, again in two steps. First, a partial fractioning in only d-dependent denominators is performed. However, this step is simpler

than for the traditional Laporta basis since there are no complicated denominators depending on kinematic variables involved. Since the amplitude is now expressed in a basis of finite integrals and the 2-loop amplitude is required to be expanded only to $O(\epsilon^0)$, the expressions can be simplified drastically by setting $d = 4$ everywhere except the poles $1/(d-4)$. Note that this is possible only in the case of a d-factoring finite basis since after partial fractioning in d, the poles get isolated. Finally, partial fractioning in kinematic variables is performed on the resulting expressions to produce the final reduced amplitude. In the final representation, the size of the worst coefficients is brought down to less than 1 MB. The list of all surviving denominator factors are given in Appendix E. A `C++` library is created for quick and efficient numerical evaluation of the coefficients. All the coefficients for a generic point in phase space can be evaluated within half a minute using rational arithmetic or within $3s$ using floating point arithmetic with a target precision of 15 digits on a single CPU core.

A slightly different approach is used for $\gamma\gamma + jet$. Since the integrals are already reduced to a canonical basis, there are no d-dependent denominators that also depend on kinematic variables. However, the basis is not finite, so it is not possible to set $d = 4$ after partial fractioning in d. In addition, the amplitude in this case involves many crossings of the integrals. Performing a partial fraction decomposition for each crossing would be quite cumbersome and computationally wasteful. Instead, the uncrossed IBP identities, after simplifying through `Fermat`, are partial fractioned using `MultivariateApart` [278] and then the crossings are applied. The crossed IBPs are then inserted into the amplitude and the resulting expressions are partial fractioned again. At the end, the canonical master integrals are expanded in terms of the "Pentagon functions" defined in [311] and the resulting coefficients of the pentagon functions are partial fractioned again. The final expressions, as expected, are drastically simpler with the largest helicity coefficient for the most complicated colour factor only 4.5 MB in size.

5.2 Renormalisation, IR subtraction and checks

5.2.1 UV renormalisation and IR subtraction

For $gg \to ZZ$, the bare form factors A_i can be expanded perturbatively according to

$$A_i = \frac{\alpha_{\mathrm{s},0}}{2\pi} A_i^{(1)} + \left(\frac{\alpha_{\mathrm{s},0}}{2\pi}\right)^2 A_i^{(2)} + O(\alpha_{\mathrm{s}}^3)\,, \tag{5.2.1}$$

where $\alpha_{\mathrm{s},0}$ is the bare QCD coupling. Since the LO process for $gg \to ZZ$ already starts at one loop, the two-loop process is effectively an NLO correction.

First, UV renormalisation of α_{s} is performed in the 5-flavour $\overline{\mathrm{MS}}$ scheme i.e. $n_f = 5$ using

$$\alpha_{\mathrm{s},0} = \alpha_{\mathrm{s}}\, S_\epsilon^{-1}\, Z_{\alpha_{\mathrm{s}}} \left(\frac{\mu_R^2}{{\mu_0}^2}\right)^{\epsilon}, \tag{5.2.2}$$

where $S_\epsilon = (4\pi)^\epsilon e^{-\gamma_E \epsilon}$, $\gamma_E \approx 0.577$ is Euler's constant, μ_R is the renormalisation scale, and μ_0 is the 't Hooft scale introduced in the bare amplitude through conventional dimensional regularisation. Note that the top-quark contribution to the gluon self energy is subtracted at zero momentum [348].

The renormalisation constant $Z_{\alpha_{\mathrm{s}}}$ in the above equation is given by

$$Z_{\alpha_{\mathrm{s}}} = 1 + \frac{\alpha_{\mathrm{s}}}{2\pi}\,\delta Z_{\alpha_{\mathrm{s}}} + \mathcal{O}(\alpha_{\mathrm{s}}^2), \tag{5.2.3}$$

where

$$\delta Z_{\alpha_{\mathrm{s}}} = -\frac{1}{\epsilon}\,\beta_0 + \frac{1}{\epsilon}\left(\frac{2}{3}\,T_F\,\left(\frac{\mu_R^2}{m_t^2}\right)^{\epsilon}\right). \tag{5.2.4}$$

In the above equation, β_0 is the first coefficient of the beta function expanded in α_{s}, given

in Eq. 1.5.38,

$$\beta_0 = \frac{11\,C_A - 4\,T_F\,n_f}{6}\,, \tag{5.2.5}$$

and C_A, C_F are the quadratic Casimir invariants

$$C_A = N, \quad C_F = \frac{N^2-1}{2N}\,, \tag{5.2.6}$$

with $T_F = \frac{1}{2}$.

The top-quark mass is renormalised in the on-shell scheme. The renormalised top-quark mass is related to its bare mass according to

$$m_{t,0}^2 \;=\; m_t^2\,Z_m\,, \tag{5.2.7}$$

with the renormalisation constant defined as

$$Z_m = 1 + \frac{\alpha_\mathrm{s}}{2\pi}\,\delta Z_m, \quad \delta Z_m \;=\; C_F\,\left(-\frac{3}{\epsilon}\,-4\right)\,\left(\frac{\mu_R^2}{m_t^2}\right)^{\epsilon}\,. \tag{5.2.8}$$

In principle, the top-quark mass in the amplitude can simply be replaced by the renormalised mass in Eq. 5.2.7. However, in practice it is a lot more convenient to instead explicitly subtract 1-loop counterterm diagrams (See Fig.).

Lastly, the gluon wave function is renormalised by multiplying the amplitude with $Z_G^{1/2}$ for each external gluon, where the gluon renormalisation constant Z_G is defined as

$$Z_G = 1 + \frac{\alpha_\mathrm{s}}{2\pi}\,\left(-\frac{2}{3}\,T_F\,\left(\frac{\mu_R^2}{m_t^2}\right)^{\epsilon}\right)\,+\,\mathcal{O}(\alpha_\mathrm{s}^2)\,. \tag{5.2.9}$$

This results in renormalised form factors given by

$$A_i^{\mathrm{ren}} = \frac{\alpha_\mathrm{s}}{2\pi}\,A_i^{(1),\mathrm{ren}} + \left(\frac{\alpha_\mathrm{s}}{2\pi}\right)^2 A_i^{(2),\mathrm{ren}} + \mathcal{O}(\alpha_\mathrm{s}^3). \tag{5.2.10}$$

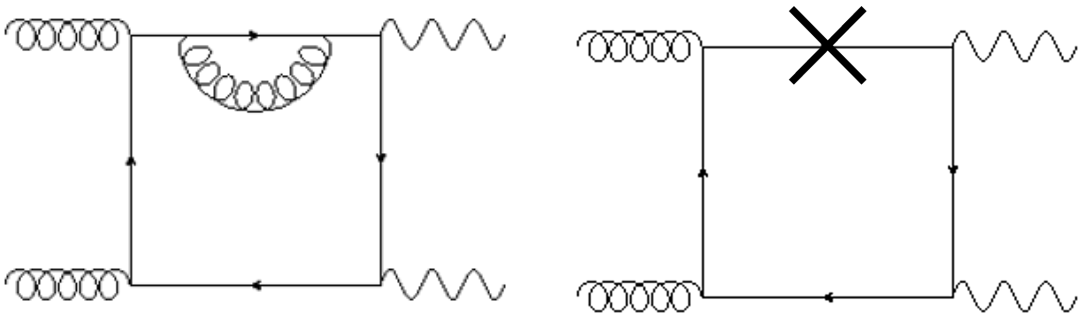

(a) Divergent diagram.

(b) Mass counterterm diagram.

Figure 5.1: Mass counterterm diagrams required at 2-loops. The big dark cross in Fig. 5.1b corresponds to the counterterm vertex insertion.

The renormalisation constants in the above equations are derived in Appendix D.

After UV renormalisation, IR subtraction must be performed to obtain finite results. The IR structure of NLO amplitudes was first predicted by Catani in [14]. IR subtraction for this calculation is performed using the "$q_{\rm T}$ scheme" described in [349]. The finite remainders resulting from IR subtraction are given by

$$A_i^{(2),\rm fin} = A_i^{(2),\rm ren} - A_i^{(1),\rm ren}\, I_{(1)}(\epsilon)\,. \tag{5.2.11}$$

The I-operators in the "$q_{\rm T}$ scheme" are given by

$$I_{(1)}(\epsilon) = I_{(1)}^{\rm soft}(\epsilon) + I_{(1)}^{\rm collinear}(\epsilon), \tag{5.2.12}$$

$$I_{(1)}^{\rm soft}(\epsilon) = -\frac{e^{\epsilon\gamma}}{\Gamma(1-\epsilon)} \left(\frac{\mu_R^2}{s}\right)^{\epsilon} \left(\frac{1}{\epsilon^2} + \frac{i\pi}{\epsilon} + \delta_{q_T}^{(0)}\right) C_A, \tag{5.2.13}$$

$$I_{(1)}^{\rm collinear}(\epsilon) = -\left(\frac{\mu_R^2}{s}\right)^{\epsilon} \frac{\beta_0}{\epsilon}, \tag{5.2.14}$$

where $\delta_{q_T}^{(0)} = 0$. UV and IR finite form factors are then given by

$$A_i^{\rm fin} = \frac{\alpha_{\rm s}}{2\pi}\, A_i^{(1),\rm fin} + \left(\frac{\alpha_{\rm s}}{2\pi}\right)^2 A_i^{(2),\rm fin} + \mathcal{O}(\alpha_{\rm s}^3). \tag{5.2.15}$$

Note that the renormalisation scale $\mu_R^2 = s$ for all the results presented in this work.

5.2.2 Checks of the calculation

Multiple checks are performed to establish the correctness of this calculation and results, as described below:

1. The 2-loop form factors are explicitly checked to satisfy the identities in Eq. 2.1.16. These identities hold at the level of reduced amplitude with fully symbolic kinematic dependence.

2. The crossing relations in Eq. 2.1.17, on the other hand, are highly non-trivial to check analytically. Instead, these relations are verified numerically for a phase-space point within numerical precision.

3. All the finite linear combinations used in the basis are checked by numerically evaluating them and comparing them against their explicit definitions in terms of divergent integrals for a phase space point.

4. Algebraic cancellation of the spurious $1/\epsilon^4$ pole is seen when the amplitude is expressed in the chosen basis of finite integrals; the spurious $1/\epsilon^3$ pole remains, however, for the amplitude reduced in terms of symbolic master integrals. The $1/\epsilon^3$ pole is verified to vanish to 15 digits by calculating the amplitude numerically for a phase-space point in the Euclidean region.

5. The $1/\epsilon^2$ and $1/\epsilon$ poles are verified to match Catani's IR formula [14] numerically, for a phase-space point in the Euclidean region, to 9 digits for the double pole and 7 digits for the single pole. Numbers are shown explicitly in Appendix F.

6. The $1/\epsilon^2$ and $1/\epsilon$ poles are also verified to match Catani's IR formula [14] for a point in the physical region with explicit numbers shown in Appendix F.

7. The amplitude is also evaluated using an alternate finite basis constructed along the same lines as the primary basis. The numerical results from the two bases are compared

and found to agree within expected numerical error. It must be pointed out that this is a very stringent check on the correctness of the calculation since it simultaneously checks the IBP reductions, the basis change from the primary to the alternate basis, definitions of the finite integrals chosen, and their numerical evaluation. An error in any one of these steps would imply disagreement between the two bases. Note that the alternate basis, while composed of finite integrals, is numerically not as stable as the primary basis and although it is useful for validating the calculation, it is generally unsuitable for evaluation at a large number of phase-space points.

8. The axial-axial (a_t^2) piece of the 2-loop amplitude is evaluated using the Kreimer's anti-commuting γ_5 scheme [211, 212]. In addition, a separate numerical calculation is performed by a collaborator on this project, Stephen Jones, using Larin's γ_5 scheme [350, 351]. Agreement is found at the level of helicity amplitudes (but not for the form factors A_i) defined using Eq. 2.1.19 between the two schemes for a physical as well as Euclidean phase space point within numerical precision. This provides another strong check of the calculation since only physical gauge-invariant observables are expected to agree for two different schemes.

9. Lastly, the calculation is compared against several known approximations in the literature, specifically the heavy top approximation [104–106] below the top-quark pair production threshold and the small top-mass expansion [13] above the threshold (at high center of mass energies). Agreement is found with both approximations in the relevant regions of phase-space with the results of the comparison presented in Sec. 6.

Chapter 6

Results

6.1 Results for the 2-loop $gg \to ZZ$ amplitude

In this section, the results for the 2-loop amplitude for $gg \to ZZ$ are presented and compared against several approximations. Before presenting the results however, some quantities relevant for presentation of the results need to be defined. For most of the results presented below, the helicity basis defined in Eq. 2.1.19 is used. Similar to the bare form factors, UV renormalised and IR subtracted helicity amplitudes can be written as

$$\mathcal{M}^{\text{fin}}_{\lambda_1\lambda_2\lambda_3\lambda_4} = \mathcal{M}^{\text{fin}}_{\mu\nu\rho\sigma}\epsilon^{\mu}_{\lambda_1}(p_1)\epsilon^{\nu}_{\lambda_2}(p_2)\epsilon^{*\rho}_{\lambda_3}(p_3)\epsilon^{*\sigma}_{\lambda_4}(p_4). \tag{6.1.1}$$

where λ_1, λ_2 are the helicities of the incoming gluons and λ_3, λ_4 are the helicities of the outgoing Z-bosons. The helicity amplitudes can be expanded in $\left(\frac{\alpha_s}{2\pi}\right)$ similar to form factors in Eq. 5.2.15 as

$$\mathcal{M}^{\text{fin}}_{\lambda_1\lambda_2\lambda_3\lambda_4} = \left(\frac{\alpha_s}{2\pi}\right)\mathcal{M}^{(1)}_{\lambda_1\lambda_2\lambda_3\lambda_4} + \left(\frac{\alpha_s}{2\pi}\right)^2\mathcal{M}^{(2)}_{\lambda_1\lambda_2\lambda_3\lambda_4} + \mathcal{O}(\alpha_s^3). \tag{6.1.2}$$

It is useful to consider the squared 1-loop helicity amplitudes $\mathcal{V}^{(1)}_{\lambda_1\lambda_2\lambda_3\lambda_4}$ as well as the interference between the 1-loop and 2-loop helicity amplitudes $\mathcal{V}^{(2)}_{\lambda_1\lambda_2\lambda_3\lambda_4}$, which can be defined

as

$$\mathcal{V}^{(1)}_{\lambda_1\lambda_2\lambda_3\lambda_4} = \mathcal{M}^{*(1)}_{\lambda_1\lambda_2\lambda_3\lambda_4}\mathcal{M}^{(1)}_{\lambda_1\lambda_2\lambda_3\lambda_4}, \tag{6.1.3}$$

$$\mathcal{V}^{(2)}_{\lambda_1\lambda_2\lambda_3\lambda_4} = 2\,\mathrm{Re}\left(\mathcal{M}^{*(1)}_{\lambda_1\lambda_2\lambda_3\lambda_4}\,\mathcal{M}^{(2)}_{\lambda_1\lambda_2\lambda_3\lambda_4}\right). \tag{6.1.4}$$

Most of the results shown below are obtained by averaging over the helicities of the incoming gluons as

$$\mathcal{V}^{(i)}_{\lambda_3\lambda_4} = \frac{1}{4}\sum_{\lambda_1,\lambda_2}\mathcal{V}^{(i)}_{\lambda_1\lambda_2\lambda_3\lambda_4}, \quad (i=1,2)\,, \tag{6.1.5}$$

with $\lambda_1, \lambda_2 \in \{+,-\}$, and by summing over the helicities of the outgoing Z-bosons as

$$\mathcal{V}^{(i)} = \sum_{\lambda_3,\lambda_4}\mathcal{V}^{(i)}_{\lambda_3\lambda_4}, \quad (i=1,2)\,, \tag{6.1.6}$$

with $\lambda_3, \lambda_4 \in \{+,-,0\}$. Note that the 1-loop amplitudes used in calculating $\mathcal{V}^{(i)}_{\lambda_1\lambda_2\lambda_3\lambda_4}$ are just the top-quark contributions. Contributions from massless quarks are ignored for the purpose of presentation of the numerical results below.

For the numerical results shown, the electroweak couplings are chosen as

$$\begin{aligned} G_F &= 1.1663787\cdot 10^{-5}\ \mathrm{GeV}^{-2}\,, \\ m_Z &= 91.1876\ \mathrm{GeV}\,, \end{aligned} \tag{6.1.7}$$

where the Fermi constant G_F and Z boson mass m_Z are fixed according to [1]. Since the ratio of top-mass and Z-boson mass is fixed to $m_Z^2/m_t^2 = 5/18$, inserting the above value of $m_Z = 91.1876\,\mathrm{GeV}$ implies the top-mass value $m_t = 173.016\,\mathrm{GeV}$. The W-boson mass is fixed according to the ratio

$$m_W^2/m_t^2 = 14/65\,. \tag{6.1.8}$$

This fixes the mass of the W-boson to $m_W = 80.296\,\text{GeV}$. For this calculation, the so-called G_μ scheme is used i.e. G_F, m_Z, and m_W are chosen as input quantities for the electroweak parameters. The weak mixing angle is then fixed according to $\sin(\theta_W) = \sqrt{1 - m_W^2/m_Z^2}$.

To numerically evaluate the master integrals, `pySecDec` [3, 5] is used. Sector decomposition is applied and the integration is performed using the quasi-Monte Carlo (QMC) algorithm [4, 352]. The QMC algorithm has been observed to show a much better convergence compared to the traditional Monte-Carlo algorithms [337]. The different colour structures appearing in the form factors (C_F and C_A) as well as the vector-vector (v_t^2) and axial-axial (a_t^2) pieces are all evaluated separately. The target precision for each form factor, for each colour structure and coupling type (v_t^2 or a_t^2), is set to percent level. This is achieved using a variant of the optimisation algorithm presented in [337]. The helicity amplitudes are then calculated from the form factors.

Using the optimisation algorithm, requiring percent level precision on all form factors, the time taken for numerical evaluation varies between 1.5-24 hours on 2 Nvidia Tesla v100 GPUs; this usually results in most form factors being calculated to per mille or better. Almost the entire runtime is spent on calculating master integrals; the time taken to evaluate the coefficients is negligible in comparison (see Sec. 5.1). The independent helicity amplitudes for a phase-space point in the physical region are shown in Tab. 6.1

Fig. 6.1 shows a comparison of the interference term $\mathcal{V}^{(2)}$ calculated in this work against the large top-mass and the small top-mass expansions (using the analytic expressions for the expansions provided in [13]) for varying $\sqrt{s}/m_t$ and fixed value of $\cos(\theta) = -0.1286$, with the scattering angle θ defined in Eq. 2.1.18. Also compared is the Padé improved small top-mass expansion. The plot shows excellent agreement for this calculation with the expansion results in the regions of phase-space where the approximation is expected to hold. For the smallest value of $\sqrt{s} = 235\,\text{GeV}$ shown on the plot, the large top-mass expansion agrees within 0.1% with our result. Similar agreement to sub-per mille level is observed for the point with the largest $\sqrt{s} = 878\,\text{GeV}$ when compared to the small top-mass expansion as well as the Padé

$\lambda_1, \lambda_2, \lambda_3, \lambda_4$	$\mathcal{M}^{(1)}_{\lambda_1\lambda_2\lambda_3\lambda_4}$ (1-loop)	$\mathcal{M}^{(2)}_{\lambda_1\lambda_2\lambda_3\lambda_4}$ (2-loop)
$++++$	$0.1337854(1) - 0.0286060(1)\,i$	$3.15549(8) + 0.47235(8)\,i$
$+++-$	$0.0015573(1) + 0.0052282(1)\,i$	$0.15950(7) + 0.14052(8)\,i$
$+-+-$	$-0.01512820(8) - 0.01060416(8)\,i$	$-0.38609(7) + 0.10539(7)\,i$
$-+++$	$-0.0291599(1) - 0.0062178(1)\,i$	$-0.46990(8) + 0.40207(8)\,i$
$+++0$	$0.0292668(5) + 0.0212966(5)\,i$	$1.1248(2) - 0.0805(2)\,i$
$+-+0$	$-0.0643073(5) - 0.0459584(5)\,i$	$-1.4803(2) + 0.4940(2)\,i$
$++00$	$0.910006(2) + 1.132536(2)\,i$	$17.2585(6) + 29.5669(6)\,i$
$+-00$	$0.355092(2) + 0.404469(2)\,i$	$10.2869(5) - 1.0571(6)\,i$

Table 6.1: 1-loop and 2-loop helicity amplitudes for $gg \to ZZ$ for the phase-space point $s/m_t^2 = 142/17$, $t/m_t^2 = -125/22$, $m_Z^2/m_t^2 = 5/18$, and $m_t = 1$, with $\mathcal{M}^{(1)}_{\lambda_1\lambda_2\lambda_3\lambda_4}$ and $\mathcal{M}^{(2)}_{\lambda_1\lambda_2\lambda_3\lambda_4}$ defined in Eq. 6.1.2. Only the 8 independent helicity amplitudes (See Eqs. 2.1.20, 2.1.21, and 2.1.22) are shown here. Note that these include only the top-quark contributions from class A diagrams defined in Sec. 2.3.2. The numbers in parentheses denote the uncertainty in the last digit. Reproduced from [6].

improved result. Also observed is the fact that the Padé approximation improves drastically the agreement with our exact result compared to the regular small top-mass expansion. Note that the regular small-mass expansion result is only visible for the two highest values of $\sqrt{s}$ and diverges rapidly from the exact result for smaller values. The Padé improved result, on the other hand, agrees to much lower energies closer to the $\sqrt{s} = 2m_t$ threshold. In fact, this plot also shows that the expansions considered here can reproduce the exact result within a few percent for most values of $\sqrt{s}$ except for the region near the top-quark pair production threshold $\sqrt{s} = 2m_t$, for the value of $\cos\theta$ considered here.

In Fig. 6.2, a comparison of the interference term $\mathcal{V}^{(2)}$ is shown for varying $\cos\theta$ for several fixed values of $\sqrt{s}$. The large top-mass expansion changes very little with variation in $\cos\theta$, as is clear from the top-left panel. On the other hand, the small top-mass expansion diverges rapidly away from central scattering angles ($\cos\theta \sim 0$) as seen in the bottom panel. In fact, for the points far away from the centre, the small top-mass expansion is way off the plotting range. This can be understood from the way the expansion is performed i.e. in the limit $m_Z^2 \ll m_t^2 \ll s, |t|, |u|$. In this limit, $|t| \sim |u| \sim s/2$ for central scattering which

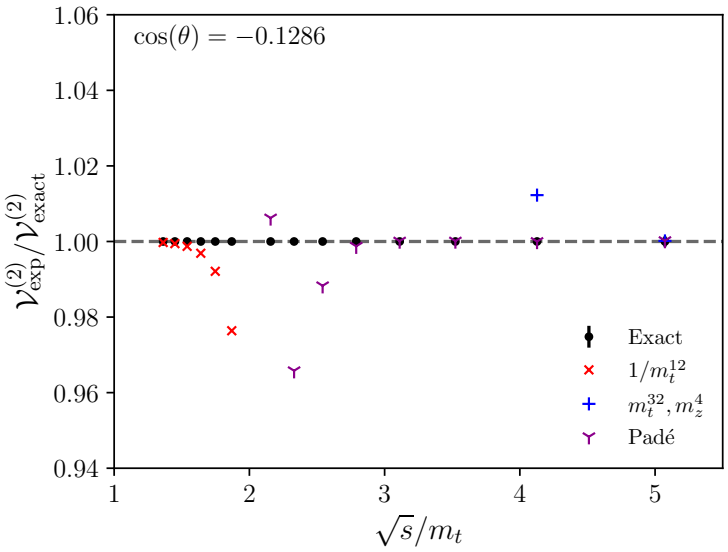

Figure 6.1: Comparison of the $\sqrt{s}$ dependence of the unpolarised interference $\mathcal{V}^{(2)}$ with expansion for large and small top-quark mass [13] at fixed $\cos(\theta) = -0.1286$. The large top-mass expansion is shown in colour red, the small top-mass expansion in blue, and the Padé improved small top-mass expansion in purple. The exact result is shown in black. Note that the error bars have been plotted for the exact result, they are too small to be visible on the plot, however. Reproduced from [6].

justifies the expansion. However for back-to-back scattering ($|\cos\theta| \sim 1$), $|t|$ and $|u|$ are no longer guaranteed to be large compared to m_t^2 and hence the approximation breaks down. It must be pointed out that Padé approximation significantly improves the convergence of the expansion. For the high energy point ($\sqrt{s} = 814\,\text{GeV}$) in the bottom panel, the agreement of our result with the Padé improved result is almost perfect. Even for the intermediate energy point in the top-right panel ($\sqrt{s} = 403\,\text{GeV}$), the agreement is generally within a few percent close to the central scattering region.

Fig. 6.3 shows comparisons for specific outgoing helicities averaged over the incoming gluon helicities as defined in Eq. 6.1.5 against the expansions. Both the 1-loop amplitude squared $\mathcal{V}^{(1)}_{\lambda_3\lambda_4}$ and the 2-loop interference with 1-loop $\mathcal{V}^{(2)}_{\lambda_3\lambda_4}$ is shown for varying $\sqrt{s}$ with a fixed scattering angle $\cos(\theta) = -0.1286$. Note that the expansions are only plotted for the 2-

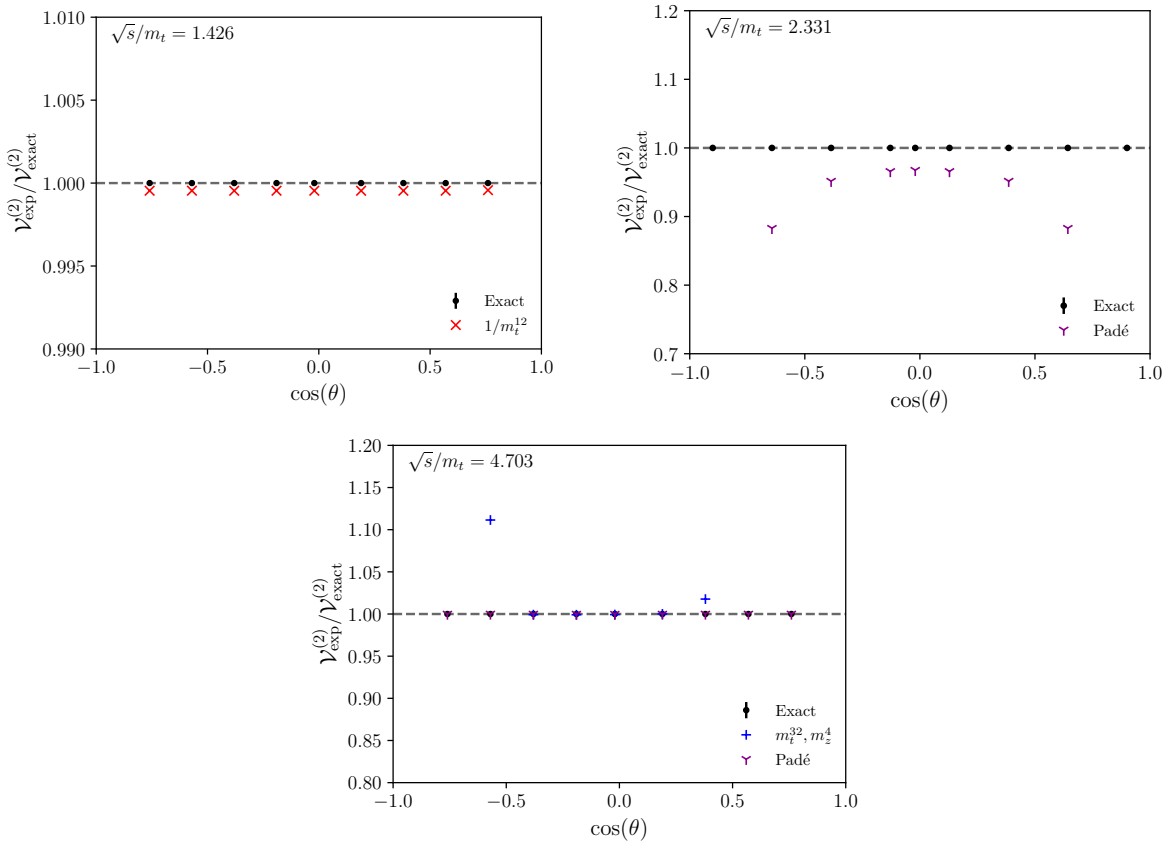

Figure 6.2: Comparison of the $\cos(\theta)$ dependence of the unpolarised interference $\mathcal{V}^{(2)}$ with the results expanded in the limit of large top-quark mass for $\sqrt{s} = 247$ GeV (Top Left Panel) and small top-quark mass for $\sqrt{s} = 403$ GeV (Top Right Panel) and $\sqrt{s} = 814$ GeV (Bottom Panel). Reproduced from [6].

loop interference term. Looking at the plots, there is good agreement with the best available expansions in the relevant regions. Unsurprisingly, the small top-mass expansion lies far outside the plotting range for most points. The Padé improved expansion, however, agrees well all the way down to lower $\sqrt{s}$ near the $\sqrt{s} = 2m_t$ threshold. The level of agreement of our result with the expansions greatly depends on the specific helicity configuration under consideration. E.g. good agreement is seen for the $\mathcal{V}^{(2)}_{00}$ configuration while agreement for $\mathcal{V}^{(2)}_{+-}$ and $\mathcal{V}^{(2)}_{+0}$ clearly starts to appear worse closer to the threshold. Note that the longitudinal configuration $\mathcal{V}^{(2)}_{00}$ is dominant over the others even at the 2-loop level, similar to what was observed for 1-loop in Sec. 2.2.3 as well as in the above plots. A rapid increase in $\mathcal{V}^{(1)}_{00}$ and

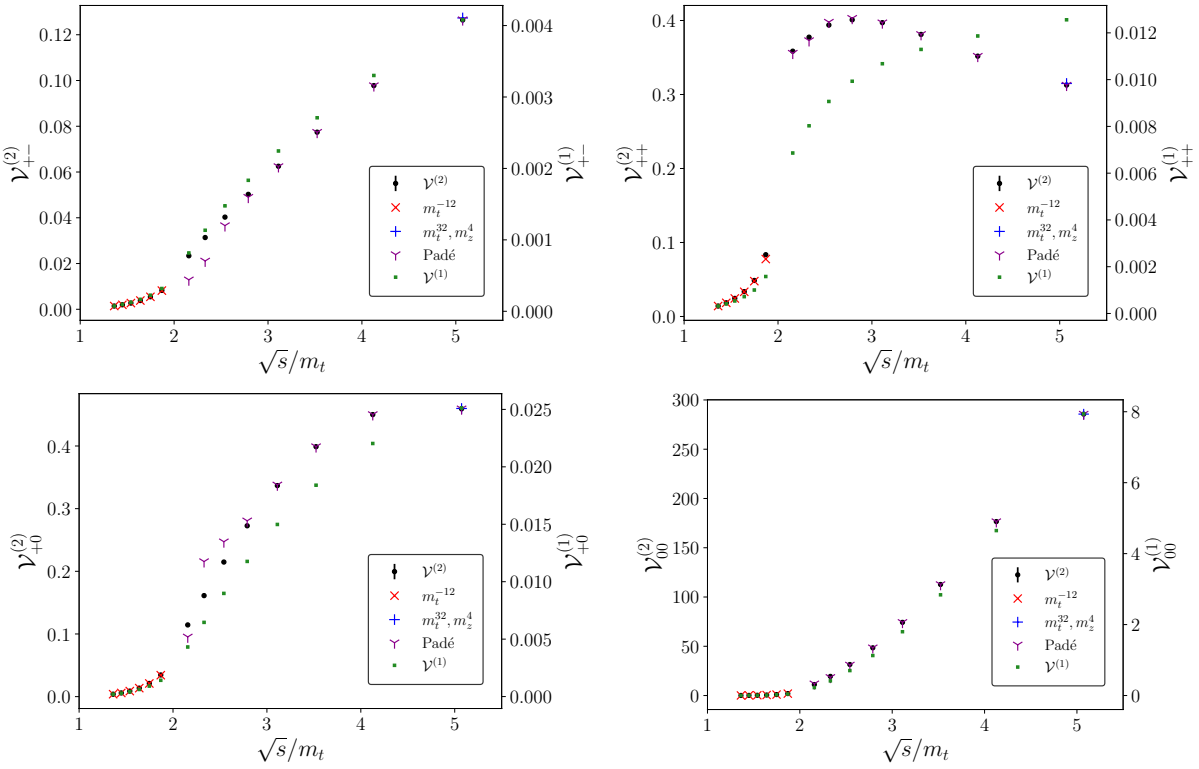

Figure 6.3: The $\sqrt{s}$ dependence of 1-loop and 2-loop interferences for polarised ZZ production in gluon fusion at $\cos(\theta) = -0.1286$. Reproduced from [6].

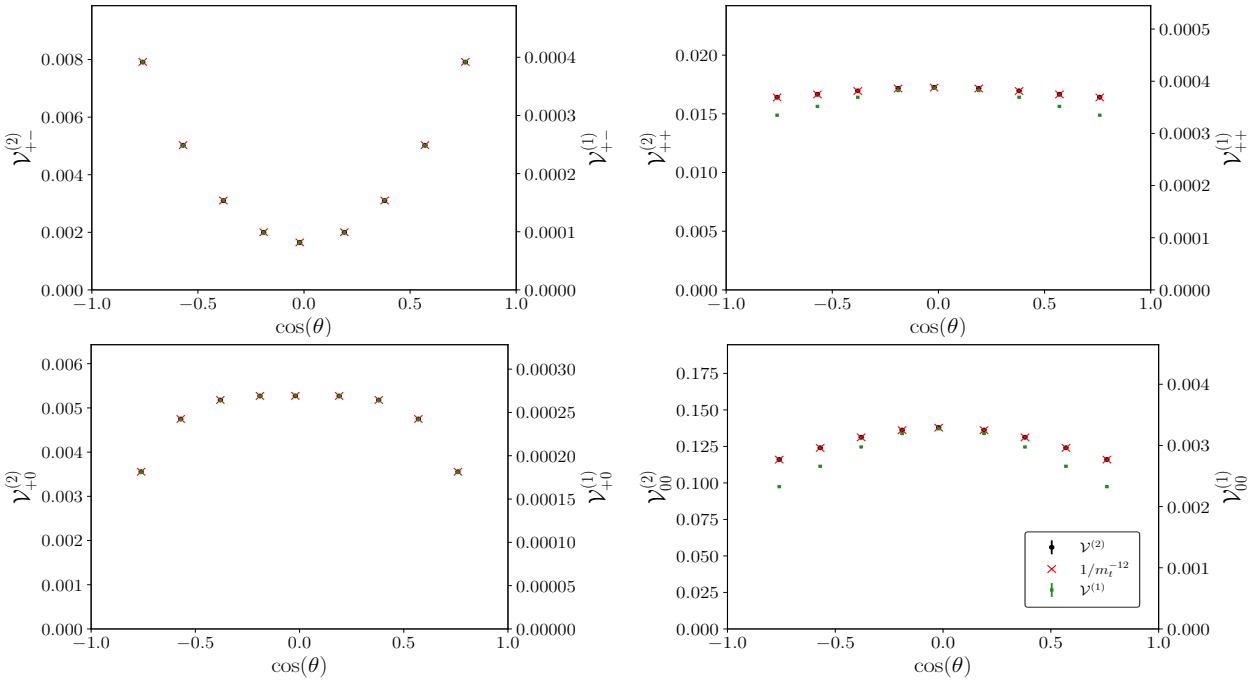

Figure 6.4: The $\cos(\theta)$ dependence of 1-loop and 2-loop interferences for polarised ZZ production in gluon fusion at $\sqrt{s}/m_t = 1.426$. The large top-quark mass expansion [13] (to order $1/m_t^{12}$) is shown for comparison. Reproduced from [6].

$\mathcal{V}^{(2)}_{00}$ past the top-quark pair production threshold $\sqrt{s} = 2m_t$ is also seen, similar to what was observed for 1-loop in Sec. 2.2.3.

Figs. 6.4, 6.5 and 6.6 show the comparisons for interference terms with specific helicity configurations for varying $\cos\theta$ and 3 different fixed values of $\sqrt{s}$. Fig. 6.4 shows the comparison against large top-mass expansion. It is clear from the plot that there is very good agreement for all helicity configurations. Note that in the chosen scaling, the 1-loop points almost lie on top of the 2-loop point with an almost complete overlap for $\mathcal{V}^{(2)}_{+-}$ and $\mathcal{V}^{(2)}_{+0}$.

Fig. 6.5 shows the comparison against the Padé improved small top-mass expansion for intermediate energy. While in general the Padé approximation agrees well with our result, there are some deviations, notably for $\cos\theta$ away from 0 and sub-dominant helicities.

Fig. 6.6 shows the comparison plots for a high energy point with $\sqrt{s} = 814\,\text{GeV}$. The Padé improved small top-mass expansion again shows excellent agreement with our result for even larger values of $|\cos\theta|$, away from the center. This is a drastic improvement over

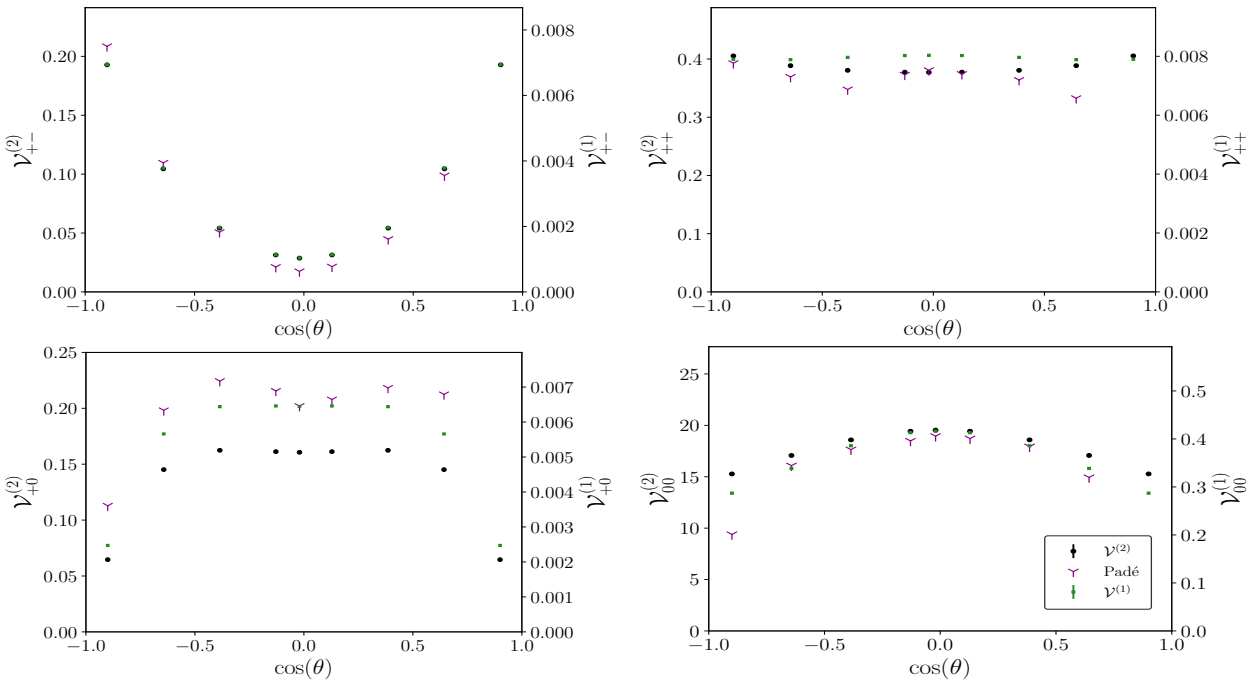

Figure 6.5: The $\cos(\theta)$ dependence of 1-loop and 2-loop interferences for polarised ZZ production in gluon fusion at $\sqrt{s}/m_t = 2.331$. The Padé improved small top-quark mass expansion [13] is shown for comparison. Reproduced from [6].

the "regular" small top-mass expansion which is highly divergent away from the center.

It must be pointed out that the *relative* level of agreement shown in the above plots between our exact result and the various expansions depends significantly on the exact scheme used for IR subtraction. The comparisons shown in the above plots are done in the "q_{T} scheme" [349]. Conversion to Catani's original subtraction scheme [14] can be performed using

$$A_i^{(1),\mathrm{fin,Catani}} = A_i^{(1),\mathrm{fin}}, \tag{6.1.9}$$

$$A_i^{(2),\mathrm{fin,Catani}} = A_i^{(2),\mathrm{fin}} + \Delta I_1 A_i^{(1),\mathrm{fin}}, \tag{6.1.10}$$

where

$$\Delta I_1 = -\frac{1}{2}\pi^2 C_A + i\pi\beta_0, \tag{6.1.11}$$

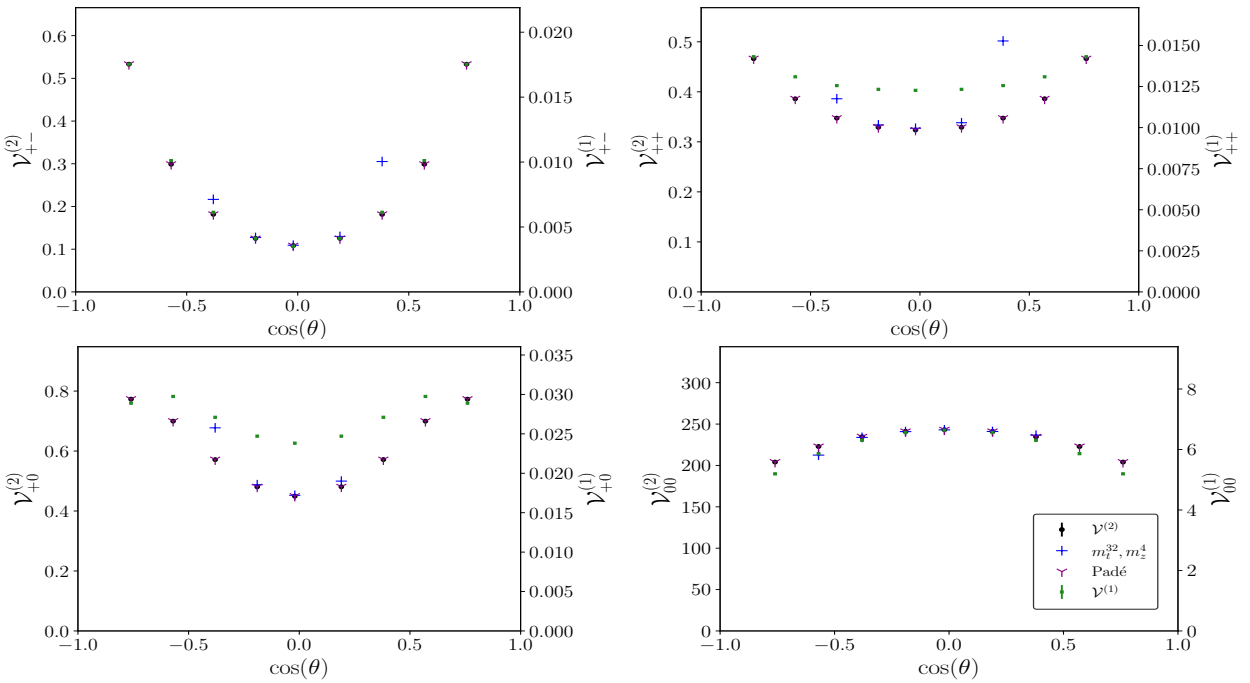

Figure 6.6: The cos(θ) dependence of 1-loop and 2-loop interferences for polarised ZZ production in gluon fusion at $\sqrt{s}/m_t = 4.703$. The small top-quark mass expansion (to order m_t^{32}) and Padé improved expansion [13] are shown for comparison. Reproduced from [6].

Similar transformation rules apply for the helicity amplitudes. This implies that conversion from the "q_{T} scheme" to Catani's original scheme requires subtraction of $\pi^2 C_A \mathcal{V}^{(1)}$ where the factor of 2 compared to Eq. 6.1.11 comes from interference (see Eq. 6.1.4) and the $i\pi\beta_0$ term is ignored since it does not contribute to the interference. This corresponds to a difference of $\sim 30\mathcal{V}^{(1)}$ which can be as large as $\mathcal{V}^{(2)}$. Consequently, the 2-loop results can show a very different qualitative behaviour compared to the 1-loop results when using Catani's original scheme as can be seen in Figs. 6.7, 6.8, 6.9, and 6.10. Note that the relative agreement between our results and the expansions is visibly better in the "q_{T} scheme" than in Catani's original scheme.

The above discussion implies that the comparisons shown above are largely scheme dependent, at least looking at relative agreement. As such, to better understand the deviation of the expansions from the exact result and estimate their impact on the physically relevant observables, real radiation contributions also need to be taken into account.

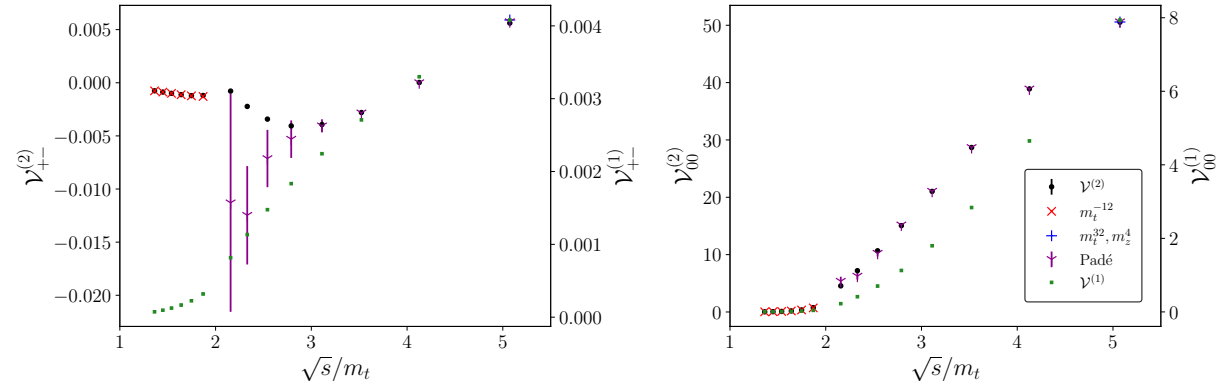

Figure 6.7: The $\sqrt{s}$ dependence of 1-loop and 2-loop interferences for polarised ZZ production in gluon fusion at $\cos(\theta) = -0.1286$. Here, the top left and bottom right panels of Fig. 6.3 are reproduced using Catani's original subtraction scheme [14]. Reproduced from [6].

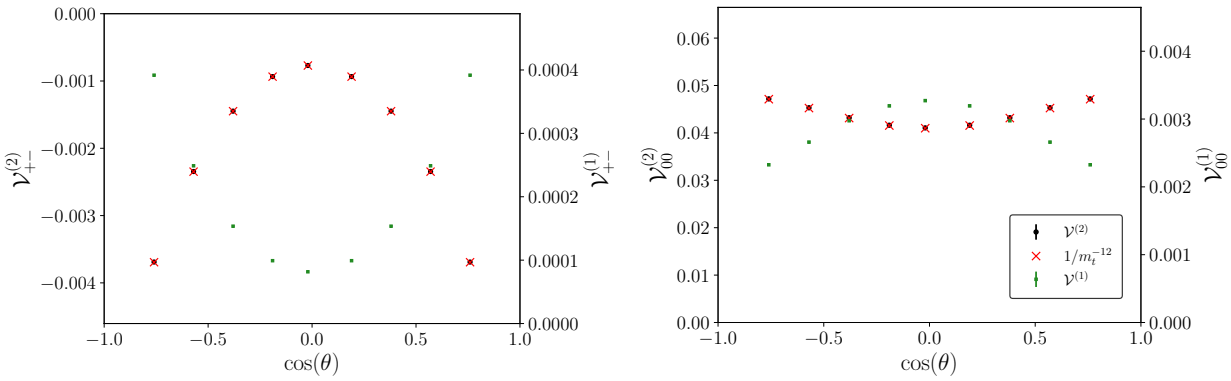

Figure 6.8: The $\cos(\theta)$ dependence of 1-loop and 2-loop interferences for polarised ZZ production in gluon fusion at $\sqrt{s}/m_t = 1.426$. The large top-quark mass expansion [13] (to order $1/m_t^{12}$) is shown for comparison. Here, the top left and bottom right panels of Fig. 6.4 are reproduced using Catani's original subtraction scheme [14]. Reproduced from [6].

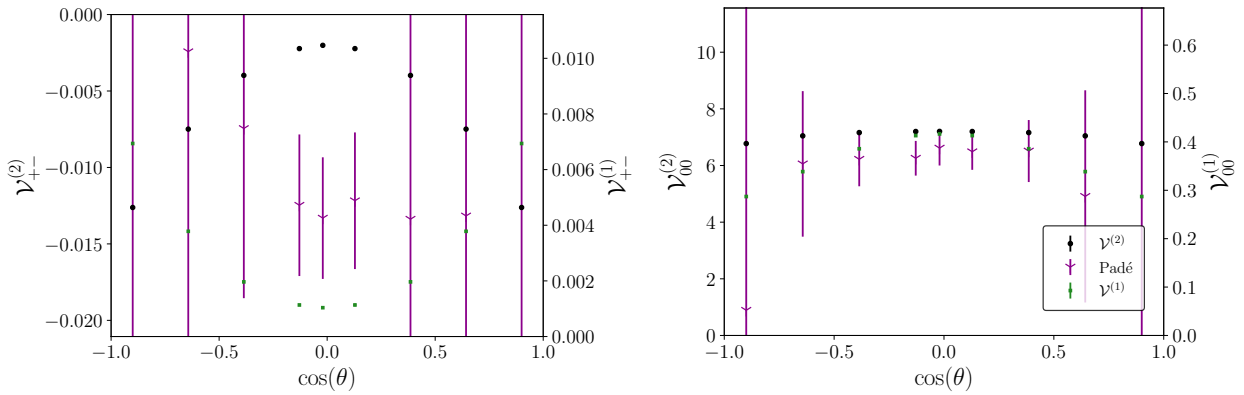

Figure 6.9: The $\cos(\theta)$ dependence of 1-loop and 2-loop interferences for polarised ZZ production in gluon fusion at $\sqrt{s}/m_t = 2.331$. The Padé improved small top-quark mass expansion [13] is shown for comparison. Here, the top left and bottom right panels of Fig. 6.5 are reproduced using Catani's original subtraction scheme [14]. Reproduced from [6].

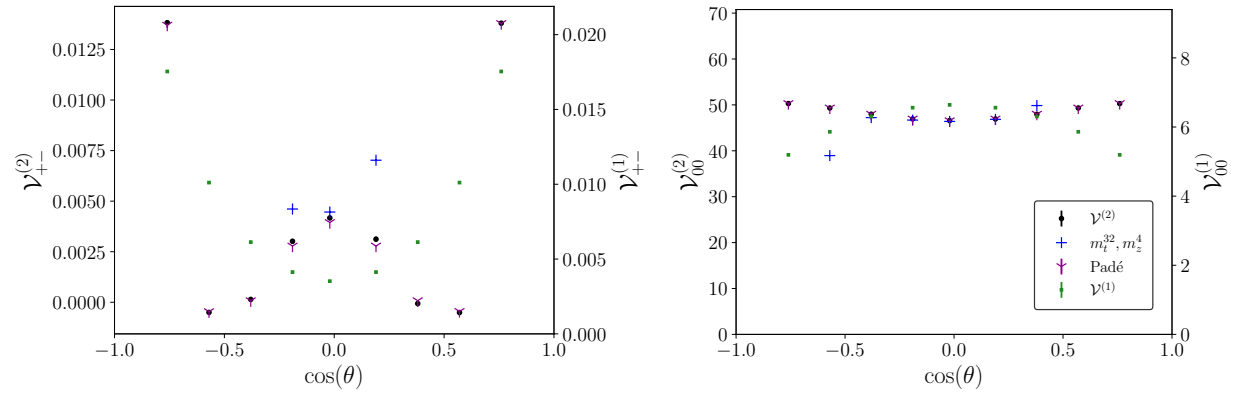

Figure 6.10: The $\cos(\theta)$ dependence of 1-loop and 2-loop interferences for polarised ZZ production in gluon fusion at $\sqrt{s}/m_t = 4.703$. The small top-quark mass expansion (to order m_t^{32}) and Padé improved expansion [13] are shown for comparison. Here, the top left and bottom right panels of Fig. 6.6 are reproduced using Catani's original subtraction scheme [14]. Reproduced from [6].

Chapter 7

Conclusions

In this work, the calculation of the 2-loop corrections to the process $gg \to ZZ$ with internal top quarks has been presented. The exact dependence on the mass of the top quark has been kept. The amplitude is represented in terms of a basis of finite master integrals which are evaluated numerically.

To perform the very challenging Integration-By-Parts reductions of the Feynman integrals, the method of syzygies is used. This is to avoid the introduction of integrals with dots in the linear systems; a new algorithm to construct such syzygies using linear algebra is employed. The resulting system of equations is then reduced using finite field techniques.

A new algorithm is presented to construct finite integrals as linear combinations with the building blocks being Feynman integrals with numerators, higher powers of propagators, dimensionally shifted integrals, and subsector integrals. The resulting parametric integrand for such integrals is integrable for $d = 4$ and admits an expansion around $d = 4$ allowing for numerical integration. This approach allows the construction of finite integrals considered more natural since the constituent integrals in the linear combinations appear in the amplitudes already. To evaluate the master integrals numerically, `pySecDec`, based on the method of sector decomposition, is employed. Choice of such finite integrals is observed to significantly improve the numerical performance.

Results are provided for our 2-loop amplitudes along with comparisons against various approximations. Good agreement is observed with the large top-mass and small top-mass expansions in the regions where the approximations are expected to perform well. In comparison to the regular small top-mass expansion, the Padé improved small top-mass expansion

is found to work over a significantly larger region of phase space, in particular for moderate energies and/or non-central scattering. The amplitudes presented in this paper provide the building block required to include the full top-quark mass effects in the next-to-leading order cross section for ZZ production in gluon fusion.

APPENDICES

APPENDIX A

Feynman Rules

A.1 QCD Lagrangian

In this appendix, the Feynman rules relevant to this calculation are provided. The QCD Lagrangian can be written as:

$$\mathcal{L} = \overline{\psi}^i (i\gamma^\mu D^{ij}_\mu - \delta^{ij} m)\psi^j - \frac{1}{4} G^{a,\mu\nu} G^a_{\mu\nu} - \frac{1}{2\xi}(\partial^\mu G^a_\mu)^2 + (\partial^\mu c^{*a}) D^{ab}_\mu c^b \,, \tag{A.1}$$

with the following definitions:

- ψ^i : Quark field with colour index i in fundamental representation
- $G^a_{\mu\nu}$: Gluon field strength tensor with colour index a in the adjoint representation
- c^a : Faddeev-Popov ghost field with colour index a in the adjoint representation
- $D^{ij}_\mu = \delta^{ij}\partial_\mu - i g_s T^{a,ij} G^a_\mu$: Covariant derivative in the fundamental representation
- $D^{ab}_\mu = \delta^{ab}\partial_\mu - g_s f^{abc} G^a_\mu$: Covariant derivative in the adjoint representation
- $T^{a,ij}$: SU(N) generator
- f^{abc} : Structure functions

Splitting the Lagrangian into free and interacting part,

$$\mathcal{L}_{free} = \overline{\psi}^i (i\gamma^\mu \partial_\mu - m)\psi^i - \frac{1}{4}(\partial^\mu G^{a,\nu} - \partial^\nu G^{a,\mu})(\partial_\mu G^a_\nu - \partial_\nu G^a_\mu) \underbrace{-\frac{1}{2\xi}(\partial^\mu G^a_\mu)(\partial^\nu G^a_\nu)}_{\text{Gauge fixing term}}$$

$$+ \underbrace{(\partial^\mu c^{*a})(\partial_\mu c^a)}_{\text{Ghost field}} \,, \tag{A.2}$$

$$\mathcal{L}_{int} = \underbrace{g_s T^{a,ij} \overline{\psi}^i \not{G}^a \psi^i}_{\text{Fermion-Gauge term}} - \underbrace{\frac{g_s}{2} f^{abc} (\partial^\mu G^{a,\nu} - \partial^\nu G^{a,\mu}) G^b_\mu G^c_\nu}_{\text{3-point Gauge interaction}} + \underbrace{\frac{g_s^2}{4} f^{abe} f^{cde} G^{a,\mu} G^{b,\nu} G^c_\mu G^d_\nu}_{\text{4-point Gauge interaction}}$$

$$- \underbrace{g_s f^{abc} (\partial^\mu c^{*a}) c^b G^c_\mu}_{\text{Gauge-Ghost interaction}} . \tag{A.3}$$

This allows us to read the QCD Feynman rules. Similar considerations give us the EW Feynman rules.

A.2 Feynman rules

The following Feynman rules are used in this work:

QCD Propagators:

1. Quark

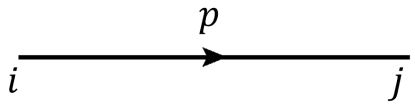

$$i \frac{\delta_{ij}}{\not{p} - m}$$

2. Gluon

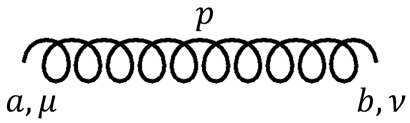

$$-i \frac{\delta^{ab}}{p^2} \left(g^{\mu\nu} + (\xi - 1) \frac{p^\mu p^\nu}{p^2} \right)$$

3. Faddev-Popov Ghost

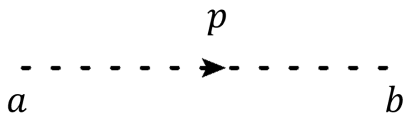

$$i \frac{\delta_{ab}}{p^2}$$

QCD Vertices:

1. Quark-gluon vertex

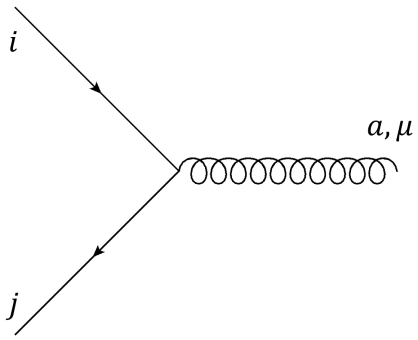

$$i\, g_s T^a_{ij} \gamma^\mu$$

2. Ghost-gluon vertex

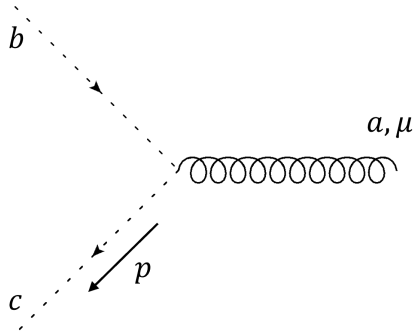

$$g_s f^{abc} p^\mu$$

3. 3-gluon vertex

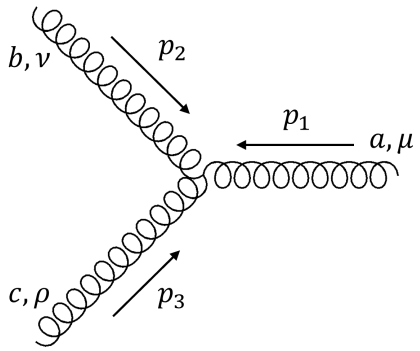

$$g_s f^{abc}\left(g^{\mu\nu}(p_1-p_2)^\rho + g^{\nu\rho}(p_2-p_3)^\mu + g^{\mu\rho}(p_3-p_1)^\nu\right)$$

4. 4-gluon vertex

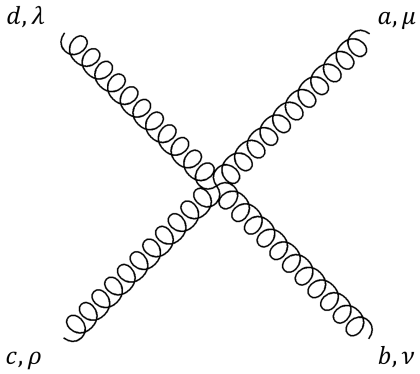

$$\begin{aligned}-ig_s^2\Big[&f^{abe}f^{cde}(g^{\mu\rho}g^{\nu\lambda}-g^{\mu\lambda}g^{\nu\rho})\\&+f^{ace}f^{bde}(g^{\mu\nu}g^{\rho\lambda}-g^{\mu\lambda}g^{\nu\rho})\\&+f^{ade}f^{bce}(g^{\mu\nu}g^{\rho\lambda}-g^{\mu\rho}g^{\nu\lambda})\Big]\end{aligned}$$

Electroweak vertices relevant for $gg \to ZZ$:

1. Higgs-top vertex

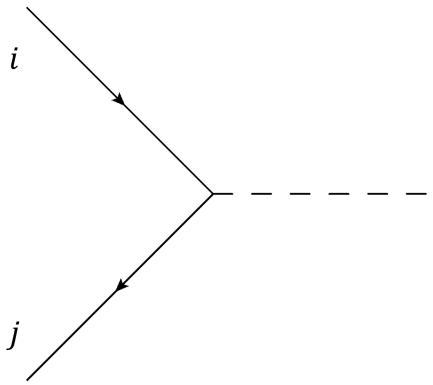

$$i\delta_{ij}\frac{m}{v}$$

2. Z-quark vertex

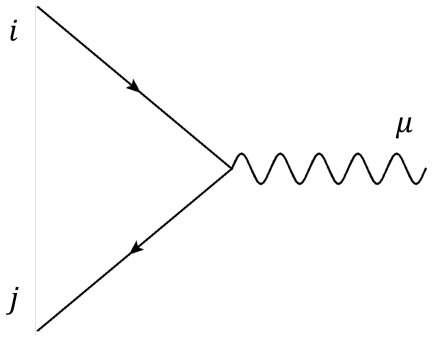

$$i\frac{e}{2\sin\theta_W\cos\theta_W}\gamma_\mu\left(v_t+a_t\gamma_5\right)$$

3. Higgs-Z vertex

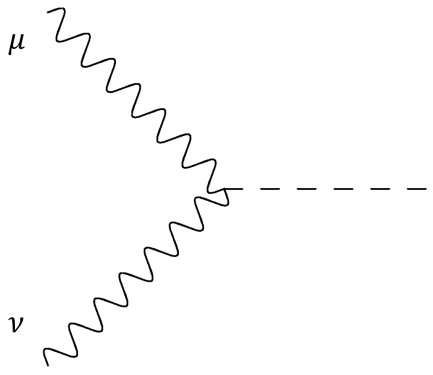

$$i\frac{e}{\sin\theta_W\cos\theta_W}m_Z\,g^{\mu\nu}$$

A.3 SU(N) algebra

For the $SU(N)$ group, the Lie generators are defined using the commutation relation

$$[T^a, T^b] = -F^a_{bc} T^c \,, \tag{A.4}$$

where the structure constants F^a_{bc} themselves satisfy the commutation relation

$$[F^a_{de}, F^b_{ef}] = -F^a_{bc} F^c_{df} \,. \tag{A.5}$$

T^a are the generators in the fundamental representation while F^a_{bc} are the generators in the adjoint representation. The generators T^a are normalised according to

$$Tr\left(T^a T^b\right) = T_F \delta^{ab} \tag{A.6}$$

where $T_F = 1/2$ by convention. The quadratic Casimir C_r invariant for the representation r is defined as

$$\mathbf{T^a T^a} = C_r \mathbb{1}_n \tag{A.7}$$

with n being the dimensions of the representation r of T^a. For the fundamental representation,

$$C_F = \frac{N^2 - 1}{2N} \,. \tag{A.8}$$

This is easily derived by taking the trace of Eq. A.7.

The generators in the adjoint representation can be written in terms of the generators in

fundamental representation as

$$F^a_{bc} = -2\,\mathrm{Tr}\left(\left[T^a, T^b\right] T^c\right)\ . \tag{A.9}$$

This can be used, along with the Fierz identity

$$T^a_{ij} T^a_{kl} = \frac{1}{2}\left(\delta_{il}\delta_{jk} - \frac{1}{N}\delta_{ij}\delta_{kl}\right)\ , \tag{A.10}$$

to write down trace relation for adjoint representation similar to Eq. A.6:

$$Tr\left(F^a F^b\right) = N\delta^{ab}\,. \tag{A.11}$$

The Casimir invariant in the adjoint representation is

$$C_A = N \tag{A.12}$$

derived simply by taking the trace of $F^a F^a = C_A \mathbb{1}_n$ with $n = N^2 - 1$ and Eq. A.11.

An explicit representation for the generators T^a can be written in terms of the Gell-Mann

matrices $T^a = \lambda_a/2$ where the Gell-Mann matrices are

$$\lambda_1 = \begin{pmatrix} 0 & 1 & 0 \\ 1 & 0 & 0 \\ 0 & 0 & 0 \end{pmatrix}, \qquad \lambda_2 = \begin{pmatrix} 0 & -i & 0 \\ i & 0 & 0 \\ 0 & 0 & 0 \end{pmatrix}, \qquad \lambda_3 = \begin{pmatrix} 1 & 0 & 0 \\ 0 & -1 & 0 \\ 0 & 0 & 0 \end{pmatrix},$$

$$\lambda_4 = \begin{pmatrix} 0 & 0 & 1 \\ 0 & 0 & 0 \\ 1 & 0 & 0 \end{pmatrix}, \qquad \lambda_5 = \begin{pmatrix} 0 & 0 & -i \\ 0 & 0 & 0 \\ i & 0 & 0 \end{pmatrix}, \qquad \lambda_6 = \begin{pmatrix} 0 & 0 & 0 \\ 0 & 0 & 1 \\ 0 & 1 & 0 \end{pmatrix},$$

$$\lambda_7 = \begin{pmatrix} 0 & 0 & 0 \\ 0 & 0 & -i \\ 0 & i & 0 \end{pmatrix}, \qquad \lambda_8 = \frac{1}{\sqrt{3}} \begin{pmatrix} 1 & 0 & 0 \\ 0 & 1 & 0 \\ 0 & 0 & -2 \end{pmatrix}.$$

The adjoint generators F^a can be written in terms of the totally antisymmetric structure constants f^{abc}

$$F^a_{bc} = -i\, f^{abc}\,. \tag{A.13}$$

Explicit values of f^{abc} for a given representation can be determined using Eq. A.9.

A.4 Colour factors of some simple diagrams

We obtain:

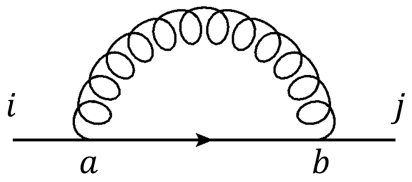

$$\mathcal{C} = T^a_{ik}\delta_{kl}T^b_{lj}\delta^{ab} = T^a_{il}T^a_{lj} = C_F\delta_{ij}$$

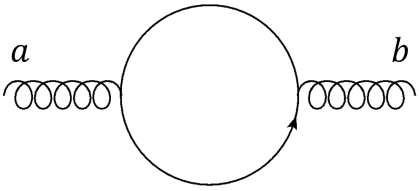

$$\mathcal{C} = T^a_{ik}\delta_{kl}T^b_{lj}\delta_{ji} = T^a_{il}T^b_{li} = Tr(T^aT^b) = T_F\delta^{ab}$$

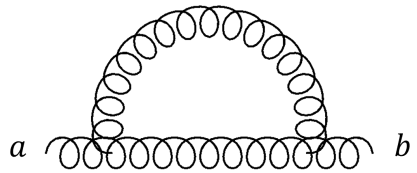

$$\mathcal{C} = f^{acd}f^{bcd} = Tr\left(F^aF^b\right) = C_A\delta^{ab}$$

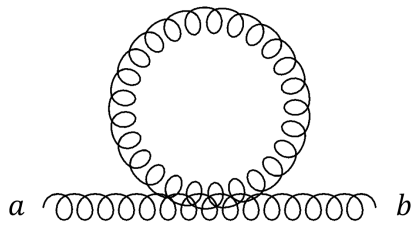

$$\mathcal{C} = f^{ace}f^{bce} = Tr\left(F^aF^b\right) = C_A\delta^{ab}$$

At 2-loops, considering diagrams with 1 closed fermion loop:

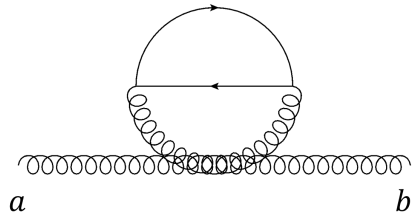

$$\mathcal{C} = f^{acd}f^{bcd} \times T_F = Tr\left(F^aF^b\right)T_F = T_FC_A\delta^{ab}$$

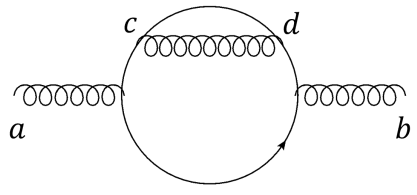

$$\begin{aligned}\mathcal{C} &= Tr\left(T^aT^cT^dT^b\right)\delta^{cd} = Tr\left(T^aT^cT^cT^b\right)\\ &= Tr\left(T^aT^b\right)C_F = T_FC_F\delta^{ab}\end{aligned}$$

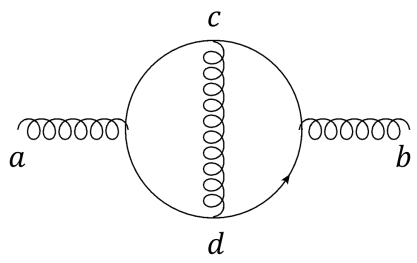

$$\mathcal{C} = Tr\left(T^a T^c T^b T^d\right)\delta^{cd} = Tr\left(T^a T^c T^b T^c\right)$$
$$= -\frac{1}{2N} T_F \delta^{ab} = T_F\left(C_F - \frac{1}{2}C_A\right)\delta^{ab}$$

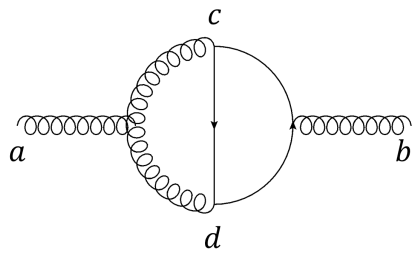

$$\mathcal{C} = Tr\left(T^b T^c T^d\right) f^{acd} = i\frac{1}{4N}\delta^{ab}$$
$$= -\,i\,T_F\left(C_F - \frac{1}{2}C_A\right)\delta^{ab}$$

APPENDIX B

Evaluation using Feynman parameters

In this Appendix, a few simple examples of direct integration using Feynman parametric representation are shown.

B.1 Massive tadpole

Consider the integral in Minkowski space

$$\int \frac{\mathrm{d}^d k}{i\pi^{d/2}} \frac{1}{k^2 - m^2 + i0} \,. \tag{B.1}$$

This integrand is dependent on $k^2 = k_0^2 - k_1^2 - k_2^2 - k_3^2$. To perform the integration, Wick rotation (Fig. 7.1) can be used to transform Minkowski space into Euclidean space using $k_0 \to ik_{0,E}$ with spatial components remaining unchanged. Thus, the integral over k_0 can be replaced by the integral over $k_{0,E}$ as

$$\int_{-\infty}^{\infty} \mathrm{d}k_0 \, F(k_0) \to i \int_{-\infty}^{\infty} \mathrm{d}k_{0,E} \, F(ik_{0,E}) \,. \tag{B.2}$$

This is easy to see using Cauchy's theorem; the integrals over the arcs in Fig. 7.1 can be shown to vanish near infinity leaving the above relation. Note that the $i0$ prescription is essential to ensure that the poles lie outside the integration contour (see Fig. 7.1). The integral over loop momentum then becomes

$$\int \frac{\mathrm{d}^d k}{i\pi^{d/2}} \frac{1}{k^2 - m^2 + i0} = i \int \frac{\mathrm{d}^d k_E}{i\pi^{d/2}} \frac{1}{-k_E^2 - m^2 + i0} \tag{B.3}$$

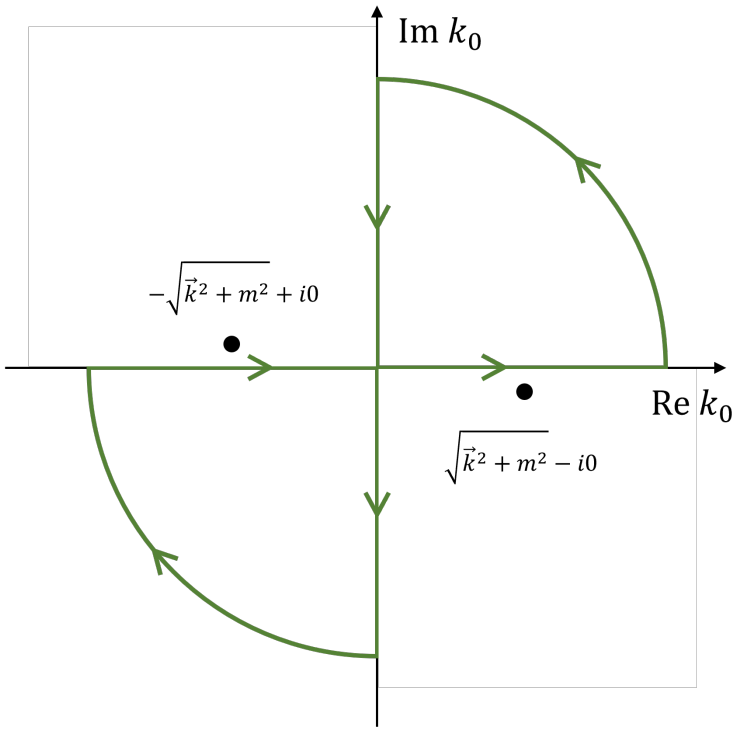

Figure 7.1: The integration contour to perform Wick rotation. Note that the poles lie outside the contour.

where $k_E^2 = k_{0,E}^2 + k_{1,E}^2 + k_{2,E}^2 + k_{3,E}^2$. The d dimensional Euclidean integral above can be written in spherical coordinates using

$$\mathrm{d}^d k_E = k_E^{d-1} \mathrm{d}k_E \, \mathrm{d}\Omega_d \,. \tag{B.4}$$

Integral over the d dimensional solid angle gives

$$\int \mathrm{d}\Omega_d = \left(\prod_{i=1}^{d-2} \int_0^{\pi} \mathrm{d}\theta_i \sin^{d-1-i}\theta_i \right) \int_0^{2\pi} \mathrm{d}\theta_{d-1} = \frac{2\pi^{d/2}}{\Gamma(d/2)} \,. \tag{B.5}$$

The remaining integral in k_E is straightforward:

$$\int_0^{\infty} k_E^{d-1} \mathrm{d}k_E \frac{1}{k_E^2 + m^2} = \frac{1}{2} m^{d-2} \, \Gamma\left(1 - \frac{d}{2}\right) \Gamma\left(\frac{d}{2}\right) \,. \tag{B.6}$$

Combining the two, the integral gives

$$\int \frac{\mathrm{d}^d k}{i\pi^{d/2}} \frac{1}{k^2 - m^2 + i0} = -m^{d-2}\,\Gamma\left(1 - \frac{d}{2}\right). \tag{B.7}$$

Note that the integral converges only for $\mathrm{Re}\,(d) < 2$. Using $d = 4-2\epsilon$ and expanding around $\epsilon = 0$,

$$\int \frac{\mathrm{d}^d k}{i\pi^{d/2}} \frac{1}{k^2 - m^2 + i0} = \frac{1}{\epsilon} m^2 + m^2(1 - \gamma_E - \log m^2) + O(\epsilon) \tag{B.8}$$

where γ_E is the Euler-Mascheroni constant. It is common to remove these factors of γ_E appearing in ϵ expansions of Feynman integrals by multiplying the integrals with $e^{\epsilon\gamma_E}$. Note that as expected, the divergence shows up as the $1/\epsilon$ pole.

Evaluating the tadpole integral with the propagator raised to power 3 instead gives

$$\int \frac{\mathrm{d}^d k}{i\pi^{d/2}} \frac{1}{(k^2 - m^2 + i0)^3} = -\frac{1}{8}(d-4)(d-2)m^{d-6}\Gamma\left(1 - \frac{d}{2}\right) \tag{B.9}$$

which when expanded gives

$$\int \frac{\mathrm{d}^d k}{i\pi^{d/2}} \frac{1}{(k^2 - m^2 + i0)^3} = -\frac{1}{2m^2} + \frac{1}{2m^2}(\gamma_E + \log m^2)\epsilon + O(\epsilon^2)\,. \tag{B.10}$$

Simple power counting shows that this integral should be finite in $d = 4$ as seen above.

B.2 Massless bubble

The massless bubble integral from Fig. 3.3 (without cuts) can be written as

$$I = e^{\epsilon\gamma_E} \int \frac{\mathrm{d}^d k}{i\pi^{d/2}} \frac{1}{(k^2 + i0)((k-p)^2 + i0)}\,. \tag{B.11}$$

Applying Feynman's trick, this becomes

$$I = \int_0^1 \mathrm{d}x \int \frac{\mathrm{d}^d k}{i\pi^{d/2}} \frac{e^{\epsilon\gamma_E}\Gamma(2)}{((1-x)k^2 + x(k-p))^2} = \int_0^1 \mathrm{d}x \int \frac{\mathrm{d}^d k}{i\pi^{d/2}} \frac{e^{\epsilon\gamma_E}\Gamma(2)}{(k^2 + 2xk.p + xp^2 + i0)^2}\,. \tag{B.12}$$

Completing the square $(k+xp)^2$ gives

$$I = \int_0^1 \mathrm{d}x \int \frac{\mathrm{d}^d k}{i\pi^{d/2}} \frac{e^{\epsilon\gamma_E}\Gamma(2)}{((k+xp)^2 - (\Delta - i0))^2} = \int_0^1 \mathrm{d}x \int \frac{\mathrm{d}^d k}{i\pi^{d/2}} \frac{e^{\epsilon\gamma_E}\Gamma(2)}{(k^2 - \Delta + i0))^2} \tag{B.13}$$

where $\Delta = -p^2 x(1-x)$. Integrating over the loop momentum, we get

$$\begin{aligned} I =& e^{\epsilon\gamma_E}\Gamma(2)\Gamma(2-d/2) \int_0^1 \mathrm{d}x \frac{1}{(\Delta - i0)^{\frac{4-d}{2}}} \\ =& e^{\epsilon\gamma_E}\Gamma(2)\Gamma(2-d/2) \int_0^1 \mathrm{d}x \frac{1}{(-p^2 - i0)^{\frac{4-d}{2}} (x - x^2)^{\frac{4-d}{2}}}\,. \end{aligned} \tag{B.14}$$

The integral over x converges for $Re(d) > 2$. Integrating, and expanding in ϵ, we get

$$I = \frac{1}{\epsilon} + \big(2 - \log(-p^2 - i0)\big) + O(\epsilon)\,. \tag{B.15}$$

APPENDIX C

Dirac algebra and γ^5 schemes

C.1 Gamma matrices and identities

Fermions in a free theory satisfy the Dirac equation

$$(i\gamma^\mu \partial_\mu - m)\,\psi = 0\,. \tag{C.1}$$

γ^μ are referred to as the Dirac or Gamma matrices. They generate a Clifford algebra and satisfy the following anti-commutation relations

$$\{\gamma^\mu, \gamma^\nu\}_+ = 2\eta^{\mu\nu}\mathbb{1}_d\,. \tag{C.2}$$

where $\mathbb{1}_d$ is the d-dimensional identity matrix and $\eta^{\mu\nu}$ is the metric tensor for Minkowski space. An explicit representation can be written for the Gamma matrices in 4 dimensions in the Dirac representation

$$\gamma^0 = \begin{pmatrix} \mathbb{1}_2 & 0 \\ 0 & \mathbb{1}_2 \end{pmatrix}, \tag{C.3}$$

$$\gamma^i = \begin{pmatrix} 0 & \sigma^i \\ -\sigma_i & 0 \end{pmatrix}, \tag{C.4}$$

for $i = 1, 2, 3$. Here σ^i are the Pauli matrices:

$$\sigma^1 = \begin{pmatrix} 0 & 1 \\ 1 & 0 \end{pmatrix},$$

$$\sigma^2 = \begin{pmatrix} 0 & -i \\ i & 0 \end{pmatrix},$$

$$\sigma^3 = \begin{pmatrix} 1 & 0 \\ 0 & -1 \end{pmatrix}. \tag{C.5}$$

The Gamma matrices satisfy the following identities in d-dimensions following from the anti-commutation rule in Eq. C.2

$$\gamma^\mu \gamma_\mu = d\, \mathbb{1}_d\,, \tag{C.6}$$

$$\gamma^\mu \gamma^\nu \gamma_\mu = (2-d)\gamma^\nu\,, \tag{C.7}$$

$$\gamma^\mu \gamma^\nu \gamma_\rho \gamma_\mu = 2\,\eta^{\nu\rho} - (2-d)\gamma^\rho \gamma^\nu\,, \tag{C.8}$$

as well as the following trace identities

$$Tr(\gamma^\mu) = 0\,, \tag{C.9}$$

$$Tr(\gamma^\mu \gamma^\nu) = 4\eta^{\mu\nu}\,, \tag{C.10}$$

$$Tr(\gamma^{\mu_1} ... \gamma^{\mu_m}) = Tr(\gamma^{\mu_m} ... \gamma^{\mu_1})\,, \tag{C.11}$$

$$Tr(\gamma^{\mu_1} ... \gamma^{\mu_{2m+1}}) = 0\,, \tag{C.12}$$

$$Tr(\gamma^{\mu_1} ... \gamma^{\mu_{2m}}) = 4 \sum_{perms} \mathbf{Sgn}(\sigma)\, g_{\mu_{i_1}\mu_{j_1}} ... g_{\mu_{i_n}\mu_{j_n}} \tag{C.13}$$

with $1 = i_1 < ... < i_n$ and $i_k < j_k$. σ refers to permutation of the indices $i_1, j_1, ..., i_n j_n$ and $\mathbf{Sgn}(\sigma)$ is the sign of the permutation.

C.2 γ^5 in d dimensions

In $d = 4$ dimensions, we can define a fifth Gamma matrix γ^5 as

$$\gamma^5 = i\gamma^0\gamma^1\gamma^2\gamma^3 \,. \tag{C.14}$$

An explicit representation in the Dirac basis is given by

$$\gamma^5 = \begin{pmatrix} 0 & \mathbb{1}_2 \\ \mathbb{1}_2 & 0 \end{pmatrix} . \tag{C.15}$$

γ^5 can also be defined using the totally anti-symmetric Levi-Civita tensor $\epsilon^{\mu\nu\rho\sigma}$

$$\gamma^5 = \frac{i}{4!}\epsilon^{\mu\nu\rho\sigma}\gamma_\mu\gamma_\nu\gamma_\rho\gamma_\sigma \,, \tag{C.16}$$

which leads to the trace identity

$$Tr(\gamma^\mu\gamma^\nu\gamma^\rho\gamma^\sigma) = -4i\epsilon^{\mu\nu\rho\sigma} \tag{C.17}$$

in $d = 4$. An anti-commutation relation follows from Eq. C.2 and C.14,

$$\{\gamma^\mu, \gamma^5\}_+ = 0 \,, \tag{C.18}$$

as well as the identity

$$(\gamma^5)^2 = \mathbb{1}_4 \,. \tag{C.19}$$

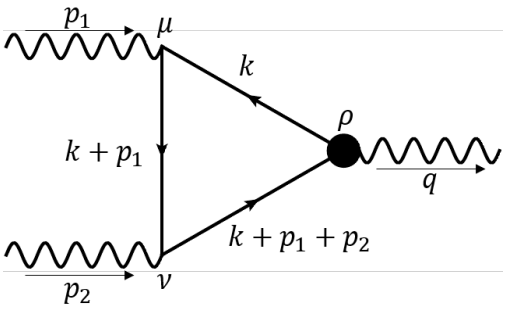

Figure 7.2: The triangle anomaly graph. Here the dark blob vertex represents the axial-vector coupling.

Since the anti-symmetric tensor $\epsilon^{\mu\nu\rho\sigma}$ is a purely 4-dimensional object, γ^5 and, as a consequence, the trace identity in Eq. C.17 are not defined for $d \neq 4$. Dimensional regularisation is one of the most popular methods to perform higher-order calculations. It preserves gauge invariance which makes it highly attractive and simpler to implement. However, for processes involving parity violating interactions, the naive regularisation scheme with the 4-dimensional γ^5 cannot be used.

There are several methods to "extend" the trace relation of Eq. C.17 to d dimensions. For a consistent definition of γ^5 in d-dimensions, both the cyclicity of the trace and Eq. C.18 cannot be preserved [153, 154]. This can be seen most easily through the triangle anomaly graph in Fig. 7.2. The sum of the above diagram and its crossed diagram, where the incoming legs with momenta p_1, p_2 are exchanged, can be written as

$$I^{\mu\nu\rho} = \int \frac{\mathrm{d}^d k}{i\pi^{d/2}} \frac{Tr(\gamma^\rho \gamma^5 \not{k} \gamma^\mu (\not{k} + \not{p}_1) \gamma^\nu (\not{k} + \not{p}_1 + \not{p}_2))}{k^2 \, (k+p_1)^2 \, (k+p_1+p_2)^2} + [p_1 \leftrightarrow p_2, \mu \leftrightarrow \nu] \, . \tag{C.20}$$

It is straightforward to show that assuming cyclicity of trace along with the anti-commuting γ^5 (Eq. C.18) implies that the above integral, vanishes. This is of course incorrect and demonstrates the erroneous approach to evaluating the anomaly. To appropriately deal with this issue, there are two major classes of schemes:

1. Schemes where the anti-commutation relation in Eq. C.18 is violated in favour of

preserving cyclicity of trace e.g. the HVBM scheme [153, 214–216] and the Larin scheme [350, 351].

2. Schemes where the anti-commutation relation in Eq. C.18 is preserved while cyclicity of the trace is violated [211–213]

C.3 Anti-commuting γ^5 scheme

In Kreimer's anti-commuting γ^5 scheme [211–213], the cyclicity of traces is not preserved. This also implies that the traces need to be read from a specific point and the result in general depends on the "reading point", which is chosen to be the axial-vector vertex so as to conserve vector currents. All diagrams, and their traces, must be read from the same reading point and in case of multiple γ^5's, the traces need to be symmetrised.

Assuming that trace is not cyclic, the triangle anomaly above can be calculated using the following trace identities concerning γ^5 in addition to the trace identities in the previous section for the "regular" γ-matrices:

$$Tr(\gamma^5) = 0\,, \tag{C.21}$$

$$Tr(\gamma^{\mu_1}...\gamma^{\mu_{2m+1}}\gamma^5) = 0\,, \tag{C.22}$$

$$Tr(\gamma^{\mu}\gamma^{\nu}\gamma^5) = 0\,, \tag{C.23}$$

$$Tr(\gamma^{\mu_1}...\gamma^{\mu_4}\gamma^5) = 4i\epsilon^{\mu_1\mu_2\mu_3\mu_4}\,, \tag{C.24}$$

$$Tr(\gamma^{\mu_1}...\gamma^{\mu_m}\gamma^5) = Tr(\gamma^{\mu_m}...\gamma^{\mu_1}\gamma^5)\,, \tag{C.25}$$

$$Tr(\gamma^{\mu_1}...\gamma^{\mu_{2m}}\gamma^5) = 4i\sum_{\sigma}\mathbf{Sgn}(\sigma)\epsilon^{\mu_{i_{n+1}}\mu_{i_{n+2}}\mu_{j_{n+1}}\mu_{j_{n+2}}}\,g_{\mu_{i_1}\mu_{j_1}}...g_{\mu_{i_{n+2}}\mu_{j_{n+2}}} \tag{C.26}$$

with $1 = i_1 < ... < i_{n+2}$ and $i_k < j_k$. σ refers to permutation of the indices $i_1, j_1, ..., i_{n+2}j_{n+2}$ and $\mathbf{Sgn}(\sigma)$ is the sign of the permutation. Note that any contractions with the ϵ-tensor are treated in a 4-dimensional subspace of the d-dimensional space since the ϵ-tensor is a 4-dimensional object.

Using the above trace rules, along with the requirement of reading traces from the same

vertex in each diagram, the correct result for the anomalous triangle diagram can be recovered.

APPENDIX D

UV renormalisation

D.1 Renormalised Lagrangian

The bare Lagrangian can be written as

$$\begin{aligned}\mathcal{L}_{bare} = &\overline{\psi}^i_0(i\gamma^\mu\partial_\mu - m_0)\psi^i_0 - \frac{1}{4}(\partial^\mu G^{a,\nu}_0 - \partial^\nu G^{a,\mu}_0)(\partial_\mu G^a_{0,\nu} - \partial_\nu G^a_{0,\mu}) - \frac{1}{2\xi}(\partial^\mu G^a_{\mu,0})(\partial^\nu G^a_{\nu,0}) \\ &+ (\partial^\mu c^{*a}_0)(\partial_\mu c^a_0) + g_{S,0}T^{a,ij}\overline{\psi}^i_0\gamma^\mu G^a_{0,\mu}\psi^i_0 - \frac{g_{S,0}}{2}f^{abc}(\partial^\mu G^{a,\nu}_0 - \partial^\nu G^{a,\mu}_0)G^b_{0,\mu}G^c_{0,\nu} \\ &+ \frac{g^2_{S,0}}{4}f^{abe}f^{cde}G^{a,\mu}_0 G^{b,\nu}_0 G^c_{0,\mu}G^d_{0,\nu} - g_{S,0}f^{abc}(\partial^\mu c^{*a}_0)c^b_0 G^c_{0,\mu} \end{aligned} \tag{D.1}$$

where all the bare parameters and fields are denoted by the subscript "0" e.g. $G^a_{0,\mu}$. The bare parameters can be replaced by the *renormalised* parameters:

$$\begin{aligned}\psi_0 &= \sqrt{Z_\psi}\,\psi_R \\ G^{a,\mu}_0 &= \sqrt{Z_G}\,G^{a,\mu}_R \\ c^a_0 &= \sqrt{Z_c}\,c^a_R \\ m_0 &= Z_m m_R \\ g_{S,0} &= Z_g\, g_{S,R} \\ \alpha_{S,0} &= Z_{\alpha_S}\alpha_{S,R} \\ \xi_0 &= Z_\xi \xi \end{aligned} \tag{D.2}$$

where Z_ψ etc. are referred to as renormalisation constants. In what follows, the R subscript has been dropped for the sake of brevity and any quantity without the subscript 0 is understood to be renormalised.

The renormalisation constants can be expanded order-by-order in $\alpha_S/(2\pi)$ e.g.

$$Z_\psi = 1 + \frac{\alpha_S}{2\pi}\,\delta Z_\psi + O(\alpha_S^2) \tag{D.3}$$

keeping terms only up to $O(\alpha_S)$. For brevity, it is useful to define

$$\begin{aligned}
&\delta_\psi = \alpha_S/(2\pi)\,\delta Z_\psi\,, \quad \delta_G = \alpha_S/(2\pi)\,\delta Z_G\,, \quad \delta_c = \alpha_S/(2\pi)\,\delta Z_c \\
&\delta_m = \alpha_S/(2\pi)\,\delta Z_m\,, \quad \delta_g = \alpha_S/(2\pi)\,\delta Z_g\,, \quad \delta_{\alpha_S} = \alpha_S/(2\pi)\,\delta Z_{\alpha_S}\,.
\end{aligned} \tag{D.4}$$

Replacing the bare parameters in the Lagrangian with the renormalised parameters and expanding the renormalisation constants gives

$$\mathcal{L} = \mathcal{L}_{ren} + \mathcal{L}_{ct} \tag{D.5}$$

where

$$\begin{aligned}
\mathcal{L}_{ren} =& \overline{\psi}^i(i\gamma^\mu\partial_\mu - m)\psi^i - \frac{1}{4}(\partial^\mu G^{a,\nu} - \partial^\nu G^{a,\mu})(\partial_\mu G^a_\nu - \partial_\nu G^a_\mu) - \frac{1}{2\xi}(\partial^\mu G^a_\mu)(\partial^\nu G^a_\nu) \\
&+ (\partial^\mu c^{*a})(\partial_\mu c^a) + g_S T^{a,ij}\overline{\psi}^i\gamma^\mu G^a_\mu\psi^i - \frac{g_S}{2}f^{abc}(\partial^\mu G^{a,\nu} - \partial^\nu G^{a,\mu})G^b_\mu G^c_\nu \\
&+ \frac{g_S^2}{4}f^{abe}f^{cde}G^{a,\mu}G^{b,\nu}G^c_\mu G^d_\nu - g_S f^{abc}(\partial^\mu c^{*a})c^b G^c_\mu\,, \\
\mathcal{L}_{ct} =& \overline{\psi}^i(i(\delta_\psi)\gamma^\mu\partial_\mu - (\delta_\psi + \delta_m)m)\psi^i - \frac{1}{4}\delta_G\,(\partial^\mu G^{a,\nu} - \partial^\nu G^{a,\mu})(\partial_\mu G^a_\nu - \partial_\nu G^a_\mu) \\
&- \frac{1}{2\xi}\delta_G\,(\partial^\mu G^a_\mu)(\partial^\nu G^a_\nu) + \delta_c(\partial^\mu c^{*a})(\partial_\mu c^a) + (\delta_\psi + \delta_g + 1/2\delta_G)g_S T^{a,ij}\overline{\psi}^i\gamma^\mu G^a_\mu\psi^i \\
&- (\delta_g + 3/2\delta_G)\frac{g_S}{2}f^{abc}(\partial^\mu G^{a,\nu} - \partial^\nu G^{a,\mu})G^b_\mu G^c_\nu + 2(\delta_g + \delta_G)\frac{g_S^2}{4}f^{abe}f^{cde}G^{a,\mu}G^{b,\nu}G^c_\mu G^d_\nu \\
&- (\delta_g + \delta_c + 1/2\delta_G)\,g_S f^{abc}(\partial^\mu c^{*a})c^b G^c_\mu\,.
\end{aligned} \tag{D.6}$$

D.2 1-loop counterterms

From the above Lagrangian, counterterm diagrams can be written as follows:

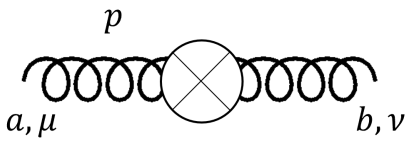

$$i\delta_G\delta^{ab}\left(p^\mu p^\nu - g^{\mu\nu}p^2\right)$$

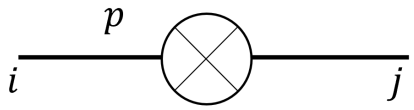

$$i\delta_{ij}\left(\delta_\psi \not{p} - (\delta_\psi + \delta_m)m\right)$$

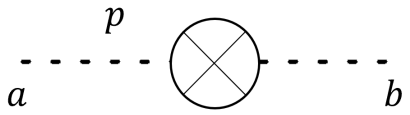

$$i\delta_c\delta^{ab}p^2$$

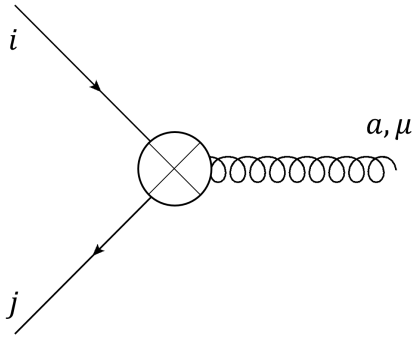

$$i(\delta_\psi + \delta_g + \frac{1}{2}\delta_G)\, g_S T^a_{ij}\gamma_\mu$$

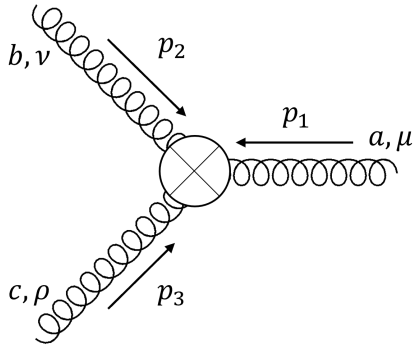

$$(\delta_g + \frac{3}{2}\delta_G)\, g_s f^{abc}\Big[g^{\mu\nu}(p_1 - p_2)^\rho + g^{\nu\rho}(p_2 - p_3)^\mu + g^{\mu\rho}(p_3 - p_1)^\nu\Big]$$

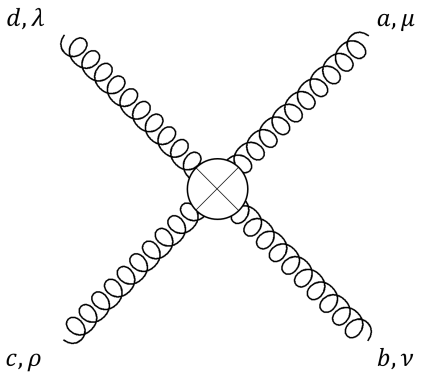

$$-i(2\delta_g + 2\delta_G)\, g_s^2 \Big[f^{abe} f^{cde} (g^{\mu\rho} g^{\nu\lambda} - g^{\mu\lambda} g^{\nu\rho}) + f^{ace} f^{bde} (g^{\mu\nu} g^{\rho\lambda} - g^{\mu\lambda} g^{\nu\rho}) + f^{ade} f^{bce} (g^{\mu\nu} g^{\rho\lambda} - g^{\mu\rho} g^{\nu\lambda}) \Big]$$

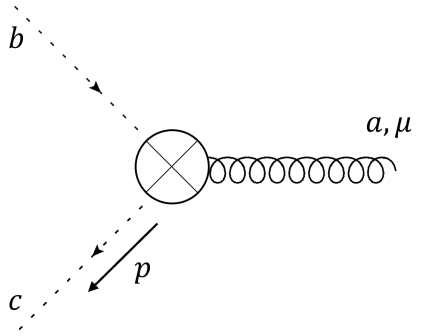

$$(\delta_c + \delta_g + \frac{1}{2}\delta_G)\, g_s f^{abc} p^\mu \gamma_\mu$$

The counterterms can be determined by requiring that the divergences in the 1-loop contributions are cancelled by the counterterm vertices. E.g. for gluon field renormalisation, all the diagrams contributing to the 2-point function at 1-loop and the 1-loop counterterm must sum up to be finite as shown in Fig. 7.3. Note that in principle, any arbitrary finite term can be added to the counterterm without affecting the divergent piece. This allows a lot of freedom in choosing the exact form of the counterterms. There are multiple renormalisation "schemes" that differ in the choice of these finite terms. The most popular is the so-called modified minimal subtraction ($\overline{MS}$) scheme. In this scheme, an additional $-\gamma_E + \ln 4\pi$ is added to the counterterm.

Consider the 1-loop corrections to the gluon propagator in Fig. 7.3. The sum of all the

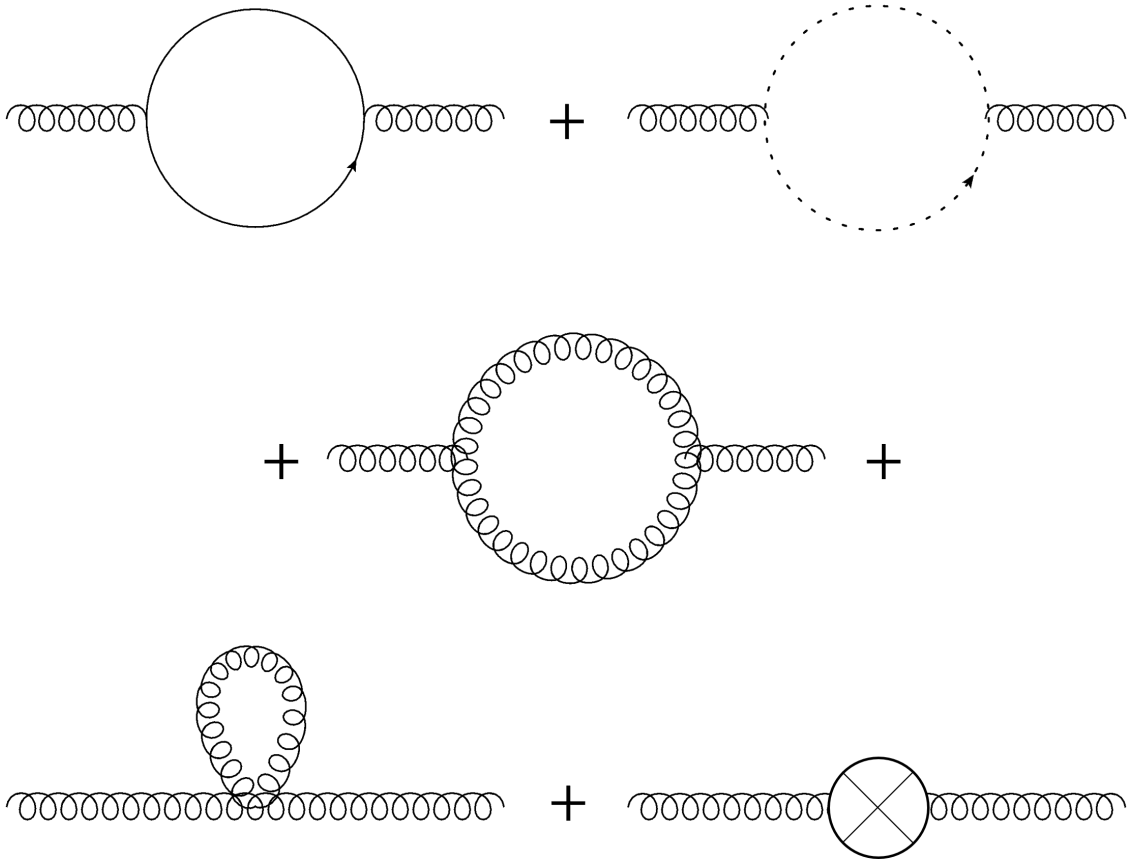

Figure 7.3: All the diagrams contributing to 1-loop correction to the gluon propagator, including the counterterm diagram. Requiring that the sum is finite allows the calculation of the counterterm δ_G.

contributions to the gluon self-energy can be written as

$$\Sigma(p) = n_f \Sigma_f(p) + n_h \Sigma_h(p) + \Sigma_c(p) + \Sigma_G(p) + \Sigma_{ct}(p) \tag{D.7}$$

where $\Sigma_f(p)$ is the contribution from light quarks, $\Sigma_h(p)$ from heavy quarks, $\Sigma_c(p)$ from ghost fields, $\Sigma_G(p)$ from gluon self-interactions, and $\Sigma_{ct}(p)$ from the counterterm. For example, the contribution from massless quarks can be written as

$$\Sigma_f(p) = \frac{1}{2}(4\pi\mu^2)^{2-d/2} \frac{g_s^2}{16\pi^2} \delta^{ab} \int \frac{\mathrm{d}^d k}{(i\pi^{d/2})} \frac{Tr\left(\not{k}\gamma^\mu(\not{k}+\not{p})\gamma^\nu\right)}{k^2(k+p)^2}\,, \tag{D.8}$$

with a factor of μ^{4-d} added to render it dimensionless. The integral above is straightforward to evaluate and yields

$$\Sigma_f(p) = \frac{\alpha_S}{6\pi}\delta^{ab}(p^\mu p^\nu - g^{\mu\nu}p^2)\left(\frac{1}{\epsilon} - \gamma_E + \ln 4\pi + O(\epsilon^0)\right) . \tag{D.9}$$

Rest of the integrals can be evaluated similarly yielding, for the counterterm,

$$\delta_G = \left[C_A\left(\frac{13-3\xi}{12}\right) - \frac{2n_f + 2n_h}{3}T_F\right]\left(\frac{1}{\epsilon} - \gamma_E + \ln 4\pi\right) - \frac{2}{3}T_F\sum_i^{n_h}\ln\frac{\mu_R^2}{m_i^2} \tag{D.10}$$

with the heavy quark diagrams subtracted at zero momentum. Note that the longitudinal part of the gluon propagator does not receive any corrections. Ghost propagator counterterm can be calculated similarly:

$$\delta_c = -C_A\left(\frac{3-\xi}{8}\right)\left(\frac{1}{\epsilon} - \gamma_E + \ln 4\pi\right) . \tag{D.11}$$

Above counterterms were calculated using the $\overline{MS}$ scheme. For massive quarks, the on-shell renormalisation scheme is commonly used. In this scheme, the renormalisation conditions are set as

$$\begin{aligned}\delta_\psi =& \left[- \frac{\mathrm{d}}{\mathrm{d}\not{p}}\Sigma(p)\right]_{\not{p}=m_p} \\ \delta_m =& \frac{1}{m_p}\Sigma(m_p) .\end{aligned} \tag{D.12}$$

Evaluating $\Sigma(p)$ from the 1-loop quark self-energy diagram yields

$$\delta_\psi = \delta_m = -\frac{1}{2}C_F\left(\frac{3}{\epsilon} + 4 + 3\ln\left(4\pi e^{-\gamma_E}\frac{\mu_R^2}{m_p^2}\right)\right) . \tag{D.13}$$

With $\delta_\psi, \delta_G, \delta_c, \delta_m$ known, δ_g can be calculated using the 3-point gluon vertex. In Feyn-

man gauge

$$\delta_\psi + \delta_g + \frac{1}{2}\delta_G = -\frac{1}{2}(C_F + C_A)\left(\frac{1}{\epsilon} - \gamma_E + \ln 4\pi\right) . \tag{D.14}$$

In the $\overline{MS}$ scheme, δ_g is

$$\delta_g = -\left(\frac{11C_A - 4(n_f + n_h)T_F}{12}\right)\left(\frac{1}{\epsilon} - \gamma_E + \ln 4\pi\right) + \frac{1}{3}T_F \sum_i^{n_h} \ln\frac{\mu_R^2}{m_i^2} . \tag{D.15}$$

D.3 QCD β-function

From the above result, considering only the top-quark as the heavy particle,

$$Z_{\alpha_S} = 1 + 2\delta_g = 1 + \frac{\alpha_S}{2\pi}\left[-\beta_0\left(\frac{1}{\epsilon} - \gamma_E + \ln 4\pi\right) + \frac{1}{\epsilon}\left(\frac{2}{3}T_F + \epsilon \ln\left(4\pi e^{-\gamma_E}\frac{\mu_R^2}{m_t^2}\right)\right)\right] \tag{D.16}$$

where

$$\beta_0 = \frac{11C_A - 4n_f T_F}{6} \tag{D.17}$$

is the beta function at 1-loop.

APPENDIX E

List of denominators

In this appendix, the denominator factors which occur in the coefficients of the master integrals in the helicity amplitudes for $gg \to ZZ$ are listed. In the calculation, the masses of the top quark and the Z boson, m_t and m_Z, have been set to $m_t = 1$ and $(m_z/m_t)^2 = 5/18$. The exact set of denominator factors depends on the choice of master integrals. In this work, the basis is chosen such that the dependence on the space-time dimension d factorises from that of the kinematic invariants $s = (p_1 + p_2)^2$ and $t = (p_1 - p_3)^2$.

We find 9 d-dependent denominators

$$d-5,\ d-4,\ d-3,\ d-2,\ d,\ 2d-7,\ 3d-10,\ 3d-8,\ 5d+52$$

and the 48 d-independent denominators sorted according to the polynomial ordering used for partial fractioning.

8 polynomials dependent only on s:

$$s, \quad -4+s, \quad -5+9\,s, \quad -10+9\,s, \quad -5+18\,s, \quad 134+9\,s, \quad -335+324\,s,$$
$$90-245\,s+324\,s^2\,.$$

6 polynomials dependent only on t:

$$t, \quad -4+t, \quad 10+13\,t, \quad -5+18\,t, \quad 5+18\,t, \quad 5+31\,t\,.$$

9 degree 1 polynomials in s, t:

$$-5+6\,s+6\,t, \quad -5+9\,s+9\,t, \quad 31+9\,s+9\,t, \quad -5+9\,s+18\,t, \quad -5-18\,s+18\,t,$$
$$-5+18\,s+18\,t, \quad -5+36\,s+18\,t, \quad -155+117\,s+117\,t, \quad -200+279\,s+279\,t.$$

13 degree 2 polynomials in s, t:

$$25-90\,t+324\,s\,t, \quad 25+180\,s-90\,t+558\,s\,t, \quad 5\,s-5\,t+18\,s\,t+18\,t^2$$
$$25-135\,t+162\,s\,t+162\,t^2, \quad 25-180\,t+324\,s\,t+324\,t^2,$$
$$25-180\,t+648\,s\,t+324\,t^2, \quad 25-270\,s-90\,t+324\,s^2+324\,s\,t,$$
$$25-580\,s-90\,t+558\,s^2+558\,s\,t, \quad 25+180\,s-180\,t-324\,s^2+324\,t^2,$$
$$25-1296\,s-180\,t+324\,s\,t+324\,t^2, \quad 25-25\,s-180\,t+90\,s^2+90\,s\,t+324\,t^2$$
$$25-155\,s-180\,t+324\,s^2+558\,s\,t+324\,t^2,$$
$$3350-6030\,s-1675\,t+2916\,s^2+3015\,s\,t+3015\,t^2.$$

2 degree 3 polynomials in s, t:

$$-25+180\,t-324\,s\,t-324\,t^2+81\,s\,t^2,$$
$$-25+25\,s+180\,t-90\,s^2-414\,s\,t-324\,t^2+81\,s^3+162\,s^2\,t+81\,s\,t^2.$$

8 degree 4 polynomials in s, t:

$$400 - 3080\,s - 2880\,t + 4489\,s^2 + 11808\,s\,t + 5184\,t^2 - 2772\,s^2\,t - 2592\,s\,t^2 + 324\,s^2\,t^2,$$

$$400 - 200\,s - 2880\,t - 695\,s^2 + 1440\,s\,t + 5184\,t^2 - 180\,s^3 - 2772\,s^2\,t - 2592\,s\,t^2 + 324\,s^4 + 648\,s^3\,t + 324\,s^2\,t^2,$$

$$112225 - 997920\,s - 808020\,t + 1679616\,s^2 + 3841992\,s\,t + 1454436\,t^2 - 839808\,s^2\,t - 898128\,s\,t^2 + 104976\,s^2\,t^2,$$

$$112225 + 51300\,s - 808020\,t - 144180\,s^2 + 64800\,s\,t + 1454436\,t^2 - 174960\,s^3 - 1073088\,s^2\,t - 898128\,s\,t^2 + 104976\,s^4 + 209952\,s^3\,t + 104976\,s^2\,t^2,$$

$$3125 + 173250\,s - 45000\,t + 145800\,s^2 - 1206900\,s\,t + 243000\,t^2 + 3149280\,s^2\,t + 1953720\,s\,t^2 - 583200\,t^3 + 1889568\,s^2\,t^2 + 524880\,s\,t^3 + 524880\,t^4,$$

$$-8375 - 23400\,s + 88200\,t - 32400\,s^2 + 68040\,s\,t - 301320\,t^2 + 29160\,s^3 - 244944\,s^2\,t + 29160\,s\,t^2 + 303264\,t^3 - 104976\,s^3\,t - 104976\,s^2\,t^2 + 104976\,s\,t^3 + 104976\,t^4,$$

$$+9625 - 64800\,s - 106200\,t + 599400\,s\,t + 398520\,t^2 - 839808\,s^2\,t - 1405512\,s\,t^2 - 536544\,t^3 + 209952\,s^2\,t^2 + 314928\,s\,t^3 + 104976\,t^4,$$

$$-2750 + 1800\,s + 22725\,t + 2025\,s^2 - 52650\,s\,t - 56700\,t^2 + 26973\,s^2\,t + 64881\,s\,t^2 + 37908\,t^3 + 13122\,s^3\,t + 26244\,s^2\,t^2 + 13122\,s\,t^3\,.$$

2 degree 6 polynomials in s, t:

$$
\begin{aligned}
&+ 2500 - 18000\,t + 64800\,s\,t + 27900\,t^2 - 249480\,s\,t^2 + 32400\,t^3 + 419904\,s^2\,t^2 \\
&\quad + 116640\,s\,t^3 - 56295\,t^4 - 209952\,s^2\,t^3 - 224532\,s\,t^4 - 14580\,t^5 + 26244\,s^2\,t^4 \\
&\quad + 52488\,s\,t^5 + 26244\,t^6, \\
&+ 105625 - 3676500\,s - 468000\,t + 25891650\,s^2 + 17309700\,s\,t - 797850\,t^2 - 50490540\,s^3 \\
&\quad - 73614420\,s^2\,t - 19260180\,s\,t^2 + 3863700\,t^3 + 29452329\,s^4 + 80752788\,s^3\,t \\
&\quad + 75149694\,s^2\,t^2 + 25850340\,s\,t^3 + 2001105\,t^4 - 18187092\,s^4\,t - 60466176\,s^3\,t^2 \\
&\quad - 72275976\,s^2\,t^3 - 35901792\,s\,t^4 - 5904900\,t^5 + 2125764\,s^4\,t^2 + 8503056\,s^3\,t^3 \\
&\quad + 12754584\,s^2\,t^4 + 8503056\,s\,t^5 + 2125764\,t^6\,.
\end{aligned}
$$

Note that during the initial IBP reduction to the traditional Laporta basis, spurious denominators with mixed dependence on d and kinematic invariants were indeed introduced. Rotation to the current basis followed by the partial fractioning approach described in Sec. 5.1 allowed us to systematically eliminate those denominators.

APPENDIX F

Numerical checks

In this appendix, details of the pole cancellation are provided. The amplitudes are evaluated in the chosen basis of finite integrals using Kreimer's anti-commuting γ_5 scheme. For an L loop amplitude, at worst $1/\epsilon^{2L}$ could appear. However, since this process is only an NLO correction, only the $1/\epsilon^2$ and $1/\epsilon$ poles should remain before UV renormalisation and IR subtraction. Indeed, for the spurious $1/\epsilon^4$ and $1/\epsilon^3$ poles, analytical and high precision numerical cancellations are seen, respectively. For the Euclidean point with $s/m_t^2 = -191$, $t/m_t^2 = -337$, $m_Z^2/m_t^2 = -853$, $m_t = 1$, 15 digits of cancellation is seen for the $1/\epsilon^3$ pole while 8 digit cancellation is seen for the point in the physical region: $s/m_t^2 = 142/17$, $t/m_t^2 = -125/22$, $m_Z^2/m_t^2 = 5/18$, $m_t = 1$.

The tables below show our results for the $1/\epsilon^2$ and $1/\epsilon$ poles, and the ϵ^0 term of the UV renormalised form factors A_i, and compare them against the predicted IR poles as in Eq. 5.2.13 and 5.2.14, for the Euclidean (Tab. 7.1) and the physical (Tab. 7.2) point. The digits in parentheses for the ϵ^0 term denote the uncertainty in the last digit. It is clear from the tables below that the calculated poles show the structure predicted in [349] with good numerical precision for both the Euclidean and the physical point which serves as a strong check for the calculation.

FF	$1/\epsilon^2$	$1/\epsilon$	ϵ^0
A_1	$+2.436734851 \cdot 10^{-1}$	$+8.212518984 \cdot 10^{-1} + 1.531045661\,i$	$-2.806661(2) + 4.18190980(3)\,i$
Pred.	$+2.436734852 \cdot 10^{-1}$	$+8.212518977 \cdot 10^{-1} + 1.531045662\,i$	
A_2	$-1.760872097 \cdot 10^{-1}$	$-6.021429768 \cdot 10^{-1} - 1.106388569\,i$	$+2.509969(1) - 3.07651654(4)\,i$
Pred.	$-1.760872097 \cdot 10^{-1}$	$-6.021429781 \cdot 10^{-1} - 1.106388569\,i$	
A_3	$-3.815946068 \cdot 10^{-2}$	$-7.236587884 \cdot 10^{-2} - 2.397629627 \cdot 10^{-1}\,i$	$+1.2102(3) \cdot 10^{-2} - 3.015063(4) \cdot 10^{-1}\,i$
Pred.	$-3.815946069 \cdot 10^{-2}$	$-7.236587838 \cdot 10^{-2} - 2.397629627 \cdot 10^{-1}\,i$	
A_4	$-1.565000574 \cdot 10^{-4}$	$-5.374251500 \cdot 10^{-4} - 9.833188615 \cdot 10^{-4}\,i$	$+2.18538(3) \cdot 10^{-3} - 2.748510(3) \cdot 10^{-3}\,i$
Pred.	$-1.565000575 \cdot 10^{-4}$	$-5.374251489 \cdot 10^{-4} - 9.833188622 \cdot 10^{-4}\,i$	
A_5	$+7.608919171 \cdot 10^{-4}$	$+1.926944077 \cdot 10^{-3} + 4.780824914 \cdot 10^{-3}\,i$	$-1.051486(4) \cdot 10^{-2} + 9.052930(4) \cdot 10^{-3}\,i$
Pred.	$+7.608919168 \cdot 10^{-4}$	$+1.926944068 \cdot 10^{-3} + 4.780824912 \cdot 10^{-3}\,i$	
A_6	$+7.576619247 \cdot 10^{-4}$	$+2.735071357 \cdot 10^{-3} + 4.760530273 \cdot 10^{-3}\,i$	$-7.02484(5) \cdot 10^{-3} + 1.41435102(3) \cdot 10^{-2}\,i$
Pred.	$+7.576619247 \cdot 10^{-4}$	$+2.735071351 \cdot 10^{-3} + 4.760530273 \cdot 10^{-3}\,i$	
A_7	$-1.565000574 \cdot 10^{-4}$	$-5.374251500 \cdot 10^{-4} - 9.833188615 \cdot 10^{-4}\,i$	$+2.18538(3) \cdot 10^{-3} - 2.748510(3) \cdot 10^{-3}\,i$
Pred.	$-1.565000575 \cdot 10^{-4}$	$-5.374251489 \cdot 10^{-4} - 9.833188622 \cdot 10^{-4}\,i$	
A_8	$-3.055600405 \cdot 10^{-4}$	$-1.158849558 \cdot 10^{-3} - 1.919890357 \cdot 10^{-3}\,i$	$+4.35036(1) \cdot 10^{-3} - 6.0546699(5) \cdot 10^{-3}\,i$
Pred.	$-3.055600405 \cdot 10^{-4}$	$-1.158849559 \cdot 10^{-3} - 1.919890357 \cdot 10^{-3}\,i$	
A_9	$+2.001982671 \cdot 10^{-4}$	$+7.482078266 \cdot 10^{-4} + 1.257882810 \cdot 10^{-3}\,i$	$-3.07299(1) \cdot 10^{-3} + 3.897481(1) \cdot 10^{-3}\,i$
Pred.	$+2.001982671 \cdot 10^{-4}$	$+7.482078292 \cdot 10^{-4} + 1.257882810 \cdot 10^{-3}\,i$	
A_{10}	$+3.636573767 \cdot 10^{-4}$	$+1.390161598 \cdot 10^{-3} + 2.284926686 \cdot 10^{-3}\,i$	$-4.77622(2) \cdot 10^{-3} + 7.274828(2) \cdot 10^{-3}\,i$
Pred.	$+3.636573768 \cdot 10^{-4}$	$+1.390161596 \cdot 10^{-3} + 2.284926686 \cdot 10^{-3}\,i$	
A_{11}	$+5.388240322 \cdot 10^{-6}$	$-1.272166624 \cdot 10^{-4} + 3.385531242 \cdot 10^{-5}\,i$	$+1.04254(1) \cdot 10^{-3} - 8.20955(1) \cdot 10^{-4}\,i$
Pred.	$+5.388240348 \cdot 10^{-6}$	$-1.272166651 \cdot 10^{-4} + 3.385531259 \cdot 10^{-5}\,i$	
A_{12}	$-5.388240322 \cdot 10^{-6}$	$+1.272166624 \cdot 10^{-4} - 3.385531242 \cdot 10^{-5}\,i$	$-1.04254(1) \cdot 10^{-3} + 8.20955(1) \cdot 10^{-4}\,i$
Pred.	$-5.388240348 \cdot 10^{-6}$	$+1.272166651 \cdot 10^{-4} - 3.385531259 \cdot 10^{-5}\,i$	
A_{13}	$-3.636573767 \cdot 10^{-4}$	$-1.390161598 \cdot 10^{-3} - 2.284926686 \cdot 10^{-3}\,i$	$+4.77622(2) \cdot 10^{-3} - 7.274828(2) \cdot 10^{-3}\,i$
Pred.	$-3.636573768 \cdot 10^{-4}$	$-1.390161596 \cdot 10^{-3} - 2.284926686 \cdot 10^{-3}\,i$	
A_{14}	$-2.001982671 \cdot 10^{-4}$	$-7.482078266 \cdot 10^{-4} - 1.257882810 \cdot 10^{-3}\,i$	$+3.07299(1) \cdot 10^{-3} - 3.897481(1) \cdot 10^{-3}\,i$
Pred.	$-2.001982671 \cdot 10^{-4}$	$-7.482078292 \cdot 10^{-4} - 1.257882810 \cdot 10^{-3}\,i$	
A_{15}	$+3.055600405 \cdot 10^{-4}$	$+1.158849558 \cdot 10^{-3} + 1.919890357 \cdot 10^{-3}\,i$	$-4.35036(1) \cdot 10^{-3} + 6.0546699(5) \cdot 10^{-3}\,i$
Pred.	$+3.055600405 \cdot 10^{-4}$	$+1.158849559 \cdot 10^{-3} + 1.919890357 \cdot 10^{-3}\,i$	
A_{16}	$+1.898361362 \cdot 10^{-4}$	$+6.165488820 \cdot 10^{-4} + 1.192775622 \cdot 10^{-3}\,i$	$-2.233448(2) \cdot 10^{-3} + 3.11183978(6) \cdot 10^{-3}\,i$
Pred.	$+1.898361362 \cdot 10^{-4}$	$+6.165488809 \cdot 10^{-4} + 1.192775622 \cdot 10^{-3}\,i$	
A_{17}	$-4.235989659 \cdot 10^{-8}$	$-1.659620988 \cdot 10^{-7} - 2.661550798 \cdot 10^{-7}\,i$	$+8.1249(2) \cdot 10^{-7} - 8.72727(4) \cdot 10^{-7}\,i$
Pred.	$-4.235989677 \cdot 10^{-8}$	$-1.659621000 \cdot 10^{-7} - 2.661550810 \cdot 10^{-7}\,i$	
A_{18}	$-9.857950093 \cdot 10^{-8}$	$-9.594603102 \cdot 10^{-7} - 6.193932718 \cdot 10^{-7}\,i$	$+4.4198(6) \cdot 10^{-7} - 5.632743(5) \cdot 10^{-6}\,i$
Pred.	$-9.857950139 \cdot 10^{-8}$	$-9.594603103 \cdot 10^{-7} - 6.193932747 \cdot 10^{-7}\,i$	
A_{19}	$+8.932087549 \cdot 10^{-7}$	$+3.205282901 \cdot 10^{-6} + 5.612196125 \cdot 10^{-6}\,i$	$-7.43447(5) \cdot 10^{-6} + 1.6553816(4) \cdot 10^{-5}\,i$
Pred.	$+8.932087551 \cdot 10^{-7}$	$+3.205282889 \cdot 10^{-6} + 5.612196126 \cdot 10^{-6}\,i$	
A_{20}	$-4.235989659 \cdot 10^{-8}$	$-1.659620988 \cdot 10^{-7} - 2.661550798 \cdot 10^{-7}\,i$	$+8.1249(2) \cdot 10^{-7} - 8.72727(4) \cdot 10^{-7}\,i$
Pred.	$-4.235989677 \cdot 10^{-8}$	$-1.659621000 \cdot 10^{-7} - 2.661550810 \cdot 10^{-7}\,i$	

Table 7.1: Numerical poles for the Euclidean phase-space point $s/m_t^2 = -191$, $t/m_t^2 = -337$, $m_Z^2/m_t^2 = -853$, $m_t = 1$ compared against the predicted values. Also shown are the ϵ^0 terms before IR subtraction with the digits in parentheses denoting the uncertainty in the last digit.

FF	$1/\epsilon^2$	$1/\epsilon$	ϵ^0
A_1	$-5.726898 \cdot 10^{-1} - 4.634791 \cdot 10^{-1} i$	$-6.75706 \cdot 10^{-1} - 4.05460\, i$	$6.87787(1) - 7.90340(1)\, i$
Pred.	$-5.726897 \cdot 10^{-1} - 4.634791 \cdot 10^{-1} i$	$-6.75704 \cdot 10^{-1} - 4.05460\, i$	
A_2	$+4.153857 \cdot 10^{-1} + 1.097935 \cdot 10^{-1} i$	$+1.40864 + 2.02204\, i$	$-2.53566(2) + 7.06651(3)\, i$
Pred.	$+4.153857 \cdot 10^{-1} + 1.097934 \cdot 10^{-1} i$	$+1.40865 + 2.02204\, i$	
A_3	$+2.003102 \cdot 10^{-1} + 3.116062 \cdot 10^{-1} i$	$-5.02052 \cdot 10^{-1} + 1.86425\, i$	$-3.99592(2) + 2.59711(2)\, i$
Pred.	$+2.003101 \cdot 10^{-1} + 3.116062 \cdot 10^{-1} i$	$-5.02053 \cdot 10^{-1} + 1.86425\, i$	
A_4	$+3.147592 \cdot 10^{-2} + 9.237206 \cdot 10^{-4} i$	$+1.39272 \cdot 10^{-1} + 1.16086 \cdot 10^{-1} i$	$-4.1039(4) \cdot 10^{-2} + 5.40365(5) \cdot 10^{-1}\, i$
Pred.	$+3.147591 \cdot 10^{-2} + 9.237121 \cdot 10^{-4} i$	$+1.39272 \cdot 10^{-1} + 1.16086 \cdot 10^{-1} i$	
A_5	$+1.041667 \cdot 10^{-1} + 5.382124 \cdot 10^{-2} i$	$+2.44023 \cdot 10^{-1} + 5.97453 \cdot 10^{-1} i$	$-8.96421(5) \cdot 10^{-1} + 1.736695(6)\, i$
Pred.	$+1.041667 \cdot 10^{-1} + 5.382123 \cdot 10^{-2} i$	$+2.44022 \cdot 10^{-1} + 5.97453 \cdot 10^{-1} i$	
A_6	$+1.242527 \cdot 10^{-1} + 6.941130 \cdot 10^{-2} i$	$+2.52191 \cdot 10^{-1} + 7.24307 \cdot 10^{-1} i$	$-1.20930(2) + 1.93865(2)\, i$
Pred.	$+1.242527 \cdot 10^{-1} + 6.941131 \cdot 10^{-2} i$	$+2.52189 \cdot 10^{-1} + 7.24307 \cdot 10^{-1} i$	
A_7	$+3.147592 \cdot 10^{-2} + 9.237206 \cdot 10^{-4} i$	$+1.39272 \cdot 10^{-1} + 1.16086 \cdot 10^{-1} i$	$-4.1039(4) \cdot 10^{-2} + 5.40365(4) \cdot 10^{-1}\, i$
Pred.	$+3.147591 \cdot 10^{-2} + 9.237121 \cdot 10^{-4} i$	$+1.39272 \cdot 10^{-1} + 1.16086 \cdot 10^{-1} i$	
A_8	$-1.017708 \cdot 10^{-2} + 8.808524 \cdot 10^{-2} i$	$-4.41618 \cdot 10^{-1} + 2.61228 \cdot 10^{-1} i$	$-1.00384(5) - 4.4284(4) \cdot 10^{-1}\, i$
Pred.	$-1.017707 \cdot 10^{-2} + 8.808519 \cdot 10^{-2} i$	$-4.41613 \cdot 10^{-1} + 2.61225 \cdot 10^{-1} i$	
A_9	$+7.168287 \cdot 10^{-2} - 5.063902 \cdot 10^{-2} i$	$+5.37076 \cdot 10^{-1} + 9.24698 \cdot 10^{-2} i$	$3.07426(8) \cdot 10^{-1} 1.266108(9)\, i$
Pred.	$+7.168286 \cdot 10^{-2} - 5.063902 \cdot 10^{-2} i$	$+5.37075 \cdot 10^{-1} + 9.24707 \cdot 10^{-2} i$	
A_{10}	$+1.873343 \cdot 10^{-2} - 8.497011 \cdot 10^{-2} i$	$+4.70733 \cdot 10^{-1} - 2.17284 \cdot 10^{-1} i$	$+9.3643(1) \cdot 10^{-1} + 6.3029(1) \cdot 10^{-1}\, i$
Pred.	$+1.873344 \cdot 10^{-2} - 8.497010 \cdot 10^{-2} i$	$+4.70734 \cdot 10^{-1} - 2.17286 \cdot 10^{-1} i$	
A_{11}	$-7.675742 \cdot 10^{-2} + 5.097567 \cdot 10^{-2} i$	$-5.57824 \cdot 10^{-1} - 1.06514 \cdot 10^{-1} i$	$-3.1397(3) \cdot 10^{-1} - 1.35727(4)\, i$
Pred.	$-7.675741 \cdot 10^{-2} + 5.097571 \cdot 10^{-2} i$	$-5.57827 \cdot 10^{-1} - 1.06513 \cdot 10^{-1} i$	
A_{12}	$+7.675742 \cdot 10^{-2} - 5.097567 \cdot 10^{-2} i$	$+5.57824 \cdot 10^{-1} + 1.06514 \cdot 10^{-1} i$	$+3.1397(3) \cdot 10^{-1} + 1.35727(4)\, i$
Pred.	$+7.675741 \cdot 10^{-2} - 5.097571 \cdot 10^{-2} i$	$+5.57827 \cdot 10^{-1} + 1.06513 \cdot 10^{-1} i$	
A_{13}	$-1.873343 \cdot 10^{-2} + 8.497011 \cdot 10^{-2} i$	$-4.70733 \cdot 10^{-1} + 2.17284 \cdot 10^{-1} i$	$-9.3644(1) \cdot 10^{-1} - 6.3029(1) \cdot 10^{-1}\, i$
Pred.	$-1.873344 \cdot 10^{-2} + 8.497010 \cdot 10^{-2} i$	$-4.70734 \cdot 10^{-1} + 2.17286 \cdot 10^{-1} i$	
A_{14}	$-7.168287 \cdot 10^{-2} + 5.063902 \cdot 10^{-2} i$	$-5.37076 \cdot 10^{-1} - 9.24698 \cdot 10^{-2} i$	$-3.07426(8) \cdot 10^{-1} - 1.266108(9)\, i$
Pred.	$-7.168286 \cdot 10^{-2} + 5.063902 \cdot 10^{-2} i$	$-5.37075 \cdot 10^{-1} - 9.24707 \cdot 10^{-2} i$	
A_{15}	$+1.017708 \cdot 10^{-2} - 8.808524 \cdot 10^{-2} i$	$+4.41618 \cdot 10^{-1} - 2.61228 \cdot 10^{-1} i$	$1.00384(4) + 4.4283(4) \cdot 10^{-1}\, i$
Pred.	$+1.017707 \cdot 10^{-2} - 8.808519 \cdot 10^{-2} i$	$+4.41613 \cdot 10^{-1} - 2.61225 \cdot 10^{-1} i$	
A_{16}	$-6.195421 \cdot 10^{-2} - 9.197693 \cdot 10^{-2} i$	$+1.25592 \cdot 10^{-1} - 6.06299 \cdot 10^{-1} i$	$1.76383(3) - 9.4291(3) \cdot 10^{-1}\, i$
Pred.	$-6.195417 \cdot 10^{-2} - 9.197695 \cdot 10^{-2} i$	$+1.25596 \cdot 10^{-1} - 6.06299 \cdot 10^{-1} i$	
A_{17}	$+9.152404 \cdot 10^{-4} + 4.922399 \cdot 10^{-3} i$	$-1.47185 \cdot 10^{-2} + 2.71477 \cdot 10^{-2} i$	$-8.6390(6) \cdot 10^{-2} + 2.7504(7) \cdot 10^{-2}\, i$
Pred.	$+9.152368 \cdot 10^{-4} + 4.922402 \cdot 10^{-3} i$	$-1.47187 \cdot 10^{-2} + 2.71472 \cdot 10^{-2} i$	
A_{18}	$+6.800443 \cdot 10^{-3} + 5.687424 \cdot 10^{-3} i$	$+7.80438 \cdot 10^{-3} + 4.98318 \cdot 10^{-2} i$	$-1.02182(8) \cdot 10^{-1} + 1.37512(8) \cdot 10^{-1}\, i$
Pred.	$+6.800439 \cdot 10^{-3} + 5.687435 \cdot 10^{-3} i$	$+7.80405 \cdot 10^{-3} + 4.98315 \cdot 10^{-2} i$	
A_{19}	$+4.208648 \cdot 10^{-3} + 4.547692 \cdot 10^{-3} i$	$-3.01730 \cdot 10^{-4} + 3.55035 \cdot 10^{-2} i$	$-7.895(10) \cdot 10^{-2} + 7.980(11) \cdot 10^{-2}\, i$
Pred.	$+4.208616 \cdot 10^{-3} + 4.547808 \cdot 10^{-3} i$	$-3.13880 \cdot 10^{-4} + 3.55067 \cdot 10^{-2} i$	
A_{20}	$+9.152403 \cdot 10^{-4} + 4.922399 \cdot 10^{-3} i$	$-1.47185 \cdot 10^{-2} + 2.71477 \cdot 10^{-2} i$	$-8.6391(6) \cdot 10^{-2} + 2.7504(7) \cdot 10^{-2}\, i$
Pred.	$+9.152368 \cdot 10^{-4} + 4.922402 \cdot 10^{-3} i$	$-1.47187 \cdot 10^{-2} + 2.71472 \cdot 10^{-2} i$	

Table 7.2: Numerical poles for the physical phase-space point $s/m_t^2 = 142/17$, $t/m_t^2 = -125/22$, $m_Z^2/m_t^2 = 5/18$, $m_t = 1$ compared against the predicted values. Also shown are the ϵ^0 terms before IR subtraction with the digits in parentheses denoting the uncertainty in the last digit.

BIBLIOGRAPHY

BIBLIOGRAPHY

[1] Particle Data Group collaboration, *Review of Particle Physics*, *PTEP* **2020** (2020) 083C01.

[2] LHC Higgs Cross Section Working Group collaboration, *Handbook of LHC Higgs Cross Sections: 3. Higgs Properties*, 1307.1347.

[3] S. Borowka, G. Heinrich, S. Jahn, S.P. Jones, M. Kerner, J. Schlenk et al., *pySecDec: a toolbox for the numerical evaluation of multi-scale integrals*, *Comput. Phys. Commun.* **222** (2018) 313 [1703.09692].

[4] Z. Li, J. Wang, Q.-S. Yan and X. Zhao, *Efficient numerical evaluation of Feynman integrals*, *Chin. Phys. C* **40** (2016) 033103 [1508.02512].

[5] S. Borowka, G. Heinrich, S. Jahn, S. Jones, M. Kerner and J. Schlenk, *A GPU compatible quasi-Monte Carlo integrator interfaced to pySecDec*, *Comput. Phys. Commun.* **240** (2019) 120 [1811.11720].

[6] B. Agarwal, S.P. Jones and A. von Manteuffel, *Two-loop helicity amplitudes for $gg \to ZZ$ with full top-quark mass effects*, 2011.15113.

[7] A. Signer, *Low-energy precision physics and the high-energy frontier*, *Physics Procedia* **51** (2014) 25.

[8] LHC Higgs Cross Section Working Group collaboration, *Handbook of LHC Higgs Cross Sections: 1. Inclusive Observables*, 1101.0593.

[9] ATLAS collaboration, *Observation of a new particle in the search for the Standard Model Higgs boson with the ATLAS detector at the LHC*, *Phys. Lett. B* **716** (2012) 1 [1207.7214].

[10] CMS collaboration, *Observation of a New Boson at a Mass of 125 GeV with the CMS Experiment at the LHC*, *Phys. Lett. B* **716** (2012) 30 [1207.7235].

[11] ATLAS collaboration, *A combination of measurements of Higgs boson production*

and decay using up to 139 fb^{-1} *of proton–proton collision data at* $\sqrt{s} = 13$ *TeV collected with the ATLAS experiment*, .

[12] C. Anastasiou, C. Duhr, F. Dulat, F. Herzog and B. Mistlberger, *Higgs Boson Gluon-Fusion Production in QCD at Three Loops*, *Phys. Rev. Lett.* **114** (2015) 212001 [1503.06056].

[13] J. Davies, G. Mishima, M. Steinhauser and D. Wellmann, $gg \to ZZ$*: analytic two-loop results for the low- and high-energy regions*, *JHEP* **04** (2020) 024 [2002.05558].

[14] S. Catani, *The Singular behavior of QCD amplitudes at two loop order*, *Phys. Lett. B* **427** (1998) 161 [hep-ph/9802439].

[15] R.H. Parker, C. Yu, W. Zhong, B. Estey and H. Müller, *Measurement of the fine-structure constant as a test of the standard model*, *Science* **360** (2018) 191 [https://science.sciencemag.org/content/360/6385/191.full.pdf].

[16] T. Aoyama, M. Hayakawa, T. Kinoshita and M. Nio, *Tenth-Order Electron Anomalous Magnetic Moment — Contribution of Diagrams without Closed Lepton Loops*, *Phys. Rev. D* **91** (2015) 033006 [1412.8284].

[17] D. Hanneke, S.F. Hoogerheide and G. Gabrielse, *Cavity Control of a Single-Electron Quantum Cyclotron: Measuring the Electron Magnetic Moment*, *Phys. Rev. A* **83** (2011) 052122 [1009.4831].

[18] P.W. Higgs, *Broken symmetries, massless particles and gauge fields*, *Phys. Lett.* **12** (1964) 132.

[19] P.W. Higgs, *Broken Symmetries and the Masses of Gauge Bosons*, *Phys. Rev. Lett.* **13** (1964) 508.

[20] F. Englert and R. Brout, *Broken Symmetry and the Mass of Gauge Vector Mesons*, *Phys. Rev. Lett.* **13** (1964) 321.

[21] G.S. Guralnik, C.R. Hagen and T.W.B. Kibble, *Global Conservation Laws and Massless Particles*, *Phys. Rev. Lett.* **13** (1964) 585.

[22] J. Goodman, M. Ibe, A. Rajaraman, W. Shepherd, T.M.P. Tait and H.-B. Yu, *Constraints on Dark Matter from Colliders*, *Phys. Rev. D* **82** (2010) 116010 [1008.1783].

[23] P. Cushman et al., *Working Group Report: WIMP Dark Matter Direct Detection*, in *Community Summer Study 2013: Snowmass on the Mississippi*, 10, 2013 [1310.8327].

[24] M. Battaglieri et al., *US Cosmic Visions: New Ideas in Dark Matter 2017: Community Report*, in *U.S. Cosmic Visions: New Ideas in Dark Matter*, 7, 2017 [1707.04591].

[25] G. Arcadi, M. Dutra, P. Ghosh, M. Lindner, Y. Mambrini, M. Pierre et al., *The waning of the WIMP? A review of models, searches, and constraints*, *Eur. Phys. J. C* **78** (2018) 203 [1703.07364].

[26] E.J. Copeland, M. Sami and S. Tsujikawa, *Dynamics of dark energy*, *Int. J. Mod. Phys. D* **15** (2006) 1753 [hep-th/0603057].

[27] A. Strumia and F. Vissani, *Neutrino masses and mixings and...*, hep-ph/0606054.

[28] S. Weinberg, *Gauge Hierarchies*, *Phys. Lett. B* **82** (1979) 387.

[29] A. de Gouvea, D. Hernandez and T.M.P. Tait, *Criteria for Natural Hierarchies*, *Phys. Rev. D* **89** (2014) 115005 [1402.2658].

[30] M. Dine, *TASI lectures on the strong CP problem*, in *Theoretical Advanced Study Institute in Elementary Particle Physics (TASI 2000): Flavor Physics for the Millennium*, 6, 2000 [hep-ph/0011376].

[31] L. Canetti, M. Drewes and M. Shaposhnikov, *Matter and Antimatter in the Universe*, *New J. Phys.* **14** (2012) 095012 [1204.4186].

[32] R.P. Feynman, *Very high-energy collisions of hadrons*, *Phys. Rev. Lett.* **23** (1969) 1415.

[33] B.W. Lee, C. Quigg and H. Thacker, *Weak Interactions at Very High-Energies: The Role of the Higgs Boson Mass*, *Phys. Rev. D* **16** (1977) 1519.

[34] M.S. Chanowitz and M.K. Gaillard, *The TeV Physics of Strongly Interacting W's and Z's*, *Nucl. Phys. B* **261** (1985) 379.

[35] N. Kauer and G. Passarino, *Inadequacy of zero-width approximation for a light Higgs boson signal*, *JHEP* **08** (2012) 116 [1206.4803].

[36] N. Kauer, *Interference effects for $H \to WW/ZZ \to \ell\bar{\nu}_\ell\bar{\ell}\nu_\ell$ searches in gluon fusion at the LHC*, *JHEP* **12** (2013) 082 [1310.7011].

[37] F. Caola and K. Melnikov, *Constraining the Higgs boson width with ZZ production at the LHC*, *Phys. Rev.* **D88** (2013) 054024 [1307.4935].

[38] A. Azatov, C. Grojean, A. Paul and E. Salvioni, *Resolving gluon fusion loops at current and future hadron colliders*, *JHEP* **09** (2016) 123 [1608.00977].

[39] Q.-H. Cao, B. Yan, C. Yuan and Y. Zhang, *Probing $Zt\bar{t}$ couplings using Z boson polarization in ZZ production at hadron colliders*, *Phys. Rev. D* **102** (2020) 055010 [2004.02031].

[40] C.-N. Yang and R.L. Mills, *Conservation of Isotopic Spin and Isotopic Gauge Invariance*, *Phys. Rev.* **96** (1954) 191.

[41] Y. Nambu, *Quasi-particles and gauge invariance in the theory of superconductivity*, *Phys. Rev.* **117** (1960) 648.

[42] J. Goldstone, *Field Theories with Superconductor Solutions*, *Nuovo Cim.* **19** (1961) 154.

[43] P.W. Higgs, *Spontaneous Symmetry Breakdown without Massless Bosons*, *Phys. Rev.* **145** (1966) 1156.

[44] S. Weinberg, *A model of leptons*, *Phys. Rev. Lett.* **19** (1967) 1264.

[45] ATLAS collaboration, *Observation of $H \to b\bar{b}$ decays and VH production with the ATLAS detector*, *Phys. Lett. B* **786** (2018) 59 [1808.08238].

[46] CMS collaboration, *Observation of Higgs boson decay to bottom quarks*, *Phys. Rev.*

Lett. **121** (2018) 121801 [1808.08242].

[47] ATLAS collaboration, *A search for the dimuon decay of the Standard Model Higgs boson with the ATLAS detector*, *Phys. Lett. B* **812** (2021) 135980 [2007.07830].

[48] CMS collaboration, *Evidence for Higgs boson decay to a pair of muons*, *JHEP* **01** (2021) 148 [2009.04363].

[49] S. Dittmaier et al., *Handbook of LHC Higgs Cross Sections: 2. Differential Distributions*, 1201.3084.

[50] LHC Higgs Cross Section Working Group collaboration, *Handbook of LHC Higgs Cross Sections: 4. Deciphering the Nature of the Higgs Sector*, 1610.07922.

[51] D. De Florian and J. Mazzitelli, *Soft gluon resummation for Higgs boson pair production including finite M_t effects*, *JHEP* **08** (2018) 156 [1807.03704].

[52] J. Chang, K. Cheung, J.S. Lee and J. Park, *Probing the trilinear Higgs boson self-coupling at the high-luminosity LHC via multivariate analysis*, *Phys. Rev. D* **101** (2020) 016004 [1908.00753].

[53] M.L. Mangano, G. Ortona and M. Selvaggi, *Measuring the Higgs self-coupling via Higgs-pair production at a 100 TeV p-p collider*, *Eur. Phys. J. C* **80** (2020) 1030 [2004.03505].

[54] M. Chiesa, F. Maltoni, L. Mantani, B. Mele, F. Piccinini and X. Zhao, *Measuring the quartic Higgs self-coupling at a multi-TeV muon collider*, *JHEP* **09** (2020) 098 [2003.13628].

[55] CMS collaboration, *Precise determination of the mass of the Higgs boson and tests of compatibility of its couplings with the standard model predictions using proton collisions at 7 and 8 TeV*, *Eur. Phys. J. C* **75** (2015) 212 [1412.8662].

[56] ATLAS collaboration, *Measurement of the Higgs boson mass from the $H \to \gamma\gamma$ and $H \to ZZ^* \to 4\ell$ channels with the ATLAS detector using 25 fb^{-1} of pp collision data*, *Phys. Rev. D* **90** (2014) 052004 [1406.3827].

[57] CMS collaboration, *Measurements of properties of the Higgs boson decaying into the four-lepton final state in pp collisions at* $\sqrt{s} = 13$ *TeV*, *JHEP* **11** (2017) 047 [1706.09936].

[58] J.M. Campbell, R.K. Ellis and C. Williams, *Bounding the Higgs Width at the LHC Using Full Analytic Results for* $gg- > e^-e^+\mu^-\mu^+$, *JHEP* **04** (2014) 060 [1311.3589].

[59] CMS collaboration, *Measurements of the Higgs boson width and anomalous HVV couplings from on-shell and off-shell production in the four-lepton final state*, *Phys. Rev. D* **99** (2019) 112003 [1901.00174].

[60] ATLAS collaboration, $ZZ \to \ell^+\ell^-\ell'^+\ell'^-$ *cross-section measurements and search for anomalous triple gauge couplings in 13 TeV pp collisions with the ATLAS detector*, *Phys. Rev. D* **97** (2018) 032005 [1709.07703].

[61] ATLAS collaboration, *Measurement of the four-lepton invariant mass spectrum in 13 TeV proton-proton collisions with the ATLAS detector*, *JHEP* **04** (2019) 048 [1902.05892].

[62] ATLAS collaboration, *Measurement of ZZ production in the* $\ell\ell\nu\nu$ *final state with the ATLAS detector in pp collisions at* $\sqrt{s} = 13$ *TeV*, *JHEP* **10** (2019) 127 [1905.07163].

[63] CMS collaboration, *Measurements of the* $\mathrm{pp} \to \mathrm{ZZ}$ *production cross section and the* $\mathrm{Z} \to 4\ell$ *branching fraction, and constraints on anomalous triple gauge couplings at* $\sqrt{s} = 13$ *TeV*, *Eur. Phys. J. C* **78** (2018) 165 [1709.08601].

[64] CMS collaboration, *Measurements of* $pp \to ZZ$ *production cross sections and constraints on anomalous triple gauge couplings at* $\sqrt{s} = 13$ *TeV*, 2009.01186.

[65] ATLAS collaboration, *Constraints on off-shell Higgs boson production and the Higgs boson total width in* $ZZ \to 4\ell$ *and* $ZZ \to 2\ell 2\nu$ *final states with the ATLAS detector*, *Phys. Lett. B* **786** (2018) 223 [1808.01191].

[66] CMS collaboration, *Measurement and interpretation of differential cross sections for Higgs boson production at* $\sqrt{s} = 13$ *TeV*, *Phys. Lett. B* **792** (2019) 369 [1812.06504].

[67] ATLAS collaboration, *Measurements of the Higgs boson inclusive and differential fiducial cross sections in the* 4ℓ *decay channel at* $\sqrt{s} = 13$ *TeV*, *Eur. Phys. J. C* **80**

(2020) 942 [2004.03969].

[68] F. Cascioli, T. Gehrmann, M. Grazzini, S. Kallweit, P. Maierhöfer, A. von Manteuffel et al., *ZZ production at hadron colliders in NNLO QCD*, *Phys. Lett.* **B735** (2014) 311 [1405.2219].

[69] F. Caola, K. Melnikov, R. Röntsch and L. Tancredi, *QCD corrections to ZZ production in gluon fusion at the LHC*, *Phys. Rev.* **D92** (2015) 094028 [1509.06734].

[70] M. Grazzini, S. Kallweit, M. Wiesemann and J.Y. Yook, *ZZ production at the LHC: NLO QCD corrections to the loop-induced gluon fusion channel*, *JHEP* **03** (2019) 070 [1811.09593].

[71] J. Ohnemus, *Order $\alpha^- s$ calculations of hadronic $W^{\pm}\gamma$ and $Z\gamma$ production*, *Phys. Rev. D* **47** (1993) 940.

[72] U. Baur, T. Han and J. Ohnemus, *QCD corrections to hadronic $W\gamma$ production with nonstandard $WW\gamma$ couplings*, *Phys. Rev. D* **48** (1993) 5140 [hep-ph/9305314].

[73] U. Baur, T. Han and J. Ohnemus, *QCD corrections and anomalous couplings in $Z\gamma$ production at hadron colliders*, *Phys. Rev. D* **57** (1998) 2823 [hep-ph/9710416].

[74] L.J. Dixon, Z. Kunszt and A. Signer, *Helicity amplitudes for O(alpha-s) production of W^+W^-, $W^{\pm}Z$, ZZ, $W^{\pm}\gamma$, or $Z\gamma$ pairs at hadron colliders*, *Nucl. Phys. B* **531** (1998) 3 [hep-ph/9803250].

[75] J.M. Campbell and R.K. Ellis, *An Update on vector boson pair production at hadron colliders*, *Phys. Rev. D* **60** (1999) 113006 [hep-ph/9905386].

[76] L.J. Dixon, Z. Kunszt and A. Signer, *Vector boson pair production in hadronic collisions at order α_s : Lepton correlations and anomalous couplings*, *Phys. Rev. D* **60** (1999) 114037 [hep-ph/9907305].

[77] E. Accomando, A. Denner and A. Kaiser, *Logarithmic electroweak corrections to gauge-boson pair production at the LHC*, *Nucl. Phys. B* **706** (2005) 325 [hep-ph/0409247].

[78] E. Accomando, A. Denner and C. Meier, *Electroweak corrections to $W\gamma$ and $Z\gamma$ production at the LHC*, *Eur. Phys. J. C* **47** (2006) 125 [hep-ph/0509234].

[79] E. Accomando and A. Kaiser, *Electroweak corrections and anomalous triple gauge-boson couplings in W^+W^- and $W^\pm Z$ production at the LHC*, *Phys. Rev. D* **73** (2006) 093006 [hep-ph/0511088].

[80] A. Bierweiler, T. Kasprzik and J.H. Kühn, *Vector-boson pair production at the LHC to $\mathcal{O}(\alpha^3)$ accuracy*, *JHEP* **12** (2013) 071 [1305.5402].

[81] J. Baglio, L.D. Ninh and M.M. Weber, *Massive gauge boson pair production at the LHC: a next-to-leading order story*, *Phys. Rev. D* **88** (2013) 113005 [1307.4331].

[82] M. Billoni, S. Dittmaier, B. Jäger and C. Speckner, *Next-to-leading order electroweak corrections to pp -> W+W- -> 4 leptons at the LHC in double-pole approximation*, *JHEP* **12** (2013) 043 [1310.1564].

[83] S. Gieseke, T. Kasprzik and J.H. Kühn, *Vector-boson pair production and electroweak corrections in HERWIG++*, *Eur. Phys. J. C* **74** (2014) 2988 [1401.3964].

[84] A. Denner, S. Dittmaier, M. Hecht and C. Pasold, *NLO QCD and electroweak corrections to W+\gamma\ production with leptonic W-boson decays*, *JHEP* **04** (2015) 018 [1412.7421].

[85] R. Britto, F. Cachazo and B. Feng, *Generalized unitarity and one-loop amplitudes in N=4 super-Yang-Mills*, *Nucl. Phys. B* **725** (2005) 275 [hep-th/0412103].

[86] G. Ossola, C.G. Papadopoulos and R. Pittau, *Reducing full one-loop amplitudes to scalar integrals at the integrand level*, *Nucl. Phys. B* **763** (2007) 147 [hep-ph/0609007].

[87] R.K. Ellis, W.T. Giele, Z. Kunszt and K. Melnikov, *Masses, fermions and generalized D-dimensional unitarity*, *Nucl. Phys. B* **822** (2009) 270 [0806.3467].

[88] C.F. Berger and D. Forde, *Multi-Parton Scattering Amplitudes via On-Shell Methods*, *Ann. Rev. Nucl. Part. Sci.* **60** (2010) 181 [0912.3534].

[89] F. Cascioli, P. Maierhofer and S. Pozzorini, *Scattering Amplitudes with Open Loops*, *Phys. Rev. Lett.* **108** (2012) 111601 [1111.5206].

[90] Z. Bern, L.J. Dixon and D.A. Kosower, *On-Shell Methods in Perturbative QCD*, *Annals Phys.* **322** (2007) 1587 [0704.2798].

[91] R.K. Ellis, Z. Kunszt, K. Melnikov and G. Zanderighi, *One-loop calculations in quantum field theory: from Feynman diagrams to unitarity cuts*, *Phys. Rept.* **518** (2012) 141 [1105.4319].

[92] V. Costantini, B. De Tollis and G. Pistoni, *Nonlinear effects in quantum electrodynamics*, *Nuovo Cim. A* **2** (1971) 733.

[93] D.A. Dicus, C. Kao and W. Repko, *Gluon Production of Gauge Bosons*, *Phys. Rev. D* **36** (1987) 1570.

[94] J.J. van der Bij and E.W.N. Glover, *PHOTON Z BOSON PAIR PRODUCTION VIA GLUON FUSION*, *Phys. Lett. B* **206** (1988) 701.

[95] E.W.N. Glover and J.J. van der Bij, *VECTOR BOSON PAIR PRODUCTION VIA GLUON FUSION*, *Phys. Lett. B* **219** (1989) 488.

[96] E.W.N. Glover and J.J. van der Bij, *Z BOSON PAIR PRODUCTION VIA GLUON FUSION*, *Nucl. Phys.* **B321** (1989) 561.

[97] C. Zecher, T. Matsuura and J. van der Bij, *Leptonic signals from off-shell Z boson pairs at hadron colliders*, *Z. Phys. C* **64** (1994) 219 [hep-ph/9404295].

[98] K.L. Adamson, D. de Florian and A. Signer, *Gluon induced contributions to WZ and W gamma production at NNLO*, *Phys. Rev. D* **65** (2002) 094041 [hep-ph/0202132].

[99] K.L. Adamson, D. de Florian and A. Signer, *Gluon induced contributions to $Z\gamma$ production at hadron colliders*, *Phys. Rev. D* **67** (2003) 034016 [hep-ph/0211295].

[100] T. Binoth, M. Ciccolini, N. Kauer and M. Kramer, *Gluon-induced WW background to Higgs boson searches at the LHC*, *JHEP* **03** (2005) 065 [hep-ph/0503094].

[101] T. Binoth, M. Ciccolini, N. Kauer and M. Kramer, *Gluon-induced W-boson pair production at the LHC*, *JHEP* **12** (2006) 046 [hep-ph/0611170].

[102] A. von Manteuffel and L. Tancredi, *The two-loop helicity amplitudes for $gg \to V_1V_2 \to 4$ leptons*, *JHEP* **06** (2015) 197 [1503.08835].

[103] F. Caola, J.M. Henn, K. Melnikov, A.V. Smirnov and V.A. Smirnov, *Two-loop helicity amplitudes for the production of two off-shell electroweak bosons in gluon fusion*, *JHEP* **06** (2015) 129 [1503.08759].

[104] K. Melnikov and M. Dowling, *Production of two Z-bosons in gluon fusion in the heavy top quark approximation*, *Phys. Lett.* **B744** (2015) 43 [1503.01274].

[105] F. Caola, M. Dowling, K. Melnikov, R. Röntsch and L. Tancredi, *QCD corrections to vector boson pair production in gluon fusion including interference effects with off-shell Higgs at the LHC*, *JHEP* **07** (2016) 087 [1605.04610].

[106] J.M. Campbell, R.K. Ellis, M. Czakon and S. Kirchner, *Two loop correction to interference in $gg \to ZZ$*, *JHEP* **08** (2016) 011 [1605.01380].

[107] R. Gröber, A. Maier and T. Rauh, *Top quark mass effects in $gg \to ZZ$ at two loops and off-shell Higgs interference*, *Phys. Rev.* **D100** (2019) 114013 [1908.04061].

[108] M. Spira, A. Djouadi, D. Graudenz and P. Zerwas, *Higgs boson production at the LHC*, *Nucl. Phys. B* **453** (1995) 17 [hep-ph/9504378].

[109] R. Harlander and P. Kant, *Higgs production and decay: Analytic results at next-to-leading order QCD*, *JHEP* **12** (2005) 015 [hep-ph/0509189].

[110] C. Anastasiou, S. Beerli, S. Bucherer, A. Daleo and Z. Kunszt, *Two-loop amplitudes and master integrals for the production of a Higgs boson via a massive quark and a scalar-quark loop*, *JHEP* **01** (2007) 082 [hep-ph/0611236].

[111] U. Aglietti, R. Bonciani, G. Degrassi and A. Vicini, *Analytic Results for Virtual QCD Corrections to Higgs Production and Decay*, *JHEP* **01** (2007) 021 [hep-ph/0611266].

[112] C. Brønnum-Hansen and C.-Y. Wang, *Contribution of third generation quarks to*

two-loop helicity amplitudes for W boson pair production in gluon fusion, 2009.03742.

[113] C. Brønnum-Hansen and C.-Y. Wang, *Top quark contribution to two-loop helicity amplitudes for Z boson pair production in gluon fusion*, 2101.12095.

[114] ATLAS collaboration, *Search for resonances in diphoton events at $\sqrt{s}$=13 TeV with the ATLAS detector*, *JHEP* **09** (2016) 001 [1606.03833].

[115] CMS collaboration, *Search for physics beyond the standard model in high-mass diphoton events from proton-proton collisions at $\sqrt{s}$ = 13 TeV*, *Phys. Rev. D* **98** (2018) 092001 [1809.00327].

[116] S. Amoroso et al., *Les Houches 2019: Physics at TeV Colliders: Standard Model Working Group Report*, in *11th Les Houches Workshop on Physics at TeV Colliders: PhysTeV Les Houches*, 3, 2020 [2003.01700].

[117] E.W.N. Glover and M.E. Tejeda-Yeomans, *Two loop QCD helicity amplitudes for massless quark massless gauge boson scattering*, *JHEP* **06** (2003) 033 [hep-ph/0304169].

[118] Z. Bern, A. De Freitas and L.J. Dixon, *Two loop amplitudes for gluon fusion into two photons*, *JHEP* **09** (2001) 037 [hep-ph/0109078].

[119] S. Catani, L. Cieri, D. de Florian, G. Ferrera and M. Grazzini, *Diphoton production at hadron colliders: a fully-differential QCD calculation at NNLO*, *Phys. Rev. Lett.* **108** (2012) 072001 [1110.2375].

[120] T. Gehrmann, N. Glover, A. Huss and J. Whitehead, *Scale and isolation sensitivity of diphoton distributions at the LHC*, *JHEP* **01** (2021) 108 [2009.11310].

[121] T. Ahmed, J. Henn and B. Mistlberger, *Four-particle scattering amplitudes in QCD at NNLO to higher orders in the dimensional regulator*, *JHEP* **12** (2019) 177 [1910.06684].

[122] J. Henn, B. Mistlberger, V.A. Smirnov and P. Wasser, *Constructing d-log integrands and computing master integrals for three-loop four-particle scattering*, *JHEP* **04** (2020) 167 [2002.09492].

[123] F. Caola, A. Von Manteuffel and L. Tancredi, *Diphoton Amplitudes in Three-Loop Quantum Chromodynamics*, *Phys. Rev. Lett.* **126** (2021) 112004 [2011.13946].

[124] V. Del Duca, F. Maltoni, Z. Nagy and Z. Trocsanyi, *QCD radiative corrections to prompt diphoton production in association with a jet at hadron colliders*, *JHEP* **04** (2003) 059 [hep-ph/0303012].

[125] T. Gehrmann, N. Greiner and G. Heinrich, *Photon isolation effects at NLO in $\gamma\gamma$ + jet final states in hadronic collisions*, *JHEP* **06** (2013) 058 [1303.0824].

[126] T. Gehrmann, J.M. Henn and N.A. Lo Presti, *Analytic form of the two-loop planar five-gluon all-plus-helicity amplitude in QCD*, *Phys. Rev. Lett.* **116** (2016) 062001 [1511.05409].

[127] S. Badger, C. Brønnum-Hansen, H.B. Hartanto and T. Peraro, *First look at two-loop five-gluon scattering in QCD*, *Phys. Rev. Lett.* **120** (2018) 092001 [1712.02229].

[128] S. Abreu, F. Febres Cordero, H. Ita, B. Page and M. Zeng, *Planar Two-Loop Five-Gluon Amplitudes from Numerical Unitarity*, *Phys. Rev.* **D97** (2018) 116014 [1712.03946].

[129] S. Abreu, F. Febres Cordero, H. Ita, B. Page and V. Sotnikov, *Planar Two-Loop Five-Parton Amplitudes from Numerical Unitarity*, *JHEP* **11** (2018) 116 [1809.09067].

[130] S. Abreu, B. Page, E. Pascual and V. Sotnikov, *Leading-Color Two-Loop QCD Corrections for Three-Photon Production at Hadron Colliders*, *JHEP* **01** (2021) 078 [2010.15834].

[131] S. Badger, C. Brønnum-Hansen, H.B. Hartanto and T. Peraro, *Analytic helicity amplitudes for two-loop five-gluon scattering: the single-minus case*, *JHEP* **01** (2019) 186 [1811.11699].

[132] H.A. Chawdhry, M. Czakon, A. Mitov and R. Poncelet, *Two-loop leading-color helicity amplitudes for three-photon production at the LHC*, 2012.13553.

[133] G. De Laurentis and D. Maître, *Two-Loop Five-Parton Leading-Colour Finite Remainders in the Spinor-Helicity Formalism*, *JHEP* **02** (2021) 016 [2010.14525].

[134] B. Agarwal, F. Buccioni, A. von Manteuffel and L. Tancredi, *Two-loop leading colour QCD corrections to $q\bar{q} \to \gamma\gamma g$ and $qg \to \gamma\gamma q$*, *JHEP* **04** (2021) 201 [2102.01820].

[135] S. Badger, H.B. Hartanto and S. Zoia, *Two-loop QCD corrections to $Wb\bar{b}$ production at hadron colliders*, 2102.02516.

[136] S. Abreu, F. Febres Cordero, H. Ita, B. Page and V. Sotnikov, *Leading-Color Two-Loop QCD Corrections for Three-Jet Production at Hadron Colliders*, 2102.13609.

[137] S. Badger, D. Chicherin, T. Gehrmann, G. Heinrich, J.M. Henn, T. Peraro et al., *Analytic form of the full two-loop five-gluon all-plus helicity amplitude*, *Phys. Rev. Lett.* **123** (2019) 071601 [1905.03733].

[138] B. Agarwal, F. Buccioni, A. von Manteuffel and L. Tancredi, *Two-loop helicity amplitudes for diphoton plus jet production in full color*, 2105.04585.

[139] S. Badger, C. Brønnum-Hansen, D. Chicherin, T. Gehrmann, H.B. Hartanto, J. Henn et al., *Virtual QCD corrections to gluon-initiated diphoton plus jet production at hadron colliders*, 2106.08664.

[140] M. Gell-Mann, *Isotopic spin and new unstable particles*, *Phys. Rev.* **92** (1953) 833.

[141] T. Nakano and K. Nishijima, *Charge Independence for V-particles**, *Progress of Theoretical Physics* **10** (1953) 581 [https://academic.oup.com/ptp/article-pdf/10/5/581/5364926/10-5-581.pdf].

[142] M. Gell-Mann, *The eightfold way: A theory of strong interaction symmetry*, .

[143] Y. Ne'eman, *Derivation of strong interactions from a gauge invariance*, *Nuclear Physics* **26** (1961) 222.

[144] M. Gell-Mann, *A schematic model of baryons and mesons*, *Physics Letters* **8** (1964) 214.

[145] G. Zweig, *An SU(3) model for strong interaction symmetry and its breaking. Version 2*, in *DEVELOPMENTS IN THE QUARK THEORY OF HADRONS. VOL. 1. 1964*

- *1978*, D.B. Lichtenberg and S.P. Rosen, eds. (1964).

[146] O.W. Greenberg, *Spin and Unitary Spin Independence in a Paraquark Model of Baryons and Mesons*, *Phys. Rev. Lett.* **13** (1964) 598.

[147] M.Y. Han and Y. Nambu, *Three Triplet Model with Double SU(3) Symmetry*, *Phys. Rev.* **139** (1965) B1006.

[148] H. Fritzsch, M. Gell-Mann and H. Leutwyler, *Advantages of the Color Octet Gluon Picture*, *Phys. Lett. B* **47** (1973) 365.

[149] L.D. Faddeev and V.N. Popov, *Feynman Diagrams for the Yang-Mills Field*, *Phys. Lett. B* **25** (1967) 29.

[150] D.F. Litim and J.M. Pawlowski, *Flow equations for Yang-Mills theories in general axial gauges*, *Phys. Lett. B* **435** (1998) 181 [hep-th/9802064].

[151] C.G. Bollini and J.J. Giambiagi, *Dimensional Renormalization: The Number of Dimensions as a Regularizing Parameter*, *Nuovo Cim. B* **12** (1972) 20.

[152] G.M. Cicuta and E. Montaldi, *Analytic renormalization via continuous space dimension*, *Lett. Nuovo Cim.* **4** (1972) 329.

[153] G. 't Hooft and M.J.G. Veltman, *Regularization and Renormalization of Gauge Fields*, *Nucl. Phys. B* **44** (1972) 189.

[154] J.F. Ashmore, *A Method of Gauge Invariant Regularization*, *Lett. Nuovo Cim.* **4** (1972) 289.

[155] W.J. Marciano, *Dimensional Regularization and Mass Singularities*, *Phys. Rev. D* **12** (1975) 3861.

[156] T. Peraro and L. Tancredi, *Physical projectors for multi-leg helicity amplitudes*, *JHEP* **07** (2019) 114 [1906.03298].

[157] T. Peraro and L. Tancredi, *Tensor decomposition for bosonic and fermionic scattering amplitudes*, *Phys. Rev. D* **103** (2021) 054042 [2012.00820].

[158] G. 't Hooft, *Dimensional regularization and the renormalization group*, *Nucl. Phys. B* **61** (1973) 455.

[159] S. Weinberg, *New approach to the renormalization group*, *Phys. Rev. D* **8** (1973) 3497.

[160] N.N. Bogoliubov and O.S. Parasiuk, *On the Multiplication of the causal function in the quantum theory of fields*, *Acta Math.* **97** (1957) 227.

[161] K. Hepp, *Proof of the Bogolyubov-Parasiuk theorem on renormalization*, *Commun. Math. Phys.* **2** (1966) 301.

[162] W. Zimmermann, *Convergence of Bogolyubov's method of renormalization in momentum space*, *Commun. Math. Phys.* **15** (1969) 208.

[163] G. 't Hooft, *Renormalizable Lagrangians for Massive Yang-Mills Fields*, *Nucl. Phys. B* **35** (1971) 167.

[164] F. Bloch and A. Nordsieck, *Note on the Radiation Field of the electron*, *Phys. Rev.* **52** (1937) 54.

[165] D.R. Yennie, S.C. Frautschi and H. Suura, *The infrared divergence phenomena and high-energy processes*, *Annals Phys.* **13** (1961) 379.

[166] T. Kinoshita, *Mass singularities of Feynman amplitudes*, *J. Math. Phys.* **3** (1962) 650.

[167] T.D. Lee and M. Nauenberg, *Degenerate Systems and Mass Singularities*, *Phys. Rev.* **133** (1964) B1549.

[168] N. Nakanishi, *General Theory of Infrared Divergence*, *Progress of Theoretical Physics* **19** (1958) 159 [https://academic.oup.com/ptp/article-pdf/19/2/159/5387237/19-2-159.pdf].

[169] S. Catani, S. Dittmaier, M.H. Seymour and Z. Trocsanyi, *The Dipole formalism for next-to-leading order QCD calculations with massive partons*, *Nucl. Phys. B* **627** (2002) 189 [hep-ph/0201036].

[170] S. Frixione, Z. Kunszt and A. Signer, *Three jet cross-sections to next-to-leading*

order, *Nucl. Phys. B* **467** (1996) 399 [hep-ph/9512328].

[171] S. Frixione, *A General approach to jet cross-sections in QCD*, *Nucl. Phys. B* **507** (1997) 295 [hep-ph/9706545].

[172] Z. Nagy and D.E. Soper, *General subtraction method for numerical calculation of one loop QCD matrix elements*, *JHEP* **09** (2003) 055 [hep-ph/0308127].

[173] T. Gleisberg and F. Krauss, *Automating dipole subtraction for QCD NLO calculations*, *Eur. Phys. J. C* **53** (2008) 501 [0709.2881].

[174] R. Frederix, S. Frixione, F. Maltoni and T. Stelzer, *Automation of next-to-leading order computations in QCD: The FKS subtraction*, *JHEP* **10** (2009) 003 [0908.4272].

[175] W.J. Torres Bobadilla et al., *May the four be with you: Novel IR-subtraction methods to tackle NNLO calculations*, *Eur. Phys. J. C* **81** (2021) 250 [2012.02567].

[176] D.J. Gross and F. Wilczek, *Ultraviolet Behavior of Nonabelian Gauge Theories*, *Phys. Rev. Lett.* **30** (1973) 1343.

[177] H.D. Politzer, *Reliable Perturbative Results for Strong Interactions?*, *Phys. Rev. Lett.* **30** (1973) 1346.

[178] *78 - the removal of infinities in quantum electrodynamics*, in *Collected Papers of L.D. Landau*, D. TER HAAR, ed., pp. 607–610, Pergamon (1965), DOI.

[179] NNPDF collaboration, *Parton distributions from high-precision collider data*, *Eur. Phys. J. C* **77** (2017) 663 [1706.00428].

[180] T.-J. Hou et al., *New CTEQ global analysis of quantum chromodynamics with high-precision data from the LHC*, *Phys. Rev. D* **103** (2021) 014013 [1912.10053].

[181] S. Bailey, T. Cridge, L.A. Harland-Lang, A.D. Martin and R.S. Thorne, *Parton distributions from LHC, HERA, Tevatron and fixed target data: MSHT20 PDFs*, *Eur. Phys. J. C* **81** (2021) 341 [2012.04684].

[182] Y.L. Dokshitzer, *Calculation of the Structure Functions for Deep Inelastic Scattering*

and e+ e- Annihilation by Perturbation Theory in Quantum Chromodynamics., *Sov. Phys. JETP* **46** (1977) 641.

[183] V.N. Gribov and L.N. Lipatov, *Deep inelastic e p scattering in perturbation theory*, *Sov. J. Nucl. Phys.* **15** (1972) 438.

[184] G. Altarelli and G. Parisi, *Asymptotic Freedom in Parton Language*, *Nucl. Phys. B* **126** (1977) 298.

[185] G.T. Bodwin, *Factorization of the Drell-Yan Cross-Section in Perturbation Theory*, *Phys. Rev. D* **31** (1985) 2616.

[186] J.C. Collins, D.E. Soper and G.F. Sterman, *Factorization for Short Distance Hadron - Hadron Scattering*, *Nucl. Phys. B* **261** (1985) 104.

[187] J.C. Collins, D.E. Soper and G.F. Sterman, *Soft Gluons and Factorization*, *Nucl. Phys. B* **308** (1988) 833.

[188] J.C. Collins, D.E. Soper and G.F. Sterman, *Factorization of Hard Processes in QCD*, *Adv. Ser. Direct. High Energy Phys.* **5** (1989) 1 [hep-ph/0409313].

[189] S.D. Ellis, J. Huston, K. Hatakeyama, P. Loch and M. Tonnesmann, *Jets in hadron-hadron collisions*, *Prog. Part. Nucl. Phys.* **60** (2008) 484 [0712.2447].

[190] G.P. Salam, *Towards Jetography*, *Eur. Phys. J. C* **67** (2010) 637 [0906.1833].

[191] M. Cacciari, *Phenomenological and theoretical developments in jet physics at the LHC*, *Int. J. Mod. Phys. A* **30** (2015) 1546001 [1509.02272].

[192] S.L. Glashow, *The renormalizability of vector meson interactions*, *Nucl. Phys.* **10** (1959) 107.

[193] A. Salam and J.C. Ward, *Weak and electromagnetic interactions*, *Nuovo Cim.* **11** (1959) 568.

[194] A. Salam and J.C. Ward, *Electromagnetic and weak interactions*, *Phys. Lett.* **13** (1964) 168.

[195] S. Weinberg, *A Model of Leptons*, *Phys. Rev. Lett.* **19** (1967) 1264.

[196] P. Sikivie, L. Susskind, M.B. Voloshin and V.I. Zakharov, *Isospin Breaking in Technicolor Models*, *Nucl. Phys. B* **173** (1980) 189.

[197] H. Georgi, *Effective field theory*, *Ann. Rev. Nucl. Part. Sci.* **43** (1993) 209.

[198] S. Bilenky, *Neutrino oscillations: From a historical perspective to the present status*, *Nucl. Phys. B* **908** (2016) 2 [1602.00170].

[199] F. Capozzi, E. Lisi, A. Marrone, D. Montanino and A. Palazzo, *Neutrino masses and mixings: Status of known and unknown* 3ν *parameters*, *Nucl. Phys. B* **908** (2016) 218 [1601.07777].

[200] F. Berends, R. Kleiss, P. De Causmaecker, R. Gastmans and T.T. Wu, *Single bremsstrahlung processes in gauge theories*, *Physics Letters B* **103** (1981) 124.

[201] Z. Xu, D.-H. Zhang and L. Chang, *Helicity Amplitudes for Multiple Bremsstrahlung in Massless Nonabelian Gauge Theories*, *Nucl. Phys. B* **291** (1987) 392.

[202] L.J. Dixon, *Calculating scattering amplitudes efficiently*, in *Theoretical Advanced Study Institute in Elementary Particle Physics (TASI 95): QCD and Beyond*, 1, 1996 [hep-ph/9601359].

[203] M.L. Mangano and S.J. Parke, *Multiparton amplitudes in gauge theories*, *Phys. Rept.* **200** (1991) 301 [hep-th/0509223].

[204] M.E. Peskin, *Simplifying Multi-Jet QCD Computation*, in *13th Mexican School of Particles and Fields*, 1, 2011 [1101.2414].

[205] S.J. Parke and T.R. Taylor, *Amplitude for n-gluon scattering*, *Phys. Rev. Lett.* **56** (1986) 2459.

[206] F. Berends and W. Giele, *Recursive calculations for processes with n gluons*, *Nuclear Physics B* **306** (1988) 759.

[207] P. Nogueira, *Automatic feynman graph generation*, *Journal of Computational Physics*

105 (1993) 279 .

[208] B. Ruijl, T. Ueda and J. Vermaseren, *FORM version 4.2*, 1707.06453.

[209] J. Kuipers, T. Ueda, J.A.M. Vermaseren and J. Vollinga, `FORM` *version 4.0*, *Comput. Phys. Commun.* **184** (2013) 1453 [1203.6543].

[210] J.A.M. Vermaseren, *New features of FORM*, math-ph/0010025.

[211] D. Kreimer, *The $\gamma(5)$ Problem and Anomalies: A Clifford Algebra Approach*, *Phys. Lett. B* **237** (1990) 59.

[212] J. Korner, D. Kreimer and K. Schilcher, *A Practicable gamma(5) scheme in dimensional regularization*, *Z. Phys. C* **54** (1992) 503.

[213] D. Kreimer, *The Role of gamma(5) in dimensional regularization*, hep-ph/9401354.

[214] P. Breitenlohner and D. Maison, *Dimensionally Renormalized Green's Functions for Theories with Massless Particles. 1.*, *Commun. Math. Phys.* **52** (1977) 39.

[215] P. Breitenlohner and D. Maison, *Dimensionally Renormalized Green's Functions for Theories with Massless Particles. 2.*, *Commun. Math. Phys.* **52** (1977) 55.

[216] P. Breitenlohner and D. Maison, *Dimensional Renormalization and the Action Principle*, *Commun. Math. Phys.* **52** (1977) 11.

[217] D.B. Melrose, *Reduction of Feynman diagrams*, *Nuovo Cim.* **40** (1965) 181.

[218] W.L. van Neerven and J.A.M. Vermaseren, *LARGE LOOP INTEGRALS*, *Phys. Lett. B* **137** (1984) 241.

[219] Z. Bern, L.J. Dixon and D.A. Kosower, *Dimensionally regulated one loop integrals*, *Phys. Lett. B* **302** (1993) 299 [hep-ph/9212308].

[220] G. Passarino and M.J.G. Veltman, *One Loop Corrections for e+ e- Annihilation Into mu+ mu- in the Weinberg Model*, *Nucl. Phys. B* **160** (1979) 151.

[221] T. Hahn and M. Perez-Victoria, *Automatized one loop calculations in four-dimensions and D-dimensions*, *Comput. Phys. Commun.* **118** (1999) 153 [hep-ph/9807565].

[222] R.K. Ellis and G. Zanderighi, *Scalar one-loop integrals for QCD*, *JHEP* **02** (2008) 002 [0712.1851].

[223] A. van Hameren, *OneLOop: For the evaluation of one-loop scalar functions*, *Comput. Phys. Commun.* **182** (2011) 2427 [1007.4716].

[224] G. Cullen, J.P. Guillet, G. Heinrich, T. Kleinschmidt, E. Pilon, T. Reiter et al., *Golem95C: A library for one-loop integrals with complex masses*, *Comput. Phys. Commun.* **182** (2011) 2276 [1101.5595].

[225] A. Denner, S. Dittmaier and L. Hofer, *COLLIER - A fortran-library for one-loop integrals*, *PoS* **LL2014** (2014) 071 [1407.0087].

[226] H.H. Patel, *Package-X: A Mathematica package for the analytic calculation of one-loop integrals*, *Comput. Phys. Commun.* **197** (2015) 276 [1503.01469].

[227] L.J. Dixon, *A brief introduction to modern amplitude methods*, in *Theoretical Advanced Study Institute in Elementary Particle Physics: Particle Physics: The Higgs Boson and Beyond*, 10, 2013, DOI [1310.5353].

[228] Z. Bern, L.J. Dixon and D.A. Kosower, *One loop amplitudes for e+ e- to four partons*, *Nucl. Phys. B* **513** (1998) 3 [hep-ph/9708239].

[229] R.K. Ellis, W.T. Giele and Z. Kunszt, *A Numerical Unitarity Formalism for Evaluating One-Loop Amplitudes*, *JHEP* **03** (2008) 003 [0708.2398].

[230] W.T. Giele, Z. Kunszt and K. Melnikov, *Full one-loop amplitudes from tree amplitudes*, *JHEP* **04** (2008) 049 [0801.2237].

[231] P. Mastrolia, G. Ossola, C.G. Papadopoulos and R. Pittau, *Optimizing the Reduction of One-Loop Amplitudes*, *JHEP* **06** (2008) 030 [0803.3964].

[232] P. Mastrolia, E. Mirabella and T. Peraro, *Integrand reduction of one-loop scattering amplitudes through Laurent series expansion*, *JHEP* **06** (2012) 095 [1203.0291].

[233] G. Ossola, C.G. Papadopoulos and R. Pittau, *CutTools: A Program implementing the OPP reduction method to compute one-loop amplitudes*, *JHEP* **03** (2008) 042 [0711.3596].

[234] P. Mastrolia, G. Ossola, T. Reiter and F. Tramontano, *Scattering AMplitudes from Unitarity-based Reduction Algorithm at the Integrand-level*, *JHEP* **08** (2010) 080 [1006.0710].

[235] T. Peraro, *Ninja: Automated Integrand Reduction via Laurent Expansion for One-Loop Amplitudes*, *Comput. Phys. Commun.* **185** (2014) 2771 [1403.1229].

[236] C.F. Berger, Z. Bern, L.J. Dixon, F. Febres Cordero, D. Forde, H. Ita et al., *An Automated Implementation of On-Shell Methods for One-Loop Amplitudes*, *Phys. Rev. D* **78** (2008) 036003 [0803.4180].

[237] G. Bevilacqua, M. Czakon, M.V. Garzelli, A. van Hameren, A. Kardos, C.G. Papadopoulos et al., *HELAC-NLO*, *Comput. Phys. Commun.* **184** (2013) 986 [1110.1499].

[238] J. Alwall, R. Frederix, S. Frixione, V. Hirschi, F. Maltoni, O. Mattelaer et al., *The automated computation of tree-level and next-to-leading order differential cross sections, and their matching to parton shower simulations*, *JHEP* **07** (2014) 079 [1405.0301].

[239] G. Cullen et al., *GOSAM-2.0: a tool for automated one-loop calculations within the Standard Model and beyond*, *Eur. Phys. J. C* **74** (2014) 3001 [1404.7096].

[240] F. Buccioni, J.-N. Lang, J.M. Lindert, P. Maierhöfer, S. Pozzorini, H. Zhang et al., *OpenLoops 2*, *Eur. Phys. J. C* **79** (2019) 866 [1907.13071].

[241] F. del Aguila and R. Pittau, *Recursive numerical calculus of one-loop tensor integrals*, *JHEP* **07** (2004) 017 [hep-ph/0404120].

[242] K.G. Chetyrkin and F.V. Tkachov, *Integration by Parts: The Algorithm to Calculate beta Functions in 4 Loops*, *Nucl. Phys.* **B192** (1981) 159.

[243] C. Studerus, `Reduze`-*Feynman Integral Reduction in* `C++`, *Comput. Phys. Commun.* **181** (2010) 1293 [0912.2546].

[244] A. von Manteuffel and C. Studerus, *Reduze 2 - Distributed Feynman Integral Reduction*, 1201.4330.

[245] C.W. Bauer, A. Frink and R. Kreckel, *Introduction to the* `GiNaC` *framework for symbolic computation within the* `C++` *programming language*, *J. Symb. Comput.* **33** (2002) 1 [cs/0004015].

[246] R.H. Lewis, "*Computer Algebra System* `Fermat`." `http://home.bway.net/lewis/`.

[247] S. Laporta, *High precision calculation of multiloop Feynman integrals by difference equations*, *Int. J. Mod. Phys.* **A15** (2000) 5087 [hep-ph/0102033].

[248] C. Anastasiou and A. Lazopoulos, *Automatic integral reduction for higher order perturbative calculations*, *JHEP* **07** (2004) 046 [hep-ph/0404258].

[249] R.N. Lee, *Presenting LiteRed: a tool for the Loop InTEgrals REDuction*, 1212.2685.

[250] P. Maierhöfer, J. Usovitsch and P. Uwer, *Kira—A Feynman integral reduction program*, *Comput. Phys. Commun.* **230** (2018) 99 [1705.05610].

[251] A. Smirnov and F. Chuharev, *FIRE6: Feynman Integral REduction with Modular Arithmetic*, 1901.07808.

[252] J. Gluza, K. Kajda and D.A. Kosower, *Towards a Basis for Planar Two-Loop Integrals*, *Phys. Rev.* **D83** (2011) 045012 [1009.0472].

[253] R.M. Schabinger, *A New Algorithm For The Generation Of Unitarity-Compatible Integration By Parts Relations*, *JHEP* **01** (2012) 077 [1111.4220].

[254] P.A. Baikov, *Explicit solutions of the three loop vacuum integral recurrence relations*, *Phys. Lett.* **B385** (1996) 404 [hep-ph/9603267].

[255] R.N. Lee, *Calculating multiloop integrals using dimensional recurrence relation and D-analyticity*, *Nucl. Phys. B Proc. Suppl.* **205-206** (2010) 135 [1007.2256].

[256] H. Frellesvig and C.G. Papadopoulos, *Cuts of Feynman Integrals in Baikov representation*, *JHEP* **04** (2017) 083 [1701.07356].

[257] M. Harley, F. Moriello and R.M. Schabinger, *Baikov-Lee Representations Of Cut Feynman Integrals*, *JHEP* **06** (2017) 049 [1705.03478].

[258] R.E. Cutkosky, *Singularities and discontinuities of Feynman amplitudes*, *J. Math. Phys.* **1** (1960) 429.

[259] R.N. Lee and V.A. Smirnov, *The Dimensional Recurrence and Analyticity Method for Multicomponent Master Integrals: Using Unitarity Cuts to Construct Homogeneous Solutions*, *JHEP* **12** (2012) 104 [1209.0339].

[260] S. Abreu, R. Britto, C. Duhr and E. Gardi, *Cuts from residues: the one-loop case*, *JHEP* **06** (2017) 114 [1702.03163].

[261] G. 't Hooft and M.J.G. Veltman, *DIAGRAMMAR*, *NATO Sci. Ser. B* **4** (1974) 177.

[262] M.J.G. Veltman, *Diagrammatica: The Path to Feynman rules*, vol. 4, Cambridge University Press (5, 2012).

[263] R.G. Newton, *Optical theorem and beyond*, *American Journal of Physics* **44** (1976) 639 [https://doi.org/10.1119/1.10324].

[264] A. Primo and L. Tancredi, *On the maximal cut of Feynman integrals and the solution of their differential equations*, *Nucl. Phys. B* **916** (2017) 94 [1610.08397].

[265] D. Chicherin, T. Gehrmann, J.M. Henn, P. Wasser, Y. Zhang and S. Zoia, *All Master Integrals for Three-Jet Production at Next-to-Next-to-Leading Order*, *Phys. Rev. Lett.* **123** (2019) 041603 [1812.11160].

[266] C. Dlapa, X. Li and Y. Zhang, *Leading singularities in Baikov representation and Feynman integrals with uniform transcendental weight*, 2103.04638.

[267] H. Ita, *Two-loop Integrand Decomposition into Master Integrals and Surface Terms*, *Phys. Rev.* **D94** (2016) 116015 [1510.05626].

[268] K.J. Larsen and Y. Zhang, *Integration-by-parts reductions from unitarity cuts and algebraic geometry*, *Phys. Rev.* **D93** (2016) 041701 [1511.01071].

[269] R.N. Lee, *Modern techniques of multiloop calculations*, in *49th Rencontres de Moriond on QCD and High Energy Interactions*, pp. 297–300, 2014 [1405.5616].

[270] Y. Zhang, *Lecture Notes on Multi-loop Integral Reduction and Applied Algebraic Geometry*, 12, 2016 [1612.02249].

[271] J. Böhm, A. Georgoudis, K.J. Larsen, M. Schulze and Y. Zhang, *Complete sets of logarithmic vector fields for integration-by-parts identities of Feynman integrals*, *Phys. Rev.* **D98** (2018) 025023 [1712.09737].

[272] W. Decker, G.-M. Greuel, G. Pfister and H. Schönemann, "SINGULAR 4-1-2 — A computer algebra system for polynomial computations." `http://www.singular.uni-kl.de`, 2019.

[273] A. von Manteuffel and R.M. Schabinger, *A novel approach to integration by parts reduction*, *Phys. Lett.* **B744** (2015) 101 [1406.4513].

[274] T. Peraro, *Scattering amplitudes over finite fields and multivariate functional reconstruction*, *JHEP* **12** (2016) 030 [1608.01902].

[275] D. Cabarcas and J. Ding, *Linear Algebra to Compute Syzygies and Gröbner Bases*, *ACM Press* (2011) .

[276] A. von Manteuffel, *Finred, (to appear)* .

[277] S. Abreu, J. Dormans, F. Febres Cordero, H. Ita and B. Page, *Analytic Form of Planar Two-Loop Five-Gluon Scattering Amplitudes in QCD*, *Phys. Rev. Lett.* **122** (2019) 082002 [1812.04586].

[278] M. Heller and A. von Manteuffel, *MultivariateApart: Generalized Partial Fractions*, 2101.08283.

[279] A.V. Kotikov, *Differential equations method: New technique for massive Feynman diagrams calculation*, *Phys. Lett.* **B254** (1991) 158.

[280] E. Remiddi, *Differential equations for Feynman graph amplitudes*, *Nuovo Cim.* **A110** (1997) 1435 [hep-th/9711188].

[281] T. Gehrmann and E. Remiddi, *Differential equations for two loop four point functions*, *Nucl. Phys.* **B580** (2000) 485 [hep-ph/9912329].

[282] M. Argeri and P. Mastrolia, *Feynman Diagrams and Differential Equations*, *Int. J. Mod. Phys.* **A22** (2007) 4375 [0707.4037].

[283] J.M. Henn, *Multiloop integrals in dimensional regularization made simple*, *Phys. Rev. Lett.* **110** (2013) 251601 [1304.1806].

[284] M. Heller, A. von Manteuffel and R.M. Schabinger, *Multiple polylogarithms with algebraic arguments and the two-loop EW-QCD Drell-Yan master integrals*, *Phys. Rev. D* **102** (2020) 016025 [1907.00491].

[285] M. Roth and A. Denner, *High-energy approximation of one loop Feynman integrals*, *Nucl. Phys. B* **479** (1996) 495 [hep-ph/9605420].

[286] T. Binoth and G. Heinrich, *An automatized algorithm to compute infrared divergent multiloop integrals*, *Nucl. Phys. B* **585** (2000) 741 [hep-ph/0004013].

[287] C. Bogner and S. Weinzierl, *Resolution of singularities for multi-loop integrals*, *Comput. Phys. Commun.* **178** (2008) 596 [0709.4092].

[288] A.V. Kotikov, *The Property of maximal transcendentality in the N=4 Supersymmetric Yang-Mills*, 5, 2010 [1005.5029].

[289] E. Kummer, *Ueber die transcendenten, welche aus wiederholten integrationen rationaler formeln entstehen.*, .

[290] N. Nielsen, "Der *Euler*sche Dilogarithmus und seine Verallgemeinerungen. Eine Monographie.." Nova Acta Leop. 90, 121-211 (1909)., 1909.

[291] A.B. Goncharov, *Multiple polylogarithms, cyclotomy and modular complexes*, *Math. Res. Lett.* **5** (1998) 497 [1105.2076].

[292] A.B. Goncharov, M. Spradlin, C. Vergu and A. Volovich, *Classical Polylogarithms for Amplitudes and Wilson Loops*, *Phys. Rev. Lett.* **105** (2010) 151605 [1006.5703].

[293] C. Duhr, H. Gangl and J.R. Rhodes, *From polygons and symbols to polylogarithmic functions*, *JHEP* **10** (2012) 075 [1110.0458].

[294] C. Duhr, *Hopf algebras, coproducts and symbols: an application to Higgs boson amplitudes*, *JHEP* **08** (2012) 043 [1203.0454].

[295] C. Duhr, *Mathematical aspects of scattering amplitudes*, in *Theoretical Advanced Study Institute in Elementary Particle Physics: Journeys Through the Precision Frontier: Amplitudes for Colliders*, 11, 2014, DOI [1411.7538].

[296] T. Gehrmann and E. Remiddi, *Numerical evaluation of two-dimensional harmonic polylogarithms*, *Comput. Phys. Commun.* **144** (2002) 200 [hep-ph/0111255].

[297] T. Gehrmann and E. Remiddi, *Numerical evaluation of harmonic polylogarithms*, *Comput. Phys. Commun.* **141** (2001) 296 [hep-ph/0107173].

[298] J. Vollinga and S. Weinzierl, *Numerical evaluation of multiple polylogarithms*, *Comput. Phys. Commun.* **167** (2005) 177 [hep-ph/0410259].

[299] S. Buehler and C. Duhr, *CHAPLIN - Complex Harmonic Polylogarithms in Fortran*, *Comput. Phys. Commun.* **185** (2014) 2703 [1106.5739].

[300] C. Bogner, *MPL—A program for computations with iterated integrals on moduli spaces of curves of genus zero*, *Comput. Phys. Commun.* **203** (2016) 339 [1510.04562].

[301] H. Frellesvig, D. Tommasini and C. Wever, *On the reduction of generalized polylogarithms to Li_n and $Li_{2,2}$ and on the evaluation thereof*, *JHEP* **03** (2016) 189 [1601.02649].

[302] J. Ablinger, J. Blümlein, M. Round and C. Schneider, *Numerical Implementation of Harmonic Polylogarithms to Weight $w = 8$*, *Comput. Phys. Commun.* **240** (2019) 189 [1809.07084].

[303] C. Duhr and F. Dulat, *PolyLogTools — polylogs for the masses*, *JHEP* **08** (2019) 135 [1904.07279].

[304] T. Gehrmann, A. von Manteuffel, L. Tancredi and E. Weihs, *The two-loop master*

integrals for $q\overline{q} \to VV$, *JHEP* **06** (2014) 032 [1404.4853].

[305] T. Gehrmann, A. von Manteuffel and L. Tancredi, *The two-loop helicity amplitudes for $q\overline{q}' \to V_1V_2 \to 4$ leptons*, *JHEP* **09** (2015) 128 [1503.04812].

[306] J.M. Henn, K. Melnikov and V.A. Smirnov, *Two-loop planar master integrals for the production of off-shell vector bosons in hadron collisions*, *JHEP* **05** (2014) 090 [1402.7078].

[307] F. Caola, J.M. Henn, K. Melnikov and V.A. Smirnov, *Non-planar master integrals for the production of two off-shell vector bosons in collisions of massless partons*, *JHEP* **09** (2014) 043 [1404.5590].

[308] C.G. Papadopoulos, D. Tommasini and C. Wever, *The Pentabox Master Integrals with the Simplified Differential Equations approach*, *JHEP* **04** (2016) 078 [1511.09404].

[309] T. Gehrmann, J. Henn and N. Lo Presti, *Pentagon functions for massless planar scattering amplitudes*, *JHEP* **10** (2018) 103 [1807.09812].

[310] D. Chicherin, T. Gehrmann, J. Henn, N. Lo Presti, V. Mitev and P. Wasser, *Analytic result for the nonplanar hexa-box integrals*, *JHEP* **03** (2019) 042 [1809.06240].

[311] D. Chicherin and V. Sotnikov, *Pentagon Functions for Scattering of Five Massless Particles*, *JHEP* **20** (2020) 167 [2009.07803].

[312] R. Bonciani, V. Del Duca, H. Frellesvig, J.M. Henn, F. Moriello and V.A. Smirnov, *Two-loop planar master integrals for Higgs$\to$ 3 partons with full heavy-quark mass dependence*, *JHEP* **12** (2016) 096 [1609.06685].

[313] A. von Manteuffel and L. Tancredi, *A non-planar two-loop three-point function beyond multiple polylogarithms*, *JHEP* **06** (2017) 127 [1701.05905].

[314] J. Broedel, C. Duhr, F. Dulat, B. Penante and L. Tancredi, *Elliptic symbol calculus: from elliptic polylogarithms to iterated integrals of Eisenstein series*, *JHEP* **08** (2018) 014 [1803.10256].

[315] L. Adams, E. Chaubey and S. Weinzierl, *Analytic results for the planar double box*

integral relevant to top-pair production with a closed top loop, *JHEP* **10** (2018) 206 [1806.04981].

[316] R.N. Lee, *Symmetric ϵ- and $(\epsilon + 1/2)$-forms and quadratic constraints in "elliptic" sectors*, *JHEP* **10** (2018) 176 [1806.04846].

[317] M. Walden and S. Weinzierl, *Numerical evaluation of iterated integrals related to elliptic Feynman integrals*, 2010.05271.

[318] F. Brown and C. Duhr, *A double integral of dlog forms which is not polylogarithmic*, 6, 2020 [2006.09413].

[319] U. Aglietti, R. Bonciani, L. Grassi and E. Remiddi, *The Two loop crossed ladder vertex diagram with two massive exchanges*, *Nucl. Phys. B* **789** (2008) 45 [0705.2616].

[320] R.N. Lee, A.V. Smirnov and V.A. Smirnov, *Solving differential equations for Feynman integrals by expansions near singular points*, *JHEP* **03** (2018) 008 [1709.07525].

[321] R. Bonciani, V. Del Duca, H. Frellesvig, J. Henn, M. Hidding, L. Maestri et al., *Evaluating a family of two-loop non-planar master integrals for Higgs + jet production with full heavy-quark mass dependence*, *JHEP* **01** (2020) 132 [1907.13156].

[322] H. Frellesvig, M. Hidding, L. Maestri, F. Moriello and G. Salvatori, *The complete set of two-loop master integrals for Higgs + jet production in QCD*, *JHEP* **06** (2020) 093 [1911.06308].

[323] S. Abreu, H. Ita, F. Moriello, B. Page, W. Tschernow and M. Zeng, *Two-Loop Integrals for Planar Five-Point One-Mass Processes*, *JHEP* **11** (2020) 117 [2005.04195].

[324] L. Adams and S. Weinzierl, *The ε-form of the differential equations for Feynman integrals in the elliptic case*, *Phys. Lett. B* **781** (2018) 270 [1802.05020].

[325] C. Bogner, S. Müller-Stach and S. Weinzierl, *The unequal mass sunrise integral expressed through iterated integrals on $\overline{\mathcal{M}}_{1,3}$*, *Nucl. Phys. B* **954** (2020) 114991 [1907.01251].

[326] V.A. Smirnov, *Evaluating Feynman integrals*, *Springer Tracts Mod. Phys.* **211** (2004) .

[327] G. Heinrich, *Collider Physics at the Precision Frontier*, 2009.00516.

[328] V.A. Smirnov, *Analytic tools for Feynman integrals*, *Springer Tracts Mod. Phys.* **250** (2012) .

[329] F.C.S. Brown, *On the periods of some feynman integrals*, 2010.

[330] E. Panzer, *Feynman integrals and hyperlogarithms*, Ph.D. thesis, Humboldt U., 2015. 1506.07243. 10.18452/17157.

[331] E. Panzer, *Algorithms for the symbolic integration of hyperlogarithms with applications to Feynman integrals*, *Comput. Phys. Commun.* **188** (2015) 148 [1403.3385].

[332] H. Cheng and T.T. Wu, *EXPANDING PROTONS: SCATTERING AT HIGH-ENERGIES* (1987).

[333] E. Panzer, *On the analytic computation of massless propagators in dimensional regularization*, *Nucl. Phys. B* **874** (2013) 567 [1305.2161].

[334] A. von Manteuffel, E. Panzer and R.M. Schabinger, *A quasi-finite basis for multi-loop Feynman integrals*, *JHEP* **02** (2015) 120 [1411.7392].

[335] G. Heinrich, *Sector Decomposition*, *Int. J. Mod. Phys.* **A23** (2008) 1457 [0803.4177].

[336] A.V. Smirnov, *FIESTA4: Optimized Feynman integral calculations with GPU support*, *Comput. Phys. Commun.* **204** (2016) 189 [1511.03614].

[337] S. Borowka, N. Greiner, G. Heinrich, S.P. Jones, M. Kerner, J. Schlenk et al., *Full top quark mass dependence in Higgs boson pair production at NLO*, *JHEP* **10** (2016) 107 [1608.04798].

[338] A. von Manteuffel and R.M. Schabinger, *Numerical Multi-Loop Calculations via Finite Integrals and One-Mass EW-QCD Drell-Yan Master Integrals*, *JHEP* **04**

(2017) 129 [1701.06583].

[339] Z. Bern, L.J. Dixon and D.A. Kosower, *The Five gluon amplitude and one loop integrals*, in *The Fermilab Meeting DPF 92. Proceedings, 7th Meeting of the American Physical Society, Division of Particles and Fields, Batavia, USA, November 10-14, 1992. Vol. 1, 2*, pp. 901–905, 1992, http://preprints.cern.ch/cgi-bin/setlink?base=preprintcateg=cernid=th.6733-92 [hep-ph/9212237].

[340] E. Panzer, *On hyperlogarithms and Feynman integrals with divergences and many scales*, *JHEP* **03** (2014) 071 [1401.4361].

[341] B. Agarwal and A. Von Manteuffel, *On the two-loop amplitude for $gg \to ZZ$ production with full top-mass dependence*, *PoS* **RADCOR2019** (2019) 008 [1912.08794].

[342] S. Borowka, G. Heinrich, S. Jones, M. Kerner, J. Schlenk and T. Zirke, *SecDec-3.0: numerical evaluation of multi-scale integrals beyond one loop*, *Comput. Phys. Commun.* **196** (2015) 470 [1502.06595].

[343] A. Smirnov and V. Smirnov, *How to choose master integrals*, 2002.08042.

[344] J. Usovitsch, *Factorization of denominators in integration-by-parts reductions*, 2002.08173.

[345] R.M. Schabinger, *Constructing multiloop scattering amplitudes with manifest singularity structure*, *Phys. Rev. D* **99** (2019) 105010 [1806.05682].

[346] A. Pak, *The Toolbox of modern multi-loop calculations: novel analytic and semi-analytic techniques*, *J. Phys. Conf. Ser.* **368** (2012) 012049 [1111.0868].

[347] J. Boehm, M. Wittmann, Z. Wu, Y. Xu and Y. Zhang, *IBP reduction coefficients made simple*, 2008.13194.

[348] W. Beenakker, S. Dittmaier, M. Kramer, B. Plumper, M. Spira and P. Zerwas, *NLO QCD corrections to t anti-t H production in hadron collisions*, *Nucl. Phys. B* **653** (2003) 151 [hep-ph/0211352].

[349] S. Catani, L. Cieri, D. de Florian, G. Ferrera and M. Grazzini, *Universality of transverse-momentum resummation and hard factors at the NNLO*, *Nucl. Phys. B* **881** (2014) 414 [1311.1654].

[350] S. Larin and J. Vermaseren, *The alpha-s**3 corrections to the Bjorken sum rule for polarized electroproduction and to the Gross-Llewellyn Smith sum rule*, *Phys. Lett. B* **259** (1991) 345.

[351] S. Larin, *The Renormalization of the axial anomaly in dimensional regularization*, *Phys. Lett. B* **303** (1993) 113 [hep-ph/9302240].

[352] J. Dick, F.Y. Kuo and I.H. Sloan, *High-dimensional integration: The quasi-monte carlo way*, *Acta Numerica* **22** (2013) 133–288.